Kazan Federal University
Zavoiskii Physical-Technical Institute
“Dynasty” Foundation
Bruker Ltd (Moscow)

ACTUAL PROBLEMS OF MAGNETIC RESONANCE AND ITS APPLICATION

XIII International Youth Scientific School

Program Lecture Notes Proceedings

Kazan
4 - 8 October 2010

Kazan Federal University
Zavoiskii Physical-Technical Institute
“Dynasty” Foundation
Bruker Ltd (Moscow)

ACTUAL PROBLEMS OF MAGNETIC RESONANCE AND ITS APPLICATION

XIII International Youth Scientific School

Program
Lecture Notes
Proceedings

Kazan
4 – 8 October 2010

KAZAN UNIVERSITY
2010

The administration of School

Professor M.S. Tagirov (KSU, Kazan) — rector
Professor V.A. Zhikharev (KSTU, Kazan) — vice-rector
V.K. Voronkova (KFTI RAS, Kazan) — scientific secretary
I.P. Volodina (KSU, Kazan) — secretary

The program committee

The chairman
Professor V.A. Atsarkin (IREE, Moscow)

Committee members

Professor A.V. Aganov (KSU, Kazan)
Professor B.I. Kochelaev (KSU, Kazan)
Professor I.V. Ovchinnikov (KFTI RAS, Kazan)
Professor K.M. Salikhov (KFTI RAS, Kazan)

Proceedings of the XIII International Youth Scientific School “Actual problems of magnetic resonance and its application”, 4 – 8 October 2010, Kazan. Edited by professor M.S. Tagirov (Kazan Federal University) and professor V.A. Zhikharev (Kazan State Technological University). – Kazan: Kazan Federal University, 2010. – 198 p.

The reports of young scientists submitted on XIII International Youth Scientific School “Actual problems of magnetic resonance and its application” carry out by Kazan Federal University and Zavoiskii Physical-Technical Institute are included in the present collection.

The organizing committee of School’2010

M.S. Tagirov, V.A. Zhikharev, I.P. Volodina, I.G. Motygullin
O.N. Chibisova, M.P. Rodionova, A.A. Rodionov, A.V. Klochkov,
E.M. Alakshin, V.V. Kuzmin

ISBN 978-5-98180-835-7

Program

Monday, October 4

11:00 – 11:30 **Opening Ceremony**

Lectures

11:30 – 12:30 **V.A. Atsarkin,** “Influence of a magnetic resonance on conductivity of materials with colossal magnetoresistance”

12:30 – 14:00 **Lunch**

14:00 – 15:00 D**.A. Konstantinov,** “Inter-subband Microwave Resonance in Surface Electrons on Liquid Helium”

Oral session

15:00 – 15:15 **N.R. Beysengulov,** “Microwave absorption study of pinning effects in novel iron-based pnictide superconductors”
15:15 – 15:30 **T.P. Gavrilova,** “ESR in new spin dimer system $Ba_3Cr_2O_8$ and $Sr_3Cr_2O_8$”
15:30 – 15:45 **D.R. Abdullin,** “ESR investigation of $Li_2Mn_2(MoO_4)_3$ compound as material for lithium-ion batteries”
15:45 – 16:00 **M.M. Akhmetov,** “Investigation of influence of excipients on paramagnetic centers formation at mechanoactivation of the calcium gluconate”

16:15 **Welcome party**

Tuesday, October 5

Lectures

9:30 – 10:30 **F.V. Toukach,** “Methods of 1D and 2D NMR in structural elucidation of natural glycopolymers”

10:30 – 10:45 **Coffee break**

10:45 – 11:45 **M.R. Gafurov,** “Dynamic Nuclear Polarization in High Magnetic Fields”

Oral session

11:45 – 12:00 **E.M. Alakshin,** “Low temperature magnetism of system “^3He-PrF_3 nanoparticles””
12:00 – 12:15 **D.A. Akhmetzyanov**, “High-frequency EPR – spectroscopy of Chromium Ions in Synthetic Forsterite”

12:30 – 14:00 **Lunch**

14:00 – 14:15 **A.S. Alexandrov,** “NMR spectrometer for ultra low temperatures”
14:15 – 14:30 **O.A. Babanova,** “NMR study of the reorientational motion in borohydrides: $RbBH_4$, $CsBH_4$ and α-$Mg(BH_4)_2$”
14:30 –14:45 **E.I. Baibekov,** “Role of magnetic dipole interactions in the damping of Rabi oscillations of paramagnetic centers in solids”
14:45 – 15:00 **L.A. Batalova,** “^{59}Co ZFNMR study of $YBaCo_4O_7$ compound”

15:00 – 15:15	**S.V. Blinkova,** “Intramolecular dynamics of the radical anion of 1,2,4-trifluorobenzene as studied by optically detected ESR technique”
15:15 – 15:30	**Yu.S. Chernenko,** “Double Electron-Nuclear Magnetization Transfer in Low-Field MRI”
15:30 – 16:00	**Coffee break**
16:00 – 16:15	**D.O Tolmachev,** “Formation and properties of impurity related aggregates in CsBr:Eu X-ray storage phosphor”
16:15 – 16:30	**A.I. Dmitriev,** “Charge Order-Disorder Phase Transition Detected By EPR in α'-(BEDT-TTF)$_2$IBr$_2$”
16:30 – 16:45	**A.V. Chertkov,** “Metabonomics study of human amniotic fluid and embryo culture media”
16:45 – 17:00	**A.I. Chushnikov,** “Investigation of abnormal changes in organism of donors analyzing EPR spectra of blood”
17:00 – 17:15	**A.V. Fedorova,** “Multiple quantum NMR for investigations of nanopore compounds”
17:15 – 17:30	**L.V. Khaidarshina,** “Diagnostics of radiating ions-radicals in bioorganic materials via a method of an electronic paramagnetic resonance”

Wednesday, October 6

Lectures

9:30 – 10:30	**F.S. Dzheparov,** “Combining of projection technique of Nakajima-Zwanzig with Anderson-Weiss-Kubo stochastic local field approach for calculation of correlation functions in spin dynamics”
10:30 – 10:45	**Coffee break**
10:45 – 11:45	**Yu.I. Talanov,** “Vortex excitations in high-T_c superconductors as revealed by EPR of a surface layer”

Oral session

11:45 – 12:00	**L.F. Salakhutdinov,** “Vortex excitations above T_c in the cuprate superconductor $Bi_2Sr_2Ca_{1-x}Y_xCu_2O_{8+y}$ as revealed by ESR”
12:15 – 12:30	**M.R. Gallyamov,** “Application of ^{1}H NMR for studing of mobility of building blocks and guest molecules in metal-organic frameworks”
12:30 – 14:00	**Lunch**
14:00 – 14:15	**O.N. Glotova,** ”Geometrical phase of the NQR signals”
14:15 – 14:30	**A.F. Sadykov,** “Magnetic structure in the multiferroic $LiCu_2O_2$: ^{63,65}Cu and ^{7}Li NMR studies”
14:30 – 14:45	**E.V. Morozov,** “NMR microimaging for studying and monitoring the processes of inverse opal preparation via sol-gel technology”
14:45 – 15:00	**D.A. Sunyaev,** “$2\Delta_0/k_BT_c$ ratio and temperature dependence of the superfluid density in overdoped $La_{2-x}Sr_xCuO_4$”
15:00 – 15:15	**M.S. Gruzdev,** “Synthesis and EPR study of liquid crystalline iron(III) complexes on the bases of 4,4’-dodecyloxybenzoiloxybenzoil-4-salicyliden-n’-ethyl-n-ethylenediamine”

15:15 – 15:30 **A.Yu. Zyubin,** “The magnetic properties study of nanostructures with Fe_3O_4 by ferromagnetic resonance”

15:30 – 16:00 **Coffee break**

16:00 – 16:15 **V.S. Iyudin,** “Time-Resolved EPR Spectra of Photoexcited Copper Porphyrin”
16:15 – 16:30 **N.I. Khalitov,** “Magnetic properties and FMR study of nanocomposite multiferroic formed by Co ion implantation in $BaTiO_3$”
16:30 – 16:45 **S.S. Khutsishvili,** “Paramagnetic polymer materials containing nanosized silver particles”
16:45 – 17:00 **A.A. Kipriyanov,** “Magnetic field effects on open chemical systems far from equilibrium”
17:00 – 17:15 **A.A. Kuzovkov,** “Temperature dependence of molecular mobility of 1-butyl-2,3-dimethylimidazolium tetrafluoroborate ionic liquid according to NMR ^{19}F, ^{11}B and ^{1}H”
17:15 – 17:30 **L.V. Khaidarshina,** “EPR-researches of biomaterials using the data of thermochemical ions-radicals”

Thursday, October 7

Lectures

9:30 – 10:30 **Yu.M. Bunkov,** “NMR at the Frontier of Low Temperatures”

10:30 – 10:45 **Coffee break**

10:45 – 11:45 **M.V. Eremin, “**Models of electronic structure of HTSC”

Oral session

11:45 – 12:00 **A.I. Litvinov,** “Spin probe techniques in supramolecular chemistry”
12:00 – 12:15 **K.V. Kholin,** “Electrochemistry-ESR of the sterically hindered imidazolidine zwitterions and its paramagnetic derivative”

12:30 – 14:00 **Lunch**

14:00 – 14:15 **Yu.S. Kutin,** “Identification of shallow Al donors in ZnO monocrystals by means of High-Frequency EPR and ENDOR spectroscopy”
14:15 – 14:30 **B.V. Yavkin,** “EPR/ENDOR of hydroxyapatite nanocrystals doped by lead ions”
14:30 – 14:45 **A.G. Smolnikov,** “Electric field gradient in paramagnetic phase of compounds with structure of Kagome staircase $M_3V_2O_8$ (M = Co, Ni)”
14:45 – 15:00 **A.M. Nischenko,** “Mobility of tert-butyl alcohol in solid state studied by deuterium NMR Spectroscopy”
15:00 – 15:15 **I.V. Mirzaeva,** “^{77}Se NMR and Theoretical Studies of $[Mo_3(\mu_3\text{-}Se)(\mu_2\text{-}Q)_3]^{4+}$ Clusters Q = O, S, Se ”
15:15 – 15:30 **T.I. Pichugina,** “Pulse EPR Investigation of the Triplet Fullerene C_{70} under continuous light illumination: Features of Three-Level System”

15:30 – 16:00 **Coffee break**

16:00 – 16:15 **V.V. Kuzmin,** “Thermalization of the system “^{3}He-aerogel” at low temperatures”
16:15 – 16:30 **D.T. Sitdikov,** “Multifrequency EPR of Asphaltenes”

16:30 – 16:45 **T.N. Nikolaeva,** “A new nuclear magnetic resonance approach for ontological diseases diagnostic on serum albumin properties”

16:45 – 17:00 **M.A. Malakhov,** “Solution BCS equation in case of spin fluctuation pairing”

17:00 – 17:15 **I.R. Nizameev,** “EPR, structural characteristics and intramolecular movements of some phenoxyl radicals in toluene”

17:15 – 17:30 **I.N. Gracheva,** “EPR study of the vanadium-doped forsterite crystal”

Friday, October 9

10:30 – 12:30 **Excursion in Kazan Federal University**

12:30 – 14:00 **Lunch**

14:00 **Closing ceremony**

Influence of a magnetic resonance on conductivity of materials with colossal magnetoresistance

V.A. Atsarkin, V.V. Demidov

Kotel’nikov Institute of Radio Engineering and Electronics RAS, 125009, 11 Mokhovaya Str., Moscow, Russia

e-mail: atsarkin@mail.cplire.ru

Various mechanisms of conductivity change in para- and ferromagnetics under microwave irradiation at electronic magnetic resonance conditions is reviewed. The major attention is paid to materials with colossal magnetoresistance in which electroconductivity depends on spin polarization. Experiments on the detection and investigation of electric resistance increasing in thin epitaxial film of lanthanium-strontium manganite under magnetic resonance pumping are described. The effect is observed both in paramagnetic and in ferromagnetic phases and is maximal near Curie point. It is shown, that the observed phenomena can be explained by combined account both Landau-Lifshits and Bloch mechanisms of relaxation.

Inter-subband Microwave Resonance in Surface Electrons on Liquid Helium

D.A. Konstantinov

Low Temperature Physics Laboratory, Advanced Science Institute, RIKEN, Japan

e-mail: konstantinov@riken.jp

Surface electrons on liquid helium present a unique strongly correlated (2+1)-dimensional system. Surface states are formed owing to polarization attraction of electrons to the liquid and the repulsion barrier at the surface. The electron motion normal to the surface has a discrete 1D hydrogen-like energy spectrum given by En=-R /n2 (n=1, 2, ...), with the effective Rydberg energy of several Kelvin. As a result, 2D electronic subbands are formed, in which the particles can move freely along the surface except for the scattering from helium vapor atoms or surface capillary waves (ripplons).

Our spectroscopic studies of electronic Rydberg states using millimeter-wave microwaves reveal a variety of interesting phenomena [1-3]. I will show that the coupling between different subbands allows for the efficient transfer of the microwave excitation energy into the kinetic energy of the lateral motion and leads to resonant overheating of the electron system [1]. As electrons thermally populate higher excited subbands, the electron-electron interaction leads to the Coulomb shift of their inter-suband transition frequency and results in the optical bistability of the electron system [2]. Finally, I will talk about how the application of strong magnetic fields perpendicular to the surface leads to rather unexpected vanishing of electrical conductance induced by the inter-subband n=1→2 resonance [3].

References

[1] D. Konstantinov et al., Phys. Rev. Lett. 98, 235302 (2007).

[2] D. Konstantinov et al., Phys. Rev. Lett. 103, 096801 (2009).

[3] D. Konstantinov, K. Kono, Phys. Rev. Lett. 103, 266808 (2009).

Methods of 1D and 2D NMR in structural elucidation of natural glycopolymers

F.V. Toukach

N.D. Zelinsky Institute of Organic Chemistry, Russian Academy of Sciences, 119991 Russia, Moscow, Leninsky prospekt 47

M.V. Lomonosov Academy of Fine Chemical technology, 119571 Russia, Moscow, prospekt Vernadskogo 86

e-mail: never@vilvit.net

Nowadays NMR spectroscopy is one of the most widely used methods in structural chemistry of natural compounds. Nevertheless, the experience from previous bio-organic schools and conferences in Russia showed that young scientists missed information on benefits of magnetic resonance methods in structural elucidation of natural compounds, and could not interpret NMR spectra in structural aspect. The lecture is aimed at compensation of this deficiency. It is a part of a lection series dedicated to the elucidation of polymeric structures composed of separate residues (monosaccharides, aminoacids, alditols etc.)

The lection includes a review of modern NMR spectroscopic methods applied to the determination of structure of a sample bacterial glycopolymer. The usage of most demanded NMR experiments (COSY, TOCSY, ROESY, HSQC, HMBC etc. at ^{1}H, ^{13}C, ^{31}P nuclei) is discussed. The material is focused at spectra interpretation process and the visualization of spectra assignment. The opportunities of the NMR spectroscopy are demonstrated at the example of complete structural investigation of a polysaccharide antigen of the bacterium *Citrobacter* PCM1555. The structure of its branched tetrasaccharide unit was elucidated in the Zelinsky Institute carbohydrate chemistry lab in 2008. The lection links various NMR spectra to the structural peculiarities of the O-antigen: monomeric composition, anomeric and absolute configurations of residues, linkage positions, sequence of residues, monosaccharide modifications and stoichiometry.

The lecture is an educational overview and does not provide new scientific data. It contains information on existing instrumental methods, active usage of which has become possible for the recent decades.

Dynamic Nuclear Polarization in High Magnetic Fields

M.R. Gafurov

Goethe University, Frankfurt am Main, Germany
Kazan Federal University, Kazan, Russia
Bruker Ltd, Kazan, Russia

e-mail: Marat.Gafurov@ksu.ru

This lecture concerns last experimental, technical and theoretical achievements in Dynamic Nuclear Polarization (DNP) of biological related materials in high magnetic fields (> 3.4 T). [1,2]. The main goal of this approach is to enhance NMR signals in high-resolution experiments and, therefore, drastically reduce the time of measurements by transferring large spin polarization of electron spins to the coupled nuclear spins.

References

[1] *Appl. Magn. Reson* **34** (3-4) (2008).e. Special Edition: Dynamic Nuclear Polarization: New Experimental and Methodology Approaches and Applications in Physics, Chemistry, Biology and Medicine

[2] *Phys.Chem.Chem.Phys*. **12** (22) (2010). Special Edition: High field dynamic nuclear polarization - the renaissance.

Combining of projection technique of Nakajima-Zwanzig with Anderson-Weiss-Kubo stochastic local field approach for calculation of correlation functions in spin dynamics

F.S. Dzheparov

Institute for Theoretical and Experimental Physics, 117218, B. Cheremushkinskaya 25, Moscow, Russia

e-mail: Dzheparov@itep.ru

Two famous methods of derivation of master equations in spin dynamics are synthesized into generalized approach, which combines their constructive features and advantages. It is demonstrated, that new method produces oscillations in free induction decay and reasonable frequency asymptotes for magnetically concentrated spin systems like ^{19}F in CaF$_2$. Application of the method to magnetically diluted systems like ^{29}Si in silicon is discussed.

Resonance line form function (LFF) $G(\omega)$ and free induction decay (FID) $F(t)$ are main measurable values in nuclear magnetic resonance (NMR) [1]. In typical situation energy of interaction of a spin with strong external static field $\mathbf{H}_0=(0,0,H_0)$ is small relative the temperature, and

$$F(t)=\left\langle I_- I_+(t)\right\rangle_0=\int_{-\infty}^{\infty} dt G(\omega) e^{-i\omega t} \tag{1}$$

Here standard notations for spin operators $I_+ = I_x + iI_y = \sum_{j=1}^{N} I_j^+,\ I_- = \left(I_+\right)^+$ are applied, N is total number of spins, quantum statistical average $\left\langle \bullet\bullet\bullet \right\rangle_0 = \mathrm{Tr}\left(\bullet\bullet\bullet\right)/\mathrm{Tr}\left(1\right)$ is calculated at infinite temperature, and Heisenberg's evolution $I_+(t)=\exp(iH_d t) I_+ \exp(-iH_d t)$ is defined by secular part of dipole-dipole interaction

$$H_d=\frac{1}{2}\sum_{ij} b_{ij}\left(2I_i^z I_j^z-\beta_{ij}\left(I_i^x I_j^x+I_i^y I_j^y\right)\right),\quad b_{i\neq j}=\frac{\gamma_i\gamma_j\hbar}{2r_{ij}^3}\left(1-3\cos^2\vartheta_{ij}\right),\quad b_{ii}=0, \tag{2}$$

The coefficient $\beta_{ij}=1$, if gyromagnetic ratios of spins coincide i.e. $\gamma_i=\gamma_j$, and $\beta_{ij}=0$ if $\gamma_i \neq \gamma_j$. It is supposed in (2) that any spin has its position $\mathbf{r}_j$, $\mathbf{r}_{ij}=\mathbf{r}_i-\mathbf{r}_j$, and ϑ_{ij} is an angle between $\mathbf{r}_{ij}$ and $\mathbf{H}_0$. External field is considered as strong if it is much larger than local field, produced by all spins of the crystal at any spin and if combination of Zeeman frequencies $\Delta_{ij}^{(\pm)}=\omega_{0a}\pm\omega_{0b}$ for any two spins of kinds a and b is mach larger than local field frequencies ω_{la} and ω_{lb}, corresponding to motion of the spins in their local fields.

Eq. (1) indicates that LFF and FID are directly connected with two-particle correlation functions in time $F_{ij}(t)=\left\langle I_i^- I_j^+(t)\right\rangle_0$ and frequency $F_{ij}(\omega)=\int_{-\infty}^{\infty}\frac{dt}{2\pi}F_{ij}(t)\exp(i\omega t)$ representations. It is evident that (1) contains as well one-particle correlators $F_{jj}(t)$ and $F_{jj}(\omega)$. Nearly all measurable quantities in spin dynamics can be presented by correlators of type $\left\langle Q_1 Q_2(t)\right\rangle_0$ with some operators Q_1 and Q_2.

We will distinguish magnetically concentrated (MCS) and magnetically diluted (MDS) systems. Nuclear paramagnetic MCS is a diamagnetic in electronic degrees of freedom substance where nuclear spins are arranged into crystal (sub)lattice. In MDS nuclear or electronic spins are randomly distributed among crystal lattice sites with a concentration

$c \ll 1$. Excellent example of MCS is spin system of nuclei ^{19}F in a crystal CaF$_2$. Standard MDS system is formed by nuclear spins ^{29}Si (natural abundance c_{nat}=4.67%) in silicon single crystal.

Microscopical calculation of FID is very complex problem of statistical physics which is far from completion because the problem doesn't belong to nearly exactly solvable ones even for magnetically concentrated systems. The problem became more complex for MDS due to incorporating of difficulties of theory of disordered media.

Excellent measurement [2] of FID in CaF$_2$ indicates that FID has oscillations at scale of $T_2 = \int_0^\infty dtG(t)$, which are satisfactory described by the relation

$$F(t) = \frac{a}{b} \cdot \frac{\sin(bt)}{\mathrm{sh}(at)}, \tag{3}$$

when $F(t) > 10^{-3}$. The constants $a \sim b \sim T_2^{-1}$ can be estimated using first terms of time series expansion of FID (so called second M$_2$ and firth M$_4$ moments [1]). Theoretical efforts [1,3-6] in understanding and calculating of FID and other important correlation functions in homonuclear systems were based on application of moments in some of general approaches of physical kinetics, for example, in projection technique of Nakajima-Zwanzig [1] together with model assumptions about memory function [1,4,6], or in series expansion in powers of inverse dimension of the space [3].

Fine measurements of NMR LFF $G_I(\omega)$ for impurity beta-active nuclei ^{8}Li in LiF were carried out in Refs. 7 and 8 in the frequency range, where $G_I(\omega) \geq 10^{-4} G_I(0)$. The results were satisfactory described [7-9] without adjusting parameters by an extension of Anderson-Weiss-Kubo (AWK) theory developed primary for explaining of "narrowing by motion". Theoretical methods used here were based on modeling of local field by continuous normal random process (or, that is the same, on calculation of FID using first term of cumulant expansion) that can be considered as opposition to projection technique. It should be noticed that FID $F_I(t)$ for impurity nucleus has no oscillation.

Important advantage of AWK theory consists in the fact that main approximation is introduced at level of Hamiltonian, that is much clearer than model approximations in memory kernel of master equation, and it conserves Hamiltonian structure of the dynamics. From other side projection technique is very flexible in application, because it can use many forms of projection (super)operators. Therefore we come to natural problem to find common version of the theory which combines advantages of both approaches. One of solution is described below.

It will be shown as well that new theory has natural extension at MDS basing on application of series expansion of observables in powers of concentration instead of time Taylor series [10,11]. New theory produces significant modification of existing predictions [12,13] for FID in MDS at $t \geq T_2$, which were constructed as direct generalization of AWK theory and concentration expansions [10,11]. Satisfactory measurements of FID or LFF in MDS are absent up to now. Is seems that best results are obtained in Refs. 14 and 15, but they are in contradiction with theory at small $t \leq T_2$, where theoretical predictions are reliable, that, probably, indicates on experimental difficulties in obtaining of homogeneous polarization for nuclear MDS. Results of other measurements (see references in [14,15]) have larger deviations from theoretical predictions at small times.

Projection technique and master equation

Selection of projection operator for considered problem has no unique solution. On of possible ways consists in finding of simplest form, which produce desirable property of calculated observable, and including it into some natural more wide set of projectors, which can give more detail information about the same observable. Example of effective application of this prescription to derivation of master equation for polarization transport can be found in Ref. 16.

It is known, that calculation of FID with simplest projection of equation of motion for operator $I_+(t)$ on operator I_- together with simplest Gaussian approximation for memory function can reproduce the oscillation of the FID [1]. Therefore we can expect that more detail consideration, based on study of equation of motion for operators $I_j^+(t)$ will produce better result. To realize this proposal we should consider the equation of motion

$$\frac{\partial}{\partial t} I_j^+(t) = i\left[H_d, I_j^+(t)\right] = iH_d^\times I_j^+(t), \tag{4}$$

define a projection (super)operators P and $\overline{P}$, acting on arbitrary operator Q as

$$PQ = \sum\nolimits_{j=1}^{N} I_j^+ \left\langle I_j^- Q\right\rangle_0 / \left\langle I_j^+ I_j^-\right\rangle_0, \quad \overline{P} = 1 - P, \tag{5}$$

decompose Eq. (4) in two equations on $PI_j^+(t)$ and $\overline{P}I_j^+(t)$, obtain formal solution of the second equation and substitute it into first one, that produce a master equation

$$\frac{\partial}{\partial t} F_{ij}(t) = -\int_0^t d\tau \sum\nolimits_{k=1}^{N} M_{ik}(\tau) F_{kj}(t-\tau), \tag{6}$$

where

$$M_{ij}(t) = \left\langle \left[I_i^-, H_d\right] \exp\left(i\overline{P}H_d^\times \overline{P}t\right)\left[H_d, I_j^+\right]\right\rangle_0 / \left\langle I_j^+ I_j^-\right\rangle_0 . \tag{7}$$

The relations $PH_d^\times P = 0$ and $\overline{P}\left[H_d, I_j^+\right] = \left[H_d, I_j^+\right]$ were applied here.

Below we will use numeration of the spins by their positions and apply, for example, $I_{\mathbf{r}}^+$ instead of I_j^+ with $\mathbf{r}_j$=$\mathbf{r}$. Therefore Eqs. (6) and (7) receive a form

$$\frac{\partial}{\partial t} F_{\mathbf{rq}}(t) = -\int_0^t d\tau \sum\nolimits_{\mathbf{x}} M_{\mathbf{rx}}(\tau) F_{\mathbf{xq}}(t-\tau), \tag{6a}$$

$$M_{\mathbf{rx}}(t) = \left\langle \left[I_{\mathbf{r}}^-, H_d\right] \exp\left(i\overline{P}H_d^\times \overline{P}t\right)\left[H_d, I_{\mathbf{x}}^+\right]\right\rangle_0 / \left\langle I_{\mathbf{x}}^- I_{\mathbf{x}}^+\right\rangle_0 . \tag{7a}$$

The derivation of Eqs. (6) and (7) is typical for projection technique method.

Main approximations and results for FID in MCS

Memory kernel $M_{\mathbf{rx}}(t)$ is most complex object in the theory. To calculate it we use next simple and natural approximation:

$$M_{\mathbf{rx}}(t) = m_{\mathbf{rx}} \chi(t), \tag{8}$$

where $m_{\mathbf{rx}} = M_{\mathbf{rx}}(t=0)$ is easily calculable. For homonuclear systems the coefficient β_{ij}=1 (see (2)), and

$$m_{\mathbf{rx}} = \frac{\mathrm{I(I+1)}}{3}\left(5\delta_{\mathbf{rx}} \sum\nolimits_{\mathbf{q}} b_{\mathbf{qx}}^2 + 4b_{\mathbf{rx}}^2\right). \tag{9}$$

In order to calculate $\chi(t)$ we introduce auxiliary system which has modified interaction for spin $I_{\mathbf{0}}$ only. Its Hamiltonian is

$$H_d = \frac{1}{2}\sum\nolimits_{\mathbf{r}\neq 0,\mathbf{q}\neq 0} b_{\mathbf{rq}}\left(2I_{\mathbf{r}}^z I_{\mathbf{q}}^z - \left(I_{\mathbf{r}}^x I_{\mathbf{q}}^x + I_{\mathbf{r}}^y I_{\mathbf{q}}^y\right)\right) + 2\sum\nolimits_{\mathbf{r}} b_{\mathbf{r}0} I_{\mathbf{r}}^z I_0^z, \tag{10}$$

that coincides in main with dipole Hamiltonian of a system, which has one impurity nucleus placed at **r**=0. Repeating the derivation (4)-(9), we receive, that master equation for $F_I(t) = F_{00}(t) = \left\langle I_0^- I_0^+(t)\right\rangle$ is decoupled from other $F_{\mathbf{rq}}(t)$, and we can write it as

$$\frac{\partial}{\partial t}F_I(t) = -\int_0^t d\tau M_I(\tau)F_I(t-\tau), \quad M_I(t) = m_I\chi_I(t), \quad m_I = \frac{4\mathrm{I}(\mathrm{I}+1)}{3}\sum\nolimits_{\mathbf{q}} b_{\mathbf{q}0}^2, \tag{11}$$

with $\chi_I\left(t=0\right)=1$.

Difference between the functions $\chi_I(t)$ and $\chi(t)$ should be small, of order $1/z_e$, where z_e is effective number of neighbors, therefore next main approximation is

$$\chi\left(t\right) = \chi_I\left(t\right). \tag{12}$$

Methods for calculation of FID for impurity nuclei [7-9] are based on AWK theory, and they can be applied for independent calculation of $F_I(t) = F_{00}(t)$ here directly. They use two main approximations. The first one consists in hypothesis that we can neglect of influence of impurity spin on evolution of the local field that is similar to approximation (12). The second approximation considers the local field on impurity spin

$$\omega_{l0}(t) = 2\sum\nolimits_{\mathbf{q}} b_{\mathbf{q}0} I_{\mathbf{q}}^z(t) \tag{13}$$

(where time dependence is defined by Heisenberg evolution) as classical normal stochastic process with collelator

$$\left\langle \omega_{l0}\omega_{l0}(t)\right\rangle = 4\sum\nolimits_{\mathbf{qr}} b_{\mathbf{q}0}b_{\mathbf{r}0}\left\langle I_{\mathbf{q}}^z I_{\mathbf{r}}^z(t)\right\rangle_0 = M_{2I}\kappa(t), \quad M_{2I} = \frac{4I(I+1)}{3}\sum\nolimits_{\mathbf{q}} b_{\mathbf{q}0}^2 = \left\langle \omega_{l0}^2\right\rangle_0, \tag{14}$$

that produce

$$F_I(t) = \exp\left(-M_{2I}\int_0^t d\tau\left(t-\tau\right)\kappa(\tau)\right). \tag{15}$$

The time dependence of operator $I_{\mathbf{r}}^z(t)$ in (14) is Hamiltonian again, and corresponding ways to take in into account are described in [6-9].

As a result, if correlation function (14) is calculated, then we can

a) define the memory kernel $M_I(\tau)$ solving the Eq. (11) with known (from (15)) $F_I(t)$;

b) define from (11) the function $\chi_I(\tau)$ and $\chi(\tau)=\chi_I(\tau)$, and

c) calculate $F_{\mathbf{rq}}(t)$ using Eqs. (6a), (8), and (9).

If the aim consists in calculation of FID $F(t) = \sum\nolimits_{\mathbf{q}} F_{\mathbf{rq}}(t)$, then at the step "c" we can solve more simple master equation

$$\frac{\partial}{\partial t}F(t) = -\int_0^t d\tau M(\tau)F(t-\tau), \quad M(t) = \sum\nolimits_{\mathbf{r}} M_{\mathbf{rx}}(t) = \sum\nolimits_{\mathbf{r}} m_{\mathbf{rx}}\chi(t) = \frac{9}{4}M_I(t), \tag{16}$$

which follows directly from Eq. (6a), (8), (9), (11), and (12). The translation invariance of the crystal should be taken into account as well.

Realization of this program was fulfilled for $M_4 / M_2^2 = 19/9$, that can be considered as reasonable universal approximation for any lattice. Three different forms for function $\kappa(t)$ were applied:

1) $\kappa(t) = \exp(-\tfrac{1}{4}M_2 t^2)$,

2) $\kappa(t)=1/\cosh^2\left(-\tfrac{1}{2}\left(M_2\right)^{1/2}t\right)$,

3) $\kappa(t)=1/\left(1+\tfrac{1}{3}M_2t^2\right)^{3/4}$.

Existence of oscillation of the FID was stable, and relative variations of FID due to application of these $\kappa(t)$ were reasonably small.

In conclusion of the section we see, that existence of oscillations of $F(t)$ and absence of oscillation in $F_I(t)$ is connected directly with coefficient 9/4 in (16), which reflects transfer of transversal polarization in Eqs. (6a), (8), and (9). From mathematical point of view we have the same effect, as in equation of motion for oscillator coordinate $x(t)$ with frequency Ω_0 and friction coefficient μ, written in integral form

$$\frac{\partial}{\partial t}x(t)=-\Omega_0^2\int_0^t d\tau\exp\left(-\mu\tau\right)x(t-\tau).$$

It is evident, that with increasing of Ω_0 we have here transition from simple decay to oscillation decay at $\Omega_0=\mu/2$.

NMR line form function for MCS

The NMR LFF $G(\omega)$ can be received directly from Laplace-Fourier transform of $F_I(t)$. To show it we can solve the Eqs. (11) and (16) applying Laplace transformation. We define it by the relation

$$f(\lambda)=\int_0^\infty dt\cdot f(t)\exp(-\lambda t)$$

for any reasonable function $f(t)$. Solution of Eq. (16) is

$$F(\lambda)=\left(\lambda+M(\lambda)\right)^{-1}=\left(\lambda+\frac{9}{4}M_I(\lambda)\right)^{-1},$$

while $M_I(\lambda)=\left(F_I(\lambda)\right)^{-1}-\lambda$. As a result, using the function

$$g(\omega)=F_I(\lambda=\varepsilon+i\omega)=g_c(\omega)-ig_s(\omega)$$

with real ω, $g_c(\omega)$, $g_s(\omega)$, and $\varepsilon\to+0$ we have

$$G(\omega)=\frac{36}{25\pi}\cdot\frac{g_c(\omega)}{\left(\omega g_s(\omega)-9/5\right)^2+\left(\omega g_c(\omega)\right)^2}. \tag{17}$$

In particular

$$G(\omega\to\infty)=\frac{9}{4\pi}\cdot g_c(\omega). \tag{18}$$

Results of Refs. [7,8] indicate, that this asymptotics is of exponential type for any realistic $\kappa(t)$.

Magnetically diluted systems

Numeration of spins by coordinate of its site is possible for disordered lattice as well as for ordered lattice, if occupation numbers are used [10-13]. By definition the occupation number $n_{\mathbf{r}}=1(0)$ if the site $\mathbf{r}$ is (not) occupied by the impurity spin, and averaging on random distribution of impurities over the crystal sites can be fulfilled using the relations

$$\left\langle n_{\mathbf{r}}\right\rangle_c=c,\quad n_{\mathbf{r}}^2=n_{\mathbf{r}},\quad \left\langle\prod_{j=1}^k n_{\mathbf{r}_j}\right\rangle_c=c^k. \tag{19}$$

All $\mathbf{r}_j$ are different in the last equality. In this representation

$$H_d = \frac{1}{2}\sum\nolimits_{\mathbf{rq}} n_{\mathbf{r}} n_{\mathbf{q}} b_{\mathbf{rq}} \left(2I_{\mathbf{r}}^z I_{\mathbf{q}}^z - \left(I_{\mathbf{r}}^x I_{\mathbf{q}}^x + I_{\mathbf{r}}^y I_{\mathbf{q}}^y\right)\right), \tag{20}$$

$$F(t) = \sum\nolimits_{\mathbf{q}} F_{\mathbf{qr}}(t), \quad F_{\mathbf{qr}}(t) = \left\langle n_{\mathbf{q}} n_{\mathbf{r}} I_{\mathbf{q}}^- I_{\mathbf{r}}^+(t)\right\rangle \left\langle n_{\mathbf{r}} I_{\mathbf{r}}^- I_{\mathbf{r}}^+\right\rangle^{-1}, \tag{21}$$

where $\langle \bullet\bullet\bullet \rangle = \left\langle \langle \bullet\bullet\bullet \rangle_0 \right\rangle_c$. Main equation of motion and projector P should be defined as

$$\frac{\partial}{\partial t} n_{\mathbf{r}} I_{\mathbf{r}}^+(t) = i n_{\mathbf{r}} \left[H_d, I_{\mathbf{r}}^+(t)\right] = i n_{\mathbf{r}} H_d^{\times} I_{\mathbf{r}}^+(t), \tag{22}$$

$$PQ = \sum\nolimits_{\mathbf{r}} n_{\mathbf{r}} I_{\mathbf{r}}^+ \left\langle n_{\mathbf{r}} I_{\mathbf{r}}^- Q\right\rangle \left\langle n_{\mathbf{r}} I_{\mathbf{r}}^- I_{\mathbf{r}}^+\right\rangle^{-1}. \tag{23}$$

Standard transformations produce a master equation (6a) again, but with new memory kernel

$$M_{\mathbf{rx}}(t) = \left\langle n_{\mathbf{r}} n_{\mathbf{x}} \left[I_{\mathbf{r}}^-, H_d\right] \exp\left(i\overline{P} H_d^{\times} \overline{P} t\right) \left[H_d, I_{\mathbf{x}}^+\right]\right\rangle / \left\langle n_{\mathbf{x}} I_{\mathbf{x}}^- I_{\mathbf{x}}^+\right\rangle, \tag{24}$$

which coincides with (7a) if all $n_{\mathbf{q}} \equiv 1$.

Correct theory of MDS should be reasonable in continuous medium limit (CML) when concentration $c \to 0$, but deviation of $F(t)$ from $F(0)=1$ is finite: $1-F(t) \neq 0$. We will concentrate our attention on this limit, because inverse transition to real small finite concentration can be fulfilled by simple way, indicated in [13].

It is known [12], that in 3-dimentional CML at small t

$$F(t) = 1 - D_A t + \frac{5}{9}\left(D_A t\right)^2 + O\left(\left(D_A t\right)^3\right) \tag{25}$$

and, therefore, characteristic time scale is defined by Anderson's constant

$$D_A = \frac{2\pi^2}{3\sqrt{3}} \gamma^2 n \hbar. \tag{26}$$

Here $n = c/\Omega$ is spin density, and Ω is average volume per lattice site. It is very important that D_A is of order of dipole interaction for two spins placed at average distance $r_c = n^{-1/3}$, and numerical value of D_A indicates, that effective number of neighbors for MDS $z_e = D_A / b_c = \frac{2}{3}\pi^2 \approx 6.6 \gg 1$. Here $b_c = \frac{3\gamma^2\hbar}{4r_c^3}\left\langle \left|1 - 3\cos^2 \vartheta\right| \right\rangle_{\vartheta}$ is average value of interaction of two spins, placed at average distance r_c.

Approximation (8) can not reproduce exact relation (25), therefore simplest reasonable approximation here is of the form

$$D_A = \frac{2\pi^2}{3\sqrt{3}} \gamma^2 n \hbar, \tag{27}$$

where $\sigma\left(t=0\right) = 1$, $m_{\mathbf{rx}}(t) \sim c^1$, and $m_{\mathbf{rx}}(t)$ should reproduce exactly term $\sim c^1$ in concentration series of $F_{\mathbf{qr}}(t)$. The function $\sigma(t)$ decays with time and its first term in c can be calculated from the Eq. (25).

In order to obtain reasonable model of $\sigma(t)$ for all times we can apply the receipt of the Section 2 and study auxiliary system where spin, placed at $\mathbf{r}=0$, has no flip-flop interaction. It's FID

$$\Phi(t) = F_{00}(t) = \left\langle n_0 I_0^- I_0^+(t)\right\rangle \left\langle n_0 I_0^- I_0^+\right\rangle^{-1} \tag{28}$$

again obeys separated equation

$$\frac{\partial}{\partial t}\Phi(t) = -\int_0^t d\tau M_I(\tau) \Phi(t-\tau), \tag{29}$$

but now $M_I(t) = m_0(t)\sigma_0(t)$, where $m_0(t)$ contains all contribution ~c^1, and $\sigma_0(t)$ starts from $\sigma_0(t=0)=1$. Following (12) we will apply the approximation

$$\sigma(t) = \sigma_0(t) \qquad (30)$$

Auxiliary FID $\Phi(t)$ can be independently calculated within the approach, developed in Refs. 12 and 13, much better, then *F*(*t*), to which this approach was applied in [12,13] initially. As a result

$$\Phi(t) = \exp\left(-\left(2B^2\int_0^t d\tau\left(t-\tau\right)\exp\left(-\alpha B\tau\right)\right)^{1/2}\right) \qquad (31)$$

with $B = \tfrac{2}{3}D_A$, and value of α will be obtained later. The function $\kappa(\tau) = \exp\left(-\alpha B\tau\right)$ here has the same sense as $\kappa(\tau)$ in Eq. (15). It is simplest function, which represent influence of flip-flop transitions in surrounding spins and is compatible with analytical structure of expansion (25). The radical in (31) represents static fluctuations of interactions due to random distribution of positions of spins. If $\alpha = 0$, then (31) coincides with exact Anderson's solution for impurity nucleus in absence of flip-flop transitions for surrounding spins.

In order to calculate FID *F*(*t*) we can again apply the Eq. 16, but now $M(t) = \tfrac{3}{2}M_I(t)$. Comparison of *F*(*t*) with series (25) produce $\alpha = \tfrac{1}{2}$ and

$$\Phi(t) = \exp\left(-\left(Bt + 2\exp\left(-Bt/2\right) - 2\right)^{1/2}\right).$$

The connection between Fourier-Laplace transform of auxiliary FID

$$g(\omega) = g_c(\omega) - ig_s(\omega) = \int_0^\infty dte^{-i\omega t}\Phi(t)$$

and NMR LFF of MDS reshapes as

$$G(\omega) = \frac{6}{\pi} \bullet \frac{g_c(\omega)}{\left(\omega g_s(\omega) - 3\right)^2 + \left(\omega g_c(\omega)\right)^2}.$$

Results of numerical calculation of the FID for MDS produce no oscillation, and analytical study indicates stability of this conclusion to variation of form of $\kappa(\tau)$.

Conclusion

As a result we see that unified theory, developed here, takes into account transfer of polarization in the process of phase relaxation both in MCS and MDS. The theory gives stable oscillations for MCS, but it produces no oscillation for MDS. New MDS theory, preceding treatment [12,13], and numerical simulation of FID in systems, containing 7 and 8 spins [14,15] produce approximately the same results for $D_At < 1$ in MDS, but with increasing of D_At deviation grows significantly indicating, probably, that negative values of FID, obtained in modeling [14,15] at $D_At > 3$ don't exist in real large systems.

References

[1] A.Abragam, M.Goldman. Nuclear magnetism: Order & disorder. Clarendon press, Oxford 1982.

[2] M.Engelsberg, I.J.Lowe. Phys. Rev. **B10**, 822, 1974.

[3] V.E.Zobov, M.A.Popov. ZhETF **127**, 877, 2005.

[4] V.L.Bodneva, A.A.Lundin. ZhETF **135**, 1142, 2009.

[5] B.V.Fine. Phys.Rev.Lett. **94**, 247601, 2005.

[6] T.Charpentier, D.Sakellariou, J.Virlet, F.S.Dzheparov, J.-F.Jacquinot. J. of Chem. Phys. **127**, 224506, 2007.

[7] M.I.Bulgakov, A.D.Gulko, F.S.Dzheparov, S.V.Stepanov, S.S.Trostin. Pis'ma v ZhETF **58**, 614, 1993.

[8] Yu.G.Abov, A.D.Gulko, F.S.Dzheparov, S.V.Stepanov, S.S.Trostin. Phys. Part. Nucl. **26**, 692, 1995.

[9] F.S.Dzheparov, S.V.Stepanov. Hyperfine Interactions **C1**, 609, 1996.

[10] F.S.Dzheparov, V.S.Smelov, V.E.Shestopal. Pis'ma v ZhETF **32**, 51, 1980.

[11] F.S.Dzheparov, A.A.Lundin, T.N.Khazanovich. ZhETF **92**, 554, 1987.

[12] F.S.Dzheparov, I.V.Kaganov. Pis'ma v ZhETF **75**, 309, 2002.

[13] F.S.Dzheparov. Spin Dynamics in Disordered Solids. Pp. 8588-8597 in "Encyclopedia of Complexity and Systems Science", ed. Robert A. Meyers, Springer 2009.

[14] D.Li, Y.Dong, R.G. Ramos, J.D.Murray, K.MacLean, A.E.Dementyev, S.E.Barrett. Phys. Rev. **B77**, 214306, 2008.

[15] D.Li, Y.Dong, R.G. Ramos, J.D.Murray, K.MacLean, A.E.Dementyev, S.E.Barrett. arXiv: 0704.3620v [cond-met.mes-hall].

[16] F.S.Dzheparov. ZhETF **99**, 982, 1991.

Vortex excitations in high-T_c superconductors as revealed by EPR of a surface layer

Yu.I. Talanov

Zavoisky Physical-Technical Institute, Sibirskii tract 10/7, Kazan, 420029, Russia.

e-mail: talanov@kfti.knc.ru

EPR is a powerful tool to study the local magnetic field distribution of any origin, in particular that due to the magnetic perturbations produced by the vortices. Its sensitivity depends on the ESR line width, the narrower the signal, the higher the resolution. Embedding spin probes in the form of paramagnetic ions results in a broad signal and lowers considerably the EPR resolution. To enhance the resolution, the organic free-radical compounds (for example, diphenyl-picrylhydrazyl) in the form of a surface layer are used as paramagnetic probes with a narrow EPR signal.

EPR of a thin paramagnetic layer precipitated on a surface of a superconductor (so-called "EPR-decoration") is used as a method sensitive to the local magnetic perturbations in the type-II superconductors (see, for example, [1-3]). This method was proposed in the work [1] to study the Abrikosov vortex lattice which is formed when a high-temperature superconducting material transfers to the superconducting state upon lowering the temperature below the critical temperature T_c. The appearance of vortices results necessarily in the spread of the local magnetic fields both in the superconductor bulk and on its surface. In response to the local field dispersion, the EPR signal parameters (the resonance field value and the line width) of the paramagnetic substance deposited on the surface are changed. We use this technique to detect the possible local field perturbations due to the vortex excitations in the $Bi_2Sr_2CaCu_2O_8$ and $Bi_2Sr_2Ca_2Cu_3O_{10}$ crystals at temperatures above T_c [4].

References

[1] Rakvin B., Pozek M., Dulcic A. Solid State Commun. 72, 199 (1989).

[2] R.I.Khasanov, Yu.I.Talanov, Yu.M.Vashakidze, G.B.Teitel'baum. Physics C 242, 333 (1995).

[3] Pozek M., Habermeir H., Maier A., Mehring M. Physica C 269, 61 (1996).

[4] Ю.И.Таланов, Л.Ф.Салахутдинов, Е.Джианнини, Р.И.Хасанов. Письма в ЖЭТФ 90, 222 (2009).

LECTURE NOTES

Models of electronic structure of HTSC

M.V. Eremin

Kazan Federal (Volga Region) University, 42208, Kazan, Kremlevskaya 18. Russia.
e-mail: Mikhail.Eremin@ksu.ru

Experiment

1. Phase diagram of cuprates.
2. Structures. Technical applications.
3. Where are holes distributed? Nuclear quadrupole resonance.
4. Temperature dependencies of Knight shifts and nuclear relaxation rates.
5. Superconducting gap . d-wave pairing.
6. Spin susceptibility of itinerant holes in BCS theory.
7. Superexchange interaction. Short range magnon–like mode.
8. Inelastic neutron scattering.

Theory

1. Models of conducting band.
2. Dual features of spin susceptibility.
3. Paring mechanismes; superexchange+ phonons, plasmons, spin fluctuations.
4. Temperature dependencies of superfluid density.
5. Pseudogap problem.

Microwave absorption study of pinning effects in novel iron-based pnictide superconductors

N.R. Beysengulov[1,2], N.Yu. Panarina[1], Yu.I. Talanov[1], T.S. Shaposhnikova[1], E.L. Vavilova[1]

[1]Zavoisky Physical-Technical Institute, 420029, Sibirsky tract, Kazan, Russian Federation.
[2]Kazan (Volga Region) Federal University, 420008, Kremlevskaya str, Kazan, Russian Federation.

e-mail: n.beysengulov@gmail.com

Introduction

The recent discovery of a new class of high-temperature superconductors (HTSC) *Re*FeAsO (*Re* = Sm, Nd, Pr, Ce, La) [1] has generated considerable excitement in the scientific community. Iron-based pnictides have a layered structure, complicated Fermi surface and demonsrate two phase transitions: the magnetic ordering of the spin-density-wave type at high temperatures and the superconducting transition at lower temperatures. In some pnictides the coexistence of the superconducting and magnetic ordered phases was found [2]. In our work the influence of the magnetic phase inclusions on the pinning and critical current density is studied.

Sample characterization

Four $CaFe_{2-x}Co_xAs_2$ single crystals with different Co concentration were prepared at Leibniz Institute for Solid State and Materials Research IFW, Dresden. The superconducting transition temperatures T_c were determined from ac susceptibility measurements. Results of these measurements are shown in fig.1.

As for the phase diagram, the samples with $x = 0.08$ ($T_c = 18.2$ K) and 0.10 ($T_c = 22.5$ K) lie in the area of magnetic and superconducting phases coexistence, the sample with $x = 0.13$ ($T_c = 18.6$ K) corresponds to the pure superconducting phase, and the one with $x = 0.11$ ($T_c = 21.8$ K) is on the boundary of these two areas (fig. 2).

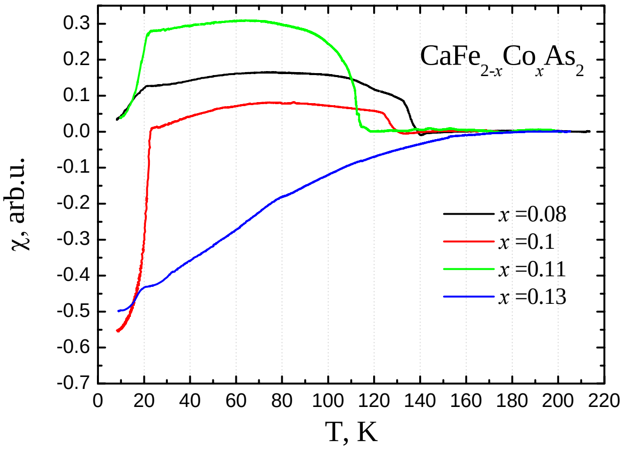

Fig.1. Temperature dependence of ac susceptibility for $CaFe_{2-x}Co_xAs_2$ samples

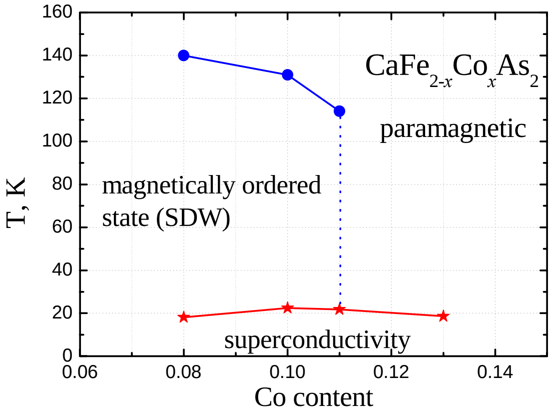

Fig.2. Phase diagram for $CaFe_{2-x}Co_xAs_2$ obtained from ac susceptibility

Experimental results and discussion

Pinning effects in the $CaFe_{2-x}Co_xAs_2$ single crystals are studied with the help of the modulated microwave absorption (MWA) technique widely used before for investigation of cuprate HTSC materials. The method is based on the dissipation of microwave power in superconducting samples by vibrating vortices and can give information about the pinning strength in the system.

MWA measurements have been carried out on a standard X-band electron paramagnetic resonance (EPR) spectrometer with magnetic field modulation (100 kHz) of small amplitude (0.5 Oe) and lock-in detection. In the experiment, a sealed sample was placed in a resonance cavity and cooled down to the measurement temperature below the critical temperature in a remanent field of the magnet. A helium-flow cryostat was used for obtaining temperatures in the range of 10–60 K. At fixed temperatures, the magnetic field was swept up from about 50 Oe to 7 kOe and then down to the initial value. The MWA hysteresis loops were registered in a wide temperature range and analyzed with the help of an appropriate theoretical model of microwave absorption [3].

The selected curves for $CaFe_{1..9}Co_{0.1}As_2$ are shown in fig.3. The information that can be obtained from the hysteresis loops directly is the field H_{irr} at which the MWA hysteresis vanishes. This is the so-called irreversibility field, which increases with temperature and at some point goes beyond the available range of magnetic fields. The temperature dependence of the irreversibility field determines an irreversibility line, which separates the areas with zero and nonzero values of the critical current density on the magnetic field-temperature phase diagram.

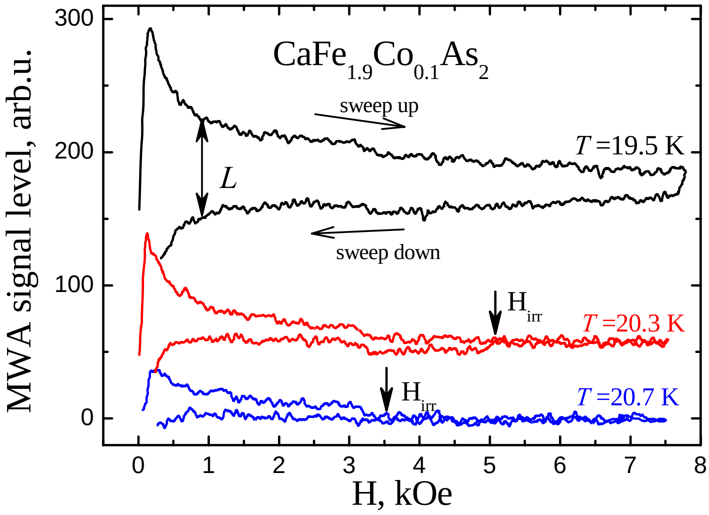

Fig.3. MWA hysteresis loops for the $CaFe_{1.9}Co_{0.1}As_2$ sample registered at different temperatures below T_c

It is interesting to compare the irreversibility line of pnictides with those of cuprate HTSC. Such a comparison of the $CaFe_{1.87}Co_{0.13}As_2$ sample with $YBa_2Cu_3O_7$ (YBCO), $La_{1.85}Sr_{0.15}CuO_4$ (LSCO), and $Bi_2Sr_2CaCu_2O_8$ (BSCCO) ceramics is shown in fig.4. Since all these compounds have different critical temperatures T_c, the comparison is drawn on a reduced temperature scale T/T_c. The samples being compared are ceramics. It is seen that the slope of the irreversibility line observed for pnictides is similar to and even sharper than that reported for YBCO samples. In this connection it should be noted that YBCO compound possesses the maximum pinning strength among unmodified HTSC cuprates.

Generally, the MWA hysteresis is a complex function of the critical current density j_c, the viscosity of the vortex system η, the ratio of the amplitude of thermal fluctuations to the mean distance between pinning centers $<u^2>/a^2$, and of the distribution of fields $H(r,t)$ and currents $j(r,t)$. In order to estimate j_c, the temperature dependence of the MWA hysteresis amplitude L was simulated numerically. An example of fitting a theoretical curve to the experimental data at fixed magnetic field is given in fig.5. The amplitude of the MWA hysteresis was determined from experimental MWA loops as the difference between magnitudes of the power absorbed upon sweeping the magnetic field up (P_{up}) and down (P_{down}). To find the magnetic field dependence of the critical current density, the procedure of fitting the theoretical curve $L(T, H = \text{const})$ [6] to the experimental data was repeated at several values of the magnetic field. Fig.6(a) shows the magnetic field dependence of the critical current density calculated at $T = 25$ K for samples with different cobalt concentration.

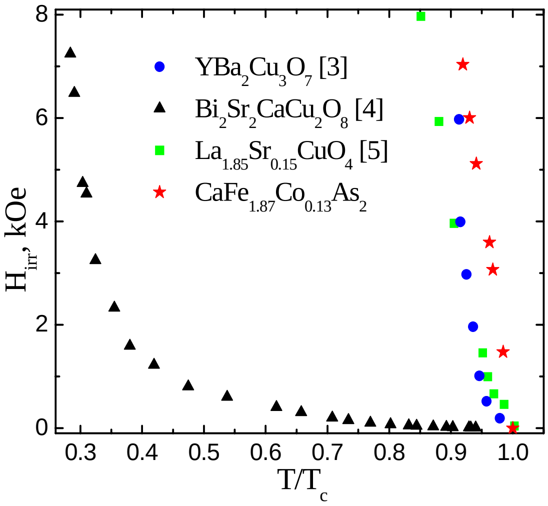

Fig.4. Irreversibility lines of various ceramic HTSC compounds

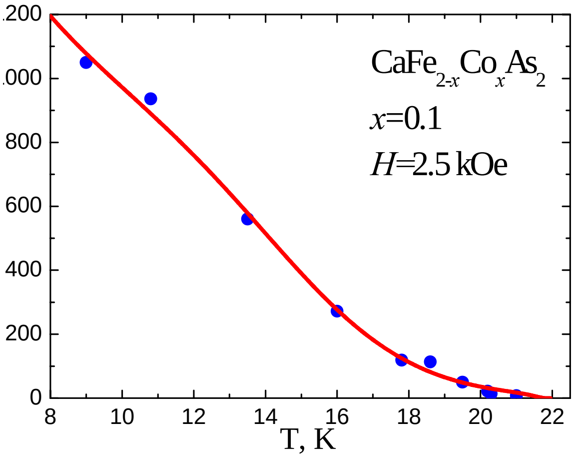

Fig.5. Temperature dependence of the MWA hysteresis amplitude. Red line is numerical calculation, blue dots are the experimental data.

The critical current density grows with Co doping, reaches a maximum at $x = 0.11$ and then decreases (fig.7). Note that the sample with $x = 0.11$ corresponds to the boundary of

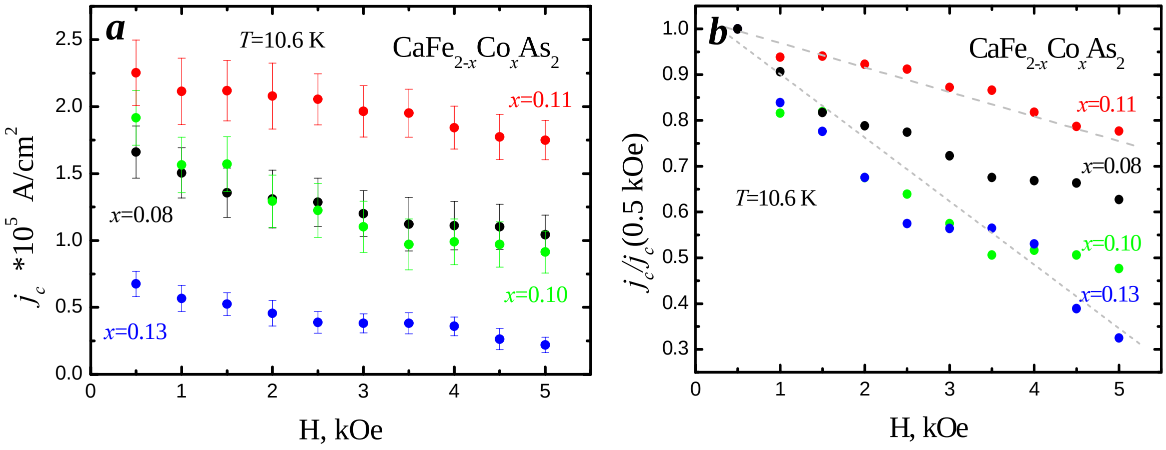

Fig.6. Magnetic field dependence of the critical current density (***a***) and normalized value of j_c (***b***) for the $CaFe_{2-x}Co_xAs_2$ samples at $T = 10.6$ K.

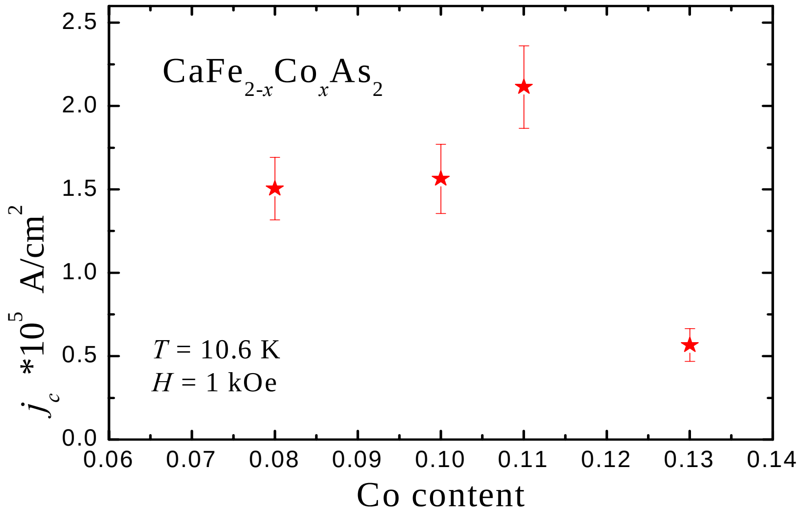

Fig.7. Absolute value of j_c for the samples with different Co concentration at the same temperature of 10.6 K.

SDW and superconducting states (x =0.11) and it has the weakest dependence of j_c on the magnetic field (fig.6(b)). It equals ~10^5 A/cm^2 at 10.6 K and 500 Oe. The obtained results suggest that the nonsuperconducting (magnetic) inclusions serve as additional pinning centers. When the Co concentration is low, the inclusion size is too big to be effective pinning center.The size reduces with increasing Co concentration and magnetic inclusions become more effective as pinning centers. That is way the sample with x = 0.11 has the maximum value of j_c and the weakest dependence on the magnetic field.

Acknowledgements

Support of the Russian Foundation for Basic Research (grants No. 08-02-91952-NNIO-a and No. 10-02-01056) is acknowledged.

References

[1] Hosono H. et al.: J. Am. Chem. Soc. 130, 3296 (2008)).

[2] Drew A.J. et al.: N. Materials, V.8, 310 (2009).

[3] Rodrigues P. Jr. et al.: Phys. Rev. B 49, 15292 (1994)

[4] Schilling A. et al.: Phys. Rev. Lett. 71, 1899 (1993)

[5] Fan X. et al.: Physica C 282-287, 2105 (1997)

[6] Shaposhnikova T. et al.: Physica C 300, 239 (1998)

ESR in new spin dimer system $Ba_3Cr_2O_8$ and $Sr_3Cr_2O_8$

T.P. Gavrilova, R.M. Eremina

Zavoisky Physical -Technical Institute, 420029, Sibirsky tract, 10/7, Kazan Russia

e-mail: tapa_left@mail.ru

The dimerization of a magnetic S=1/2 system, namely the formation of a spin-singlet ground state at low temperature with opening of a g ap (Δ) in the excitation spectrum, has been observed to date in a variety of inorganic crystals. In the limit of weak interdimer interactions, the problem maps exactly into the physics of Bose-Einstein Condensates (BEC), as explained in a recent review [**Ошибка! Источник ссылки не найден.**] and references therein. Upon application of an external magnetic field above a critical value (H_c), one can excite triplons into the network of S=0 dimers, a direct analogy to increasing the density of Bosons in a condensate, here tunable by the strength of the magnetic field. This effect has been directly observed in prototypical systems of weakly interacting dimers such as $TlCuCl_3$ [**Ошибка! Источник ссылки не найден.**] and $BaCuSi_2O_6$ [**Ошибка! Источник ссылки не найден.**]. Recent work has been directed towards more complex systems, such as $SrCu_2(BO_3)_2$, where the presence of geometrically frustrated nearest-neighbor interactions strongly increases the repulsion of magnons, promoting new types of ground states [4].

Very recently, a new family of dimerized antiferromagnet, namely $A_3M_2O_8$ (A=Ba, Sr M=Mn,Cr), has shown BEC of magnons (H_c =12.5 Tesla for $Ba_3Cr_2O_8$ [**Ошибка! Источник ссылки не найден.**] and 9.2 T for $Ba_3Mn_2O_8$ [**Ошибка! Источник ссылки не найден.**]). A unique feature in this series is the existence of isostructural compounds with variant spin state (S=1/2 for Cr and S=1 for Mn). The systems also uniquely show the presence of dimerized MO_4^{3-} tetrahedra with an M ion in the unusual 5+ oxidation state and the presence of competing exchange interactions, since the dimers are arranged in a triangular lattice presenting a high degree of geometrical frustration.

In the case of $Ba_3Cr_2O_8$ and $Sr_3Cr_2O_8$, the unusual 5+ valence state of Chromium results in a single electron in the 3d shell. The Cr^{5+} ion is surrounded by an oxygen tetrahedron and this crystal field splits the 3d levels so that electron occupies the doubly-degenerate lower lying e orbitals. The Cr^{5+} ion in this environment is thus Jahn-Teller active and a Jahn-Teller distortion would lift both the orbital degeneracy and magnetic frustration.

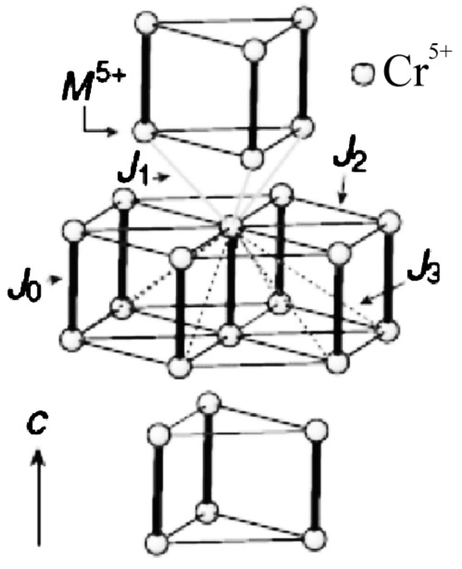

Fig.1. Arrangement of Cr^{5+} ions which have spin 1/2 in $Ba_3Cr_2O_8$ and $Sr_3Cr_2O_8$.

Also the fitting of the temperature dependence of the magnetic susceptibility in $Ba_3Cr_2O_8$ by Bleaney-Bowers equation for isolated dimer system and modified Bleaney-Bowers equation with interdimer interactions confirmed the formation of a spin-singlet ground state at low temperature [7].

In all $A_3M_2O_8$ compounds, the dimers, aligned along the hexagonal c-axis, are equivalents by symmetry and characterized by an intradimer interaction J_0 (following the convention of [8]). Each dimer has three nearest neighbors in the adjacent layer (interaction J_1), six next- nearest neighbors in-plane (interaction J_2) [8] and six further neighbors (interactions J_3) in adjacent planes [9]. A striking feature is the variation of the effective interdimer exchange energy J (defined as the sum of all inter-dimer interactions $J'=3J_1+6J_2+6J_3$) between Mn ($J/J_0=1.4$) and Cr compounds ($J/J_0=0.3$ for Ba and $J/J_0=0.1$ for Sr) [10].

All these interesting facts stimulated our study of $Ba_3Cr_2O_8$ and $Sr_3Cr_2O_8$ single crystals by the ESR method. This method makes it possible to determine immediately the parameter of isotropic exchange between magnetically nonequivalent spins from the frequency spectrum and to make some conclusions about the magnetic structure of these compounds.

ESR measurements were performed in a Bruker ELEXSYS E500 cw spectrometer at X-band (9.47 GHz) and Q-band (34 GHz) frequencies equipped with continuous He-gas-flow cryostats (Oxford Instruments) in the temperature range 4.2<T<300 K. The ESR spectrum consists of one Lorentzian-shaped line with g ~ 2 in $Ba_3Cr_2O_8$ and $Sr_3Cr_2O_8$ (see fig.2).

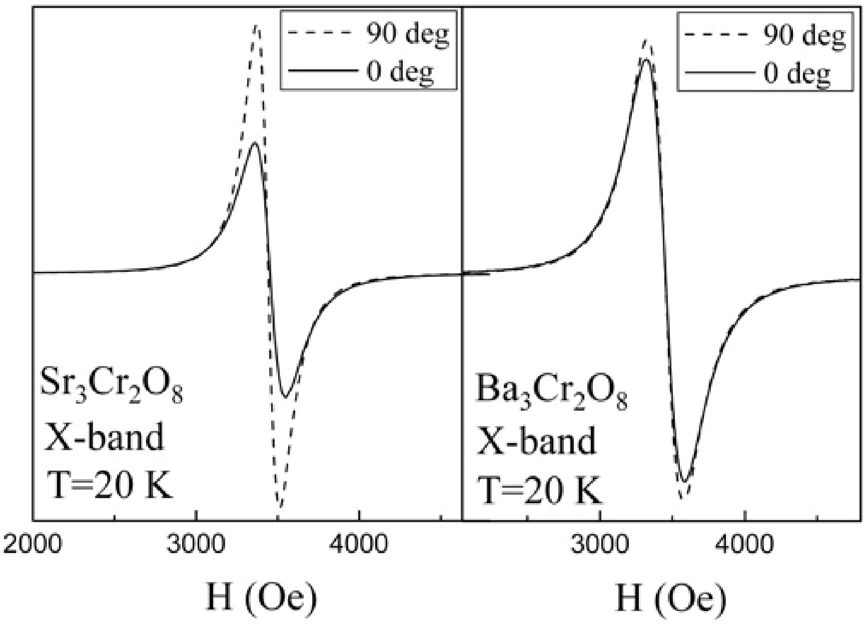

Fig.2. ESR spectra in $Ba_3Cr_2O_8$ in X-band at T=20 K.

It is clear from fig.2 that the ESR line demonstrated the significant angular dependence in both compounds. So the angular dependences of the ESR linewidth of $Ba_3Cr_2O_8$ and $Sr_3Cr_2O_8$ were measured at different temperatures in X- and Q-band frequencies. The more detailed angular dependences at T = 12 K are presented in fig.3 and fig.4 for $Ba_3Cr_2O_8$. The ESR linewidth along one of axes at the frequency of 34 GHz is greater than its value in the X band. It is logical to assume that this is associated with the difference between the g factors of interacting centers (anisotropic Zeeman effect). Indeed, from analyzing the structural data, it follows that the unit cell contains magnetically nonequivalent centers producing an EPR signal. Since the EPR spectrum exhibits one line, its effective g factor is the average of the g factors of paramagnetic centers located in nonequivalent positions.

The angular dependencies in two different planes are presented in fig.4. The largest variation of the linewidth appears in the plane 2 where it monotonously increases from 200 Oe up to 290 Oe on rotating the magnetic field.

The temperature dependence of the ESR linewidth are presented in fig.5. As shown in fig.5, the linewidth increases with increasing temperature from 200 Oe at 10K up to about 2800 Oe at 70K. The intensity of the ESR signals becomes very low at the temperature above 70 K, so the lines are not detected at the highest temperatures.

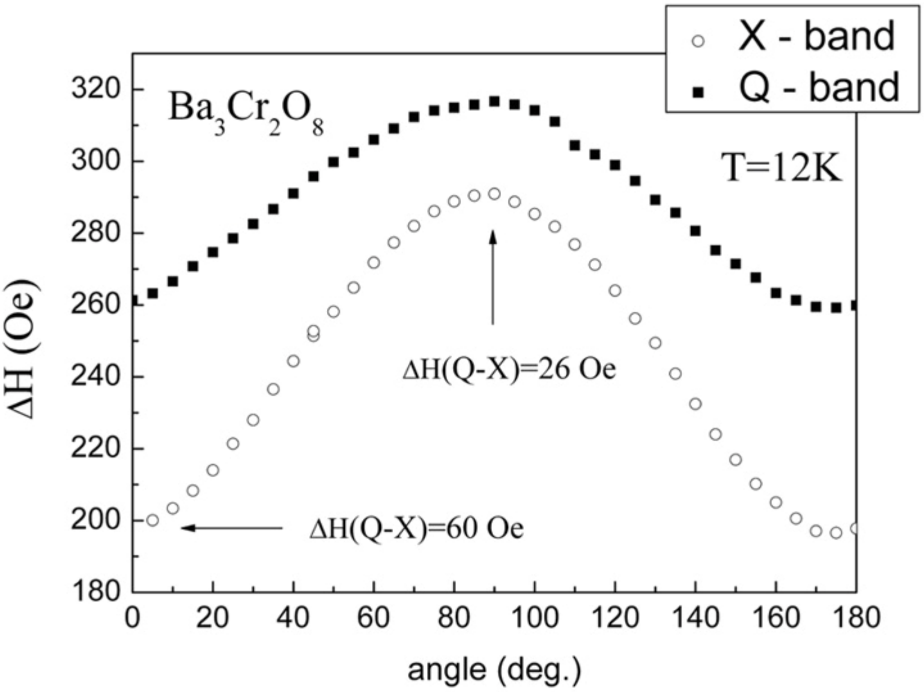

Fig.3. Angular dependence of the ESR linewidth in $Ba_3Cr_2O_8$ in X- and Q-band frequencies at T=12 K

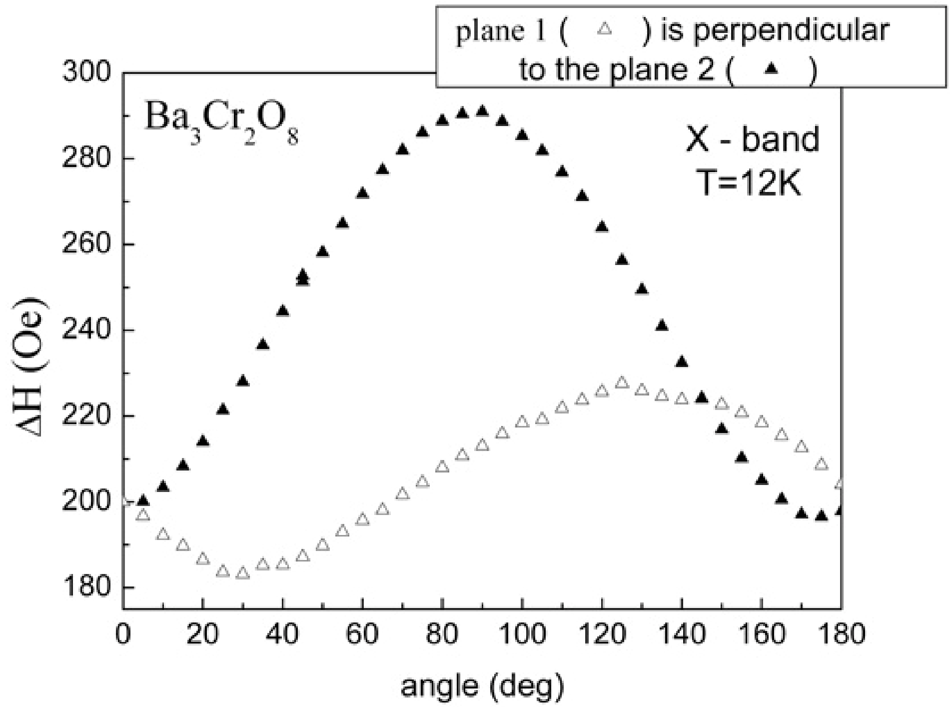

Fig.4. Angular dependence of the ESR linewidth in $Ba_3Cr_2O_8$ in X-band frequency at T=12 K in two different planes

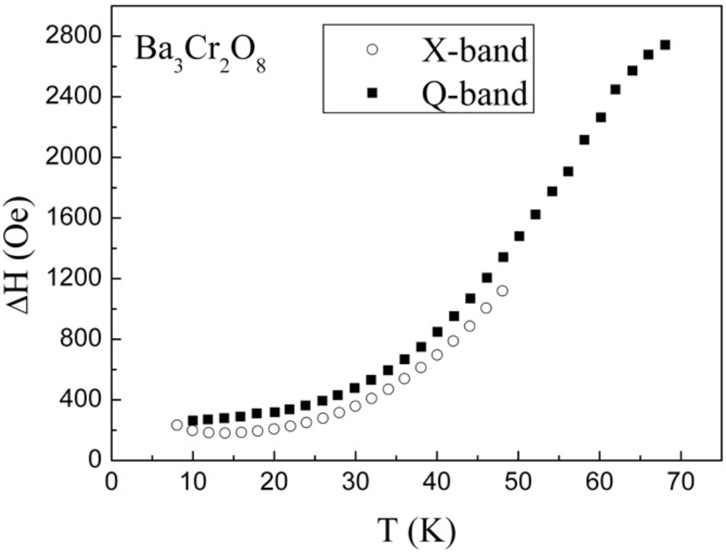

Fig.5. Temperature dependence of the ESR linewidth in $Ba_3Cr_2O_8$ in X- and Q-band frequencies.

References

[1] T. Giamarchi, C. Rueegg, and O. Tchernyshyov, Nature Physics 4, 198 (2008).

[2] T. Nikuni, M. Oshikawa, A. Oosawa, and H. Tanaka, Phys. Rev. Lett. 84, 5868 (2000).

[3] M. Jaime and V. e. a. Correa, Phys. Rev. Lett. 93, 087203 (2004).

[4] H. Kageyama, K. Yoshimura, R. Stern, N. V. Mushnikov, K. Onizuka, M. Kato, K. Kosuge, C. P. Slichter, T. Goto, and Y. Ueda, Phys. Rev. Lett. 82, 3168 (1999).

[5] A. Aczel, H. Dabkowska, G. Luke, and E.-C. Choi, Communication APS, March-Meeting Abstract: V32, 00013 (2008).

[6] H. Tsujii, B. Andraka, M. Uchida, H. Tanaka, and Y. Takano, Phys. Rev. B 72, 214434 (2005).

[7] T. Nakajima, H. Mitamura, and Yu. Ueda, J. Phys. Soc. Jpn., Vol. 75, No. 5, 054706 (2006).

[8] M. Uchida, H. Tanaka, M. Bartashevich, and T. Goto, J. Phys. Soc. Japan 70, 1790 (2001).

[9] H.-J. Koo, K.-S. Lee, and M.-H. Whangbo, Inorganic Chemistry 45, 10743 (2006).

[10] L. C. Chapon, C. Stock, P. G. Radaelli, and C. Martin, arXiv: 0807.0877v2 [cond-mat.mtrl-sci] (2008).

ESR investigation of $Li_2Mn_2(MoO_4)_3$ compound as material for lithium-ion batteries

D.R. Abdullin[1], K.M. Begam[2], S.R.S. Prabaharan[3], N.M. Suleimanov[1]

[1]Zavoisky Physical-Technical Institute of Russian Academy of Sciences, 420029, Sibirsky tract 10/7, Kazan, Russian Federation.
[2]Department of Electrical and Electronic Engineering, Universiti Teknologi PETRONAS, Tronoh, Malaysia.
[3]Faculty of Engineering, The Nottingham University, Malaysia Campus, Semenyih, Malaysia.

e-mail: ard-88@mail.ru

Introduction

The lithium-ion batteries are the inalienable and quickly developing part of portable electronics due to their higher working voltage and capacity in comparison with other types of batteries. The further development of lithium-ion batteries is connected with the improvement of working voltage, capacity and cyclability (charge/discharge cycle life of electrodes). These problems demand obviously investigation of new electrode materials, among which compounds with NASICON (Na Super Ionic Conductor) structure are intensively investigated [1-5].

The structure analysis of $Li_2M_2(MoO_4)_3$ M = Ni, Co compounds [2,3] has shown the presence of MO_6-octahedrons and MoO_4-tetrahedrons, and all oxygen atoms join various polyhedrons into the single structural motive. Lithium ions occupy interstitial positions in the framework formed by oxygen ions.

It has been found, that the use of $Li_2M_2(MoO_4)_3$ M = Ni, Co as positive electrode is hindered by structural changes occur during charge/discharge processes [2-4]. However, origin and mechanism of such structural changes in these compounds are not still investigated. In spite of insufficient cathodic performance of $Li_2M_2(MoO_4)_3$, electrochemical results obtained on $Li_2Co_2(MoO_4)_3$ as negative electrode demonstrate high lithium insertion/extraction capacity [5]. It stems from ability of Co and Mo ions reversibly change their valency state in this material during a charge/discharge cycle. Incidentally, investigation of reversible changes in valency state of transition ions in $Li_2M_2(MoO_4)_3$ M = Mn, Ni, Co is of interest.

Using ESR spectroscopy for investigation lithium-ion battery materials stimulates by the fact that the majority of cathodic and anodic materials have in their structure transition metals (Co, Ni, Mn, Fe, V). In this paper the preliminary ESR investigations of $Li_2Mn_2(MoO_4)_3$ compound are presented.

Experiment

$Li_2Mn_2(MoO_4)_3$ compounds were synthesized by a soft-combustion method in Universiti Teknologi PETRONAS (Malaysia). The morphology of the samples obtained was investigated by scanning electron microscopy. It was found that samples consist of loosely agglomerated rod-like particles with submicrometer diameter size [5].

Electron spin resonance measurements were carried out at Bruker BER-418S and Bruker BioSpin GmbH spectrometers at frequency 9.4 GHz (X-band) in the 8 - 300 K temperature interval.

Results and discussion

ESR spectra of $Li_2Mn_2(MoO_4)_3$ compound in the temperature range 8 – 300 K are presented at fig.1.

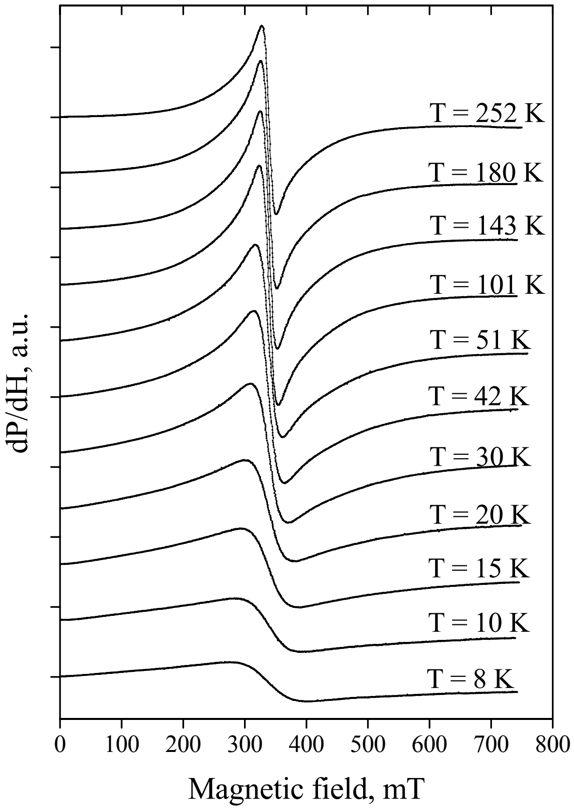

Fig.1. ESR spectra of $Li_2Mn_2(MoO_4)_3$ compound in 8 - 300 K temperature range.

ESR signals represent a symmetric absorption line at the resonance magnetic field 341.3±0.7 mT which does not depend on temperature within investigated temperature range. This magnetic field corresponds to g-factor equal to 2.007±0.004 and it is close to the g-factor of Mn^{2+} ions (electronic configuration d^5, basic term $^6S_{5/2}$) in octahedral crystal field [6]. In accordance with charge balance approach if manganese in $Li_2Mn_2(MoO_4)_3$ compound is in the valence state +2 then molybdenum is in charge state +6.

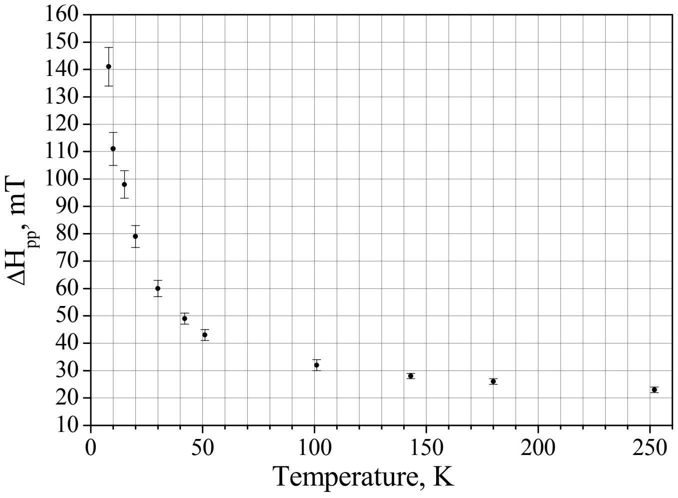

Fig.2. Temperature dependence of ESR line width of $Li_2Mn_2(MoO_4)_3$ compound.

Fig.2 shows the line width of the ESR signal as function of temperature. With the lowering of temperature the broadening of resonance line is observed. The increase of line width at low temperatures indicates the appearance of magnetic ordering of Mn^{2+} ions in $Li_2Mn_2(MoO_4)_3$ compound.

According to the EPR theory for magnetically concentrated systems the dipole-dipole and exchange interactions give rise to the EPR line width. Estimated contribution to the line width from dipole-dipole interaction ΔH_{dd} = 118 mT conform to experimentally observed ΔH_{pp} = 141±7 mT at 8 K and considerably larger as compared with ΔH_{pp} = 23±1 mT at 300 K. It follows that in $Li_2Mn_2(MoO_4)_3$ the exchange narrowing of the dipole line occurs because of exchange interaction between Mn^{2+} ions. In this case line width of ESR line can be estimated by the following expression [7]:

$$\Delta H_{\frac{1}{2}} = \frac{\gamma \cdot H_{dd}^2}{\nu_e}, \qquad (1)$$

where ν_e — frequency of exchange spin fluctuations. This enable us to determine ν_e = 9.7 GHz and also to estimate the exchange interaction integral $|J| = 0.3\ cm^{-1}$ between Mn^{2+} ions in $Li_2Mn_2(MoO_4)_3$.

As follows from structural data (fig.3), Mn^{2+} ions are situated far enough from each other and the direct exchange interaction between them is negligibly small. In this situation the determined exchange narrowing of ESR line width can arise as a result of the superexchange interaction between magnetic ions through neighboring diamagnetic anions [8,9].

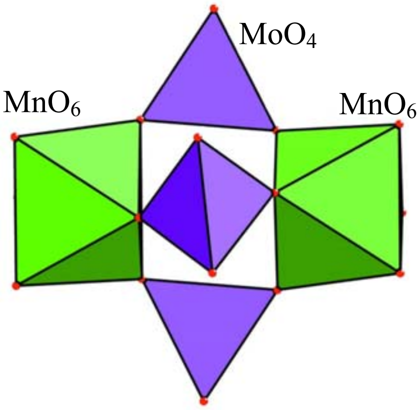

Fig.3. The central building block $[Mn_2(MoO_4)_3]$ of $Li_2Mn_2(MoO_4)_3$. Here MnO_6-octahedrons (green) and MoO_4-tetrahedrons (violet) are united by oxygen atoms (red) to the single structural motive. Li^+ ions located in interstitial positions of shown framework.

Analysis of the structure of $Li_2Mn_2(MoO_4)_3$ shows that the superexchange is possible through two oxygen ions belonging to one MoO_4-tetrahedron and two neighbor MnO_6-octahedrons. Since d-orbitals of both Mn^{2+} ions are half filled, according to the Anderson rules [9] the effective exchange integral will be negative, i.e. interaction between magnetic ions will be antiferromagnetic.

The antiferromagnetic character of interaction between Mn^{2+} ions is confirmed by negative value of Curie temperature θ = -30 K, which has been obtained from temperature dependence of a reciprocal value of integral intensity of ESR line.

Conclusion

$Li_2Mn_2(MoO_4)_3$ compound has been studied by ESR method. From ESR measurements follow that manganese in $Li_2Mn_2(MoO_4)_3$ is in valence state Mn^{2+}. Absence of the ESR signal from molybdenum allows us to assume that the valence state of molybdenum is Mo^{6+}. In this state Mo has no unpaired electrons so that Mo^{6+} is a non-magnetic.

Considerable overlapping between d orbitals of transition metal and 2p oxygen orbitals was experimentally established that leads to superexchange interaction between manganese ions and to the magnetic ordering at low temperatures. The value of exchange interaction is equal $J = -0.30\ \text{cm}^{-1}$. The antiferromagnetic character of exchange interaction between magnetic moments of Mn^{2+} ions was experimentally determined.

ESR study of $Li_2Mn_2(MoO_4)_3$ samples at various charge/discharge stages is scheduled for the near future. During the lithium intercalation to the crystalline lattice the part of its charge transfers to electronic orbitals of oxygen and transition metals [10]. Thereupon, we expect the changing of valence state of Mn ions during lithium charging and, as a consequence, the changing of ESR spectrum. Besides, due to the reduction of Mo ions, they can become paramagnetic, that will lead to ESR signal appearance from molybdenum. During the Li^+ ions intercalation process a local environment distortion of magnetic ions and hence changes in superexchange interaction strength between Mn^{2+} ions are expected. This fact can be determined in ESR spectra.

References

[1] A. S. Anderssson, B. Kalska, P. Eyob, D. Aernout, L. Haggstrom, J. O. Thomas, *Solid State Ionics* **2001**, *140*, 63-70.

[2] K. M. Begam, M. S. Michael, Y. H. Taufiq-Yap, S. R. S. Prabaharan, *Electrochem. Solid St.* **2004**, *7*, A242-A246.

[3] S. R. S. Prabaharan, S. Ramesh, M. S. Michael, K. M. Begam, *Mater. Chem. Phys.* **2004**, *87*, 318-326.

[4] S. R. S. Prabaharan, M. S. Michael, K. M. Begam, *Electrochem. Solid St.* **2004**, *7*, A416-A420.

[5] M. S. Michael, K. M. Begam, M. Cloke, S. R. S. Prabaharan, *J. Solid State Electr.* **2008**, *12*, 1025-1029.

[6] A. Abragam, B. Bleaney, Electron paramagnetic resonance of transition ions, Oxford University Press **1970**.

[7] P. W. Anderson, P. R. Weiss, Rev. Mod. Phys. **1953**, 25, 269-276.

[8] P. W. Anderson, *Phys. Rev.* **1950**, *7*, 350-356.

[9] P. W. Anderson, *Phys. Rev.* **1959**, *115*, 2-13.

[10] M. K. Aydinol, A. F. Kohan, G. Ceder, K. Cho and J. Joannopoulos, *Phys. Rev. B* **1997**, *56*, 1354-1365.

Investigation of influence of excipients on paramagnetic centers formation at mechanoactivation of the calcium gluconate

M.M. Akhmetov[1], G.G. Gumarov[1,3], V.Yu. Petukhov[1,3], G.N. Konygin[2], D.S. Rybin[2], E.P. Zheglov[2]

[1]Zavoisky Physical-Technical Institute, 420029, Sibirsky tract 10/7, Kazan, Russian Federation

[2]Physical-Technical Institute, 42600, Kirova st. 132, Izhevsk, Russian Federation

[3]Kazan Federal University, 420008, Kremlin st. 18, Kazan, Russian Federation

e-mail: mansik86@mail.ru

It is well known that mechanical activation can enhance therapeutic efficiency of medical drugs [1] due to the fact that the substance gains the capacity to pass biological barriers, i.e. it increases the drug bioavailability [2]. Studying reasons of increased assimilability of certain medical drugs is of scientific and practical interest. Mechanical impact on a substance can initiate numerous transformations, such as amorphization, conformational transformations, polymorphic transitions and etc., which can be the reasons for enhanced efficiency of medicine [3]. Earlier it has been shown that mechanical activation of calcium gluconate (CG) leads to sufficient increase of its therapeutic efficiency upon medical treatment of diseases associated with calcium deficit [4]. Moreover, the formation of paramagnetic centers (PC) responsible for appearance of an EPR signal with g =2.005 and line width ~8.5 Oe was observed in calcium gluconate subjected to mechano-chemical treatment [5]. It has been established that these centers accumulate with increasing grinding time. Radiospectroscopic experiments and theoretical calculations suggest free radical nature of emerging PC. An assumption was made that therapeutic efficiency of the medical product may be connected with the formation of polymorphic molecular modifications and stereoisomerization of the CG molecule, which are associated with formation of free radicals; therefore, it is extremely important to study the mechanism of their emergence and accumulation. Also it is known that interaction of radicals emerging during mechanical activation with environmental components can significantly influence the radical emergence and stabilization [6]. In this case, acceptance of radicals, which prevents further free-radical reactions due to changes in the molecule structure, is also possible.

Therefore, the goal of present work is to study the influence of admixtures (excipients) present in official calcium gluconate on formation and accumulation of paramagnetic centers upon mechanical activation of calcium gluconate. Calcium gluconate produced by ZAO Belvitaminy was used as an initial material. Mechanically activated powders were made following the procedure described in Ref. [7]. The grinding time was from 10 min to 1 hour. Mechanically activated samples of calcium gluconate with excipients (talc, starch and calcium stearate) present in commercially available medical product were obtained by mixing powders of appropriate weight.

The performed experiments showed that concentration of PC emerging in CG as a result of its mechanical treatment significantly depends on type and amount of introduced admixtures. As can be seen in fig.1, adding starch and calcium stearate in amount up to 5 wt% significantly increases the intensity of the EPR signal with respect to the signal of mechanically activated calcium gluconate without excipients (fourfold at t = 1 h). Further increase of the starch content up to 15 wt% only slightly influences the amplitude of the EPR signal.

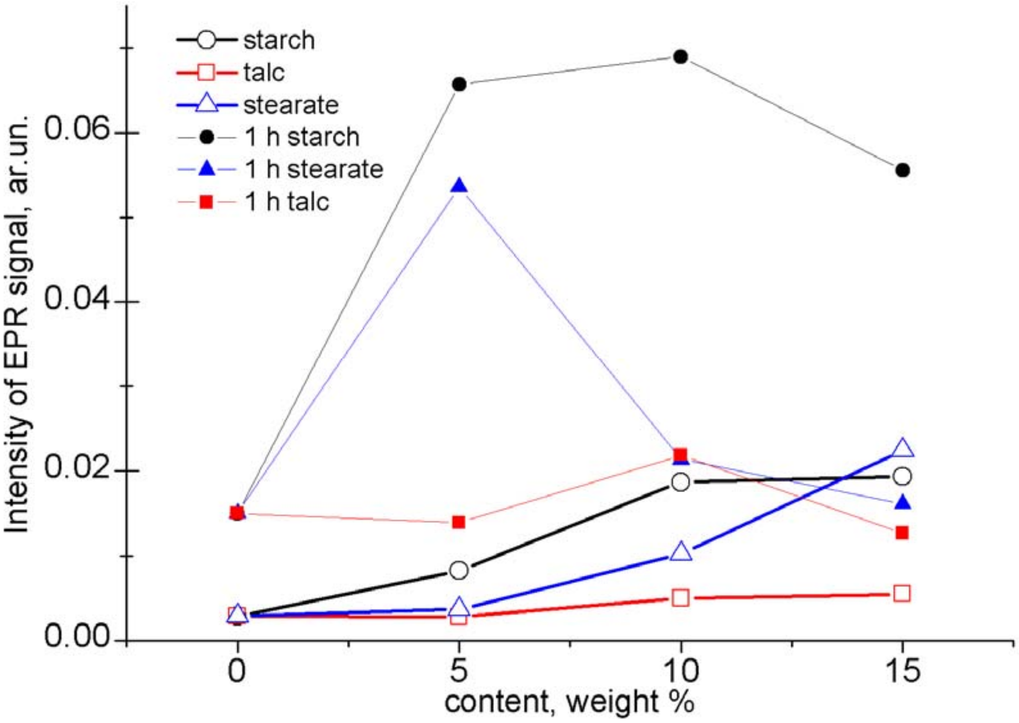

Fig.1. Intensity of EPR signal (from calcium gluconate) vs. admixture content for starch, talc and calcium stearate

EPR spectra were recorded on Varian E-12 spectrometer at a frequency of ca. 9.5 GHz and room temperature. Powder samples filled a quartz ampoule with length exceeding the cavity height in order to place the substance of equal volume in the same half of the TE104 – cavity at each set of measurements. Coal standard was placed into the second half of the cavity for qualitative measurements. The results presented in fig.2 also demonstrate that the

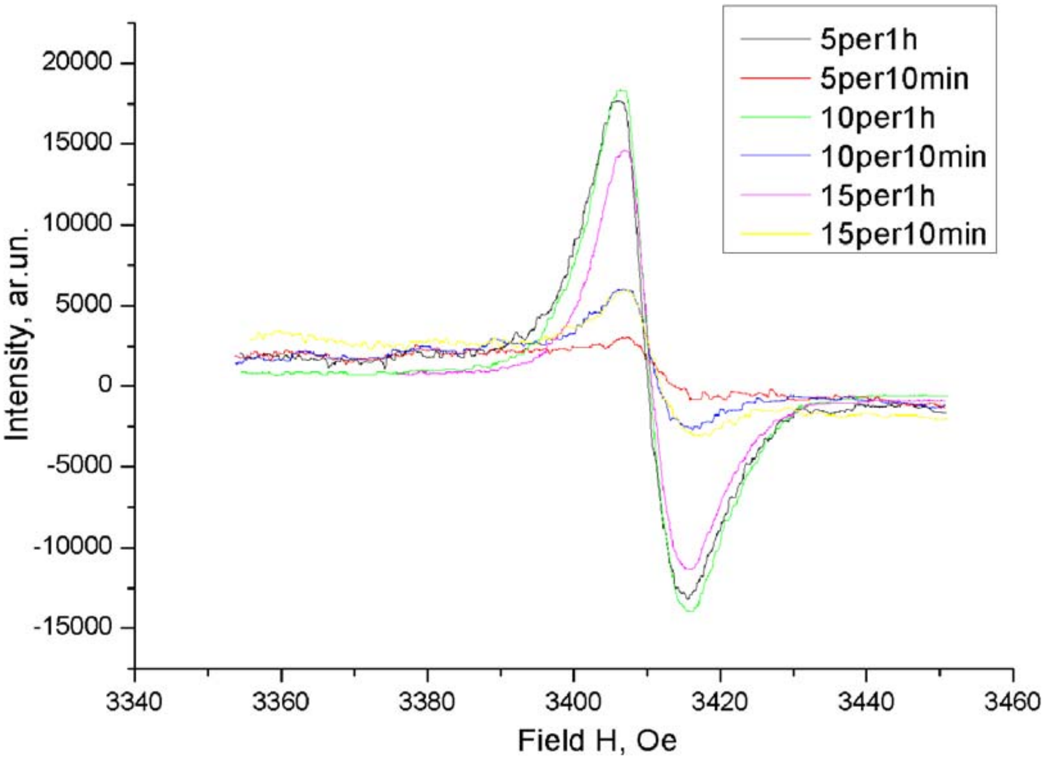

Fig.2. EPR lines of mechanically activate CG with different weight content of starch

character of the behavior of the EPR line intensity depends on the type of excipients. The line intensity sharply changes with increasing content of calcium stearate, while adding talc up to 15 wt% has almost no impact on the EPR line intensity regardless of the duration of mechanical treatment.

To find out the direct influence of input admixtures on changes in registered spectra, EPR spectra of powders of initial excipients and those after mechanical activation were recorded separately. The EPR spectra of the powder of initial starch and the same sample subjected to mechanical activation of different duration are shown in fig.3.

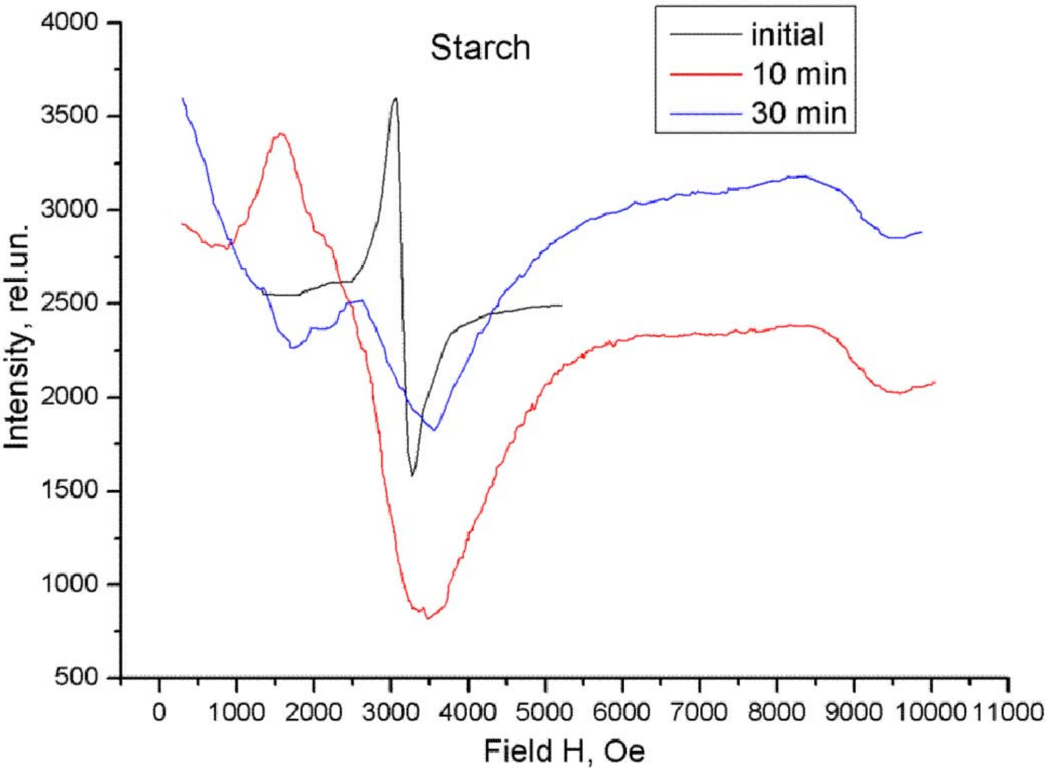

Fig.3. EPR spectrum of initial and mechanically activated powders of starch.

From these spectra one may see that starch is a paramagnet and mechanical treatment results in emergence of additional paramagnetic centers. However, the parameters of these EPR spectra significantly differs from those of a free radical emerging upon mechanical treatment of calcium gluconate. In particular, the *g*-factors and line widths of initial and mechacnically activated (for $t = 10$ min) powders of starch are $g_S = 2.162$, □$H_S \sim 265$ Oe and $g_{MAS} = 2.51$, □$H_{MAS} \sim 2000$ Oe, respectively. Similar EPR results were obtained for other excipients present in commercially available calcium gluconate. EPR spectra of initial and mechanically activated samples of calcium stearate and talc also have principal differences from the EPR line of both pure mechanically activated CG and pelleted commercially available GC with integral content of excipients of Ca 6 wt%. Thus, it has been established that an intensive line with $g \sim 2.005$ and width of ca. 8 Oe, observed in the EPR spectrum of mechanically activated binary compounds, originates from calcium gluconate and is not a superposition of lines from excipients present in the composition. At the same time, an amplitude of the line from mechanically activated calcium gluconate (and, consequently, the concentration of paramagnetic centers therein) significantly depends on the excipient type and its concentration.

Understanding the mechanism of admixture influence on increasing content of free radical centers emerging as a result of mechanical activation of calcium gluconate is an interesting and important problem demanding additional research. Apparently, excipients play role in weakening of the processes of radical recombination and their stabilization immediately after their emergence. One should also take into account that generated radicals are very stable. Experiments indicate that the EPR spectra of these radicals, line amplitude in particular, reain unchanged within a year after mechanical treatment.

References

[1] A.M. Dubinskaya // Russian Chemical Reviews. - 1999. -V. 68. - P. 708-724.

[2] E.A. Varentsov, Yu.A. Hrustalev // Russian Chemical Reviews. - 1995. - V. 64. - P. 834.

[3] M.L. Ezerskii. A.V. Savitskaya. // Zhurn. fiz. him.- 1992.- T.66.- P. 3109.

[4] G.N. Konygin et al. // Patent of the Russian Federation №2268053, 2004.

[5] G.G. Gumarov, V.Yu. Petuhov, G.N. Konygin, D.S. Rybin, E.P. Zheglov // Almanac of Clinical Medicine, V. XVII, Part I - M.: MONIKI. - 2008.- P.47.

[6] Baramboim N.K. Mechano-chemistry of macromolecular compounds.-2-nd ed.- M.: Himiya,1971.-363 p.

[7] Rybin D. S., G. N. Konygin, E. P. Elsukov, V. V. Aksenova, D. R. Sharafutdinova, Yu.Ya. Efremov // Chemistry for Sustainable Development.-2007.- № 2.- P. 163-167.

Low temperature magnetism of system “^{3}He-PrF$_3$ nanoparticles”

M.S. Tagirov[1], E.M. Alakshin[1], R.R. Gazizulin[1], A.V. Egorov[1], A.V. Klochkov[1],
S.L. Korableva[1], V.V. Kuzmin[1], A.S. Nizamutdinov[1], K.Kono[2], A.Nakao[2], A.T. Gubaidullin[3]

[1]Faculty of Physics, Kazan (Volga region) Federal University, Kremlevskaya, 18, 420008, Kazan, Russia
[2]RIKEN, Wako, Saitama, 351-0198, Japan
[3]A.E. Arbuzov Institute of Organic and Physical Chemistry of Kazan Scientific Center of Russian Academy of Sciences, Ac. Arbuzov street, 420088, Kazan, Russia

e-mail: alakshin@gmail.com

Introduction

The “PrF$_3$–liquid ^{3}He” system is in interest because of the possibility of using the magnetic coupling between the nuclei of the two spin systems for the dynamic nuclear polarization of liquid ^{3}He [1]. Van Vleck paramagnets are known to have high anisotropy of the effective nuclear magnetogyric ratio [2]. As a result, a direct interaction between magnetic moments of equal magnitude at the liquid ^{3}He–solid state substrate interface becomes possible. The resonance magnetic coupling between liquid ^{3}He nuclei and the ^{141}Pr nuclei of microsized (45 μm) Van Vleck paramagnet PrF$_3$ powder has been discovered earlier [4]. Using of nanosized PrF$_3$ powder would create a highly coupled ^{3}He - ^{141}Pr spin system and could show new aspects of discovered earlier effect.

The samples

The nanosized PrF$_3$ samples were synthesized by using methods, described in [9, 10]. Thus, two samples were obtained: sample A (without microwave radiation), sample B (with microwave radiation). The crystal structure of the samples has been characterized by XRD. All of the diffraction peaks can be readily indexed from the standard powder diffraction files of the hexagonal phase PrF$_3$. XRD also confirms hexagonal phase of the of PrF$_3$ particles crystal structure.

High-resolution transmission electron microscopy (HRTEM) images were obtained by using JEM – 2100 F/SP with resolution – 0,14 nm using an accelerating voltage of 200 kV. As shown in fig.1, nanoparticles of sample B are larger than of sample A and have more regular spherical shape. Fig.1 shows that, transition from sample A to sample B leads to transition from polycrystalline to singlecrystal structure. From these pictures it can be obtained a size distribution of nanoparticles PrF$_3$ for samples A and B (fig.2). Particle size are: 20 ± 15 nm sample A, 32 ± 10 nm sample B.

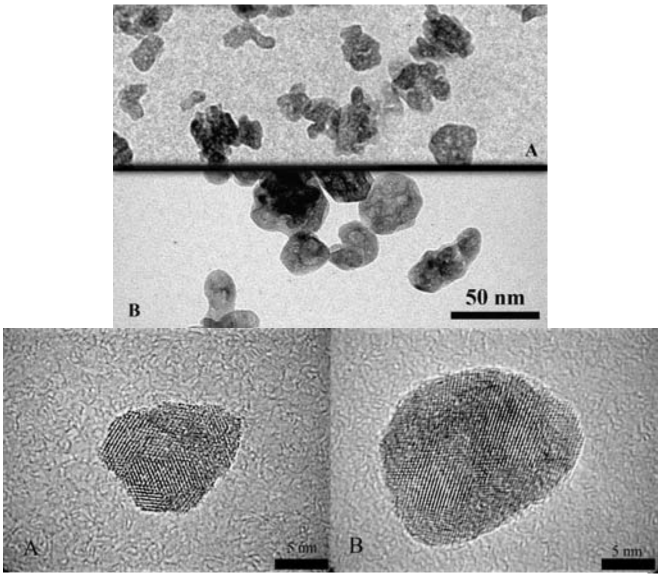

Fig.1. HRTEM image of an individual PrF$_3$ nanoparticles

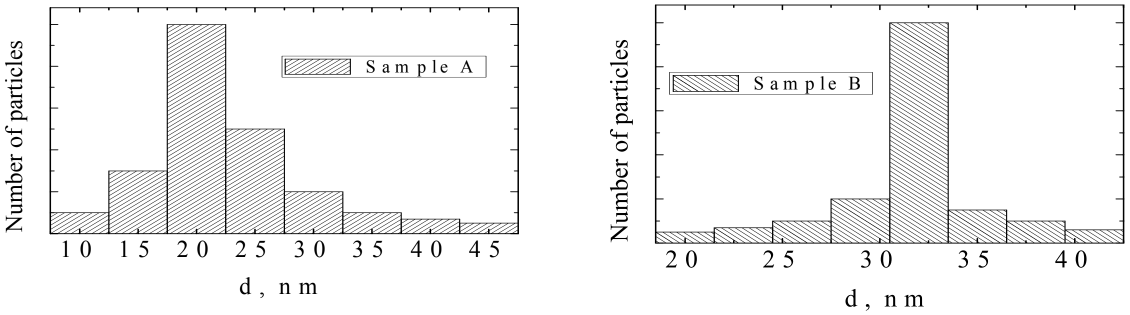

Fig. 2. The distribution of nanoparticles PrF_3 size for samples A and B

Results and discussion

The resonance spectra of the powdered PrF_3 sample in contact with liquid ^4He were measured at frequencies of 6.63 and 19.7 MHz (fig.3) (filled points - PrF_3 nanoparticles, open points- microsized particles[3]). Sample B of PrF_3 was used due to the fact it has more uniform particles and narrow size distribution. The ENMR spectra of the ^{141}Pr nuclei in PrF_3 powder were simulated. The simulated NMR spectra of ^{141}Pr for the PrF_3 powder are in good agreement with the measurements (fig.4).

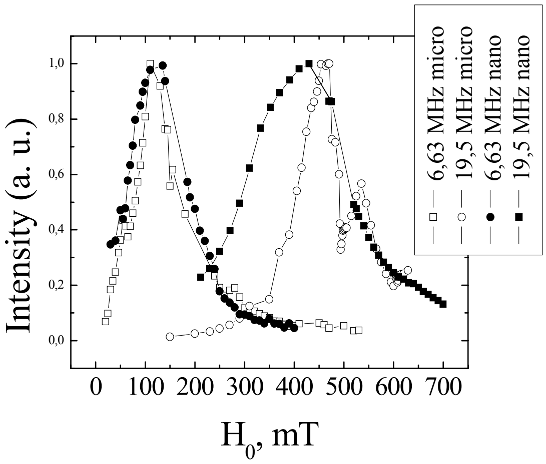

Fig.3. Enhanced nuclear magnetic resonance (ENMR) spectrum of ^{141}Pr in PrF_3 powder recorded at a frequency 6.63 and 19.5 MHz (filled points - PrF_3 nanoparticles (sample B), open points- microsized particles

Fig.4 shows that at a frequency of 19.5 MHz nanosized sample spectrum is well described by the simulated spectrum with a line width - 6 MHz, and microsized - 1 MHz. ^{141}Pr energy levels in PrF3 in the absence of a magnetic field are 9.02 and 17.08 MHz.

The study of spin kinetics of ^3He in contact with PrF_3 (sample B) nanoparticles have been conducted. The magnetic field dependences of the longitudinal magnetization relaxation rate of ^3He nuclei in the system PrF_3 (~ 32 nm) — ^3He and the dependence of the magnetic field inhomogeneity of the applied field, sensed by ^3He spins are presented in fig.5. Nanosized powder has a huge crystal surface which means that relaxation mechanisms due to the adsorbed film [5, 6] should work. Due to the fact that PrF_3 is a Van Vleck paramagnet, it's particles create a highly inhomogeneous magnetic field between them. Thus, the longitudinal relaxation mechanism of ^3He in inhomogeneous field should work [7]. This model assumes the growth of the relaxation rate with increasing magnetic field. Taking into account both described earlier mechanisms all experimental data can be fitted by following equation

$$1/T_1 = A/H_0 + BH_0 \qquad (1)$$

Conclusion

The method of synthesis of nanosized powders of crystalline trifluoride rare earths compounds was tested. As a result, two nanoscopic samples of Van Vleck paramagnet PrF_3 with size (20 ± 15) nm and (32 ± 10) nm were synthesized. X-ray analysis established a high

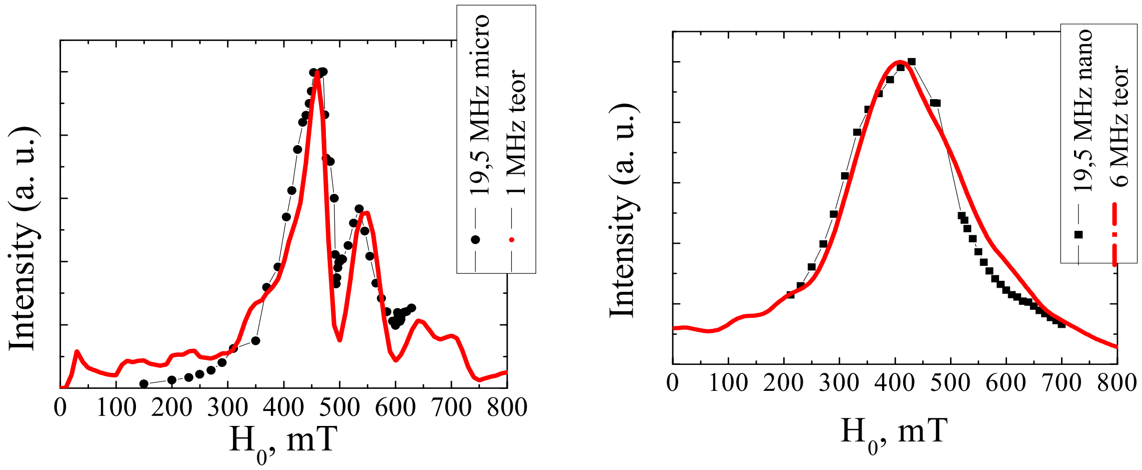

Fig.4. Simulated nuclear magnetic resonance spectrum of ^{141}Pr in PrF_3 powder recorded at the frequency 19.5 MHz microsized – left fig., nanoparticles – right fig.)

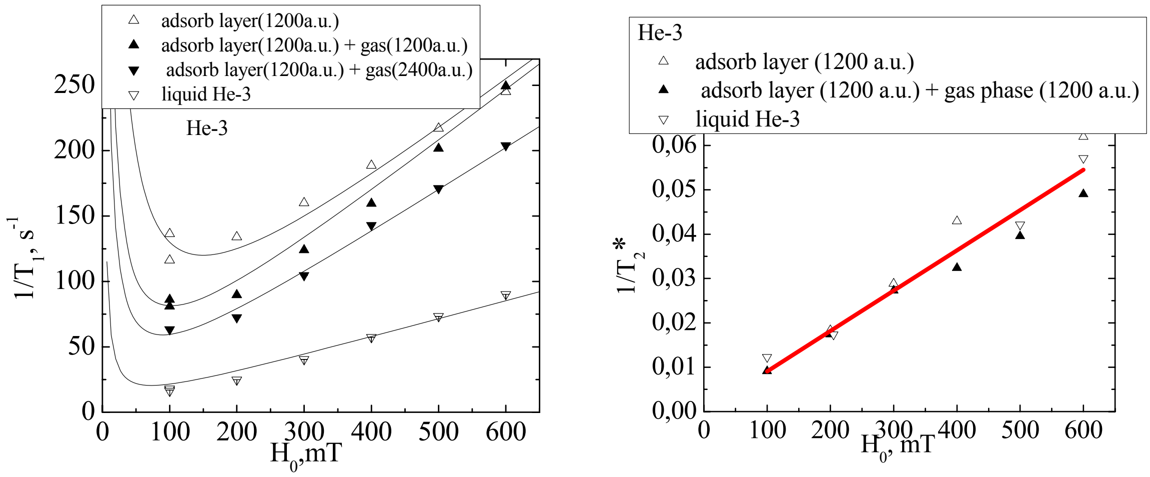

Fig.5. The magnetic field dependences of the longitudinal magnetization relaxation rate of ^{3}He nuclei in the system “^{3}He-PrF_3” (~ 32 nm) from the field.

crystallinity of the synthesized samples. According to the results of HRTEM, the transition from the first sample to the second sample leads to transition from polycrystalline to single crystal structure.

NMR spectra of ^{141}Pr in the synthesized PrF_3 powders were investigated. The spectrum of nanosized sample is wider than that of microsized PrF_3 sample, investigated earlier. The simulations of 141Pr NMR spectra are in good agreement with experimental data.

Spin kinetics of ^{3}He in the system “PrF_3-^{3}He” was investigated. The model of longitudinal magnetization relaxation of ^{3}He nuclei was proposed. According to this model the longitudinal relaxation of ^{3}He is carried out both by the ^{3}He adsorbed film on the surface and due to the modulation of dipole-dipole interaction in strongly inhomogeneous magnetic field, caused by nanosized PrF_3 particles.

This work is supported by the Ministry of Education and Science of the Russian Federation (FTP "Scientific and scientific - pedagogical personnel of the innovative Russia", CONTRACT №P900)

References

[1] M. S. Tagirov, JETP Lett, Vol. **61**, 652 (1995)

[2] L. Ma et al., Materials Letters, Vol. **61**, 2765 (2007)

[3] A.V. Egorov et al., JETP Lett, Vol. **86**, No. 6, pp. 416 (2007)

[4] M. A. Teplov, JETP Lett. **5**, 167 (1967).

[5] Richardson, R.C., Physica B.,Vol. **126**, Is. 1-3, p. 298-305 (1984)

[6] Cowan, B.P., J. Low Temp. Phys., Vol. **50**, № 1-2, p. 135-142 (1983)

[7] N.F. Fatkullin, JETP, Vol. **74** (1992)

[8] M. A. Teplov, Available from VINITI, No. 127 479 (1979).

[9] E.M. Alakshin et al., Actual problems of magnetic resonance and its application (2009)

[10] M.S. Tagirov, QFS 2010, book of abstracts, p.152

High-frequency EPR – spectroscopy of Chromium Ions in Synthetic Forsterite

D.A. Akhmetzyanov[1,2], V.F. Tarasov[1]

[1]Zavoisky Physical-Technical Institute of the Kazan Scientific Center of the Russian Academy of Sciences, 420029, Sibirskii trakt 10/7, Kazan, Russian Federation.
[2]Kazan Federal (Volga Region) University, 420008, Kremlyovskaya St. 18, Kazan, Russian Federation.

e-mail: dimaphysics@mail.ru

Chromium ions in synthetic forsterite form many different types of impurity centers, which differ in charge state of chromium ions and its localization in the crystallography structure [1,2]. Tetravalent chromium ions in synthetic forsterite and trivalent chromium ions in forsterite co-doped with chromium and lithium are the laser centers on the near Infra Red band [3,4]. Therefore control of charge state and concentration of various impurity chromium ions is of great interest for enhancement of parameters of chromium-forsterite lasers.

Tunable high-frequency electron paramagnetic resonance spectroscopy [5] is a powerful tool to study these properties, because this method allows differing one kind of chromium ions from another.

The aim of this work is to study the dependence of the concentration of Cr^{2+} and Cr^{3+} ions in forsterite doped with chromium on percentage of the oxygen in the atmosphere during the crystal growth and also influence of irradiation by electrons on appearance of new paramagnetic centre. We use for this purpose tunable high-frequency EPR spectroscopy. All experiments were carried out at 4,2K in magnetic field from -0,3 to 5 kG in frequency range of 65 – 250 GHz.

For our measurements we used three samples of synthetic forsterite which properties are presented in table 1.

Table 1. Properties of the observable samples

Samples	Atmosphere of growing (%-volume)	Content Chromium on the melt (%-mass.)
481	99,15% Ar+0,85% O_2	0,136
487	88% Ar+12% O_2	0,113
507	99,99%Ar+0,01% O_2	0,073

The 481 and 487 samples were irradiated by electrons with energy of 21 MeV.

Forsterite Mg_2SiO_4, a member of the olivine family $Mg_{2-x}Fe_xSiO_4$, has an orthorhombic lattice structure with space group *P*bnm (*a* = 4,76 Å, *b* = 10,22 Å, *c* = 5,99 Å). In the lattice, Mg^{2+} ions are in two crystallographic positions, 4*a* (M1) and 4*c* (M2), which have inversion and mirror point symmetry, respectively. Cr^{2+} and Cr^{3+} ions can substitute Mg^{2+} in both crystallographic positions [1,2]. Si^{4+} ions are in 4*c* position with mirror point symmetry and Cr^{4+} ion can substitute it.

Structure of spin sublevels of Cr^{2+} (fig.1b) and Cr^{3+} (fig.1a) in forsterite are presented in fig.1 [6]. Divalent chromium ion has electron spin S = 2 and it is a non-Kramers ion, trivalent chromium ion has electron spin S = 3/2 and it is a Kramers ion.

To define the concentration of the divalent chromium ions in the samples we used two resonance transitions between electron sublevels (1 and 2 in fig.1b) and found integral intensities of them. One of the EPR spectra that we used to our calculating is presented in fig.2.

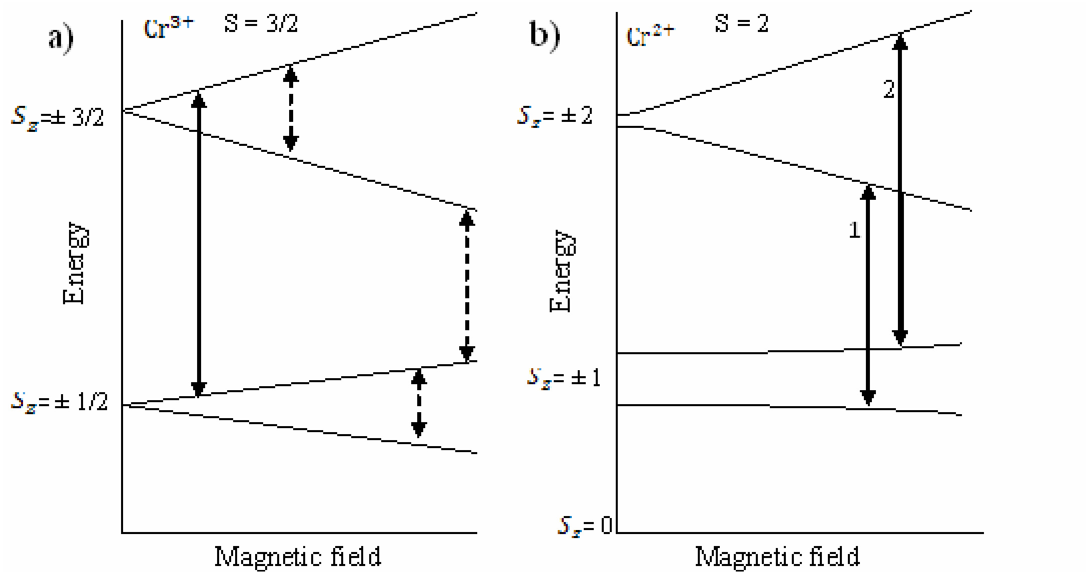

Fig.1. Structure of spin sublevels of chromium ions in forsterite [6].

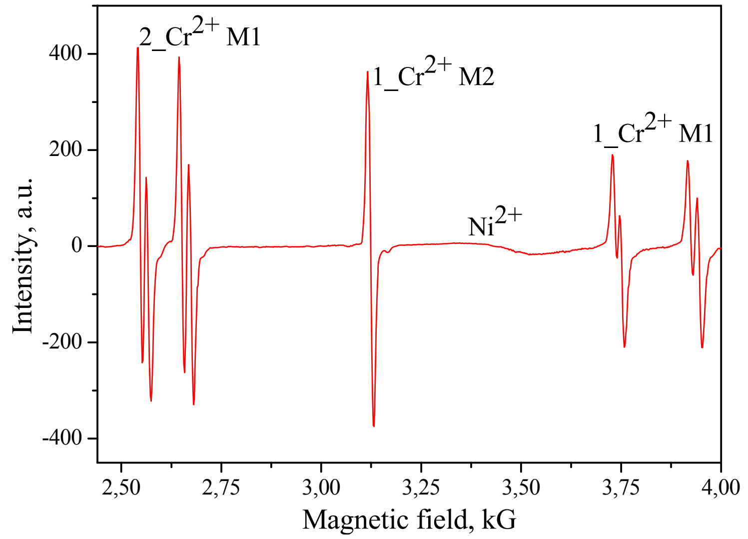

Fig.2. EPR-spectrum of divalent chromium ions in forsterite (481 sample).

The average values of the integral intensities normalized to intensity of the transition of Ni^{2+}, that was used as the reference mark are presented in table 2.

Table 2. Normalized average integral intensities of the Cr^{2+} transitions

Sample/Transition	2(M1)	1(M2)	1(M1)
481	0,692	0,200	0,548
487	0,786	0,167	0,641

We concluded: the concentration of single ions of Cr^{2+} does not depend on concentration of oxygen in the growth atmosphere in the band of 0,85-12 volume %.

The 481 and 487 samples were irradiated by electrons and in both samples new resonance transitions appeared. In the 487 sample the intensities of this transition is much lower than in 481 sample (Fig.3). In the non irradiative 507 sample this transitions were not observed.

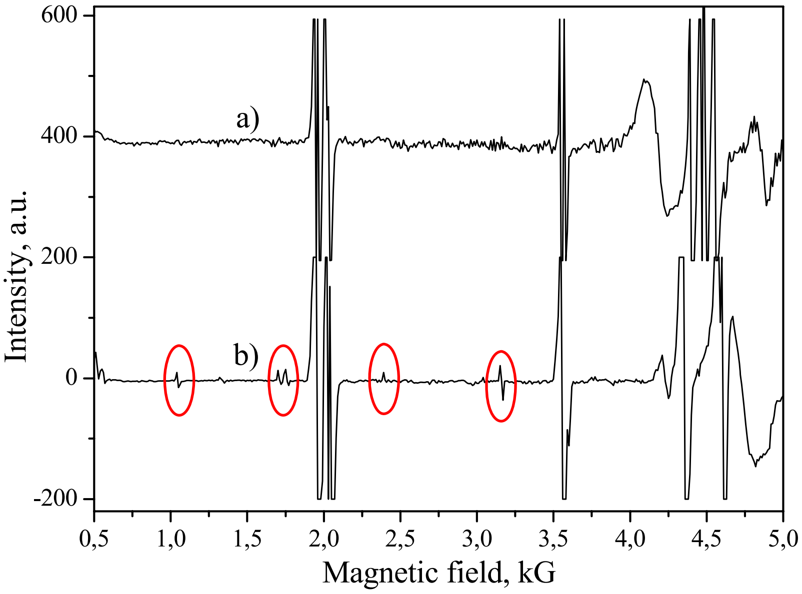

Fig.3. EPR-Spectra at 220 GHz of Cr^{2+} in forsterite in 481 (b) and 487 (a) samples.

To define the concentration of the trivalent chromium ions in the samples we used one resonance transition between electron sublevels (fig.1a solid arrow). The EPR-spectra of Cr^{3+} ions in forsterite are presented in fig.4.

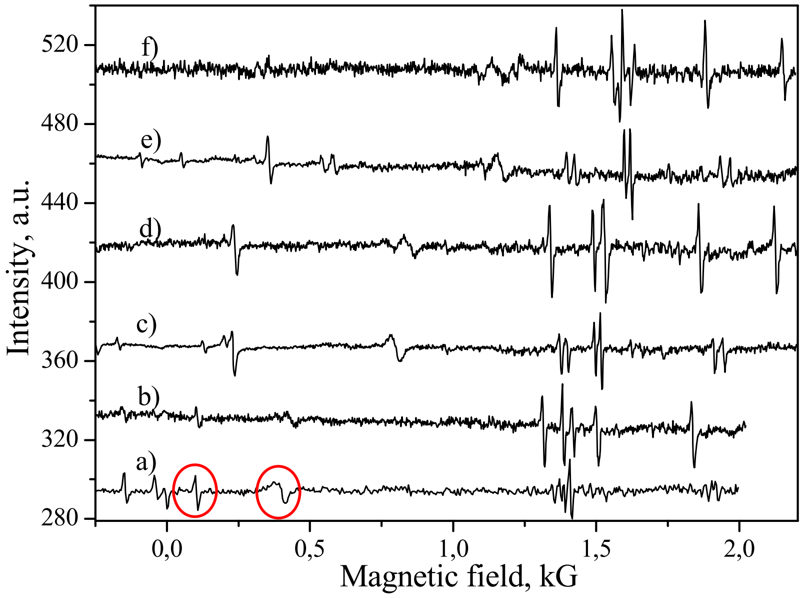

Fig.4. EPR-Spectra of Cr^{3+} in forsterite in 481 and 487 samples at different frequencies. (a) 481 sample at 73,5 GHz, (b) 487 sample at 73,5 GHz, (c) 481 sample at 74 GHz, (d) 487 sample at 74 GHz, (e) 481 sample at 74,5 GHz, (f) 487 sample at 74,5 GHz.

We concluded: the concentration of single ions of Cr^{3+} does not depend on concentration of oxygen in the growth atmosphere in observable band.

The transitions which marked on fig.4, appear in all samples. Integral intensity of these transitions in 487 sample is lower in about 10 times, than in 481 sample.

We suppose that these transitions are due to complex paramagnetic centre that is associate of trivalent chromium ion and another paramagnetic centre. Experimentally we determine, that complex centre is non Kramers, though Cr^{3+} ion is Kramers ion. So the other paramagnetic centre, that is a part of the associate, has half-integer spin.

And also we guess, that new transitions which marked on fig.3 are belong to associate of Cr^{2+} ion with another paramagnetic centre. These new transitions appear after irradiation of 481 and 487 samples. Probably after irradiation trivalent chromium ion change own valence state and transform to divalent chromium ion.

The work is supported by the RFBR grant 09-07-97006 and the grant of the President of the Russian Federation NSh -6267.2010.2.

References

[1] H. Rager. Phys. Chem. Minerals **1**, 371 (1977).

[2] В.Ф. Тарасов, Г.С. Шакуров, А.Н. Гавриленко. ФТТ **37**, 499 (1995)

[3] V. Petricevic, S.K. Gayen, R.R. Alfano, K. Yamagishi, H. Anzai, Y.Yamaguchi. Appl. Phys. Lett. **52**, 1040 (1988).

[4] А.В. Гайстер, Е.В. Жариков, В.Ф. Лебедев, А.С. Подставкин, С.Ю. Теняков, А.В. Шестаков, А.И. Щербаков. Квантовая электрон. **34**, 693 (2004).

[5] Tarasov V.F., Shakurov G.S. Appl. Magn. Res. **2**, 571 (1991).

[6] А.А. Коновалов, В.Ф. Тарасов, В.Б. Дудникова, Е.В. Жариков. ФТТ **51**, 1533 (2009).

NMR spectrometer for ultra low temperatures

A.S. Alexandrov, A.V. Egorov

Kazan Federal University, 420008, Kremlevskaja st. 18, Kazan, Russia Federation.

e-mail: alex.d.alamber@gmail.com

Introduction

A common method of continuous wave NMR (CW-NMR) employs magnetic field modulation and sweep. Therefore, a wide range of systems solid-state physics is interested in, cannot be probed by the CW-NMR. For instance, ferromagnetic and antiferromagnetic materials have high internal magnetic fields, so the external field sweep is useless. Materials with a strong magnetostriction tremble too high while magnetic field is modulated. Magnetic field modulation cannot be applied for the superconductors too.

Moreover, at ultra low temperatures (lower than 0.3 K) there is a problem to detect CW-NMR for any sample. Firstly, the cryostat is heated by currents caused by magnetic field modulation. Secondly, to obtain such temperatures adiabatic demagnetisation is sometimes applied, so the magnetic field is needed to control temperature [1].

To solve problems mentioned above we suggest using frequency sweep and frequency modulation rather than field modulation and sweeping. Besides, it gives a possibility to append to NQR, ZFNMR, where only pulsed signal were registered, the continuous wave registration. The main objectives of our work were designing, assembling and testing continuous wave NMR spectrometer with digital registration intended for ultra low-temperature experiments.

We choose Q-meter circuit, as a spin detector. Although the marginal oscillator has less noise and simple at frequency tuning, at ultra low temperatures one should employ low RF currents to avoid signal saturation, because of very long spin-lattice relaxation times. This couldn’t be done with marginal oscillator, due to instability below minimal oscillation amplitude. Thus, in spite of higher noise level and difficulties in frequency tuning of a Q-meter, there is no matter about sensitivity at ultra low temperatures due to Curie law: at 0.1 K signal should be 3000 times greater than at 300K and the noises should be the same.

At the literature review we found one article, covering our subject [1]. In 1983 Veenendaal E.J and collaborators suggested a frequency modulated Q-meter for very low temperatures. The scheme is fully analogous that makes it very hard to perform. It employs four lock-in amplifiers, several feedback loops, and two modulation frequencies. One for keep the resonance circuit tuned to generator frequency, second for the absorption signal registration. We suggest scheme with digital control and registration that gives the next advantages: no feedback loops; one modulation frequency for both tuning the resonance circuit and absorption registration; tuning and registration may be separated in time to simplify construction.

Description of apparatus

Block diagram of working spectrometer is shown in fig.1. The analogue part is presented by current source (CS), which is controlled by SML01 generator. SML01 generator is connected to the PC with RS232 interface. Thereby, one is able to control the frequency and output power via PC. Current source feds the LC circuit. The signal is taken off through matching common-drain amplifier (CDA). Then signal is amplified by radio-frequency

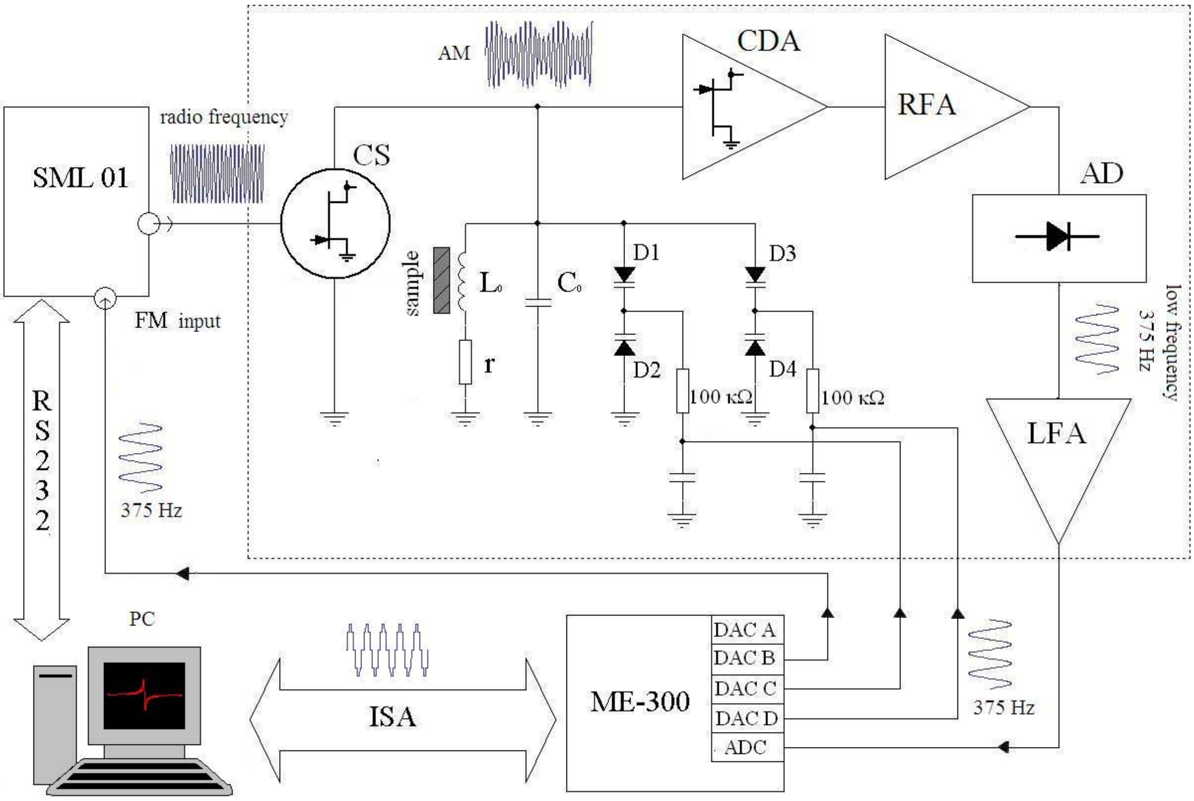

Fig.1. The block diagram of the spectrometer.

amplifier (RFA), is detected by amplitude detector and is amplified by low-frequency amplifier (LFA). LF signal then goes to digital registration board ME-300, which contains sets of DACs and ADCs, and connected to the PC via ISA interface. In this board signal is digitized by ADC, and then digital synchronous detection is being accomplished – signal points multiplied by reference points and summarized. It can be done, because the reference 375 Hz signals for capacity and frequency modulation is generated by ME-300 DACs (DAC B and DAC C), which are synchronized with ADC by internal ME-300 programmable clock. Frequency sweep is obtained by sweeping the LC circuit eigenfrequency and the generator frequency is kept tuned to it. For these purposes LC circuit is equipped with controlled varactor diodes KB109A. Generator tuning employs the capacity modulation, which leads to amplitude modulation of RF signal. The amplitude of that modulation should be zero if the LC circuit eigenfrequency equals the generator frequency, because the impedance of LC circuit has maximum value at the eigenfrequency. By varying generator frequency during capacity modulation we obtain zero AM amplitude value, thus the LC circuit is tuned. The absorption is registered differentially, what employs frequency modulation.

As RF generator the Rohde&Schwarz SML 01 signal generator was used. It is a digital synthesizer with 9 kHz – 1.1 GHz frequency band. It was used due to its properties:

1) low noise level (less than -140 dBc/√Hz);
2) short signal setting time (about 10 ms);
3) high frequency resolution (about 0.1 Hz) [2].

The SML01 manufacturer claims that broadband noise is lower than -140 dBc/√Hz. It means 0.1 µV root-mean square (rms) noise voltage per 1 Hz band, if carrier amplitude is equals to 1 V.

The RF signal is fed to the LC circuit through common-gate amplifier, built on a КП312А JFET transistor. It has to be done because, at working frequencies (~ 10 MHz) the LC circuit has impedance about 10 kΩ, and the SML 01 generator has 50 ohm RF output. The high frequency broadband transformer is applied in order to provide necessary 50 ohm input of current source. Resistance transformation ratio is Z = 1 : 4, frequency band is from 0.1 to 300 MHz. Therefore, if U = 10 mV is set at SML 01, at the second transformer coil should be U = 20 mV. The КП312А gain slope is S = 5 mA/V, so the current equals I = SU = 100 μA, thus the voltage at LC circuit should be U_{LC} = IR = 1V.

The signal from LC circuit is put to RFA through matching common-drain amplifier, which is built on the same transistor КП312А. Output resistance of the amplifier is transformed to 50 ohm input of RFA with a help of similar high frequency transformer. The main advantage of the amplifier is nearly reactive input impedance – low input capacity about 2 pF, and 0.1 – 300 MHz frequency band. Linearity is kept up to U_{in} = 2V, full gain with transformer contribution is about K_u = 0.2.

Broadband low noise amplifier Avantek UTC5-221-L was used as a radio-frequency amplifier. It has 50 ohm input and output impedance, frequency band from 10 to 500 MHz, and gain about K_u = 60. Our measurements show that RFA noise doesn’t affect full registration system noise.

The circuit of diode detector was used in order to demodulate the RF signal. The point-contact germanium diode, intended for transform and detection signal up to 150 MHz, was applied. Input is matched to the RFA output passively by 50 ohm resistor.

The LFA is represented by two-stage amplifier built on К140УД17В operational amplifiers. Gain is about 100 dB, frequency band is up to 1.5 kHz. The main advantage of chosen operational amplifier is low noise level. LFA output is connected to the differential input of ADC through transformer with electrostatic screen.

Current source, sweeping and capacity modulation circuits and common-drain amplifier were performed in one high frequency board wired point-to-point. Amplitude detector and LFA were performed in low frequency board. Galvanic separation of ADC circuits, differential connection of ADC input amplifiers, and transformers with electrostatic screen were employed to avoid low frequency disturbance and noise. The spectrometer is controlled via PC by the program written in Basic language with subroutines written in assembler.

Spectrometer frequency range is defined by the spin detector construction and equals 1 - 100 MHz. The sweeping range is defined by applied varactor diodes and for KB109A equals 50% of frequency, defined by LC coil. Measured root-mean square noise voltage at the 1 Hz band, reduced to the registration system input, equals 0.15 μV. Generator noise is 0.1 μV, thus spectrometer noise is completely defined by the generator noise.

Experiment

In the terms of testing the spectrometer we make NQR experiment on ^{63}Cu in cuprous oxide powder Cu_2O at room temperature T = 300K. The theoretical calculations of signal magnitude were carried out for proving the received results. Abragam described the calculation method for quadruple resonance in seventh chapter [3].

In the experiment was used the coil with 14 mm diameter and 12 mm length. Cuprous oxide placed in ampoule with 12 mm internal diameter, filling factor relating to powder noncompact filling is about 0.7. The Cu_2O density is ρ = 6 g/cm^3, molar mass is μ = 143 g/mole, natural abundance of ^{63}Cu is about 69%. ^{63}Cu nuclei has I = 3/2 spin and $\gamma/2\pi$ = 1.1285 kHz/Oe gyro magnetic ratio. Consider that the spin system is described by the Bloch equations, for Lorenz line shape at ν = 26 MHz and $\Delta\nu$ = 3 kHz line width calculation resulted χ'' = 4.8*10^{-8} maximum susceptibility. The LC circuit quality is Q = 36, filing factor equals η

= 0.25. Thereby for U = 1V RF voltage at LC circuit receive the absorption signal magnitude about $\delta U = 4\pi\eta Q\chi''U = 5$ μV.

Experimental dependence of AM modulation amplitude is shown in this fig.2. There is a CW-NQR signal at about 26 MHz. The magnitude of signal is about 3 μV which is very close to theoretically calculated value 5 μV. RMS noise amplitude is about 0,15 μV. Signal and noise both were measured in 1Hz frequency band.

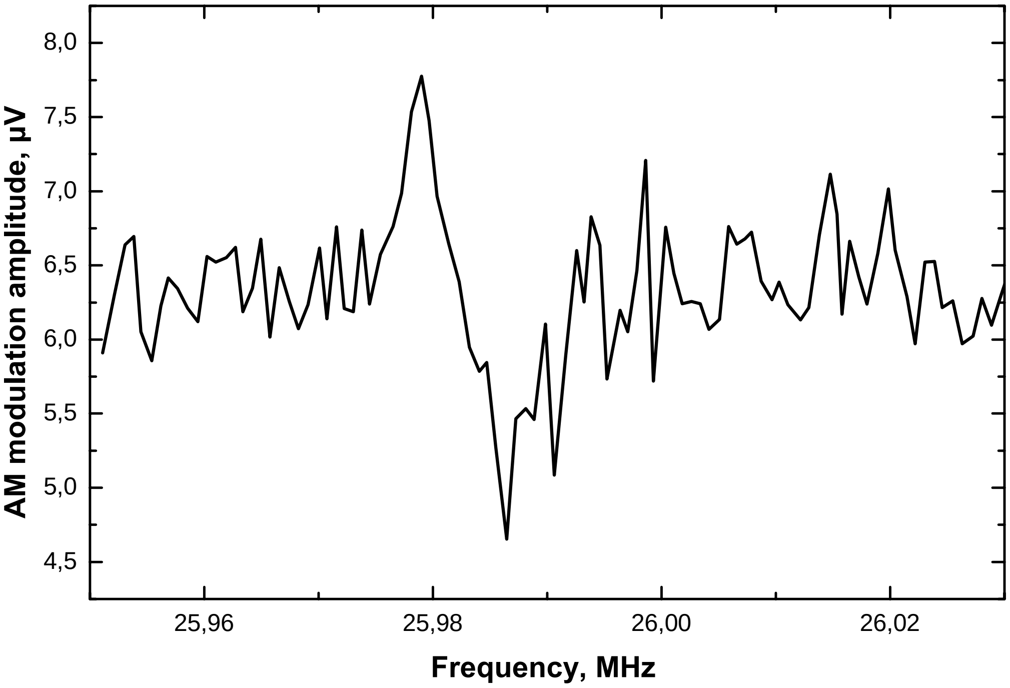

Fig.2. Experimental dependence of AM modulation amplitude.

Results

As result of this work were designed and assembled the digital control and registration CW-NMR spectrometer with frequency sweep and frequency modulation. It operability and applicability for ultra low temperatures were shown. System noise is defined by generator noise, which impossible to avoid. We plan to use it under its designation – ultra low temperature experiments in our laboratory.

References

[1] Veenendaal E.J., Hulsman R., Brom H.B., *A frequency-modulated Q-meter for very low-temperature NMR experiments* / E. J. Veenendaal, R. Hulsman, H. B. Brom // *J. Phys. E*: Sci. Instrum. – 1983. – Vol. **16** – P. 649-653.

[2] *Operating Manual Signal Generator R&S SML 01*: Rohde&Schwarrz – Federal Republic of Germany.

[3] Abragam A. *Nuclear Magnetism* / A. Abragam // Oxford University Press – 1961. – P. 599.

[4] Lee, Kenneth. *Nuclear spins, moments, and magnetic resonance frequencies* / Kenneth Lee, Weston A. Anderson // Palo Alto, Calif.: Varian Associates. – 1967.

NMR study of the reorientational motion in borohydrides: $RbBH_4$, $CsBH_4$ and α-$Mg(BH_4)_2$

O.A. Babanova, A.V. Soloninin, A.P. Stepanov, A.V. Skripov

Institute of Metal Physics, Urals Branch of the Russian Academy of Sciences, 620041, S. Kovalevskoi 18, Ekaterinburg, Russia.

e-mail: Babanova@imp.uran.ru

Introduction

Borohydrides are ionic compounds with a general formula $M(BH_4)_n$ (where $n = 1$ or 2 for alkali or alkaline-earth M elements, respectively), consisting of metal cations M^{n+} and tetrahedral $[BH_4]^-$ anions. These materials are considered as promising materials for hydrogen storage [1], since the volumetric and gravimetric hydrogen densities in them are rather high [2], but their stability with respect to thermal decomposition and the slow sorption kinetics remain the major drawbacks for a practical use. In complex hydrides, hydrogen is covalently bound to the other element B, and arranged in subunits. Hydrogen dynamics in such a system is described as a combination of several types of motion: the internal H-vibrations within each complex, the rotation of the complex about symmetry axes, the motion of the $[BH_4]^-$ units against the metal ions (external H-vibrations) and the translational diffusion of hydrogen. The reorientational motion of BH_4 groups can be represented by rotations around three 2-fold axes and four 3-fold axes. Elucidation of hydrogen dynamics in complex hydrides may contribute to improving their hydrogen-storage properties.

The aim of the present work is to study the reorientational motion of $[BH_4]^-$ units in $RbBH_4$, $CsBH_4$ and α-$Mg(BH_4)_2$ using measurements of the ^1H and ^{11}B NMR spectra and spin-lattice relaxation rates over wide ranges of temperature (78 – 420 K) and resonance frequency (14 – 90 MHz for ^1H and 14 – 28 MHz for ^{11}B). NMR appears to be especially effective for studies of atomic motion in borohydrides because nuclear spin-lattice relaxation rates in borohydrides do not contain any significant contributions not related to atomic motion (such as the conduction-electron contribution in metallic systems). This allows us to trace the atomic jump rates in borohydrides over the range of 6 orders of magnitude ($10^6 – 10^{12}$ s^{-1}).

Results and discussion

The temperature dependences of the proton spin-lattice relaxation rates R_1 measured for $RbBH_4$ and $CsBH_4$ at three resonance frequencies $\omega/2\pi$ are shown in fig.1. The general features of the observed behavior of R_1 are typical of the relaxation mechanism due to nuclear dipole-dipole interaction modulated by thermally activated atomic motion. This motion is localized (which is supported by the fact that the proton NMR linewidth at half-maximum remains to be about 20 kHz and 17 kHz for $RbBH_4$ and $CsBH_4$, respectively, over the entire temperature range) and can be identified as reorientations of the BH_4 tetrahedra.

For alkali borohydrides $RbBH_4$ and $CsBH_4$, the proton spin-lattice relaxation rate shows the frequency-dependent peak (fig.1) at the temperature at which the reorientation rate τ^{-1} becomes nearly equal to ω. The experimental results have been described in terms of the standard model with the Arrhenius-type temperature dependence of τ^{-1} [3]. The parameters of the model are the pre-exponential factor τ_0^{-1}, the activation energy E_a of the reorientations, and the fluctuating parts ΔM_{HB} and ΔM_{HH} of the dipolar second moment due to the H – B and H – H interactions. These parameters are varied to find the best fit to the $R_1(T)$ data at the three resonance frequencies *simultaneously*. The results of the fit for $RbBH_4$ and $CsBH_4$ are

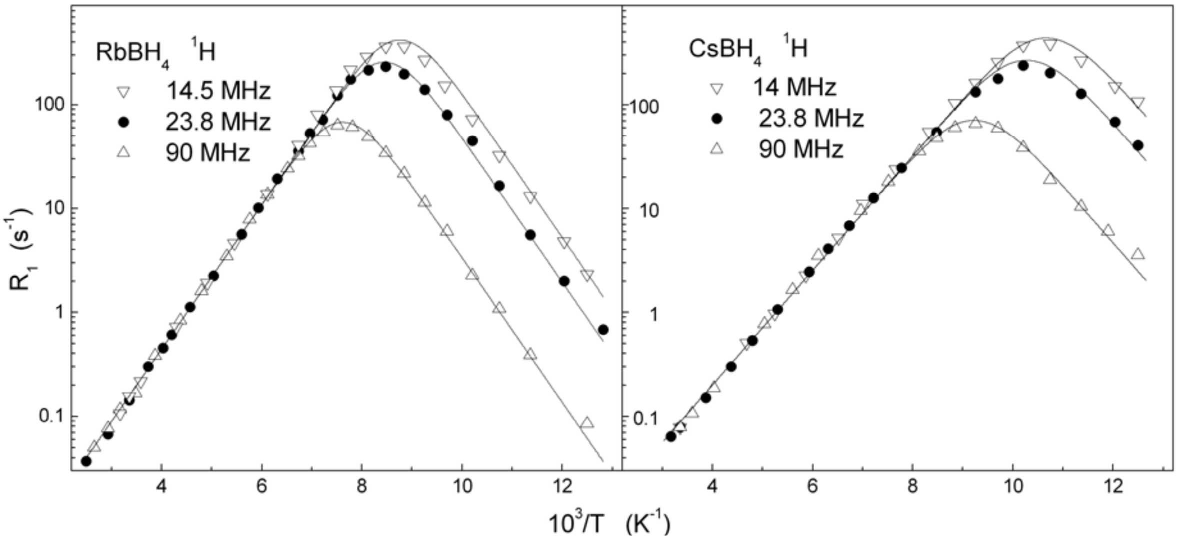

Fig.1. Proton spin-lattice relaxation rates measured at three resonance frequencies as functions of the inverse temperature for $RbBH_4$ and $CsBH_4$. The solid lines show the simultaneous fits of the standard model to the data.

shown by the solid lines in fig.1. The motional parameters resulting from the fit to the $RbBH_4$ data are $\tau_0 = 9\times10^{-15}$ s and $E_a = 138$ meV, the amplitude parameters are $\Delta M_{HB} = 1.2\times10^{10}$ and $\Delta M_{HH} = 1.3\times10^{10}$ s^{-2}. For $CsBH_4$, the corresponding values of the fit parameters are $\tau_0 = 1.4\times10^{-14}$ s, $E_a = 109$ meV, $\Delta M_{HB} = 1.2\times10^{10}$ and $\Delta M_{HH} = 1.4\times10^{10}$ s^{-2}.

In the studied temperature range of 78 – 400 K, alkali borohydrides $RbBH_4$ and $CsBH_4$ do not exhibit any phase transitions, and the $R_1(T)$ data correspond to the cubic phase (space group *Fm*-3*m*). Our results for the activation energies differ from those of the previous NMR study [4] (150 meV and 124 meV for $RbBH_4$ and $CsBH_4$, respectively). It should be noted that, in contrast to Ref. [4], our analysis is based on the data at three different resonance frequencies and includes the broader ranges of the temperature and R_1 values (in fact, the R_1 maximum was not reached in the measurements of Ref. [4]). The reorientational motion of BH_4 groups in $CsBH_4$ appears to be the fastest one among all the borohydrides studied so far. For $RbBH_4$ and $CsBH_4$, we have not found any signs of a distribution of the jump rates τ^{-1}. The presence of such a distribution would make the frequency dependence of R_1 substantially weaker [5] than that predicted by the standard model.

The temperature dependences of the ^{11}B spin-lattice relaxation rates measured for $RbBH_4$ at two resonance frequencies are shown in fig.2 (^{11}B spin-lattice relaxation data for $CsBH_4$ are not shown). It can be seen that the general features of the behavior of the ^{11}B relaxation rates are similar to those of the ^1H relaxation rates. As in the cases of $LiBH_4$ [6], $NaBH_4$ and KBH_4 [7], the dominant contribution to the ^{11}B spin-lattice relaxation rate in studied compounds should originate from the B – H dipole-dipole interaction modulated by reorientations of the BH_4 tetrahedra [8]. The results of the simultaneous fit (analogous to that used for the proton relaxation) to the ^{11}B data are shown by the solid lines in fig.2. For $RbBH_4$, the resulting parameters are $\tau_0 = 9.9\times10^{-15}$ s, $E_a = 134$ meV, and $\Delta M_{BH} = 1.1\times10^{10}$ s^{-2}. For $CsBH_4$, the corresponding parameters are $\tau_0 = 1.2\times10^{-14}$ s, $E_a = 108$ meV, and $\Delta M_{BH} = 1.2\times10^{10}$ s^{-2}. Note that for both compounds the E_a values are close to those derived from the proton relaxation data.

The temperature dependences of the proton spin-lattice relaxation rates measured for the low-temperature hexagonal (α) phase of $Mg(BH_4)_2$ at three resonance frequencies are shown in fig.3. In contrast to the case of alkali borohydrides, the temperature dependence of the

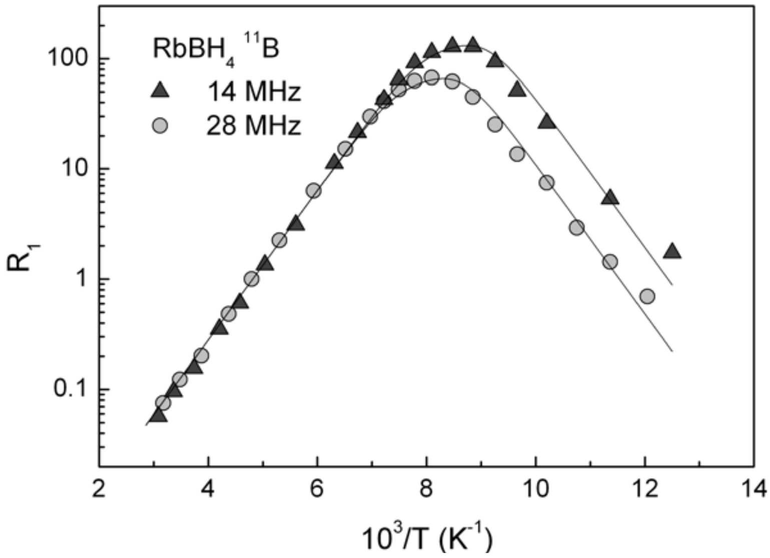

Fig.2. ^{11}B spin-lattice relaxation rates measured at 14 and 28 MHz as functions of the inverse temperature for $RbBH_4$. The solid lines show the simultaneous fits of the standard model to the data.

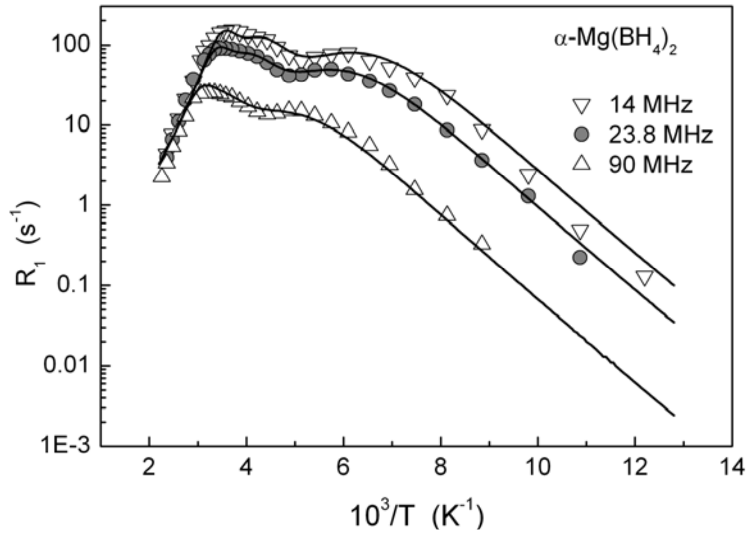

Fig.3. Proton spin-lattice relaxation rates measured at 14, 23.8 and 90 MHz for α-$Mg(BH_4)_2$ as functions of the inverse temperature. The solid lines show the simultaneous fits of the 'three-peak' model to the data.

proton spin-lattice relaxation rates $R_1(T)$ for α-$Mg(BH_4)_2$ exhibits two well-resolved maxima and can be fully described in terms of at least three reorientational processes with different jump rates. Furthermore, the description of the frequency dependence of R_1 at $T < 160$ K requires a certain distribution of jump rates for the fastest process (responsible for the low-T maximum of R_1). All jump processes correspond to localized atomic motion and can be attributed to reorientations of the BH_4 groups. For parametrization, we use a 'three-peak' model including three types of jump motion and a Gaussian distribution of activation energies for the fastest jump process. The parameters of this model are ΔM_i, τ_{0i}, E_{ai} ($i = 1, 2, 3$), and the width (dispersion) of the activation energy distribution ΔE_{a1} (the subscript $i = 1$ corresponds to the fastest type of motion, i. e., the one giving rise to the R_1 peak at lower T). The same analysis as for alkali borohydrides leads to the following results: the amplitude parameters are $\Delta M_1 = 1.5\times10^9$ s^{-2}, $\Delta M_2 = 1.6\times10^9$ s^{-2}, and $\Delta M_3 = 1.7\times10^9$ s^{-2}, and the corresponding motional parameters are $\tau_{01} = 2.3\times10^{-12}$ s, $E_{a1} = 116$ meV, $\Delta E_{a1} = 10$ meV; $\tau_{02} = 5.7\times10^{-13}$ s, $E_{a2} = 198$ meV; $\tau_{03} = 4.0\times10^{-15}$ s, and $E_{a3} = 362$ meV. Solid lines in fig.3 show the simultaneous fit of the ‘three-peak’ model to the data at three resonance frequencies.

The ‘three-peak’ model with the same set of motional parameters also provides a good description of the ^{11}B spin-lattice relaxation data for α-$Mg(BH_4)_2$.

The origin of a coexistence of strongly differing activation energies for BH_4 reorientations in α-$Mg(BH_4)_2$ can be associated with nearly linear coordination of BH_4 by two Mg atoms [9], as shown on fig.4. The fastest jump process corresponds to the rotation around the 2-fold axis along the Mg – B – Mg line, since such a rotation does not break any Mg – H bonds. A certain variation of the Mg – B – Mg angles for different BH_4 groups in α-$Mg(BH_4)_2$ [9] can explain the distribution of the jump rates for the fastest process. The slowest jump process should be associated with the rotations around two other 2-fold axes perpendicular to the Mg – B – Mg line, since such rotations break all the Mg – H bonds. The intermediate jump process can be attributed to the rotations around 3-fold axes breaking half of the Mg – H bonds. The results for α-$Mg(BH_4)_2$ are consistent with the idea [7] that the energy barriers for BH_4 reorientations in borohydrides are determined primarily by the metal – H interactions.

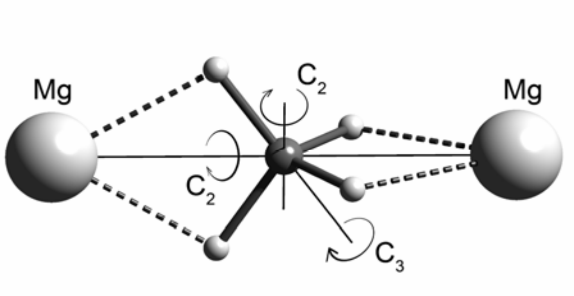

Fig.4. Schematic view of the coordination environment of BH_4 groups in α-$Mg(BH_4)_2$. Large spheres: Mg atoms, medium spheres: B, and small spheres: H. The Mg – H bonds are shown by the bold dashed lines. C_2 and C_3 are the 2-fold and 3-fold reorientation axes of the BH_4 group, respectively.

References

[1] S. Orimo, Y. Nakamori, J.R. Elisen, A. Züttel, C.M. Jensen, *Chem. Rev.* **107**, 4111 (2007).

[2] L. Schlapbach, A. Zuttel, *Nature* 414, 15 Nov. (2001).

[3] Abragam, A. *The Principles of Nuclear Magnetism*, Clarendon Press: Oxford, 1961.

[4] V.P. Tarasov, S.I. Bakum, V.I. Privalov, A.A. Shamov, Russ. *J. Inorg. Chem.* **35**, 2096 (1990).

[5] J.T. Markert, E.J. Cotts, R.M. Cotts, *Phys. Rev. B* **37**, 6446 (1988).

[6] A.V. Skripov, A.V. Soloninin, Y. Filinchuk, D. Chernyshov, *J. Phys. Chem. C* **112**, 18701 (2008).

[7] O.A. Babanova, A.V. Soloninin, A.P. Stepanov, A.V. Skripov, Y. Filinchuk, *J. Phys. Chem. C*, 114, 3712 (2010).

[8] L. Niemela, E. Ylinen, *Phys. Lett.* **31A**, 369 (1970).

[9] A.V.Skripov, A.V. Soloninin, O.A. Babanova, H. Hagemann, Y. Filinchuk, *J. Phys. Chem. C*, 114, 12370 (2010).

Role of magnetic dipole interactions in the damping of Rabi oscillations of paramagnetic centers in solids

E.I. Baibekov

Kazan Federal University, 420008, Kremlevskaya 18, Kazan, Russian Federation

e-mail: edbaibek@yandex.ru

Introduction

Rabi oscillations (RO) represent transitions between the states of quantum dipole driven by electromagnetic wave of resonant frequency [1]. In magnetic resonance, a comparison of the decay time τ_R of RO and phase relaxation time T_2 reveals how transient nutations driven by resonant microwave (MW) field affect coherence dynamics of the spin system. At sufficiently low temperatures and spin concentrations, long-range magnetic dipole (MD) interactions are the most important in the study of decoherence during the transient regime. Recent observations of Rabi oscillations in various spin systems [2-6] suggest that their decay rate is of the form $\tau_R^{-1} = \alpha + \beta\Omega_R$, where the 2nd term proportional to Rabi angular frequency Ω_R is obviously induced by the external resonant MW field. The above dependence contradicts to the predictions of Bloch model $\tau_R^{-1} = 1/2T_2$. In the present work, a more detailed quantum theory of the transient regime in the bath of spins coupled by MD interactions is derived.

Theory

Let us consider a diamagnetic solid matrix containing a small concentration of magnetic impurity (e.g. paramagnetic ions or nuclear spins). In the presence of external static magnetic field $\boldsymbol{B}_0 \parallel z$ and resonant transverse microwave field $\boldsymbol{B}_1 \cos\omega_0 t \parallel x$ ($B_0 \gg B_1$), the Hamiltonian of a system of $S = 1/2$ (pseudo-)spins coupled by MD interactions is as follows:

$$H = \hbar\sum_j \left(\omega_j S_z^j + 2\Omega_R S_x^j \cos\omega_0 t\right) + \frac{\hbar}{2}\sum_{j\neq k;\alpha,\beta=x,y,z} A_{\alpha\beta}^{jk} S_\alpha^j S_\beta^k, \tag{1}$$

where the last term represents MD interaction between j-th and k-th spins. Larmor angular precession frequencies of spins ω_j are distributed around ω_0 in magnetic resonance line of half-width σ. Especially for electronic spins in ESR, σ can well exceed Rabi angular frequency Ω_R. A transformation of Eq. (1) into the reference frame RF rotating around z axis of laboratory reference frame LF with the angular frequency ω_0 yields

$$H' \simeq \hbar\sum_j \left(\delta\omega_j S_z^j + \Omega_R S_x^j\right) + \frac{\hbar}{2}\sum_{j\neq k} A_{zz}^{jk}\left(S_z^j S_z^k - \frac{1}{2}S_x^j S_x^k - \frac{1}{2}S_y^j S_y^k\right), \tag{2}$$

where $\delta\omega_j = \omega_j - \omega_0$ is the shift of Larmor frequency of j-th spin from resonance, and we have omitted oscillating time-dependent terms in H'. Let us now introduce a new set of local axes $\tilde{x}^j, \tilde{y}^j, \tilde{z}^j$, such that $\tilde{S}_x^j = \left(\delta\omega_j S_z^j + \Omega_R S_x^j\right)\big/\Omega_j \equiv \alpha_j S_z^j + \beta_j S_x^j$, $\tilde{S}_y^j = S_y^j$, $\tilde{S}_z^j = \beta_j S_z^j - \alpha_j S_x^j$. The Hamiltonian (2) written in new spin projections is

$$H' = \hbar \sum_{j} \Omega_j \tilde{S}_x^j + \frac{\hbar}{2} \sum_{\substack{j \neq k \\ \alpha\beta}} \tilde{A}^{jk}_{\alpha\beta} \tilde{S}^j_\alpha \tilde{S}^k_\beta , \tag{3}$$

where $\Omega_j = \sqrt{\delta\omega_j^2 + \Omega_R^2}$ is the nutation frequency of j-th spin detuned by $\delta\omega_j$ from resonance. In the case of sufficiently small spin concentrations, we leave in Eq. (3) only the terms of MD interactions $\sim \tilde{S}_x^j \tilde{S}_x^k$ that are secular to the interaction with the external magnetic field in RF. These terms result in random shifts of spin nutation frequencies. We neglect nonsecular terms responsible for mutual spin flip-flops that are significant only when the average local field at the spin site induced by nearby spins is comparable with σ.

The response of a spin system to the driving resonant MW field is given by time evolution of its magnetic moment:

$$\boldsymbol{M}(t) = g_e \mu_B \operatorname{Tr}\left\{ e^{-iH't/\hbar} \rho(0) e^{iH't/\hbar} \sum_j \boldsymbol{S}^j \right\}, \tag{4}$$

where $\rho(0)$ is the initial density matrix of the spin system. Performing summation over all possible spin configurations in the trace, we obtain y-projection of magnetization:

$$M_y(t) = \frac{M_0}{N} \sum_j \beta_j \sin \Omega_j t \prod_{k(\neq j)} \cos\left(\tilde{A}^{jk}_{xx} t / 2 \right), \tag{5}$$

where M_0 is the initial magnetization of the spin system, and N is the number of spins in the volume *V*. The factor $\prod_{k(\neq j)} \cos\left(\tilde{A}^{jk}_{xx} t / 2 \right)$ in Eq. (5) is responsible for the damping of RO because of MD interactions. The averaging over random spin positions $\boldsymbol{r}_k$ and frequencies ω_k in the limit $N, V \to \infty$ yields:

$$\prod_{k(\neq j)} \left\langle \cos\left(\tilde{A}^{jk}_{xx} t / 2 \right) \right\rangle_{\boldsymbol{r}_k, \omega_k} = \exp\left\{ -C \int d\omega_k g(\omega_k) \int_{\infty} d^3 r_k \left[1 - \cos\left(\tilde{A}^{jk}_{xx} t / 2 \right) \right] \right\}, \tag{6}$$

where $C = N / V$ is the spin concentration and $g(\omega)$ is the resonance line shape. Substituting $\tilde{A}^{jk}_{xx}$ as a function of $\boldsymbol{r}_{jk}$ and performing the integration over $\boldsymbol{r}_k$ in Eq. (6), one obtains

$$M_y(t) = M_0 \int d\omega_j g(\omega_j) \beta_j \sin \Omega_j t \exp\left(-\Delta\omega_d t \int d\omega_k g(\omega_k) \left| \alpha_j \alpha_k - \beta_j \beta_k / 2 \right| \right), \tag{7}$$

where $\Delta\omega_d = \dfrac{4\pi^2 g_e^2 \mu_B^2 C}{9\sqrt{3}\hbar}$ is known as the static half-width of the resonance line due to MD interactions [7].

Given the line shape $g(\omega)$, one can calculate numerically the average magnetization (7) for the given values of C, Ω_R and σ. However, it is possible to obtain analytical expressions for $M_y(t)$ in two practically important approximations:

a) The case of strong MW field: $\sigma \ll \Omega_R$. All spins in the line nutate with the same frequency Ω_R, and

$$M_y(t) = M_0 e^{-\Delta\omega_d t / 2} \sin \Omega_R t . \tag{8}$$

b) Weak MW field: $\sigma \gg \Omega_R$. The resonance line is partially excited. Roughly, only the spins with Larmor frequencies falling into the range $\left[\omega_0 - \Omega_R, \omega_0 + \Omega_R\right]$ are involved in RO. At sufficiently small spin concentrations, the condition $\Omega_R \gg \Delta\omega_d$ is also valid. When $\sigma t \gg 1$, i.e. almost immediately after the transient regime is turned on,

$$M_y(t) = \pi M_0 g(\omega_0) \Omega_R e^{-\beta_d \Omega_R t} J_0(\Omega_R t), \tag{9}$$

where $J_0(z)$ is Bessel function of the 1st kind. It is remarkable that the parameter β_d has the same form for both Gaussian $g_G(\omega) = \left(2\pi\sigma^2\right)^{-1/2} \exp\left[-\delta\omega^2 / 2\sigma^2\right]$ and Lorentzian $g_L(\omega) = \sigma / \left[\pi\left(\delta\omega^2 + \sigma^2\right)\right]$ distributions: $\beta_d = \Delta\omega_d g(\omega_0) \ln \dfrac{2\sigma}{\Omega_R}$. RO are detected in experiment either through transverse $\left(M_\perp(t)\right)^2 = \left(M_x(t)\right)^2 + \left(M_y(t)\right)^2$ (e.g. two-photon resonance technique [2]) or longitudinal $M_z(t)$ (e.g. transient pulse followed by spin echo sequence [4]) magnetization. Following the same argumentation, one obtains $M_x(t) = 0$, in agreement with Bloch model predictions [8], and thus $M_\perp(t) = M_y(t)$. Similarly,

$$M_z(t) = \begin{cases} M_0 e^{-\Delta\omega_d t/2} \cos\Omega_R t, & \Delta\omega_d \ll \sigma \ll \Omega_R, \\ \pi M_0 g(\omega_0) \Omega_R e^{-\beta_d \Omega_R t} j_0(\Omega_R t), & \Delta\omega_d \ll \Omega_R \ll \sigma, \end{cases} \tag{10}$$

where $j_0(z) = \int_z^\infty J_0(z)\,dz$. Exponential damping $\sim e^{-\beta_d \Omega_R t}$ is induced by MD interactions between the spins driven by transient pulse. Since β_d depends on Ω_R through slowly-varying logarithmic function, the damping rate $\tau_R^{-1} = \beta_d \Omega_R$ is roughly linear in Rabi frequency in the specific range of Ω_R. When $\sigma \ll \Omega_R$, the damping rate is independent of Ω_R.

Results and discussion

In order to reveal the importance of the above decay mechanism in transient response of real systems, we have calculated RO decay rates $\tau_R^{-1} = \beta_d \Omega_R$ for E_1' and [AlO$_4$]^0 centers and compared them to the ones observed in [2,3]. The parameter β_d was obtained from numerically calculated $\tau_R^{-1}(\Omega_R)$ dependence derived from Eq. (7). Since $\beta_d \sim \Delta\omega_d \sim C$, we write $\beta_d = \gamma_d C$, with $\gamma_d\left(E_1'\right) = 1.25 \cdot 10^{-19}\,\text{cm}^3$ and $\gamma_d(\text{AlO}_4) = 4.3 \cdot 10^{-20}\,\text{cm}^3$. The measured RO decay parameters β are found to be well approximated within experimental error bounds by the sum $\beta = \beta_0 + \beta_d$ (Table 1), with $\beta_0\left(E_1'\right) = 5 \cdot 10^{-2}$ and $\beta_0(\text{AlO}_4) = 2.11 \cdot 10^{-2}$. Here the term β_d linear in spin concentration is induced by MD interactions, and the remaining constant term β_0 originates from the contributions of other kind (probably MW field inhomogeneities inside the sample volume). The calculated values of β_d agree very well with the concentration-dependent parts of β (cf. columns 4 and 6 in Table 1), which experimentally validates the RO decay mechanism considered in the present paper.

Table 1. Measured (β, [2,3]) and calculated ($\gamma_d C$, this work) RO decay parameters for E_1' centers in glassy silica and $[AlO_4]^0$ centers in quartz. The last column represents the best fit of β within the concentration error bounds by the function $\beta = \beta_0 + \gamma_d C$ (see text).

Spin centers	Sample no.	$C, 10^{16}\,\mathrm{cm}^{-3}$	$\beta, 10^{-2}$	$\gamma_d C, 10^{-2}$	$\beta_0 + \gamma_d C, 10^{-2}$
E_1'	1	7.5 ± 2	4.8 ± 0.5	0.94 ± 0.25	5.7
	2	16 ± 5	6.1 ± 0.5	2.00 ± 0.63	6.4
	3	24 ± 8	10.6 ± 0.5	3.00 ± 1.00	9.0
$[AlO_4]^0$	1	4.0 ± 0.4	2.4 ± 0.1	0.17 ± 0.02	2.30
	2	1.0 ± 0.1	2.1 ± 0.1	0.043 ± 0.004	2.15

Conclusions

We performed first-principles calculations of the relaxation processes occurring in dipolar-coupled bath of equivalent spins during transient regime. We have shown that the decoherence in a spin bath, under specific conditions, is enhanced by the external resonant microwave field. The decay rate of Rabi oscillations depends linearly on the concentration of magnetic impurity and, in the weak MW field case, almost linearly on Rabi frequency. The predictions of the model are in quantitative agreement with concentration-dependent parts of experimentally observed decay rates [2,3].

Author is grateful to B. Z. Malkin for advice and fruitful discussions of the results. This work was supprted by the RFBR grant 09-02-00930.

References

[1] [1] I. I. Rabi, Phys. Rev. **51**, 652 (1937).

[2] R. Boscaino, F. M. Gelardi, and J. P. Korb, Phys. Rev. B **48**, 7077 (1993).

[3] S. Agnello, R. Boscaino, M. Cannas, F. M. Gelardi, and R. N. Shakhmuratov, Phys. Rev. A **59**, 4087 (1999).

[4] R. M. Rakhmatullin, I. N. Kurkin, G. V. Mamin, S. B. Orlinskii, M. R. Gafurov, E. I. Baibekov, B. Z. Malkin, S. Gambarelli, S. Bertaina, and B. Barbara, Phys. Rev. B **79**, 172408 (2009).

[5] S. Nellutla, K.-Y. Choi, M. Pati, J. van Tol, I. Chiorescu, and N. S. Dalal, Phys. Rev. Lett. **99**, 137601 (2007).

[6] J. H. Shim, S. Gambarelli, S. Bertaina, T. Mitra, B. Tsukerblat, A. Müller, and B. Barbara, arXiv:1006.4960v2.

[7] W.B. Mims, Phys. Rev. **168**, 370 (1968).

[8] H. C. Torrey, Phys. Rev. **76**, 1059 (1949).

^{59}Co ZFNMR study of $YBaCo_4O_7$ compound

L.A. Batalova[1], I.R. Mukhamedshin[1], A.N. Lavrov[2]

[1]Kazan Federal University, Kremlevskaya str., 18, Kazan, 420008, Russia
[2]Institute of Inorganic Chemistry, Lavrentyeva str., 3, Novosibirsk, 630090, Russia
e-mail: batalova.liliya@yandex.ru

The cobalt oxides are currently one of the most investigated classes of transition metal oxides. They show a rich collection of interesting physical phenomena, including superconductivity, giant magneto resistance, strong thermopower, temperature-driven spin-state and metal-insulator transitions. Some of them also show a high degree of magnetic frustration, such as $YBaCo_4O_7$, which contains kagomé layers of tetrahedrally coordinated Co atoms [1].

The crystal structure of cobalt oxide $YBaCo_4O_7$ is shown in fig.1. It is consist of the alternating stack of the kagomé and triangular lattices consisting of light-gray and dark-gray CoO_4 tetrahedra, respectively, where the Y and Ba atoms are within the space formed by the tetrahedra [2]. The crystal structure is hexagonal (space group; P63mc), and the lattice parameters are a=6.2982Å and c=10.2467Å [2]. There are three types of equilateral triangles, one in the triangular lattice and the other two in the kagome lattice with different sizes. The ratio of the Co ion numbers in the kagome and triangular lattices is 3 to 1.

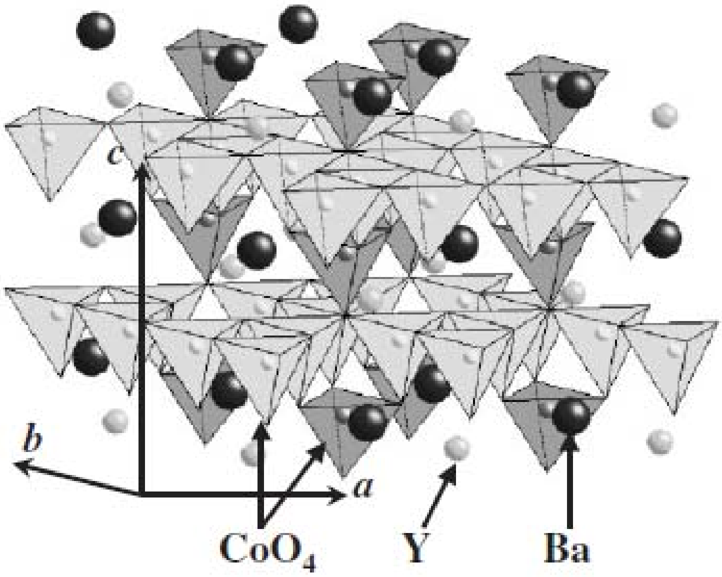

Fig.1: Schematic structure of the $YBaCo_4O_7$.

The existence of magnetic transition from the paramagnetic state at T_c~66 K was pointed out by susceptibility measurements [2]. The magnetic structure of $YBaCo_4O_7$ compound is shown in the fig.2 and it is built up of alternating kagomé and triangular cobalt lattices with magnetic Co^{2+}/Co^{3+} ions on both crystallographic site [3,4]. In tetrahedral symmetry the Co^{2+} ions have essentially the S=3/2 configuration, while the Co^{3+} are in the high-spin S=2 state [1]. As it was suggested in the paper [2], the valences of cobalt in positions Co(1)=2.31(2) and Co(2)=2.15(1) (see fig.2), therefore both sites could contain Co^{3+} charge state, however the Co(1) site should have a higher Co^{3+}/Co^{2+} ratio. Thus uncertainty of charge state of cobalt in this system is open question.

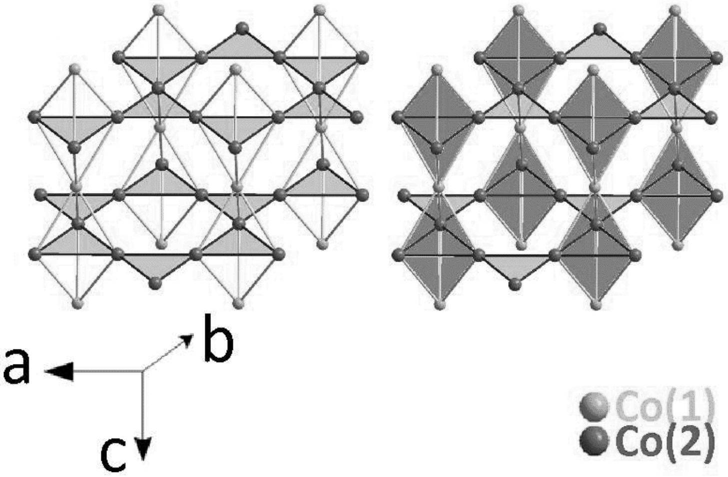

Fig.2: Sketch of the magnetic topology in the $YBaCo_4O_7$ compound. Dark-gray and light-gray spheres represent the inequivalent Co sites in, respectively, the Co(2) kagomé and Co(1) triangular layers. The triangles in the kagomé planes are colored in light gray for clarity (left panel) and bipyramids are colored in dark grey (right panel).

We used ^{59}Co zero field nuclear magnetic resonance (ZFNMR) to study the powder sample of $YBaCo_4O_7$ compound at T=4.2 K. The ZFNMR is a sensitive tool for studying solids as it gives information about static and dinamic properties of the structure on the scale of a few interatomic spacings. Thus, ZFNMR could give the additional information about cobalt charge state. Up to now there are no any NMR studies of this compound. The ZFNMR spectra of ^{59}Co in $YBaCo_4O_7$ compound at T=4.2 K is shown in fig.3. Also decomposition of the experimental spectrum to the 4 lines with Lorentzian lineshape have shown in fig.3. Intensities of the different contributions to the spectrum, corrected to the zero delay time

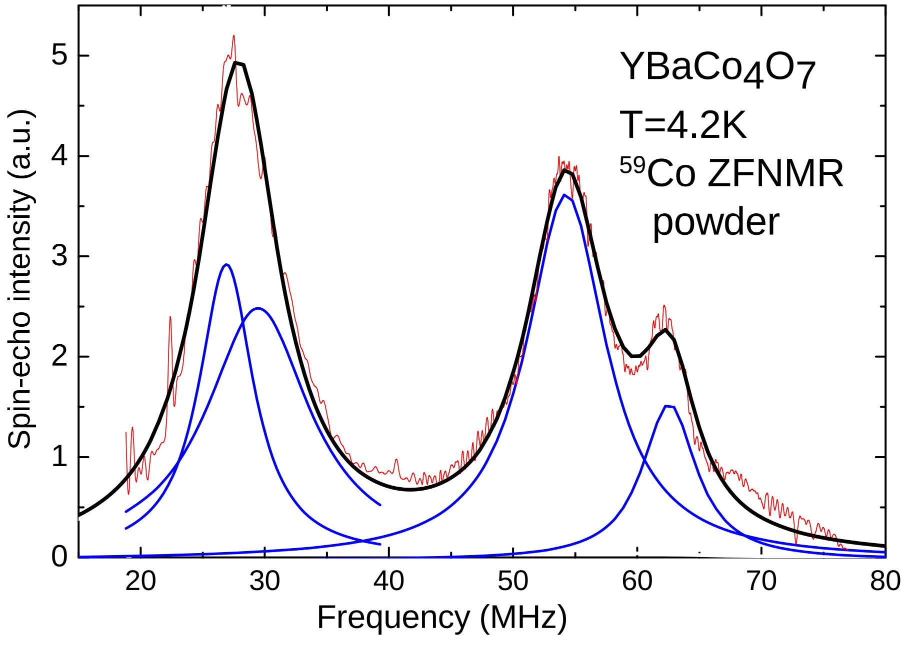

Fig.3: The ZFNMR spectra of ^{59}Co in $YBaCo_4O_7$ compound at T=4.2 K with fitting by four Lorentzian lines.

using T_2 values and other parameters are collected in table 1.

Table 1. Central frequency x_c, line area A corrected by T_2, linewidth w and corresponding internal magnetic field values h_{int} for the 4 contributions to the experimental spectra.

x_c(MHz)	26.9	29.5	54.2	62.5
A(arb.u.)	39.1±0.6	59.7±0.8	73.3±0.3	18.7±0.2
w(MHz)	5.3±0.09	10.3±0.1	8.3±0.03	5.3±0.05
h_{int} (T)	2.7	2.9	5.4	6.2

As there are no quadrupole splitting of ^{59}Co spectra in this system (see fig.3) so in the absence of an applied magnetic field Hamiltonian of a nuclear spin can be written

$$H_z = -\hbar \gamma_n \vec{h}_{\text{int}} \vec{I} \tag{1}$$

where I is the nucleus spin, h_{int} is internal magnetic field. So we can determine h_{int} using central frequency x_c – they values also collected in the table 1.

The measurements of nuclear spin-lattice and spin-spin relaxation of ^{59}Co in $YBaCo_4O_7$ were performed on the several frequencies (Table 2). All spin-lattice and spin-spin relaxations curves were fitted by the following expression respectively:

$$M(t) = M_0 \cdot (1 - B \cdot \exp(-(t/T_1)^N)) \tag{2}$$

$$M(t) = M_0 \cdot \exp(-(t/T_2))) \tag{3}$$

Examples of relaxation curves measured at frequency f=55 MHz are shown in fig.4. The solid lines represent the fitting curves corresponding to the Eq.(2) and Eq.(3) with parameters shown in table 2.

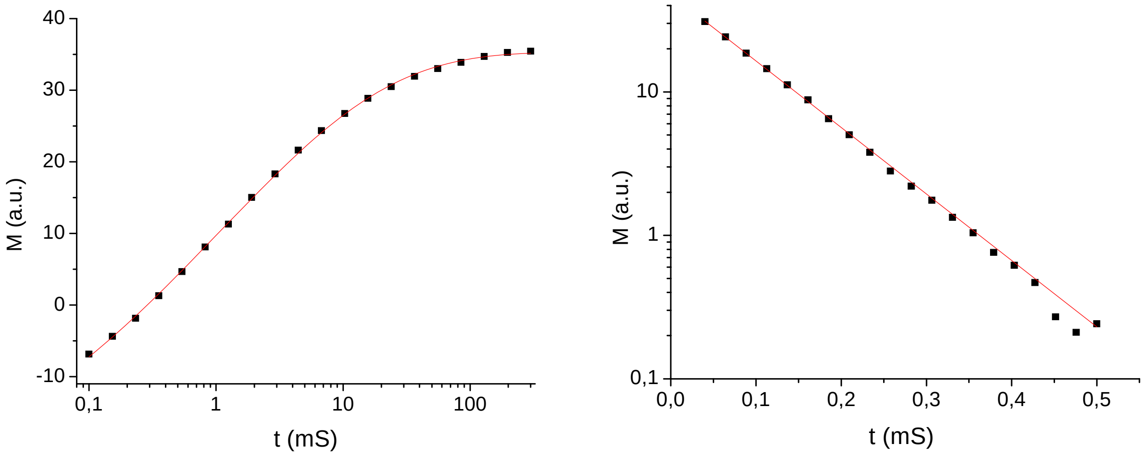

Fig.4. Examples of longitudinal magnetization recovery (top) and transverse magnetization decay (bottom) of ^{59}Co in $YBaCo_4O_7$ measured at f=55 MHz and T=4.2 K

Table 2. The relaxation parameters of ^{59}Co nuclei in $YBaCo_4O_7$ at different frequencies

f (MHz)	24.4	27.4	31.4	55	62.2
T_1 (mS)	0.27±0.11	0.43±0.035	0.62±0.049	1.1±0.11	0.94±0.07
N	0.42±0.06	0.38±0.01	0.39±0.01	0.32±0.01	0.34±0.01
T_2 (mS)	0.14±0.05	0.13±0.01	0.096±0.002	0.094±0.001	0.11±0.002

Acknowledgements

This study is supported by the RFBR under project № 10-02-01005-a.

References

[1] N. Hollmann *et al.*, Phys. Rev. B **80**, 085111 (2009)

[2] M.Valldor and M.Andersson, Solid State Sciences **4** (2002)

[3] L. C. Chapon *et al.*, Phys. Rev. B **74**, 172401 (2006)

[4] P. Manuel *et al.*, Phys. Rev. Lett. **103**, 037202 (2009)

[5] M. Soda *et al.*, J. Phys. Soc. Jpn. **75**, 054707 (2006)

Intramolecular dynamics of the radical anion of 1,2,4- trifluorobenzene as studied by optically detected ESR technique

S. Blinkova[1,2], M. Vyushkova[2], L. Shchegoleva[3], I. Beregovaya[3], V. Bagryansky[2]

[1]Novosibirsk State University, 630090, Russia, Novosibirsk, Pirogova st, 2
[2]Institute of Chemical Kinetics and Combustion of SB of RAS,630090, Russia, Novosibirsk, Institutskaya st., 2
[3]N.N. Vorozhtsov Novosibirsk Institute of Organic Chemistry of the SB or RAS, 630090, Russia, Novosibirsk, Lavrentjev Ave, 9

e-mail: blinkova@kinetics.nsc.ru

Fluoroarene radical anions (RA) attract much attention from researchers due to their unusual spatial and electronic structure. According to calculations, the pseudo-Jahn-Teller effect leads to out-of-plane distortions and structural nonrigidity of these RA's, which affects the regularity of their chemical behavior (fluoride ion abstraction) in synthetically important reactions such as selective reductive defluorination and $S_{RN}1$-substitution. Short lifetimes of fluoroarene RA's require special approaches for their registration.

This paper studies the RA of 1,2,4-trifluorobenzene (TFB), formed from the least symmetric (symmetry group C_s) representative of fluorine-substituted benzenes. The purpose of our work is to verify whether this RA conserves the structural features peculiar to highly symmetrical polyfluoroarene RA's.

Experiments have been performed with optically detected ESR (OD ESR) technique that allows selective detection of short-lived ion radicals in liquid solutions even at room temperature. The ESR spectrum of 1,2,4-TFB RA has been obtained for the first time. Temperature variation in the range of 243-309 K does not lead to broadening of the ESR lines, but causes them to shift due to the change in observed fluorine hfc values. These features are peculiar to fast exchange among the energetically nonequivalent nonplanar conformations.

Quantum chemical calculations of potential energy surface (PES) of 1,2,4-TFB RA have revealed that it has complex multi-well structure and is a pseudorotation surface of the same kind as the PES's of highly symmetrical fluorobenzene RA's.

Comparison of quantum chemical calculations with experimental data shows that inclusion of contributions from several non-planar structures in the fast exchange approximation provides qualitatively correct description the temperature dependence of the fluorine hfc values in 1,2,4-TFB RA. The calculation performed on the M06-2X/6-311 + G ** level gives the best agreement with experimental results.

Double Electron-Nuclear Magnetization Transfer in Low-Field MRI

Yu. Bogachev[1], Yu. Chernenko[1], V. Drapkin[1], M. Knyazev[1], Ya.Marchenko[1], V. Frolov[2]

[1]Department of Physics, Saint-Petersburg Electrotechnical University, 197376, ul. prof. Popova 5, Saint-Petersburg, Russia
[2]Instituite of Physics, Saint-Petersburg State University, 198504, ul. Ulianovskaya 1, St.Petersburg, Russia

e-mail: spin_ltd@mail.ru

Introduction

Molecular imaging is a new discipline, including molecular biology and in vivo imaging methods. Imaging of biophysical processes running in a living organism on cell and subcellular layers is very important for understanding of many diseases genesis. It may open new opportunities for therapy of such diseases as oncology, Alzheimer's and cardiovascular diseases.

One of the methods of molecular imaging is Magnetic Resonance Imaging (MRI). This method is non-invasive, goes very well with morphological imaging and functional imaging. Low field MRI has several advantages over MRI in higher magnetic field:

- The free radicals imaging possibility using the Overhauser effect;
- High field MRI systems can't be used for examination of people with metallic prostheses (lethal outcome is possible);
- High magnetic field influence on a living organism is not studied enough (is it dangerous or not?);
- Hardware can be made less expensive to build and operate.

But low field MRI has one serious problem — low sensitivity and resolution.

Methods

There are several methods may be used for reducing of the influence of this disadvantage on images quality.

Prepolarized Magnetic Resonance Imaging (PMRI)

In this method main magnetic field cycles between a high field to polarize the sample and a homogeneous low field for data acquisition. This architecture combines the higher SNR of the polarizing field with the imaging benefits of the lower field.

Advantages:

- Magnitude of nuclear magnetization is not dependent on the strength of the readout magnetic field. If body-noise-dominance is achieved in the receive coils of such systems, there is no SNR increase predicted for increased receive frequency.
- Hardware is less expensive to build and operate due to the use of water-cooled copper electromagnets instead of a helium-cooled superconducting magnet with a cryostat
- Susceptibility artifacts are greatly reduced by acquiring data at low field
- Allows diagnostic-quality imaging near metallic prostheses
- Lorentz forces on the gradients are lower at low field eliminating the need for ear protection and reducing the required mechanical support

- Magnetic fields can be easily turned off any time and are off when the system is not in use.

Of course this method has disadvantages and difficulties too. Among them are:

- Narrow receiver bandwidth at low field due to RF coil bandwidth scaling;
- Necessity of dedicated polarizing interval, which precludes the use of steady-state free precession techniques and gives poor efficiency for very short TR sequences;
- Inefficient slice-interleaved acquisition;
- Impossibility to use spectroscopic or spectrally selective techniques due to the narrow chemical shifts at low field
- PMRI can only achieve high SNR efficiency for volumetric imaging with 3D rapid imaging techniques, such as rapid acquisition with relaxation enhancement (RARE, FSE, TSE), because slice- interleaved acquisition and longitudinal magnetization storage are both inefficient in PMRI [1].

Magnetization Transfer

In the MT technique RF pulses are used to selectively saturate protons in the bound pool (biomacromolecules). This saturation effect is transferred subsequently (by dipolar and chemical exchange interactions) to protons in free water, and is proportional to the relative sizes of the pool, individual proton relaxation rate, and cross-relaxation rate [2].

Overhauser imaging (proton–electron double-resonance imaging (PEDRI))

This technique is based on the Overhauser effect which can be observed in solutions containing free radicals. It is combination of 2 techniques: MRI and Electron Spin Resonance (ESR).

The ESR transitions of a free radical of interest is irradiated during the collection of an MR image. The Overhauser effect causes an increase in the nuclear magnetic resonance (NMR) signal strength in parts of the sample containing free radicals, and these regions are revealed by an increased intensity in the final image.

Advantages:

- No sample size limitation
- Image resolution is independent of the ESR line width of the free radical under study
- Possibility of using standard MRI software and hardware

Difficulties:

- Requires the additional add-on device for irradiating the sample at the ESR frequency
- Reduced penetration depth of irradiation. Only small animals can be examined
- Field-cycled PEDRI (FC-PEDRI) overcomes PEDRI limitation and could potentially allow free radical imaging in humans [3].

Results and discussion

We suggest a new method of improving sensitivity and resolution of low field MRI based on the combining of spin trapping, dynamic nuclear polarization (DNP) and magnetization transfer (MT) methods. The basic principles of suggested method are shown on fig.1 and fig.2.

Experiments were set up in order to detect MT effect in aqueous solution of biopolimers. To achieve this we used simple phantoms modeling biopolymer-water systems and reproducing many of the cross-relaxation features, found in tissues and biological samples: gelatine gels of different concentration, starch aqueous solution, agarosa gels of different concentration. All experiments have been performed on home-made low-field MRI scanner at the Physics Institute of Saint-Petersburg University.

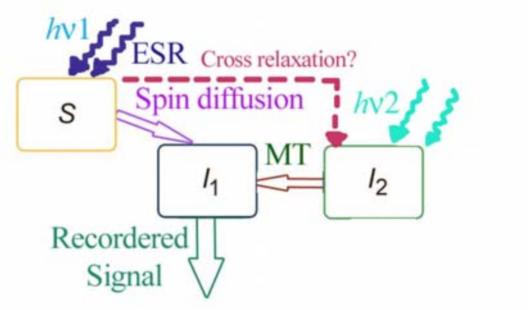

Fig.1. DNP-MT MRI – principle
S – electron spins; I1 – free water proton spins; I2 – bound water proton spins

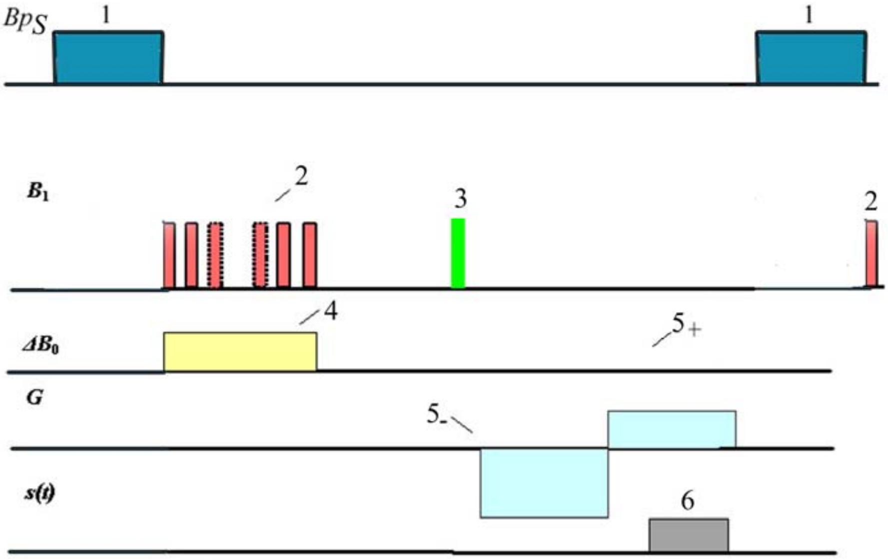

Fig.2. Pulse sequence for DNP-MT MRI
1 –HF ESR saturation pulses; 2 – HF saturation pulses. 90°-pulses; 3 – 90°-pulse to obtain signal from spin system; 4 – field offset; 5_{+-} – gradient pulses; 6 – strobe, during which signal is being read

This method can be further improved if we use superparamagnetic iron oxide (SPIO) nanoparticles utilizing off-resonance saturation or use unpaired electrons as system to be saturated (Overhauser effect). Because SPIO agents cause local field inhomogeneities, it is possible, by applying off-resonance irradiation, to exploit the effect of field inhomogeneity as an alternative contrast mechanism for these agents. The Overhauser effect would result in appreciable increase in amplitude of proton NMR signal. There is significant spin polarization in low and zero magnetic field. We decided to use these effects to enhance sensitivity and resolution of our low-field MRI scanner.

Conclusions

We observed the phenomenon of magnetization exchange between 'free water' protons and protons that are bound in macromolecules using our home-made MRI scanner.

We plan to reconstruct low-field MRI scanner add-on device to make experiments on DNP-MT MRI.

We hope that application of a double electron-nuclear magnetization transfer in low-field MRI permits to improve the contrast of images for biopolymer-water systems containing a stable paramagnetic radicals. This technique suits for the imaging of some metabolic free radicals processes in vivo using a spin trapping method.

This work was supported by Russian Federation Ministry of Education and Science (Project No. P 1169).

References

[1] Lurie D.J. Free radical imaging // The British Journal of Radiology. ─ 2001. ─ No.74.─P.782─784

[2] Magnetization transfer in MRI: a review / Henkelman R.M. [et al.] // NMR Biomed. ─ 2001.─ Vol.14.─ P.57─64

[3] Lurie D.J. Proton-electron double-resonance imaging (PEDRI). // In: Berliner L.J., editor. Biological magnetic resonance. ─ Vol. 18: In vivo EPR (ESR): theory and applications. ─ NY: Kluwer Academic ─ 2001.

Formation and properties of impurity related aggregates in CsBr:Eu X-ray storage phosphor

D.O. Tolmachev, A.G. Badalyan, R.A. Babunts, N.G. Romanov, P.G. Baranov

Ioffe Physical-Technical Institute, Russian Academy of Sciences, 194021 St. Petersburg, Russia

e-mail: Daniel.Tolmachev@gmail.com

Introduction

The storage phosphor plate technology has become the dominant method for acquiring digital radiographs [1-3].

During X-ray irradiation, dose-proportional information is deposited and stored in the phosphor in the form of locally trapped electron-hole pairs as a latent image. This stored information is recovered by optical stimulation resulting in a light emission at a wavelength different from the stimulating one. The photostimulated luminescence (PSL) is collected in a detector and processed in a digital data acquisition system. Advantages of this system compared to conventional X-ray detectors are a very high dynamical range (about 6 orders of magnitude), a linear dose dependence, and reusability of the plates.

The main commercial material used to generate digital X-ray images so far is the rare-earth-doped alkaline-earth halide crystals BaFBr:Eu^{2+}, in which optical stimulation with red light results in the recombination of the electron-hole pair under Eu^{2+} emission [4,5]. This is an efficient storage material due to energy match between the emission of the self-trapped excitons and the absorption band of Eu^{2+}. The spatial resolution of phosphor screens based on the optically anisotropic BaFBr is limited by the scattering of the read-out light, which is due to the low-symmetry structure of this material and the statistical distribution of the crystallites in the film. Thus, optically isotropic storage phosphors with CsCl-type cubic structure have gained great importance for X-ray imaging. CsBr:Eu shows characteristics comparable to those of BaFBr:Eu and is one of most promising X-ray storage materials but the mechanisms of information storage and subsequent read-out are, however, not yet fully understood and require further investigations.

There exists an essential difference between the recombination processes in BaFBr:Eu and CsBr:Eu since these two systems differ considerably in the structure of Eu^{2+}-related centers responsible for the photostimulated emission. In BaFBr europium exists in the form of isolated Eu^{2+} ions substituting Ba^{2+} and no charge compensation is required. In contrast, Eu^{2+} in CsBr:Eu has an excess positive charge and is accompanied by a cationic vacancy (v_c), which results in a very efficient aggregation of Eu^{2+}- v_c dipoles and formation of impurity-related nanoclusters even at room temperature. Precipitation-induced PSL of CsBr:Eu was investigated in [3] where the formation of phases, which are active in the PSL process, was suggested.

In our previous publications [6,7] the recombination processes were studied by ODMR in Pb doped CsBr crystals containing self-organized CsPbBr$_3$ micro- and nanocrystals embedded into the CsBr lattice. Evidences for the directional transfer of the recombination energy of electron and hole centers from the CsBr matrix to the embedded CsPbBr$_3$ crystals were presented.

Here we report on the study of recombination processes leading to TA and PSL in systems based on Eu-doped CsBr crystals by means of photoluminescence (PL), EPR and ODMR via PL, TA, PSL and MCD.

Experimental details

The crystals of CsBr:Eu (0.1 to 0.5 mol.% of Eu in the melt) were grown by the Bridgman technique. Several types of samples, those kept for a long time at room temperature (“well aged”), samples quenched from room temperature to liquid nitrogen temperature and the samples annealed from T = 440 K to room temperature were studied.

Luminescence spectra were measured at a temperature between 1.8 and 300 K. Deuterium or Xenon arc and halogen lamps as well as a semiconductor laser (= 650 nm) were used for excitation. A photomultiplier in combination with a grating monochromator was used for the light detection. EPR experiments were carried out by using X-band JEOL EPR spectrometer equipped with a helium gas-flow cryostat, which was manufactured in the laboratory and provided the temperature control within the range of 4 to 300 K.

Recombining centers were identified using optically detected magnetic resonance. ODMR was investigated with the 35 GHz ODMR spectrometer operating at 1.6 - 2 K and providing the magnetic field up to 4.5 T

Results and discussion

The intensity of the broad recombination bands in the TA and PSL spectra of CsBr:Eu and CsBr:Pb can be increased by almost an order of magnitude after quenching the sample. Fig.1 shows the photoluminescence spectra of CsBr:Eu crystals, excited in the UV region and measured at 77 K both for “well aged” and quenched crystals (curves 1 and 2, respectively).

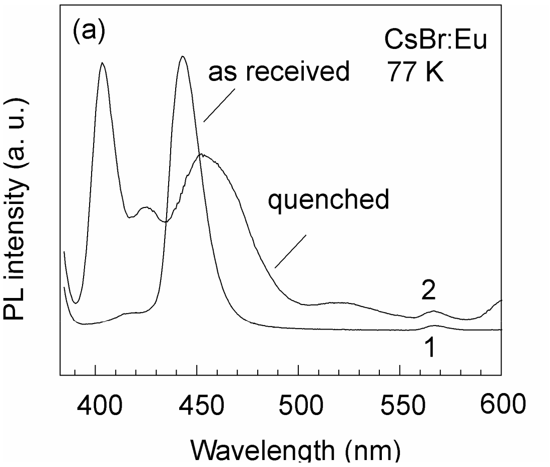

Fig.1. Photoluminescence spectra of CsBr:Eu (a) and KCl:Eu (b) crystals measured at 77 K for “well aged” crystals (1) and the crystals quenched from 650 K to 77 K (2).

The emission spectra of the “well aged” samples of Eu-doped CsBr show only one band peaking around 440 nm. It is clearly apparent from the figure that the PL spectra are strongly dependent on the aggregation state of the Eu^{2+} ions. The main result is that the intensity of PL attributed to the aggregation state of the Eu^{2+} ions drastically decreased after quenching. For the “well aged” KCl:Eu only PL band (440 nm) was ascribed to the metastable Suzuki phase of divalent europium in the KCl lattice. The emission band observed in the quenched samples at higher energy was ascribed to isolated Eu^{2+}-cationic vacancy dipoles [8].

Thus, the quenching of crystals influences essentially the nature of recombination processes and is due to structural changes in the systems under study. The quenching reduces the size of aggregate impurity aggregates clusters (including nanoclusters or nanocrystals) and increases the concentration of impurity point defects, which act as electron and hole traps and stimulates an increase in the concentration of radiation defects participating in recombination, i.e. self-trapped holes (and, as a consequence, self-trapped excitons) and *F*-centers.

Fig.2 presents the EPR spectra of CsBr:Eu (a,c) measured at 77 K for “well aged” and quenched samples. Eu^{2+} ($4f^7$ state) has the electronic spin S=7/2. Thus the EPR spectrum of an isolated Eu^{2+}-cation vacancy centre consists of a set of a set of seven fine-structure lines for a certain orientation of the centre axis. Each of these lines is further split by the hyperfine interaction between the unpaired electron of the Eu^{2+} and the nuclei of the two magnetic isotopes ^{151}Eu (47.9% natural abundance) and ^{153}Eu (52.1% natural abundance), both with a nuclear spin of I=5/2. The hyperfine interaction results in six allowed transitions for each isotope. The ratio of the hyperfine splitting for the two Eu isotopes corresponds to the ratio of nuclear g-factors of these isotopes - $g_I(^{151}Eu)/g_I(^{153}Eu) = 2.26$.

In the EPR spectra of the "well aged" CsBr:Eu crystals a very broad unresolved line can only be observed with very low intensity similar to that in KCl:Eu, where the presence of precipitates of europium (the Suzuki phase) was confirmed [8]. This proves the absence of the isolated Eu^{2+} centres in the “well aged” samples. When the crystals are quenched by dropping them into liquid nitrogen after heating up to a temperature of 670 K for about 20 minutes, well-resolved narrow-line EPR spectra appear. These spectra for CsBr:Eu are shown in fig.2(a) and (b). One can conclude that the situation is similar to that for Mn^{2+}-doped NaCl type crystals [9], i.e. the broad band in CsBr:Eu arises from Eu aggregate centres, and the resolved EPR spectrum arises from individual Eu^{2+}-vacancy pair centres. Aggregation of Eu^{2+} ions in CsBr is very fast even at room temperature [10].

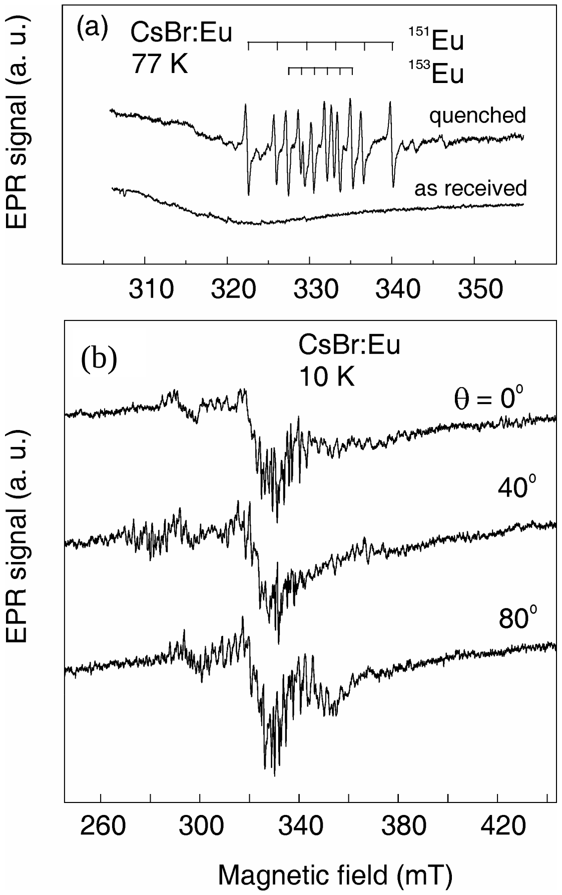

Fig.2. The X-band (9.2 GHz) EPR spectra of CsBr:Eu (a) and KCl:Eu (b) The angular variation of the EPR in the quenched CsBr:Eu.

Fig.2(b) shows the EPR spectra recorded at 10 K and different orientations in the quenched CsBr:Eu sample. In CsBr, the lattice constant is 4.29 Å, and the ionic radii of Cs^+ and Br^- are 1.65 Å and 1.96 Å, respectively, so that the Eu^{2+} ion with the ionic radius of 1.09 Å is supposed to enter into the crystal substitutionally rather than interstitially. One can conclude that the EPR spectrum is due to Eu^{2+} ions, which substitute for Cs^+ and are accompanied with vacancies at their nearest neighbour or next nearest neighbour cation sites. This means that each spectrum is composed of a superposition of several spectra which are identical except that they have different sets of equivalent principle axes similar to Mn^{2+} centres studied in reference [6]. The dominant lines are composed of two distinct types of spectra corresponding to two types of distortions from the normal cubic environment of Eu^{2+}, all equivalent distortions occurring with equal probabilities. This is similar to the case of alkali-halides with NaCl structure except that in CsBr the nearest neighbour and the next nearest neighbour cationic sites lie in the <100> and <110> directions, respectively, while in alkali-halides with NaCl structure these directions are interchanged with each other. The spectra corresponding to isolated ions of Eu^{2+} or Eu^{2+} accompanied with vacancies in the second nearest neighbour cationic sites could not be detected.

Summary and conclusions

In conclusion, CsBr:Eu^{2+} crystals, promising for X-ray storage phosphor, which can replace the commercially used X-ray storage material BaFBr:Eu^{2+}, was studied by means photoluminescence, photostimulated luminescence, EPR and optically detected magnetic resonance.

The narrow bands in the tunneling afterglow and photostimulated luminescence spectra of X-ray irradiated CsBr:Eu and CsBr:Pb coincide with the PL spectra of the samples measured prior X-ray irradiation and belong to the impurity-related micro and nanostructures. Parallel studies of PL and EPR spectra in CsBr:Eu crystals have shown that the impurity-related bands in the emission spectra definitely belong to nanosized Eu-cationic vacancy aggregates. The quenching of the samples results in dissociation of the aggregates and increase in concentration of the isolated Eu^{2+} centers.

Acknowledgments

This work was carried out with the financial support of the Programs of RAS "Spin-Dependent Effects in Solids and Spintronics", "Support of Innovations and Elaborations", and "Basic Researches of Nanotechnologies and Nanomaterials"; by the RFBR projects 09-02-00730-a and 09-02-014409-a; and by Russian Federal Agency for Science and Innovations under Contracts No. 02.513.12.3031 and No.02.740.11.0108.

References

[1] Amemiya Y and Miyahara J 1988 *Nature* **336** 89

[2] Thoms M, von Seggern H, and Winnacker A, 1991 *Phys. Rev. B* **44** 9240

[3] Hackenschmied P, Schierning G, Batentschuk M, and Winnacker A 2003 *J. Appl. Phys.* **93** 5109

[4] Rüter H H, von Seggern H, Reininger R, and Saile V, 1990 *Phys. Rev. Lett.* **65** 2438

[5] Schweizer S 2001 *Phys. Stat. Sol. (a)* **187** 335

[6] Baranov P G, Romanov N G, Badalyan A G, Tolmachev D O, Preobrazhenski V L 2005 *JETP Letters* **82** 725

[7] Romanov N G, and Baranov P G 2007 *International Journal of Nanoscience* **6** 311

[8] Urda Y, Fujita T, and Kazumata Y 1979 *J. Phys. Soc. Jpn.* **46** 889

[9] Haselhoff M and Weber H-J 1998 *Phys. Rev. B* **58** 5052

[10] Savel'ev V P, Avdonin V P, Dugarova L G, Nedashkovskii A P, and Plachenov B T 1974 *Sov. Phys.-Solid State* **16** 700

Charge Order-Disorder Phase Transition Detected By EPR in α'-(BEDT-TTF)$_2$IBr$_2$

A.I. Dmitriev, A.S. Chernenkaya

Institute of Problems of Chemical Physics RAS, 142432, Acad. Semenov av., Chernogolovka, Russia.

e-mail: aid@icp.ac.ru

Strong electron correlations in bis(ethylenedithio)tetrathiafulvalene (BEDT-TTF) attract an attention of scientists because exotic charge and spin phenomena were found [1]. Special interest was focused on the charge order-disorder phase transitions (CODT). In [2, 3] detailed investigations of α'-(BEDT-TTF)$_2$IBr$_2$ salt were reported. The CODT was reliably and evidently registered by combination of the methods at around 200 K in α'-(BEDT-TTF)$_2$IBr$_2$. X-ray diffraction confirmed the absence of structural phase transition [2]. Electrical conductivity and polarized reflection spectra in the infrared and near-infrared regions elucidated the nature of the phase transition at 200 K [3]. Details of the spin behavior during charge ordering are not cleared till now.

In this paper we explored the electron paramagnetic resonance (EPR) which is a more powerful and sensitive method for detecting of the localization effects in comparison with SQUID magnetometry. Comparatively big perfect single crystals with the sizes 0.2 × 2 × 5 mm [3] were studied in our experiments. EPR spectra were recorded by Bruker EMX EPR spectrometer of the X- range (~9.5 GHz microwave frequency) with a H_{102} type rectangular resonator, 100 kHz modulation frequency and 0 – 1.5 T static magnetic field scan range. Resonator quality Q = 6500-7000 was constant in measurements. The measured EPR signal was proportional to the first derivative $(d\chi/dH)$ of the imaginary part of magnetic susceptibility of a sample. Temperature was varied in the 4 – 290 K range in a ESR900 Oxford Instruments cryostat. Resonator microwave power was 10^{-4} W. Modulation amplitude was 10 times smaller than peak-to-peak linewidth of the measured EPR lines.

The EPR spectrum of the single crystals was recorded as a single line with the Lorenz shape (fig.1).

The linewidths and g-factors in this paper presented for the absorption component

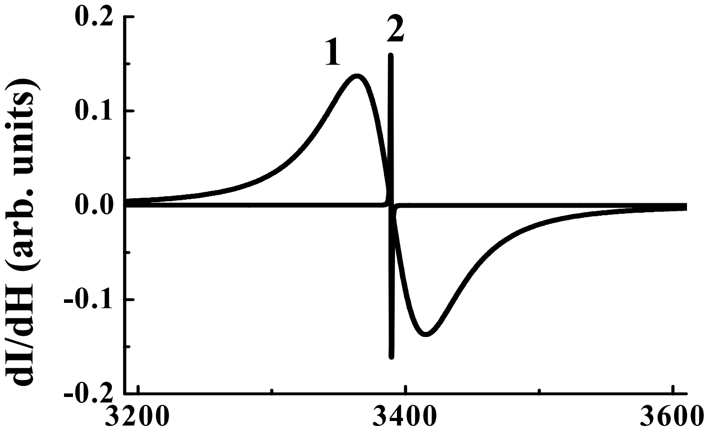

Fig.1. EPR spectra at temperatures T = 300 K (line 1) and T = 4 K (line 2). The angle between the dc magnetic field and the crystals plane is $\Theta = 0^0$.

extracted from the signal. Linewidth *ΔH* at high temperatures (above 50 K) was about 55-110 Oe that is typical for the BEDT-TTF compounds. Below 50 K sharp narrowing of the EPR line was observed till its smallest value 0.8 Oe at 5 K (fig.2). Such narrow line is very unusual for BEDT -based compounds. Probably narrow line indicates exchange interactions that might be observed because good quality of the crystals in our experiments. Charge ordering transition at about 200 K was accompanied by sharp decrease of the linewidth *ΔH* and *g*-factor (fig.1). Magnetic susceptibility χ calculated by double integration of the spectra undergoes jump at 200 K (fig.2), which was deeper than it was observed by SQUID magnetometry [3].

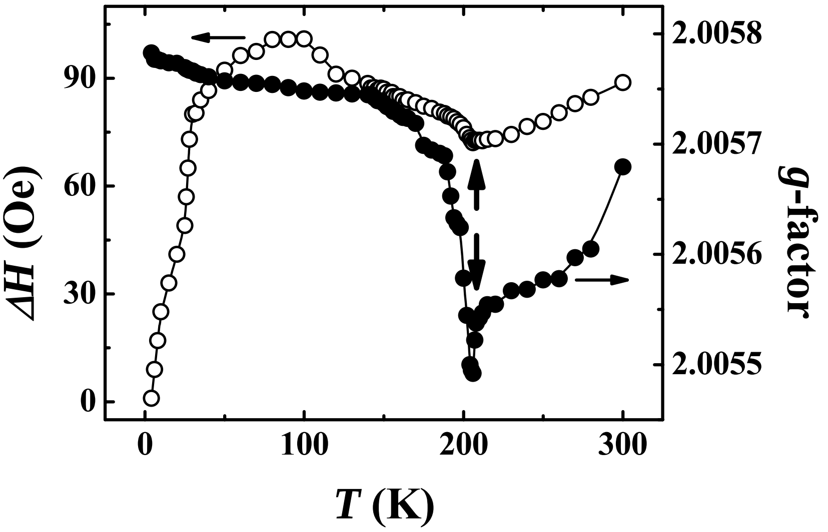

Fig.2. Temperature dependencies of the linewidth *ΔH* (white dots) and the g-factor (black dots). The angle between the dc magnetic field and the crystals plane is $\Theta = 0^0$. Arrows mark the charge order-disorder phase transition. Solid lines are guides for the eye.

Thus, charge ordering in α'-(BEDT-TTF)$_2$IBr$_2$ is accompanied by sharp changes of the EPR parameters: integral intensity, *g*-factor and linewidth *ΔH*. This fact corresponds to spin transition in the subsystem of the localized charge carriers. Exchange interaction between charge carriers provides narrowing of the EPR line as well as rapid decrease of magnetic susceptibility caused by cooling of the crystal below 50 K.

Acknowledgments

We are grateful to scientific adviser Professor R. B. Morgunov and Professors Kaoru Yamamoto, Kyuya Yakushi for samples providing.

References

[1] T. Ishiguro, K. Yamaji, Organic superconductors, Springer-Verlag Berlin Heidelberg, Berlin (1989).

[2] M. Watanabe, M. Nishikawa, Y. Nogami, K. Oshima and G. Saito, J. Korean Phys.Soc. 31 (1997) 215.

[3] Y. Yue, Ch. Nakano, K. Yamamoto, M. Uruichi, R. Wojciechowski, M. Inokuchi, K. Yakushi, A. Kawamoto, J. Phys. Soc. Jpn. 78 (2009) 044701.

Metabonomics study of human amniotic fluid and embryo culture media

A.V. Chertkov[1], V.V. Podgorsky[2], K.F. Sheberstov[1], A.V. Poltanova[1], E.Yu. Simonenko[1],
N.M. Sergeyev[1]

[1]Moscow State University, 119991, Leninskie gory, Moscow, Russia
[2]Peoples' Friendship University of Russia, 117198, Miklukho-Maklaya, Moscow, Russia

e-mail: alex@nmr-online.ru

Introduction

Proton NMR spectroscopy has become a routine tool for fast, comprehensive characterization of complex mixtures, including biofluids, liquid foods, and plant extracts. Such detailed characterization is particularly useful in metabonomic studies that aim to understand the effects of perturbations on living systems through the measurement of changes in their metabolome. ^{1}H NMR spectroscopy enables the identification of many tens or hundreds of compounds simultaneously, is noninvasive, and requires little or no sample preparation. However, when complex mixtures are analyzed, preferably without any previous sample simplification like extraction or separation, the issue of spectral complexity is a serious hindrance due to extensive signal overlap. The desired level of compound identification depends on the problem addressed, and often, partial assignment of the spectra for a selection of compounds (or family of compounds) will suffice. Also, in classification studies where reproducible sample differences are detected and validated by a range of increasingly sophisticated chemometrics methods, the full assignment of these changes may not always be necessary.

So, there are two principally different aims in research of biological fluids. First one is to determine the composition of biofluid as precise as possible and to find the specific compounds that may be used as markers for some kind of system perturbation, e.g., disease, diet, or medication. And the second one is to learn to find the statistical correlations between different samples and divide all the samples into different groups on the basis of correlations found.

Respectively, 2 different objects of the study were chosen: human amniotic fluid (HAF) and embryo culture media (ECM). HAF samples were obtained from pregnant women during childbearing and represent a colloidal solution consisting of mucoproteins with the high carbohydrate content, large amount of lipids and proteins. Also, HAF is rich in the products of protein and lipid metabolism and in some biologically active compounds, such as adrenaline, noradrenaline, thyroxine, oestadiol, histamine, caffeine and others [1]. The purpose of this study is to predict the typical for the most common gestational abnormalities (anemia, gestational pyelonephritis, arterial hypertension, adiposity), complications in childbirth in early pregnancy.

The culture of human preimplantation embryos is the base growth medium from the zygote to the blastocyst stage. On the 5th day after assessment embryo with higher cleavage rate is implanted into the woman's organism. The embryo assessment based only on morphology (Gardner scale) and cleavage rate is not enough informative today. So, it has led many investigators to find out adjunctive noninvasive technique to determine an individual embryo's reproductive potential. Such several metabolic parameters of the spent embryo culture media have been studied during last 10 years. [2,3,4,5] In the current study, we propose the ^{1}H NMR spectroscopy as the rigorous method to analyze the metabolomic profile of embryo culture media to prediction the embryo's reproductive potential.

Experimental

All the amniotic fluid samples were obtained from pregnant women during childbearing and were divided into 5 groups: control group (10 samples) and 4 groups (4x10 samples) from mothers with different malformations: anemia, adiposity, gestational pyelonephritis and arterial hypertension. All samples except the control group were selected at childbearing with some particular types of birth complications that are typical for the selected pathologies.

Then samples of HAF were centrifuged (14.000 g, 22 °C, 10 min), resulting supernatants were freeze-dried, reconstituted in D_2O (with TSP) and used for NMR analysis (1D NOESY-presat on Bruker AVANCE 600 equipped with inverse TXI-probe).

A total of 30 samples (15µl) of embryo culture media of 30 patients were evaluated using ^{1}H NMR spectroscopy (^{1}H on Bruker AVANCE 600 equipped with inverse TXI-probe and CPMG-presat on JNM-ECA 600 equipped with inverse probe).

All the spectra obtained were processed with statistical analysis using the Unscrambler 9.7 software.

Results and discussion

For each HAF sample, two 1D 1H NMR experiments were acquired: a 1D standard experiment (1D NOESY-presat), and a T2-weighted experiment (CPMG). In fig,1, representative 1D NOESY spectrum is shown.

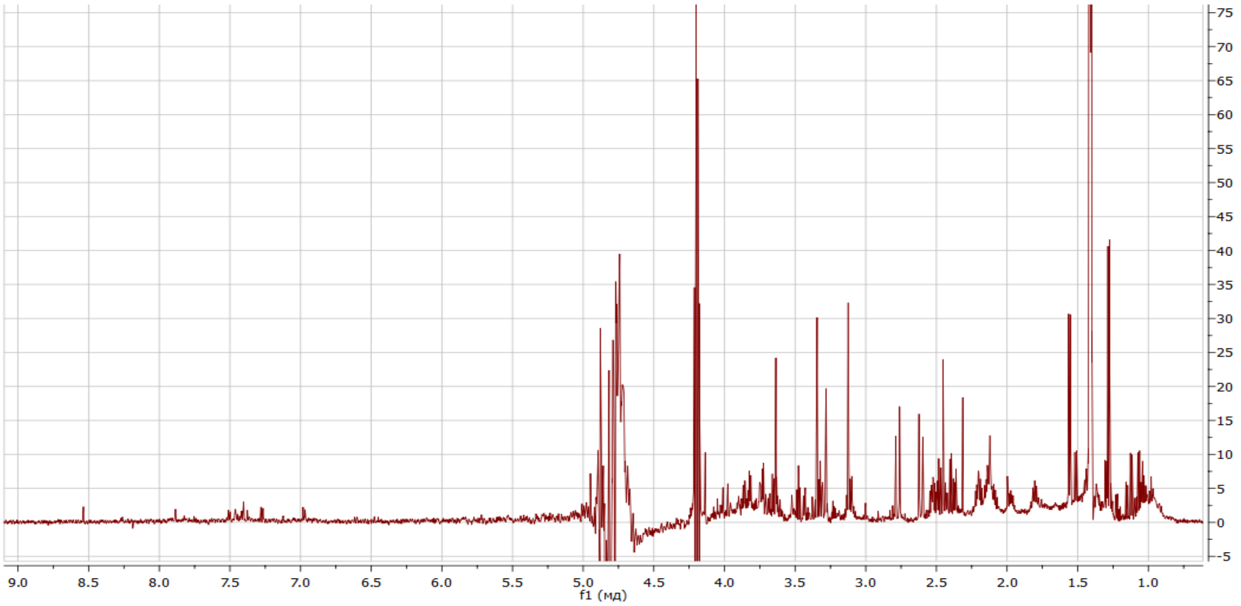

Fig.1. Bruker 600MHz 1D NOESY-presat spectrum of HAF

All the HAF spectra obtained were processed with statistical analysis using the Unscrambler 9.7 software and the O-PLS-DA analysis. As shown in fig.2, good correlations have been obtained and the “blind” experiment already works. Unfortunately, the resulting technique cannot be used in clinical practice for early diagnosis of these four diseases because of amniocentesis is a highly risky operation. But it can surely be used for fundamental learning of metabolic deviations in HAF that could be the good markers for prediction of childbearing complications. We believe that there are correlations between such markers in HAF and blood plasma or urine and that comparison of this markers allow to build an alternative technique which would be usable in clinical practice.

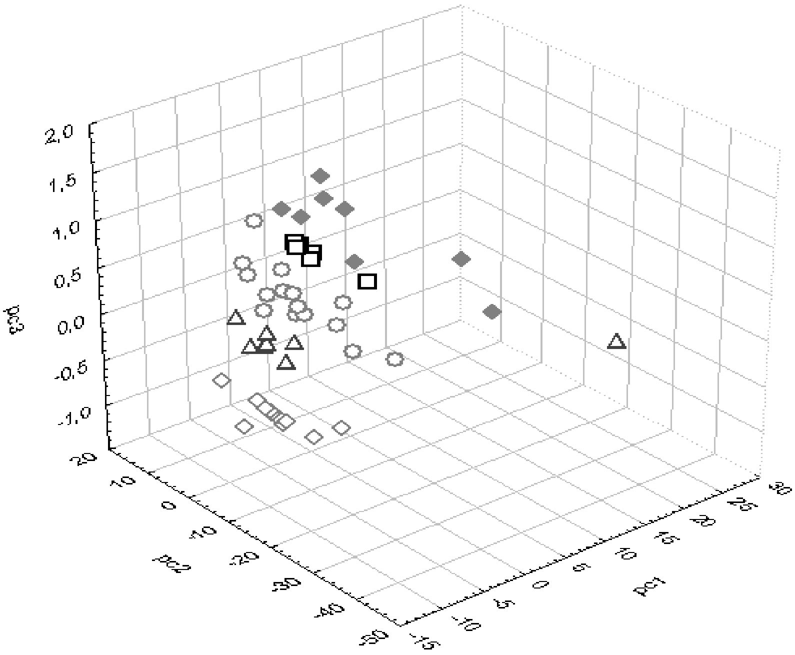

Fig.2. Different malformation types: empty diamonds – anemia, triangles – gestational pyelonephritis, circles – arterial hypertension, grey diamonds – adiposity, black squares – control group.

1H NMR Spectra of Embryo Culture Media.

For each ECM sample, two 1D 1H NMR experiments were acquired: a ^{1}H standard experiment with presaturation (zgpr overnight accumulation), and a T2-weighted experiment (CPMG). In fig.3, representative ^{1}H spectrum is shown

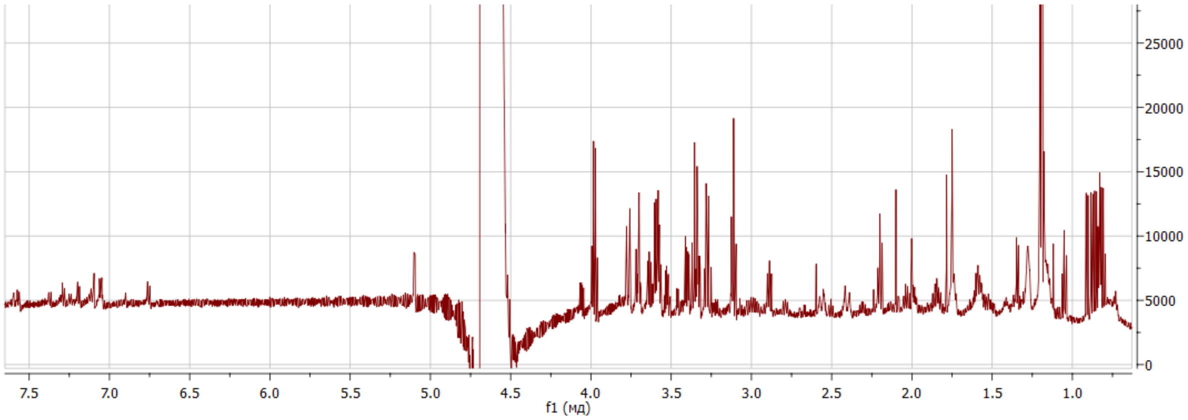

Fig.3. Bruker 600MHz 1H-presat spectrum of ECM

Firstly, we attempted to find the best pulse train resulting in a well resolved spectrum suitable for interpretation and quantitative integration. But we got a lot of troubles in calibration of CPMG-experiments because of all the ECM samples contain deferent amount of protein macromolecules, and for good protein signal suppression we needed to calibrate CPMG for every sample. And since total amount of sample is only 15 µl, the achievement of sufficient resolution took about an hour just to understand if the parameters of CPMG experiment are quite good. Sometimes registration of one T_2-edited CPMG spectrum took 2 or even 3 days.

That’s why the developing of final fast and handy methodic is still in progress. And till that moment we can only say for sure, that 15 µl samples of biofluids are nevertheless suitable for NMR analysis. The metabolites detected are shown in table 1.

Table 1. The ECM biomarker chemical shifts.

Metabolite	**Chemical shift (multiplicity), ppm**
Glucose, D-(+)	3,42 (t), 3,46 (dd), 3,72 (dd), 3,79 (m), 5,23 (d)
Lactate	1,33 (d), 4,12 (q)
Alanine	1,48 (d)
Glutamine	2,13 (m), 2,33 (t)
Arginine	3,25 (t)
Lysine	1,89 (m), 3,03 (t)
Cystine	3,41 (q), 3,72 (dd), 4,19 (dd)
Histidine	3,90 (dd), 7,73 (s)
Leucine	0,97 (t)
Isoleucine	0,99 (d), 0,94 (t)
Phenylalanine	7,33 (d), 7,38 (m), 7,42 (m),
Threonine	3,6 (d)
Tyrosine	6,89 (d), 7,19 (d)
Valine	1,01 (d), 1,04 (d), 3,6 (d)

By the results of our research, given the small sample size and greater variability of source data, it seems more appropriate the statistical modeling, using selected spectral regions corresponding to the most characteristic feature of certain metabolic states and deviations of biomarkers, rather than using the entire spectrum as a whole pattern. And so we plan to focus on identifying biomarkers of interest to us metabolic states of examined objects, not just on expanding the sampling and statistical modeling.

Acknowledgment

The work was financially supported by the Russian Foundation of Basic Research and Innovation (project 09_04_0086).

This work is a part of Analytical departmental target program “Development of Scientific Potential of Higher Education” and is supported by Federal Agency for Education (project 2.1.1/3151).

References

[1] Graca G., Duarte I.F., Goodfellow B.J., Carreira I.M., Couceiro A.B., Domingues M., Spraul M., Tseng L-H., Gil A.M. Metabolite Profiling of Human Amniotic Fluid by Hyphenated Nuclear Magnetic Resonance Spectroscopy. Anal Chem, **2008**, 80, 6085–92.

[2] Sakkas D, Gardner DK. Noninvasive methods to assess embryo quality. Curr Opin Obstet Gynecol **2005**, 17, 283-8

[3] Gardner D.K., Lane M, Stevens J, Schoolcraft WB. Noninvasive assessment of human embryo nutrient consumption as a measure of developmental potential. Fertil Steril **2001**, 76, 1175-80

[4] Brison DR, Houghton FD, Falconer D, Roberts SA, Hawkhead J, Humpherson PG, et al. Identification of viable embryos in IVF by noninvasive measurement of amino acid turnover. Hum Reprod **2004**, 19, 2319-24

[5] Seli E.,Botros L, Sakkas D, burns DH. Noninvasive metabolomic profiling of embryo culture media using proton nuclear magnetic resonance correlates with reproductive potential of embryos in women undergoing in vitro fertilization. Fertil Steril **2008**, 90, 2183-2189

Investigation of abnormal changes in organism of donors analyzing EPR spectra of blood

M.I. Ibragimova, A.I. Chushnikov, V.Yu. Petukhov, E.P. Zheglov

Kazan Physical Technical Institute, Russian Academy of Sciences, 420029, Siberian trakt 10/7, Kazan, Russia.

shuran2003@mail.ru

The actuality of blood and its properties investigation is dictated considerably by possibilities of pathological changes detection in organism of human beings. Progress of new biochemical approaches as well as using of physical methods in biology and medicine have provided impetus for the development of haematology. Biochemical methods allows to reveal pathological changes in organism from quantitative data of blood elements such as different kind of proteins, bilirubin, cholesterol, *et al*. Physical methods such as EPR make possible to detect paramagnetic centers in blood as well as to gain a more significant information about the structure of elements investigated [1,2]. However the systematic investigations of human health by EPR blood test have received only occasional attention in the literature. It should be noted that EPR is a method of express analysis for testing the blood quality of donors. Thus, ***the aim*** of this work is to determine the possibilities of EPR application for revealing the abnormal changes in organism of blood donors and to work out the method of quality control of blood samples.

Material and methods

Venous blood sampling was carried out in the blood transfusion center. In this experiment 50 blood donors took part, age interval being 18-57 years old. Blood samples were taken into 1 ml syringe and then were quickly frozen in liquid nitrogen. For EPR measurements samples were placed into quartz dewar with liquid nitrogen. EPR spectra were recorded using Varian E-12 spectrometer on frequency of ~ 9.38 GHz with microwave power 50 mW, modulation amplitude – 1 G, the temperature of measurements - 77 K. To perform the quantitative measurements the signal from standard sample (anthracite) was also recorded.

Results and discussion

The analysis of EPR spectra for venous blood from all investigated donors showed that they can be divided into two groups. In Fig.1 *a,b* two typical types of EPR spectra are presented. The first group (Fig.1a) involves donors the EPR spectra of which are practically match with that obtained previously [1,2]. In these spectra absorption lines identified as the signals from methemoglobin (MetHb with g~6), Fe^{3+}-transferrin (Fe^{3+}-Tf with g≈4,31), ceruloplasmin (Cu^{2+}-Cp with g≈2,056) and free-radical center (R with g≈2,003). This group approximated ~30% from all investigated donors. For donors from the second group the EPR spectrum along with conventional signals contains new lines, particularly the line with g=2.27 intensity of which depends on donor's status (Fig.1b). In Fig.1b the EPR spectrum of blood with anomalous high intensity of this signal for investigated group of donors is demonstrated. This line most probably can be identified as the part of spectrum from histidine gemichrome with rhombic symmetry. It is well known that the lines in this spectrum are spaced in the range of g-factor 1.8-3.0 with the most intensive component at g~2.27 [1]. Histidine gemichrome is the product of hemoglobin destruction viz. nitrogen of histidine which is placed on the 6-th ligand position of heme. The intensity of EPR signal from gemichrome gives the information on the hemoglobin irreversible losses. Gemichromes appear in human

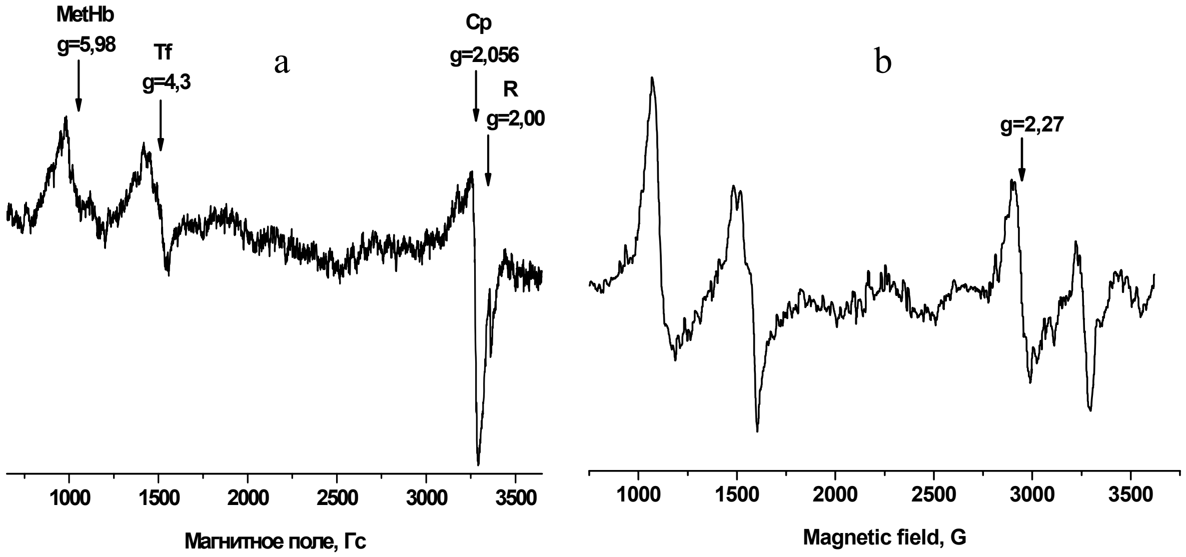

Fig.1. EPR spectra of blood donors. *a* – for first group (30% from total donor number), *b* – for second group (attend line with g=2,27. This line is identified as the part of spectrum from histidine gemichrome)

blood under the acute intoxications, at administration of sodium nitrate and nitro compounds or other oxidants. Thus, the obtained data allow us to conclude that EPR can be used as the effective express diagnostics of donor's intoxication level at the blood donation.

Obtained from EPR spectra the range of MetHb, Fe^{3+}- Tf, Cu^{2+}- Cp concentrations in blood of donors are presented in Fig.2. The firm line is the result of Gauss approximation of obtained curves.

The level of MetHb for healthy people comprises 1-1.5% from total level of hemoglobin. MetHb is the pathological form of hemoglobin arising by oxidation of diamagnetic heme iron (Fe^{2+}) up to paramagnetic Fe^{3+}. Transition of Fe^{3+} to Fe^{2+} is the reversible process in norm regulating by methemoglobinreductase. By checking MetHb's level the intensity of hemolysis can be determined. So, we can conclude that for donors ~ 15% at the point of blood donation the high level of MetHb was observed and this fact in our opinion is the indicator of the necessity for the further additional medical inspection.

Ceruloplasmin is plasma protein which concentration is one of important blood personal characteristics. Cp plays the number of substantial biological functions in particular this protein takes part in immunology reactions. For ~ 90% of investigated donors pathology in ceruloplasmin concentration was not found (see Fig.2b).

Transferrin is another paramagnetic plasma protein. Tf delivers iron to cells and tissue and takes part in the synthesis of iron-containing proteins, in particular, of hemoglobin. For donors and first of all for those who are permanent employee it is of great importance checking Tf level to be ensure that iron level satisfies the norm. By controlling the intensity of Fe^{3+}-Tf EPR signal one can inferred about the level of blood circulation. As can be seen from Fig.2c for more than 40 % of donors the problem with iron delivery by Tf exists: for ~6% the level of Fe^{3+}-Tf is rather high, whereas for ~35% (!) – its level falls in the range of the Fe^{3+} deficit.

In Table 1 EPR data for donors donated the blood more than once are summarized. The date show that the concentrations of paramagnetic proteins Fe^{3+}-Tf and Cu^{2+}-Cp are kept practically constant with time. This fact conforms to modern concepts of biochemistry viz. the

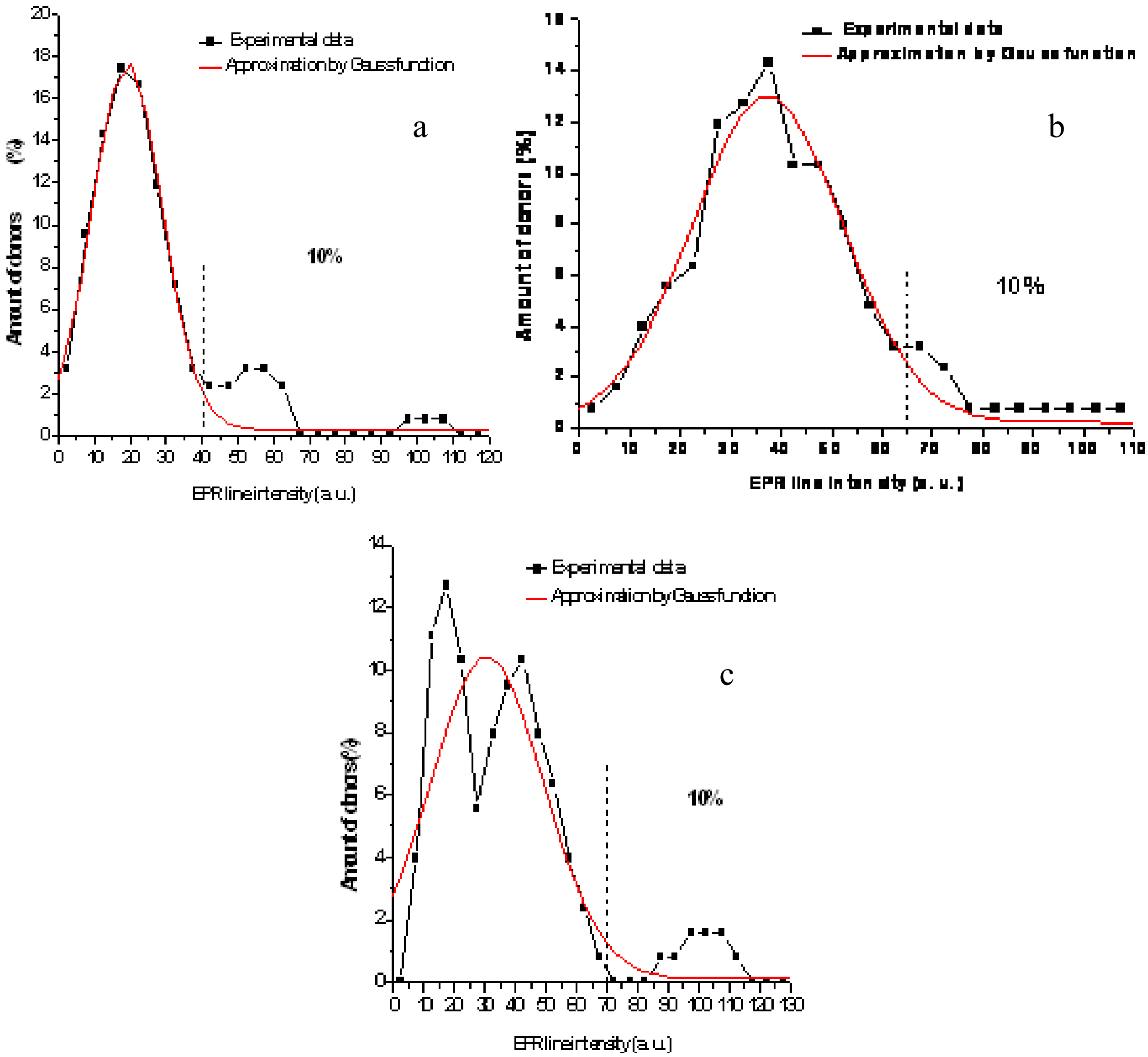

Fig.2. The distribution (black dots) and the results of approximation (red lines) of donors vs. the ranges of proteins level in blood samples: MetHb (*a*), Cu^{2+}-Cu (*b*), Fe^{3+}-Tf (*c*).

Table 1. Variation of paramagnetic centers concentration in donor's blood samples with time.

Name of protein, contain paramagnetic centers	**Donor A**		**Donor B**		**Donor C**		
	Test 1	Test 2	Test 1	Test 2	Test 1	Test 2	Test 3
Transferrin	33	43	20	23	49	51	40
Ceruloplasmin	17	17	31	25	47	47	34
Methemoglobin	19	6	44	15	61	54	15
Gemichrome	11	2	10	21	2	11	5
Free radicals	2	28	2	18	11	12	5

content of protein faction in blood plasma is rather stable for healthy people. At the same time MetHb, gemichrome and free radical concentrations are changed in rather large range. This group of paramagnetic centers as we think has one common feature. All of them represent antioxidant status of human beings at the present moment. MetHb and gemichromes – both are the products of erythrocytes reaction on different kind of oxidizing process in organism. The nature of the paramagnetic center with $g = 2.0034$ is not clear completely. We suppose that the appearence of this signal is indicative of oxidizing process. It must be mentioned that apparent correlation between the intensities of signals from MetHb, gemichrome and free radicals is not found inasmuch as they represent different antioxidant processes in organism.

Conclusion.

The possibility of EPR application for rapid and correct quality monitoring of donor blood is established. The signal from histidine gemichrome was detected in blood EPR spectra for ~70% donors; that testifies to the pathological changes in organism.

References

[1] J.I. Azhipa.: Medico- biological aspects of electron paramagnetic resonance application, M.: Nauka 1983.

[2] M.K. Pulatova, G.T. Rikhireva and Z.V. Kuropteva.: Electron paramagnetic resonance in molecular radiobiology, Energoatomizdat, Moscow 1989.

Multiple quantum NMR for investigations of nanopore compounds

A.V. Fedorova, E.B. Fel’dman

Institute of Problems of Chemical Physics of Russian Academy of Sciences, 142432, av. Semenova 1, Chernogolovka, Russia.

e-mail: panna@icp.ac.ru

Introduction

Multiple quantum (MQ) NMR [1] spectroscopy is a powerful tool to study the nuclear spin distributions in different systems (for example, in liquid crystals [2], simple organic systems [1], amorphous hydrogenated silicon [3], *etc*). The unique possibilities of MQ NMR to study dynamics of many-spin clusters has been recently used [4, 5] for a measurement of the decoherence rate for highly correlated spins.

It is well known that MQ NMR dynamics represents the theoretical basis of MQ NMR spectroscopy. However, possibilities of the theoretical methods are restricted. The main obstacle is the exponential growth of the Hilbert space dimension with an increase in the number of spins. Even supercomputer calculations allow us to study MQ NMR dynamics of a spin system consisting of no more than fifteen spins [6] which is insufficient to solve some subtle problems of MQ NMR dynamics.

Recently nanosize spin systems had a new impact on investigations of MQ NMR dynamics [7]. A closed nanopores filled by spin-carrying atoms (molecules) is an example of such a system. It is shown [7] that the MQ NMR dynamics of a gas of spin-carrying atoms (molecules) in a nanopore avoids the problem of the exponential growth of the Hilbert space dimension with an increase in the number of spins. This happens due to the high symmetry of the MQ NMR Hamiltonian in nanopores which associated with two reasons.

The first reason is determined by the possibility of describing the dipole-dipole interactions (DDI) in nanopores with only one coupling constant [8, 9]. The point is that the characteristic time scale of the molecular diffusion is much less than the NMR time scale determined by the DDI [8, 9]. We emphasize that the accuracy of this approximation is very high and any corrections are senseless. As a result , the MQ Hamiltonian commutes with the operator of the square of the total spin angular momentum and this integral of motion leads to the block structure of the Hamiltonian [7]

The second reason is the permutative symmetry of the spin system in nanopores which yields further simplifications [10]. A way of using this high symmetry in the problem of MQ NMR dynamics was developed in [10]. As a result, MQ NMR dynamics has been analyzed in systems consisting of hundreds of spins so that it has become possible to find the profiles of MQ NMR coherence intensities.

It is necessary to emphasize that all developed methods of MQ NMR dynamics use only the non-secular two-spin/two-quantum Hamiltonian in order to describe the behavior of spin systems in MQ NMR experiments. However higher order corrections of the average Hamiltonian theory [11] can also be important for MQ NMR dynamics. In the present paper we demonstrate how the first non-zero correction affects MQ NMR dynamics and study peculiarities of the profiles of MQ NMR coherences with this correction.

Multiple quantum Hamiltonian with the second order correction.

Let us consider a nanopore which is filled with a gas of spin-carrying ($s = 1/2$) atoms (molecules). The DDI of spins in a strong external magnetic field is governed by the Hamiltonian

$$H_{dz} = \sum_{j<k} D_{jk}[2I_{jz}I_{kz} - \frac{1}{2}(I_j^+ I_k^- + I_j^- I_k^+)], \tag{1}$$

where

$$D_{jk} = \frac{\gamma^2 \hbar (1 - 3\cos^2\theta_{jk})}{2r_{jk}^3} \tag{2}$$

is the DDI coupling constant between spins j and k, γ is the gyromagnetic ratio, r_{jk} is the distance between spins j and k, θ_{jk} is the angle between the the vector $\vec{r}_{jk}$ and the external magnetic field $\vec{H}$ which is parallel to the z axis [12]. The operator $I_{j\alpha}$ ($\alpha = x,y,z$) is the projection of the angular spin momentum operator on the axis α; I_j^+ and I_j^- are the raising and lowering operators of spin j. As a result of irradiating the spin system by a sequence of rf-pulses during the preparation period of MQ NMR experiment [1], the MQ Hamiltonian, H_{MQ}, can be presented according to the average Hamiltonian theory [11] in the following form

$$H_{MQ} = H_0 + H_2, \tag{3}$$

where H_0 is the averaged non-secular two-spin/two-quantum Hamiltonian

$$H_0 = H^{(2)} + H^{(-2)}, \tag{4}$$

$$H^{(\pm 2)} = -\frac{1}{2}\sum_{j<k} D_{jk} I_j^{\pm} I_k^{\pm}, \tag{5}$$

and H_2 is the first non-zero correction to the average Hamiltonian H_0 [11]:

$$H_2 = \frac{\tau_c^2}{36}\left[\left[H_{dy}, H_{dx}\right], H_{dx} - 3H_{dy}\right] \tag{6}$$

where H_{dx} (H_{dy}) can be obtained from Eq. (1) by the replacement $z \leftrightarrow x$ ($z \leftrightarrow y$). Since the MQ NMR Hamiltonian for a spin system in a nanopore is described by only one coupling constant D one can rewrite Eqs.(4,5) as follows [7]:

$$H_0 = -\frac{D}{4}\left\{(I^+)^2 + (I^-)^2\right\}, \tag{7}$$

where $I^{\pm} = \sum_{j=1}^{N} I_j^{\pm}$ and N is the number of spins in the nanopore. Analogously the correction H_2 of Eq. (7) can be written as follows

$$\begin{aligned} H_2 = D^2\tau_c^2\{ &\frac{3}{4}I_z + \frac{3}{8}(I^-)^2 + \frac{3}{8}(I^+)^2 + \frac{9}{4}I_z^2 - \frac{3}{4}(I^-)^2 I_z \\ &-\frac{3}{2}I^+I^-I_z + \frac{3}{4}(I^+)^2 I_z + \frac{3}{2}I_z^3 - \frac{3}{16}(I^-)^4 + \frac{3}{8}(I^-)^2 I_z^2 \\ &-\frac{3}{2}I^+I^-I_z^2 + \frac{3}{8}(I^+)^2(I^-)^2 - \frac{3}{16}(I^+)^4 + \frac{3}{8}(I^+)^2 I_z^2\}. \end{aligned} \tag{8}$$

At first glance, the smallness of the correction H_2 given by Eq.(8) is determined by the parameter $\varepsilon = D\tau_c$. However, the strict analysis [10] shows that the smallness is determined by the parameter $\varepsilon_N = \sqrt{N}\, D\tau_c$. In experiments [8] the parameter ε_N equals 0.53 at N=200 [8, 10]. Consequently the correction H_2 given by Eq.(8) should be taken into account in analysis of the experimental NMR data.

Intensities of MQ NMR coherences

The Hamiltonian H_{MQ} of Eq.(3) does not change sign at the replacement $x \leftrightarrow y$. As a result, calculations of MQ NMR intensities is more difficult than in the case when the correction H_2 does not take into account. One can obtain that the intensity J_n of the MQ NMR coherence of oder n is [10]

$$J_n(\tau) = \mathrm{Tr}\{\rho_n(\tau)\tilde{\rho}_{-n}(\tau)\}, \tag{9}$$

where $\rho_n(\tau)$ is a contribution of MQ NMR coherence of order n to the density matrix of the system during the preparation period of MQ NMR experiments [1] and $\tilde{\rho}_{-n}(\tau)$ is that for the mixing period [10]. One can find from Eq.(9) that

a) the intensities $J_n(\tau)$ are real;

b) the intensities are symmetric over these orders

$$J_n(\tau) = J_{-n}(\tau); \tag{10}$$

c) the sum of the intensities of MQ NMR coherences is not time invariant as in the standard MQ NMR dynamics [13].

In order to calculate MQ NMR coherences in systems with the large number of spins we use the basis of common eigenstates of the operator of the square of the total spin angular momentum and its projection on the axis z [7, 10]. One can show that the problem is reduced to the set of analogous ones for different values of the spin number S ($S = N/2$, $N/2-1$, …, $N/2-[N/2]$, where $[a]$ is an integer part of a). If the intensity $J_{k,S}(\tau)$ corresponds to one of the block of the set then the observable intensity of the MQ NMR coherence of order k is

$$J_k(\tau) = \sum_S n_N(S) J_{k,S}(\tau) \tag{11}$$

where

$$n_N(S) = \frac{N!(2S+1)}{(\frac{N}{2}+S+1)!(\frac{N}{2}-S)!}, \quad 0 \le S \le \frac{N}{2}. \tag{12}$$

is the multiplicity of the MQ coherence $J_{k,S}(\tau)$ [7, 10].

We worked out the numerical algorithm in order to calculate MQ NMR coherences according to the formula (12) [10]. The corresponding programs allow us to calculate MQ NMR coherences in the systems consisting of 200÷600 spins.

Numerical analysis of MQ NMR dynamics

Performing numerical calculations one has to take into account that the correction H_2 of Eq(8) depends on the small parameter ε_N, which depends on both the time spacing τ_c and the number of spins N. We see that in order to satisfy the condition $\varepsilon_N < 1$ one should decrease the time spacing τ_c with an increase in the number of spins N, which was used in numerical simulations. As one can see from fig.1, all intensities of MQ NMR coherences are separated into two families

$$\begin{aligned} \Gamma_1 &= \{\bar{J}_{4k-2},\ k = 1,2,...\}, \\ \Gamma_2 &= \{\bar{J}_{4k},\ k = 1,2,...\}, \end{aligned} \tag{13}$$

while $\bar{J}_0$ may not be referred to any of these families. Each family is approximated by a smooth function. Profiles of MQ coherence intensities for N =201, 401, 601 spins with different values of ε_N are represented in fig.1. If ε_N is small, then the correction H_2 to the Hamiltonian is not significant and the profiles of MQ NMR coherence intensities are exponential ones. However, the numerical results may not approximated by exponential

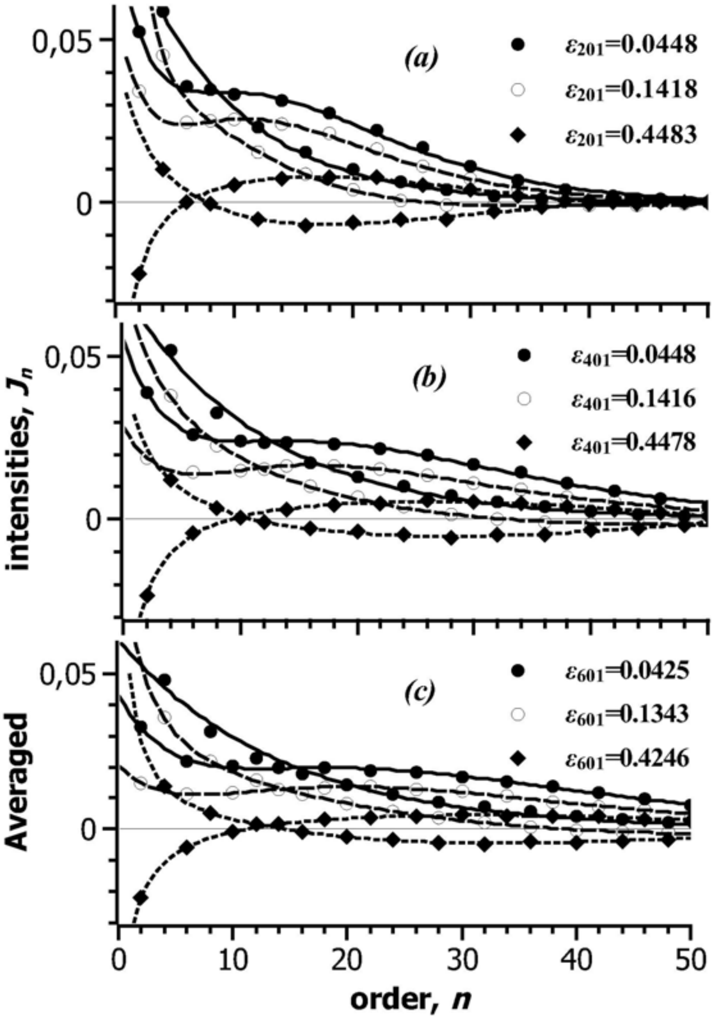

Fig.1 Profiles of the intensities of MQ coherences $\bar{J}_n$ corresponding to the different values of N and ε_N **:** (a) N=201, (b) N=401, (c) N=601

curves if ε_N is larger. In this case one has to look for more complicated curves. We remark also that the sum of the MQ NMR intensities decreases more quickly when the parameter ε_N is larger. A possible way to reduce this decrease is by decreasing ε_N (*i.e.* τ_c) during the course of the MQ NMR experiment.

The work was supported by the Program of the Presidium of RAS No.21 “Foundations of fundamental investigations of nanotechnologies and nanomaterials”.

References

[1] J. Baum, M. Munowitz, A. N. Garroway, A. Pines, *J. Chem. Phys.* **83**, 1015 (1985).

[2] J. Baum, A. Pines, *J. Am. Chem. Soc.* **108**, 7447 (1986).

[3] J. Baum, K. K. Gleason, A. Pines, A. N. Garrovay, J. A. Reimer*, Phys. Rev. Let.* **56**, 1377 (1986).

[4] H. C. Krojanski, D. Suter, *Phys. Rev. Lett.* 93, 090501 (2004).

[5] G. Cho, P. Cappellaro, D. G. Cory, C. Ramanathan, *Phys. Rev. B* **74**, 224434 (2006).

[6] S. I. Doronin, E. B. Fel’dman, I. Ya. Guinzbourg, I. I. Maximov, *Chem. Phys. Lett.*, **341**, 144 (2001).

[7] S. I. Doronin, A. V. Fedorova, E. B. Fel'dman, and A. I. Zenchuk, *J. Chem. Phys.*, 131, 104109 (2009).

[8] J. Baugh, A. Kleinhammens, D. Han, Q. Wang, Y. Wu, *Science*, **294**, 1505 (2001).

[9] E. B. Fel'dman, M. G. Rudavets, *J. Exp. Theor. Phys*., **98**, 207 (2004).

[10] S. I. Doronin, A. V. Fedorova, E. B. Fel'dman, and A. I. Zenchuk , *Physical Chemistry Chemical Physics* 2010, **12.**

[11] Haeberlen, J. S. Waugh, *Phys. Rev.,* **175**, 453-467 (1968).

[12] M. Goldman, *Spin Temperature and Nuclear Magnetic Resonance in Solids*, Clarendon, Oxford, 1970.

[13] D. A. Lathrop, E. S. Handy, and K. K. Gleason, *J. Magn. Reson*. Ser. A, **111**, 161-168 (1994).

Diagnostics of radiating ions-radicals in bioorganic materials via a method of an electronic paramagnetic resonance

L.V. Khaidarshina

Institute of metal physics UB RAS, 620990, S. Kovalevskoy str., 18, Ekaterinburg, Russia.

e-mail: haidarshina@imp.uran.ru

Application of a method of electronic paramagnetic resonance (EPR) in conditions of thermal processing of the organic substances yields quite good results [1]. However, these conditions essentially depend on the sensitivity of the used equipment, and the process of results obtaining is toilful enough, application for researches of the biomaterials with small concentration of ion-radicals demands improvement of a technique of EPR-researches.

The purpose of this work is EPR-method capability check in the diagnostics of pathogenic changes in samples of a bone tissue in conditions of application of the combined influence consisted of an electronic irradiation of samples and their subsequent thermal processing.

According to the literary data, the irradiation the biomaterial by an electronic bunch stimulates appearance of motile carriers which are captured subsequently by so-called "precentres". It can be volumetric or surface carbonaceous groupings (molecules CO^2 adsorbed on a bone apatite crystal surface) and carbonate-ions CO_3^{2-}, replacing phosphatic tetrahedrons or hydroxyl groupings in the structure of apatite that forms the paramagnetic properties of a material. Appearance of the EPR-signal is connected with radiating carbonaceous ions - radicals CO_3^-, CO_3^{3-}, CO_2^-, which appear in an inorganic component of bone tissue by the schemes $CO_3^{2-}+e^-\rightarrow CO_3^{3-}$, $CO_3^{2-}+e^+\rightarrow CO_3^-$ and others, and also with the so-called "R-centres" caused by uncompensated electrons on the broken bonds in an organic component - in the collagenic fibres "torn" by the irradiation. It is established, that in the affected bone tissue concentration of the carbonate ions-radicals is increased, and, on the contrary, concentration of ions-radicals in the normal bone tissue is lowered [2].

In this work samples of a bone tissue of the heads of the femoral joints with coxarthrosis (i.e. pathogenic) and healthy ones (i.e. normal) were investigated by EPR-method. There are no paramagnetic absorption (EPR-signals) in the bone tissues (normal and pathogenic) at the initial state.

Further samples were irradiated with a pulse electronic bunch with pulse duration is 2 ns, average electron energy is 140-150 keV, pulse-repetition frequency is 1 Hz, total number of pulses is 300. Then samples were cut in pieces with mass of 4-10 mg. They were placed in a furnace and annealed at temperatures 50°C, 100°C, 150°C, 200°C, 250°C and 300°C. After each annealing the samples were irradiated and then EPR-spectra were obtained usind the radiospectrometer ESR70-03 DX/2 with working frequency 9,3 - 9,7 GHz (i.e. $\lambda=3$ cm), the g-factor is approximately 2,00. The standard sample MgO:Mn^{2+} at 20°C has been applied for the spectrometer adjustment [3]. The samples under consideration have the complex superimposed form of the EPR-spectra (fig.1). At fig.1 we can see, that after an irradiation at room temperature for both types of samples the EPR-signals were detected, which intensity for pathogenic samples is higher than that for normal bone tissue samples. It is connected with appearance of the large concentration of radiating ions-radicals in pathogenic samples. The further analysis of EPR-spectra has shown that their forms coincide at different temperatures of sample processing both for the normal bone tissue and pathogenic one. EPR-spectra of all irradiated samples of bone tissues are in qualitative similarity and resulting from imposition

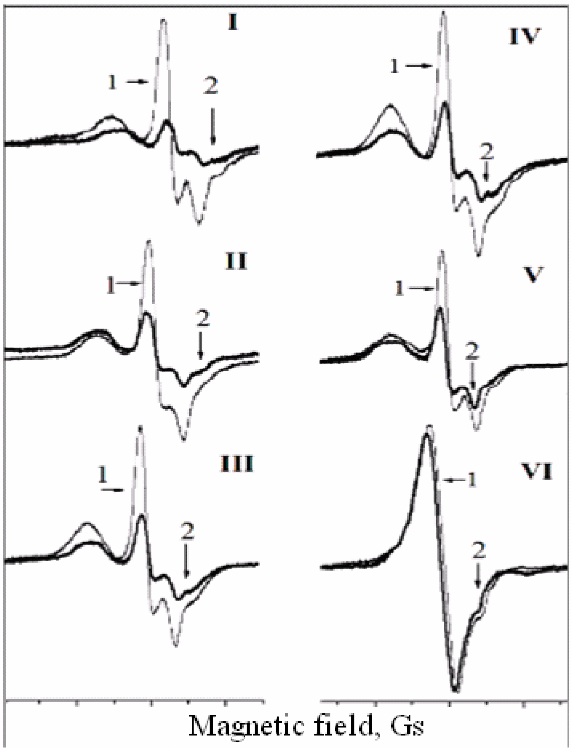

Fig.1. EPR-spectra of pathogenic (1) and normal (2) bone tissues at the combined processing

of several EPR-signals, which are detected at values of the g-factor in an interval 2,0024-2,0027.

The ions-radicals concentration curves as functions of temperature are plotted using the results of analysis of the obtained EPR-spectra of samples of healthy and pathogenic tissues (fig.2). At figure we can see that at room temperature in the irradiated pathogenic bone tissue ions-radicals concentration reaches $2,2*10^{18}$ spin /g, and for the normal irradiated tissue it is only $0,18*10^{18}$ spin/g. With temperature increase the concentration dynamics for the pathogenic and normal irradiated tissues are essentially different: for a normal tissue concentration appreciably (approximately on the order of magnitude) increases, running up to the value of $1,7*10^{18}$ spin/g at temperature of 300°C, and for pathogenic tissue concentration changes weaker with the tendency to decrease to value of $1*10^{18}$ spin/g, i.e. approximately

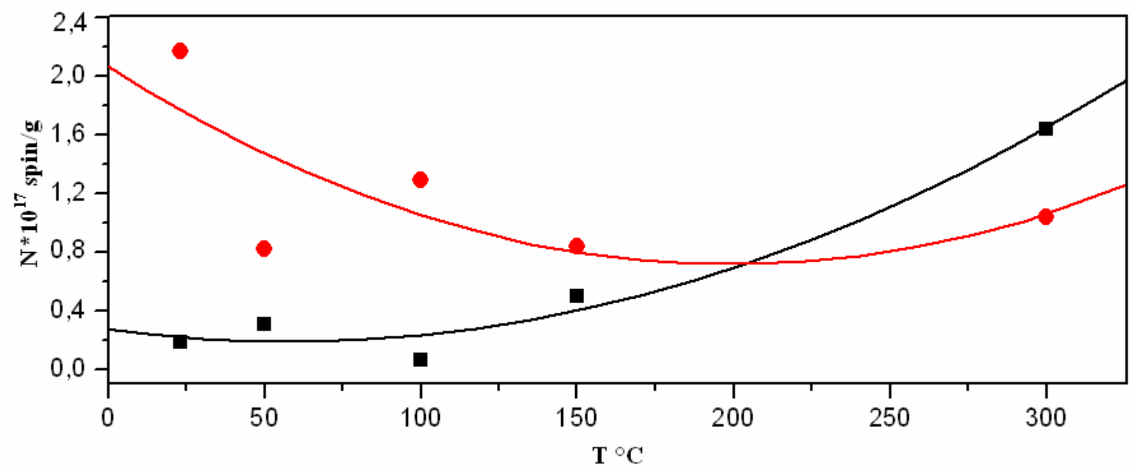

Fig.2. The approximated dependences of concentrations of ions-radicals on temperature in the irradiated samples normal (■) and pathogenic (●) bone tissues

twice. It means that, in comparison with the contribution from an irradiation of samples by an electronic bunch, the thermal processing contribution to the appearance of EPR-signal is very small up to the temperature of 150°C. The temperature raises to 300°C, the contribution of thermochemical ions-radicals becomes prevailing and the structure of EPR-spectra of both types of samples degenerates, going to the simple form; it can be explained by the delocalization effect for the different centers when their mobility increases. (see. fig.1).

The probable reasons of the discovered features of EPR-spectra are connected with increase of the organic phase contents; change of a degree of directivity of collagenous fibres structures (at degeneration); change of number of crystals of molecules of CO_2 and water, adsorbed on a surface; amorphous layer [CO_2-nH_2O] formation; reduction of an apatite crystallinity; change of pH of liquids, feeding a bone, and change of solubility of a minerals [4].

Thus, results of researches of ions - radicals dynamics by EPR-method give us a certain opportunity for diagnostics of pathogenic changes in the irradiated samples at lower temperatures (approximately up to 200 °C), when it is possible to neglect the influence of thermal processing effects. However, additional researches are required for development of this diagnostic method as well as using of more high-sensitivity equipment, for example, Q-band radiospectrometers.

References

[1] Pul Ch. EPR-spectroscopy technique // «MIR», 1970, p. 553

[2] Brik A. B., Shpak A. P., Karpovskii V. L. et al. EPR of nano-sized particles in biogenic and synthetic carbonate-inclusive apatites // Journal of mineralogy. – 2005.-V. 27. –№ 5. p. – 5-26

[3] Gilinskaya L. G., Okuneva G. N., Vlasov Yu. A. Research of mineral pathogenic formations on the human mitral valves. Part II. EPR-spectroscopy // JSC. 2003. V.44. № 5. – p. 882 – 889

[4] Votyakov S. L., Lemesheva S. L., Golovanova O. A. Thermochemical ions-radicals in organic component of a human bone tissue, influence of pathogenic changes // Materials of the III Russian conference with international participation. Syktyvkar 2009, p. 162 – 165.

Vortex excitations above T_c in the cuprate superconductor $Bi_2Sr_2Ca_{1-x}Y_xCu_2O_{8+y}$ as revealed by ESR

L.F. Salakhutdinov, Yu.I. Talanov

Zavoisky Physical-Technical Institute, 420029, Sibirsky tract, Kazan, Russian Federation

e-mail: ksu-students@mail.ru

Introduction

Many years have passed from the date of opening of superconductors, but so far there is no generally accepted theory that would simultaneously describe the behavior of superconductors both above and below T_c. At present, there are still numerous attempts to understand and create a theory that describes the phenomenon of high-temperature superconductivity. Some manifestations of superconductivity were also discovered in the pseudogap state above T_c. A possibility of existence of uncorrelated Cooper pairs was discussed in a number of works [1-4], i.e. superconductivity can survive beyond T_c. However, these works lack mechanism that could convincingly explain the reasons for the forces of attraction to appear between electrons at such high temperatures. Quite recently first indications of a vortex structure formed at temperatures above T_c have appeared. One of the few evidences of the existence of vortices in the temperature region above T_c is the observation of large Nernst effect, which is usually observed at $T < T_c$ and associated with the motion of vortices [5, 6]. However, not all members of the scientific community share this point of view as they suggest other explanations of this phenomenon [7].

Experimental results and discussion

In present work we study electron spin resonance (ESR) of a thin paramagnetic layer precipitated on a surface of a superconductor (so-called “ESR-decoration”). This method was proposed in the work [8] for registration of the Abrikosov vortex lattice which appeared when a HTSC material turns into a superconducting state upon lowering temperature below T_c. The occurrence of vortices necessarily results in a spread of local magnetic field magnitudes both in bulk superconductor, on its surface and in its immediate proximity. In response to the local field dispersion, the ESR signal of paramagnetic substance put on a surface changes its parameters such as the resonance field value H_R and the line width δH. We employ this technique for the detection of possible local distortions of the magnetic field due to vortex excitations in the $Bi_2Sr_2Ca_{1-x}Y_xCu_2O_{8+y}$ crystals at temperatures above the critical one.

ESR is a powerful tool to study the local magnetic field distribution of any origin, in particular that due to the magnetic perturbations produced by vortices. Its sensitivity depends on the ESR line width: the narrower the signal, the higher the resolution. Embedding spin probes in the form of paramagnetic ions results in a broad signal and considerably lowers the ESR resolution. To enhance the resolution, organic free-radical compounds in the form of a surface layer are used as paramagnetic probes with a narrow ESR signal. In this study 2,2-diphenyl-1-picrylhydrazyl (DPPH) is used. It has a narrow Lorentzian ESR signal with line width of 1.2 Oe. Its resonance field at the spectrometer working frequency of 9.3 GHz is about 3300 Oe ($g = 2.0036$).

DPPH is deposited on a flat surface of the sample at 100°C and in high vacuum of 10^{-5} mmHg. The DPPH layer thickness must satisfy to two requirements. On the one hand, it should not be notably larger than the spatial period of the magnetic field variation on the sample surface. If the layer is thicker, the ESR signal of DPPH will not be affected by the field inhomogeneity. An estimate of the Abrikosov vortex lattice constant in the magnetic field of 3000 Oe and at temperature below T_c yields approximately 80 nm. So the layer thickness must not exceed 100 ÷ 200 nm. On the other hand, the DPPH layer with the thickness less than 100 nm and the area of several mm^2 does not provide the ESR signal intensive enough for analysis and extracting useful information. Therefore, an optimal layer thickness, which is sufficiently sensitive to vortex perturbations of the magnetic field, has to be equal to 150 ÷ 200 nm.

ESR spectra were registered on an X-band Bruker BER-418s spectrometer. It operates at a frequency of 9.2 ÷ 9.7GHz with the magnetic field modulation at a frequency of 100 kHz. ESR signals were registered using lock-in amplifier EG&G Model 5209 and were derivatives of the absorbed power signal. A sample was cooled down to the measurement temperature with a helium-flow cryostat placed inside the spectrometer cavity. Resonance lines were recorded upon sweeping the applied field up. To enhance the precision of signal position determination, a small LiF crystal containing dendrites of pure Li metal was mounted in a resonator along with sample coated by DPPH. It has a very narrow ESR signal with the line width of 0.1 Oe and $g = 2.00226$.

Fig.1 shows the EPR spectra recorded at different temperatures. With decreasing temperature the narrow signal from the lithium Gauss-shaped line retains the width and field position unchanged. In contrast to Li, the broader signal of DPPH, which is observed in lower fields, experiences dramatic changes with decreasing temperature: it is shifted and broadened. Knowing the exact position of the EPR signal of lithium, as well as the *g*-factor of lithium, we can accurately determine the position of the ESR signal of DPPH.

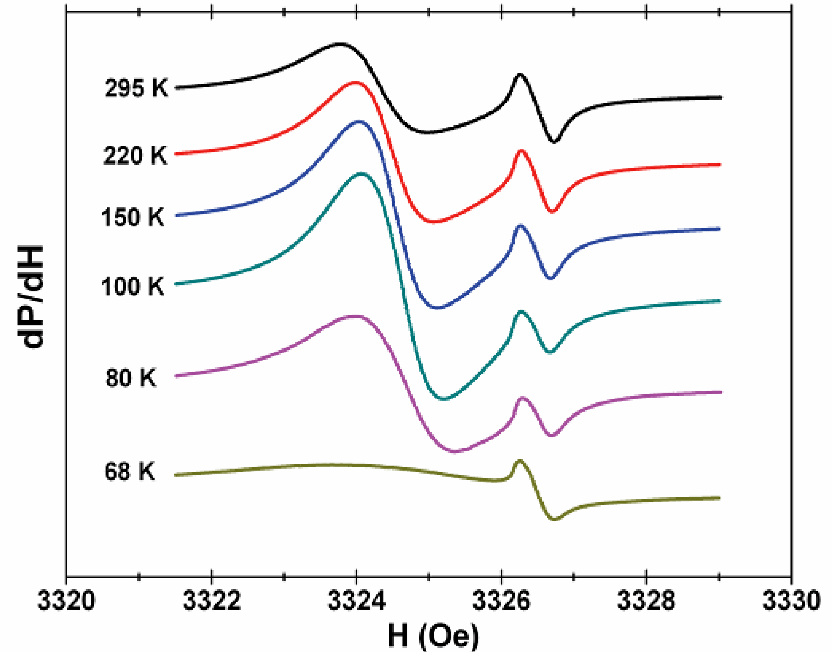

Fig.1. The EPR spectra of DPPH and Li with temperature

By recording and analyzing the EPR spectra, we obtained the temperature dependences of the ESR signal of DPPH for different samples. Some of these dependences are presented in this paper. Fig.2 shows the temperature dependence of the line width of the ESR signal of DPPH deposited on a superconductor, which is compared with that of DPPH deposited on a glass substrate. As one may notice, the broadening of the ESR signal is due to the properties of the superconductor. It is known that the reason for the dramatic broadening below T_c is penetration of the magnetic field into a superconductor in the form of vortices. Since the

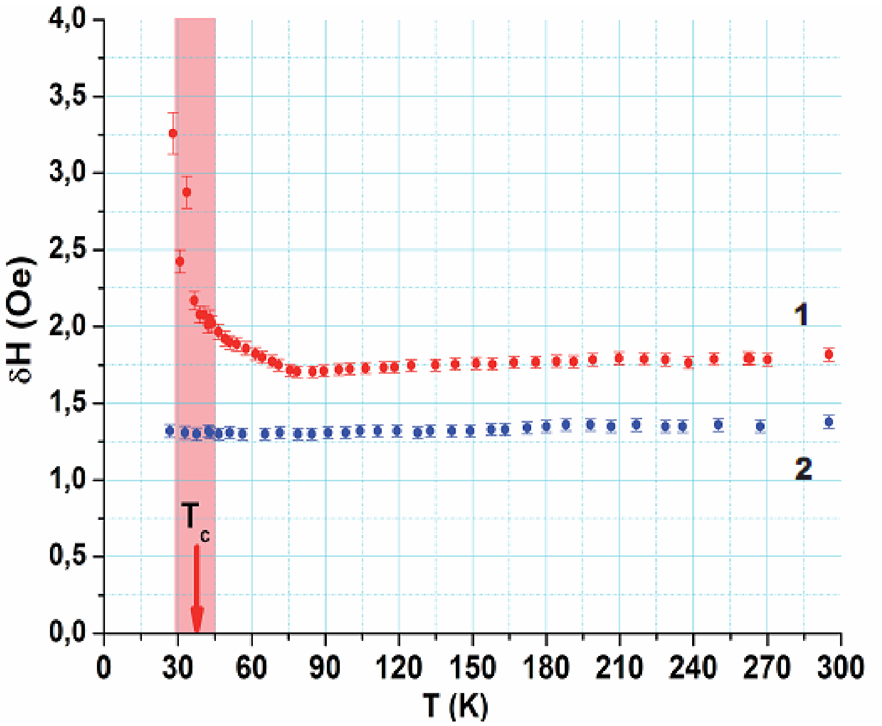

Fig.2. Temperature dependence of the linewidth of the ESR cignal of DPPH 1) on the sample $Bi_2Sr_2Ca_{1-x}Y_xCu_2O_{8+y}$; 2) on a glass substrate

signal broadening is also observed above T_c, we can assume that its origin is also connected with the presence of vortices.

In order to eliminate the influence of the frequency variation and to study the effect of the local field changes, we measure and plot the value of the DPPH-layer signal shift from the Li-signal position $\Delta H_R = H^{DPPH}{}_R - H^{Li}{}_R$ versus temperature (fig.3).

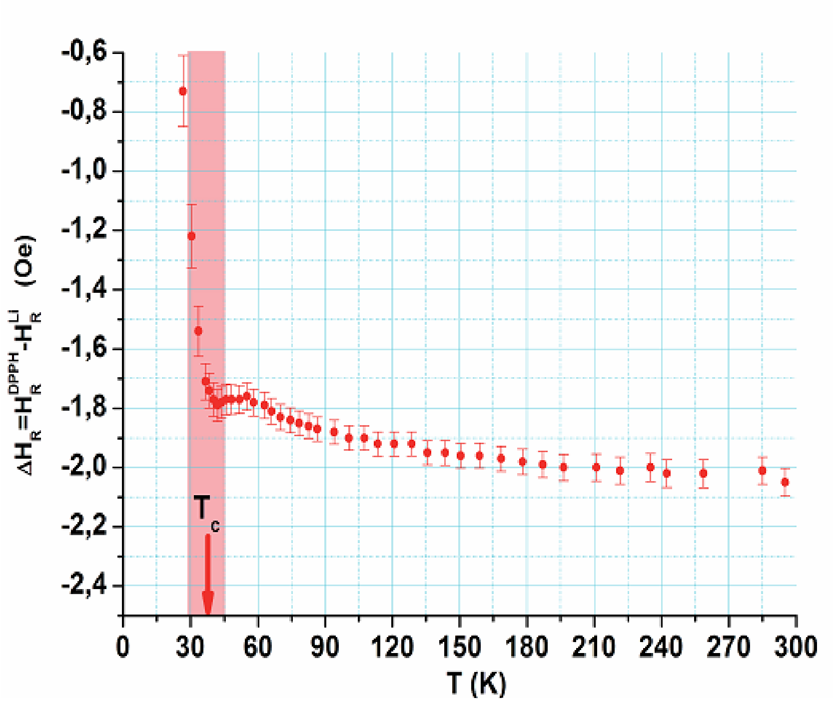

Fig.1. Temperature dependence of the shift of the ESR signal of DPPH of the position of the reference signal Li

As the temperature decreases, the susceptibility of DPPH follows the law 1/*T*. This results in additional contribution to the shift of the resonance field of a thin film of DPPH. But this contribution does not prevent us from observation of some changes in the position of the ESR signal at temperatures above the critical value. There is an assumption that these changes are caused by vortices, whose properties are different from those of Abrikosov vortices.

The temperature dependences of the ESR signal position shift and line width testify favorably to the formation of a vortex state above the critical temperature. To gain better understanding and confidence that the nature of magnetic perturbations above T_c is associated with a vortex structure, we plan to continue research.

References

[1] J. M. Harris, Z.-X. Shen, P. J. White, D. S. Marshall, M. C. Schabel, J. N. Eckstein, and I. Bozovic, Phys. Rev. B 54, R15665 (1996).

[2] G. Zheng, H. Ozaki, W. Clark, Y. Kitaoka, P. Kuhns, A. Reyes, W. Moulton, T. Kondo, Y. Shimakawa, and Y. Kubo, Phys. Rev. Lett. 85, 405 (2000).

[3] H. Raffy, V. Toma, C. Murrills, and Z. Z. Li, Physica C 460-462, 851853 (2007).

[4] C. Renner, B. Revaz, J.-Y. Genoud, K. Kadowaki, and O. Fischer, Phys. Rev. Lett. 80, 149 (1998).

[5] A. Pourret, H. Aubin, J. Lesueur, C. Marrache-Kikuchi, L. Berge, L. Dumoulin, and K. Behnia, Nature Physics 2, 683 (2006).

[6] Y. Wang, L. Li, N. Ong, Phys. Rev. B.73, 024510 (2006).

[7] S. Aleksandrov, V. Zavaritsky, Phys. Rev. Lett. V.93. N.21, P.217002 (2004).

[8] B. Rakvin, M. Požek, and A. Dulčić, Solid State Commun. 72, 199 (1989).

Application of ^{1}H NMR for studing of mobility of building blocks and guest molecules in metal-organic frameworks

M.R. Gallyamov, N.K. Moroz

Nikolaev Institute of Inorganic Chemistry SB of RAS, 630090, Acad. Lavrentiev Ave., 3, Novosibirsk, Russia.

e-mail: oihio@yandex.ru

Metal-organic frameworks (MOF) have prospects of different application due to high porosity for example as sorbents. Unlike it other sorbents as ceolites, MOFs have ability to control of size and stereoselectivity of pores during synthesis. Besides, MOFs are characterized a flexibility of framework itself, which one provides by mobility of building blocks (organic linkers). In addition physical properties of MOFs essentially depend on mobility of guest molecules (sorbats) inside framework, that are investigated by ^{2}H NMR method [1, 2]. This work considers application of solid state ^{1}H NMR permitting selective to study mobility both kinds for wide temperature interval.

Mobility of building block was studied on an example 1,4-diazobicyclo[2,2,2]octane (dabco) molecule (fig.1). In last time molecules similar dabco often are used as pillar linker at creation MOFs. One from such sorbents is $[Zn_2(bdc)_2(dabco)]$ (bdc- 1,4-benzoldicarboxylate, fig.2), in which dabco molecule, having 3-fold axis of symmetry, locate on 4-fold axis of framework. Contradiction of molecular and crystal symmetry can lead to appearance plastic crystal or glassy states, in which a great number of positions exists divided by small barriers caused by turns of a molecule around N-N axis. It's necessary to note, that reorientation of the dabco in various crystals is discovered and confirmed earlier by ^{1}H and ^{14}N NMR. However, in case crystal of pure dabco, determination of mobility was based on the analysis of temperature dependences of the second moment and T_1 [3]. For evidence of assumption about reorientational mobility of linkers dabco in mentioned above MOF we registed ^{1}H NMR-specta in wide temperature interval and performed computational modeling by the cluster approach.

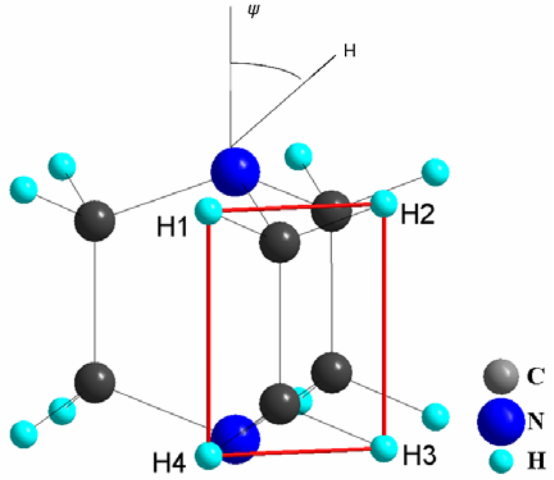

Fig.1. Reorientation of dabco (undistorted conformation) in the external magnetic field.

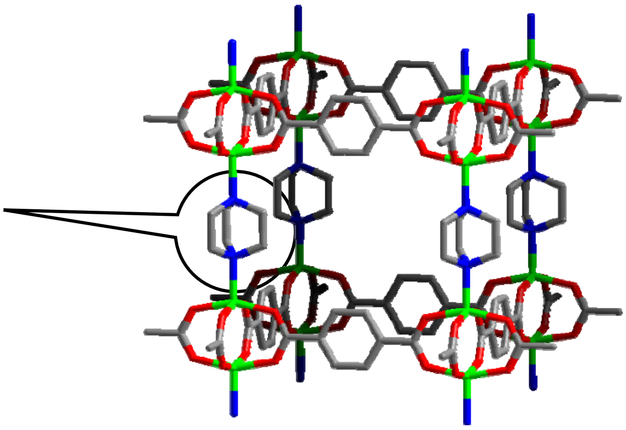

Fig.2. Fragment of framework [Zn2(bdc)2(dabco)]

At the NMR-spectrum description of dabco the problem of four-spin system has been solved for reorientation around N-N axis. Similar decisions for a tetrahedral configuration of nucleus at certain orientation of a crystal in the magnetic field, are known for a long time [4]. In dabco case, it is possible to mark out four protons of ethylene, which interact between each other as dipoles (fig.1). Thus, spectrum of reorientating dabco molecules was calculated (fig.3) Also using this approach was calculated spectrum for [$Zn_2(bdc)_2(dabco)$] (fig.4). It is visible, that at wide temperature range (290-80 K) spectrum is invariable and corresponds to reorientating dabco linkers within sorbent around N-N axis. This fact means, that barrier of reorientation is within 12 kJ/mol (Waugh-Fedina formula). Besides, it is establish, that frequency of reorientation even at 80 K is above $5 \cdot 10^4$ Hz.

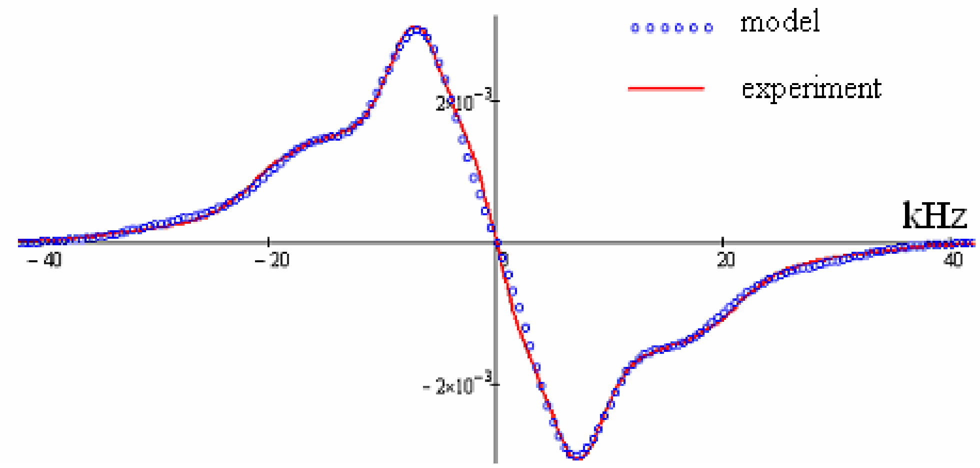

Fig.3. Comparison of experimental and calculated spectrum of pure dabco (298K).

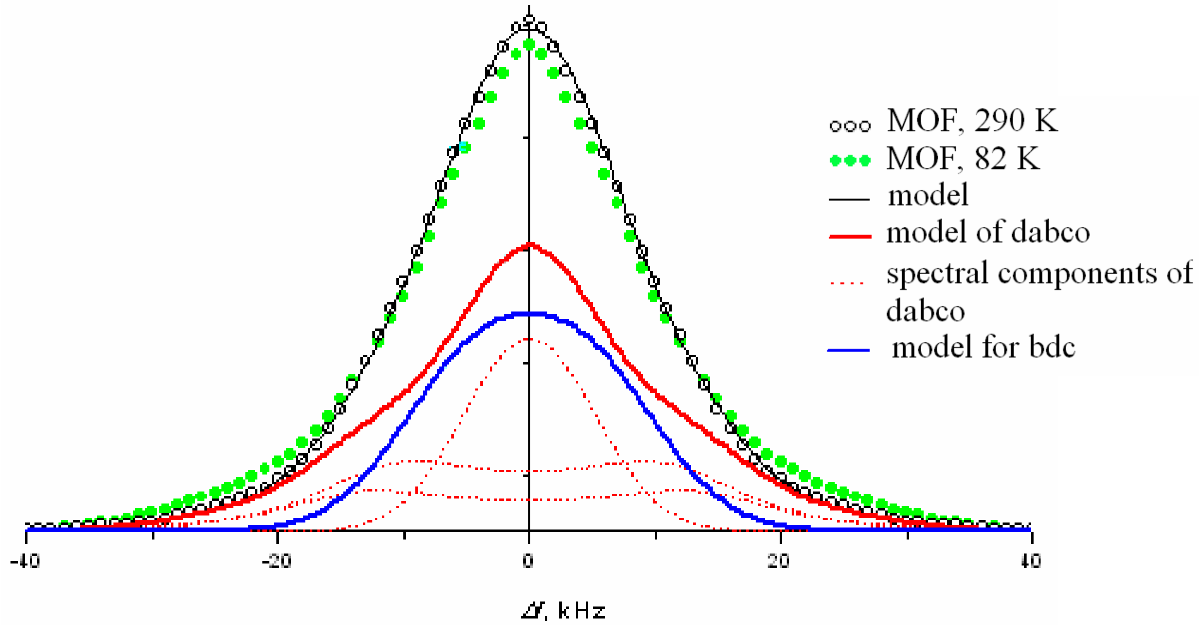

Fig.4. Absorption spectra of [$Zn_2(bdc)_2(dabco)$] for different temperatures.

Other kind is the diffusion mobility of guest molecules in MOFs. For example, MIL-101 ([$Cr_3O(H_2O)_2F(bdc)_3$]•nH_2O, fig.5) and MIL-53lt ([Cr(OH)(bdc)]•H_2O, fig.6) contains hydrophilic ligands thanks to which a reverse sorption of a significant amount of water is possible. Although presence of paramagnetic centers sophisticates an interpretation of spectra, but ones permit selective to investigate a mobility of guest and framework proton subsystems.

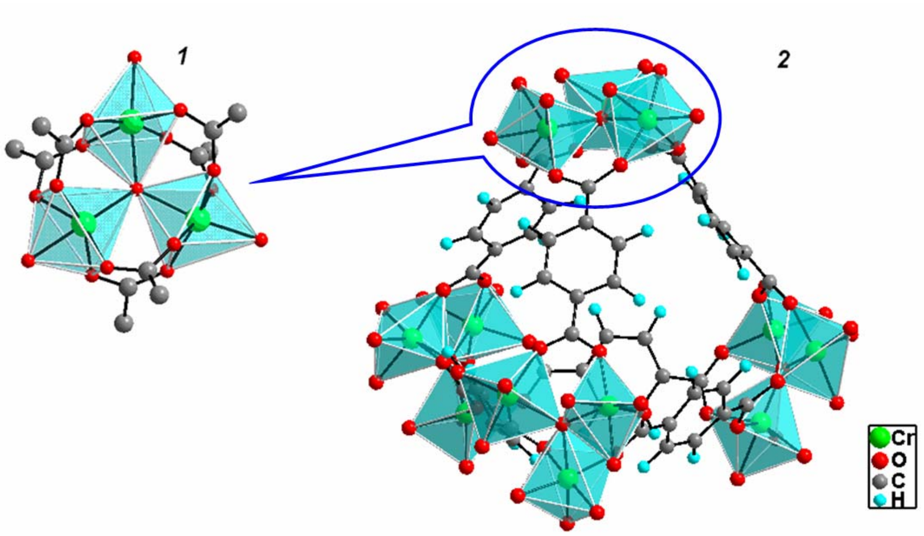

Fig.5. Fragment of structure MIL-101.The first (***1***) and second (***2***) building blocks. Last also is named the supertetrahedra, which forms small and big cells having large cavities.

Two-spin systems (in our case it is bdc-linker and guest water) in paramagnetic environment were considered earlier [5-7], but our the approach differs by an assumption of unequal paramagnetic shifts on protons of one pair, that is more general case. The analysis of the spectra registered at temperature range 150-300 K has allowed to estimate for the first time activation barriers of the diffusion mobility of guest molecules of water in channels these MOFs: 25,0±0,3 (MIL-53lt) and 19,2±0,2 (MIL-101) kJ/mol.

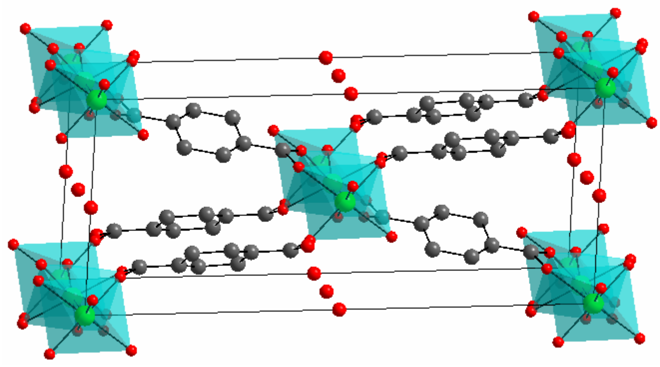

Fig.6. Cell of MIL-53 lt-phase.

References

[1] S. Horike *et. all.*, *Chem. Commun.*, **2004** , 2152 – 2153.

[2] T. Uemura *et. all.*, *J. Am. Chem. Soc.*, **2008**, 130, 6781–6788.

[3] G. W. Smith. *J. Chem. Phys.*, **1964**, 43, 4325-4336.

[4] R. Bersohn, H. G. Gutowsky. *J. Chem. Phys.*, **1954**, 22, 651-658.

[5] D. J. Kroon. *Philips Res. Repots*, **1960,** 15, 501-583**.**

[6] J. Murin, *et. all.*, *Czech. J. Phys. B*, **1981**, 31, 313-323.

[7] J. Oravckova, Murin, J., Rakos, M., Olcak, D. *Czech. J. Phys. B*, **1978**, 28, 1146-1156.

Geometrical phase of the NQR signals

O.N. Glotova[1], N.Y. Sinyavsky[2], and B. Nogaj[1]

[1]Adam Mickiewicz University, 61- 614, Umultowska 85, Poznań, Poland
[2]Baltic State Academy, 236029, Molodiozhnaya str. 6, Kaliningrad, Russia

e-mail: olga_rf@mail.ru

The first experiment of pure NQR illustrating the Berry's phase [1] with mechanical rotation of the sample was carried out by Tycko [2], using a monocrystal of sodium chlorate, in which the quadrupole nuclei of chlorine are oriented along the axis of crystal symmetry being the axis of quantization. In work [3] the Tycko's experiments for pure NQR was spread on a case of a powder and asymmetry parameter which is not equal to zero and attempted of practical use of the Berry's phase manifestation in pure NQR for obtaining of asymmetry parameter of the EFG tensor on nucleuses with spin $I = 3/2$ in powders. The Lisin et al. [4] work investigated the geometrical phase for NMR - system with two levels where the cyclic evolution was created by means of "off-resonance" 2π - pulse.

The purpose of the present work was the research of influence of the open-ended movement trajectory of nuclear magnetization on a phase of signals in off-resonance pulse NQR experiments on nucleuses with spins *3/2* in powdered samples.

The movement trajectory of nuclear magnetization in spin space at influence of the r.f. pulse is defined by nutation of magnetization around the effective field, dependent on the amplitude of excitation pulse and frequency detuning value from a resonance. Let's consider a case of nucleuses with spin $I = 3/2$ and with not axial tensor symmetry of electrical field gradient $\eta \neq 0$. The spin system for this case is not generated. For calculation of influence on spin system of r.f. pulse with frequency detuning $\Delta\omega$ concerning the resonance it is necessary to solve the non-stationary Schrödinger equation in a time interval $0 \le t \le t_w$, where t_w — pulse duration. The wave function can be present as:

$$\Psi = \sum_{m=-1}^{m=+1} C_m(t)\varphi_m \exp(-iE_m t/\hbar) \tag{1}$$

where φ_m — orthogonal own functions of quadrupole Hamiltonian H_Q, E_m — quadrupole interaction energy levels . The coefficients $C_m(t)$ in expression (1) are determined by solving of the non-stationary Schrödinger equation

$$i\hbar\dot{\psi} = [H_Q + H_1(t)]\psi \tag{2}$$

in an interval $0 \le t \le t_w$. Using orthogonal properties of own functions $\varphi_{\text{ь}}$ ($m = +1,-1,0$), from (2) the equation system for $C_m$is obtained:

$$ih\frac{dC_m}{dt} = \sum_n V_{mn} C_n \cdot e^{-i\omega_{mn}t} \tag{3}$$

where $\omega_{mn} = (E_m - E_n)/\hbar$ — frequencies of transitions between energy levels . The Hamiltonian of interaction with r.f. field will be defined as: $\vec{H}_1 = -\gamma\hbar(\vec{B}_1 \cdot \vec{I})\cos\omega t$, where $\omega = \omega_\pm + \Delta\omega$ — spectrometer frequency, $\Delta\omega$ — spectrometer frequency detuning concerning the resonance. The solving for $C_m(t)$ can be expressed through initial coefficients $C_m(0)$ and matrix R as follows: $C(t)=RC(0)$, where R — the matrix with elements:

$$R_{11}=R_{44}=\frac{2e^{-i\frac{\Delta\omega t_w}{2}}}{\omega_n}\left(\frac{\omega_n}{2}\cos\frac{\omega_n}{2}t_w+i\frac{\Delta\omega}{2}\sin\frac{\omega_n}{2}t_w\right),\ R_{12}=-R_{43}=i\frac{2e^{-i\frac{\Delta\omega t_w}{2}}}{\omega_n}A_z\sin\frac{\omega_n}{2}t_w,$$

$$R_{13}=\frac{2e^{-i\frac{\Delta\omega t_w}{2}}}{\omega_n}(A_y-iA_x)\sin\frac{\omega_n}{2}t_w,\ R_{14}=R_{23}=R_{32}=R_{41}=0,$$

$$R_{21}=-R_{34}=i\frac{2e^{i\frac{\Delta\omega t_w}{2}}}{\omega_n}A_z\sin\frac{\omega_n}{2}t_w,\ R_{22}=R_{33}=\frac{2e^{i\frac{\Delta\omega t_w}{2}}}{\omega_n}\left(\frac{\omega_n}{2}\cos\frac{\omega_n}{2}t_w-i\frac{\Delta\omega}{2}\sin\frac{\omega_n}{2}t_w\right),$$

$$R_{24}=\frac{2e^{i\frac{\Delta\omega t_w}{2}}}{\omega_n}(A_y-iA_x)\sin\frac{\omega_n}{2}t_w,\ R_{31}=-\frac{2e^{i\frac{\Delta\omega t_w}{2}}}{\omega_n}(A_y+iA_x)\sin\frac{\omega_n}{2}t_w,$$

$$R_{42}=-\frac{2e^{-i\frac{\Delta\omega t_w}{2}}}{\omega_n}(A_y+iA_x)\sin\frac{\omega_n}{2}t_w,$$

where $A_x=\frac{\gamma B_1(\eta+3)}{4\sqrt{3}\rho}\sin\theta\cos\varphi$, $A_y=\frac{\gamma B_1(\eta-3)}{4\sqrt{3}\rho}\sin\theta\sin\varphi$, $A_z=\frac{\gamma B_1\eta}{2\sqrt{3}\rho}\cos\theta$, $\rho=\sqrt{1+\eta^2/3}$, $\omega_n=\sqrt{\Delta\omega^2+4(A_x^2+A_y^2+A_z^2)}=\sqrt{\Delta\omega^2+\omega_1^2}$, ω_1 — Rabi frequency.

The total phase of induction signal consisting of geometrical and dynamic phases, can be calculated by means of formula [4]:

$$\Phi_t=\Phi_g+\Phi_d=\arg\langle\psi(0)|\psi(t_w)\rangle, \tag{4}$$

where uncyclic geometrical will be equal to:

$$\Phi_g=\arctan\left[\frac{\Delta\omega}{\omega_n}\tan\left(\frac{\omega_n t_w}{2}\right)\right]-\frac{\Delta\omega t_w}{2}=\frac{1}{2}\Omega, \tag{5}$$

$\Phi_t=\arctan\left[\frac{\Delta\omega}{\omega_n}\tan\left(\frac{\omega_n t_w}{2}\right)\right]$ — total phase, $\Phi_d=\frac{\Delta\omega t_w}{2}$ — dynamic phase, *Ω* — solid angle, formed by a trajectory of the end of a vector the unit of magnetization on sphere and geodetic curve, carried out through the final and initial point the movement. The value of this solid angle *Ω* can be calculated also only geometrically, as integral:

$$\Omega=2\int_{\theta_1}^{\theta_2}\sin\theta\arccos\left(\frac{\tan\theta_1}{\tan\theta}\right)d\theta, \tag{6}$$

where $\theta_1=\arctan\left[\cos\left(\frac{\omega_n t_w}{2}\right)\tan\theta_2\right]$, $\theta_2=\arccos\left(\frac{\Delta\omega}{\omega_n}\right)$. Integration of expression (6) results in the formula (5) for solid angle.

In the case of spin system excitation by means of two on-resonance (π/2 and π - pulses) and one off-resonance r.f. pulse of variable duration t_w, turn on after the resonance π-pulses, the geometrical phase of a spin echo signal depending on duration of a off-resonance pulse t_w and on value of frequency detuning *Δω* turns out as:

$$\Phi_g = \arctan\left[\frac{\Delta\omega\tan\left(\frac{\omega_n t_w}{2}\right)}{\omega_1\tan\left(\frac{\omega_n t_w}{2}\right)-\omega_n}\right] \tag{7}$$

and represents a solid angle formed by magnetization vector end trajectory and geodetic line segment connecting initial and final trajectory points on the sphere. The formula (7) coincides with the expression for the area of a spherical triangle and calculated by know the formula:

$$\Omega = 4\arctan\sqrt{\tan\left(\frac{\varepsilon}{2}\right)\tan\left(\frac{\varepsilon-a}{2}\right)\tan\left(\frac{\varepsilon-b}{2}\right)\tan\left(\frac{\varepsilon-c}{2}\right)}, \tag{8}$$

provided that $c=\pi/2$. Generally, for separate crystallite of a powder $\varepsilon=(a+b+c)/2$, $a=\omega_n t_w$, $b=\arccos\left[-\frac{\omega_1}{\omega_n}\sin(\omega_n t_w)\right]$, $c=\omega_1 t_w$.

The above mentioned formulas for phases are obtained for one orientation (θ and φ) of r.f. coils relating to the main axes of EFG tensor on a nucleus. The experiment registeres the average phase for all crystallites (for angles θ and φ) having own phases.

The experimental NQR measurements on nucleuses ^{35}Cl were executed on a pulsed FT NQR spectrometer (0.5 – 300 MHz) Tecmag Apollo with NTNMR software. The phases of spin echo signals were obtained during processing by means of known algorithm of automatic phase correction after Fourier transformation. Then the phase was unwrapped in monotonously increasing by means of "unwrap" procedure. The carrier frequency and not resonant pulse duration t_w varied in the experiment. The NQR measurements on nucleuses ^{35}Cl were carried out on a powdered sample $KClO_3$ at room temperature.

Fig.1 shows the dependences of signals geometrical phase for the experiment with induction signal for different detuning of spectrometer frequency from the resonance. Appropriate simulations executed for a powder are shown by continuous lines. The averaging

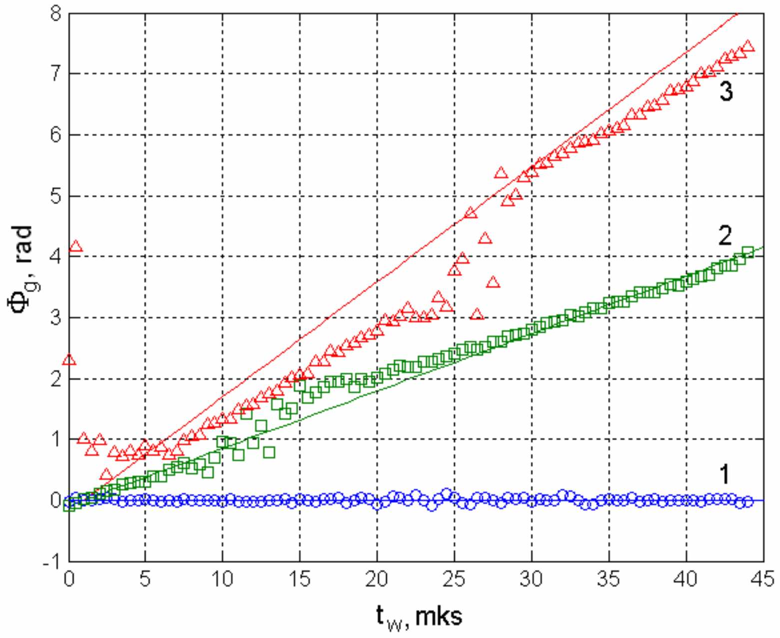

Fig.1. Dependence of a phase 35Cl NQR - echo in KClO3 from duration of off-resonance pulse tw in experiment shown in Fig. 2, for Δν = 0 kHz (1), 15 kHz (2) and 30 kHz (3). Continuous lines are simulations.

of phases in a powder results that the dependences Φ_g from t_w for different frequency detunings are linear. In this experiment the measurement of a signal is synchronized with the end of resonant π - pulse, therefore not total but geometrical phase is registered.

Fig.2 show the change of the total phase Φ_t with change of pulse duration t_w in the nutation experiment with one r.f. pulse for case $\Delta\nu = 30$ kHz. Phase Φ_t oscillations amplitude attenuation is caused by the signal amplitude attenuation in nutation experiment for a powder. However, the simulation and experiment, there is a reason to believe that the phase oscillations amplitude decrease in due course t_w, will be not such fast, as decrease of amplitude of a signal in usual nutation experiment as far as the phase will probably be less exposed to relaxation processes influence . It will allow to improve the separation of frequency singularities in a nutation spectrum Φ_{ti} (ω_n), obtained after of Fourier transformation of function $\Phi_{ti}(t_w)$, and consequently increase the determination accuracy of asymmetry parameter η for nucleuses with spins $I = 3/2$ from nutation experiment. Phase $\Phi_{ti}(t_w)$ oscillations for a powder are not harmonic and, hence, harmonics of nutation frequencies ω_n will be contained in spectrum $\Phi_{ti}(\omega_n)$.

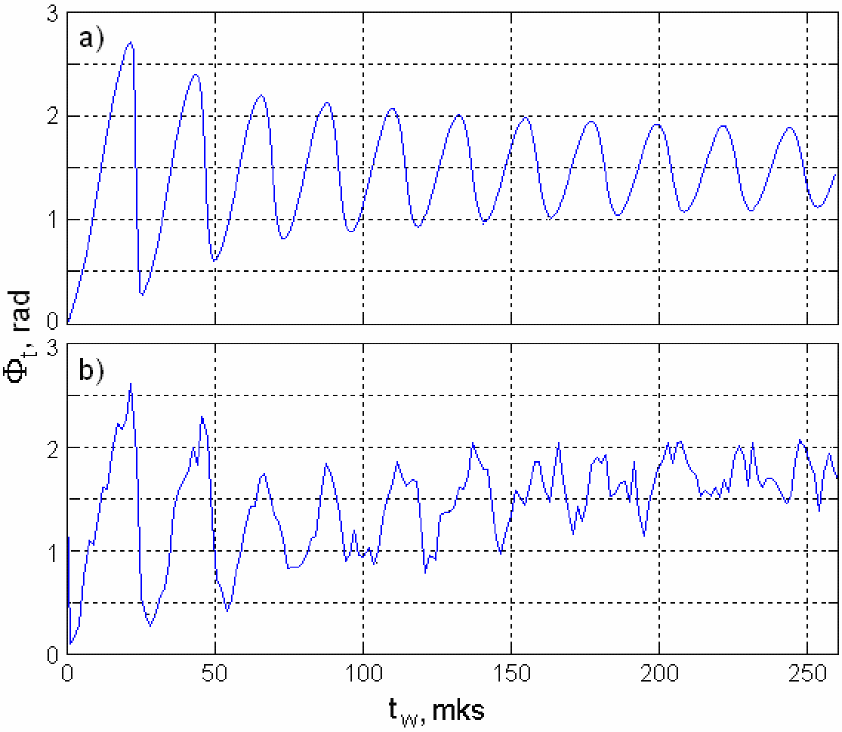

Fig.2. Change of a phase in nutation 35Cl NQR experiment with one r.f. pulse for Δν = 30 kHz in a powder of KClO3: a – simulation for an ideal signal, b – experimental dependence.

Thus, the analytical expressions for encyclical geometrical phases of NQR signals are obtained in the given work depending on r.f. pulses durations and on frequency detuning for spin 3/2. Executed simulations of signal phase dependences properly coincide with experiment for powdered samples. It is shown, that the geometrical phase is registered in case of measurements synchronization along with the beginning of r.f. pulse and the sum of geometrical and dynamic phases in case of synchronization with the end of r.f. pulse-. The geometrical phase is monotonously increasing accompanied by r.f. pulse stretching. The total phase depending on t_w is of oscillatory manner, with nutation frequency of nuclear magnetization in a powder. The loss of signal coherence due to a certain accumulation of geometrical phases caused by various factors can be considered as a new mechanism of relaxation which should be taken into account in NMR and NQR experiments.

References

[1] M.V. Berry, Proc. R. Soc. London Ser. A 392, 45 (1984).

[2] R. Tycko, Phys. Rev. Lett. 58, 2281 (1987).

[3] N. Sinyavsky, M. Mackowiak, and C. Schmidt, Z. Naturforsch. 63a, 81 (2008).

[4] W.N. Lisin, G.G. Fedoruk, and E. P. Haymovich, Pis'ma Zh. Eksp. Teor. Fiz. 50, 205 (1989) (in Russian).

[5] N. Mukunda, R. Simon, Ann. Phys. (N.Y.) **228** (1993) 205.

Magnetic structure in the multiferroic $LiCu_2O_2$: ^{63,65}Cu and ^{7}Li NMR studies

A.F. Sadykov, Y.V. Piskunov, A.P. Gerashenko, V.V. Ogloblichev, A.L. Buzlukov, K.N. Mikhalev, S.V. Verkhovskii

Institute of Metal Physics, UB RAS, 620041, S. Kovalevskaya Str. 18, Ekaterinburg, Russia

e-mail: Sadykov@imp.uran.ru

The multiferroic $LiCu_2O_2$ belong to a class of quasi-one-dimensional frustrated magnets, in which there is competition ferro- and antiferromagnetic exchange interaction of the nearest neighbor and the next nearest neighbor spins in the CuO_2 chain extending along the ***b*** axis. The crystal structure, which is described orthorhombic space group Pnma, is an alternation along the ***c*** axis of three layers: 1) –Cu^+–, 2) –$OCu^{2+}OLi$– and 3) –$LiOCu^{2+}O$–. The transition in the ordered state with the incommensurable, noncollinear magnetic structure [1,2] is observed below critical temperature T_c = 23 K in this compound. This transition is accompanied by the occurrence of a spontaneous macroscopic electric polarization, P [3]. There is a considerable quantity of the works devoted to research of magnetic and electric properties of $LiCu_2O_2$ but the concrete type of the magnetic structure realized in this compound is not found yet. The question about evolution of magnetic structure depending on amplitude and direction of an external magnetic field is open too.

We present the results of ^{63,65}Cu and ^{7}Li NMR/NQR studies of magnetic order in the $LiCu_2O_2$. ^{63,65}Cu (I = 3/2) and ^{7}Li (I = 3/2) NMR and NQR measurements have been performed on the single crystal $LiCu_2O_2$ at temperatures T = 290 K and T = 4.2 K, i.e. above and below the critical temperature of the magnetic ordering. NMR spectra of two isotopes of copper ^{63,65}Cu located in non-magnetic Cu^+ layers were recorded at the external magnetic field H_0 = 94 kOe for orientation of the single crystal in the magnetic field $\boldsymbol{H}_0 \parallel \boldsymbol{c}$. We were not able to observe the signal from the magnetic copper ions Cu^{2+}. This is associated with too rapid transverse relaxation of nuclear spins of copper ions Cu^{2+} having a non-compensated spin magnetic moment in the electron shell. At $T > T_c$ NMR spectrum for each isotope of copper is a set of three narrow lines ($\Delta f_{1/2}$ <100 kHz), and the NQR spectrum is two narrow lines, and lithium spectrum is one narrow line. At cooling the sample to T = 4.2 K the considerable broadening and complication of the NMR/NQR spectra are observed. The analysis of the NMR/NQR spectra presented in fig.1 and fig.2 has shown that they can be satisfactorily described by the assumption that each of the narrow lines observed above T_c is split in two one in the case of copper and in four lines in the case of lithium. Such a type of spectra splitting at the transition to an ordered magnetic state is a sign of the realization in the material a complex helical structure of magnetic spin moments.

At the analysis of the experimental data it was supposed that the incommensurable helix magnetic structure is realized in the $LiCu_2O_2$ [1,2], in which changing of the magnetic moment of copper Cu^{2+} ion along the chain is defined as follows:

$$\boldsymbol{m}(y) = \mu \boldsymbol{l}_1 \cos(q_y y + \varphi_0) + \mu \boldsymbol{l}_2 \sin(q_y y + \varphi_0)\,, \qquad (1)$$

where $\mathbf{l}_1$ and $\mathbf{l}_2$ are two mutually perpendicular unit vectors, $q_y = 0.826\ 2\pi/b$ [1] is the y-component of incommensurability wave vector of the magnetic structure, μ is the amplitude of the magnetic moment of the Cu^{2+} ion in the magnetically ordered phase, $\boldsymbol{n} = \boldsymbol{l}_1 \times \boldsymbol{l}_2$ is the normal to the plane of the magnetic moments. The effective magnetic field on nucleus of the nonmagnetic ions Cu^+ and Li^+ is determined by the long range dipole field induced by the magnetic environment and the “contact” hyperfine field transferred from the nearest neighbor magnetic Cu^{2+} ions.

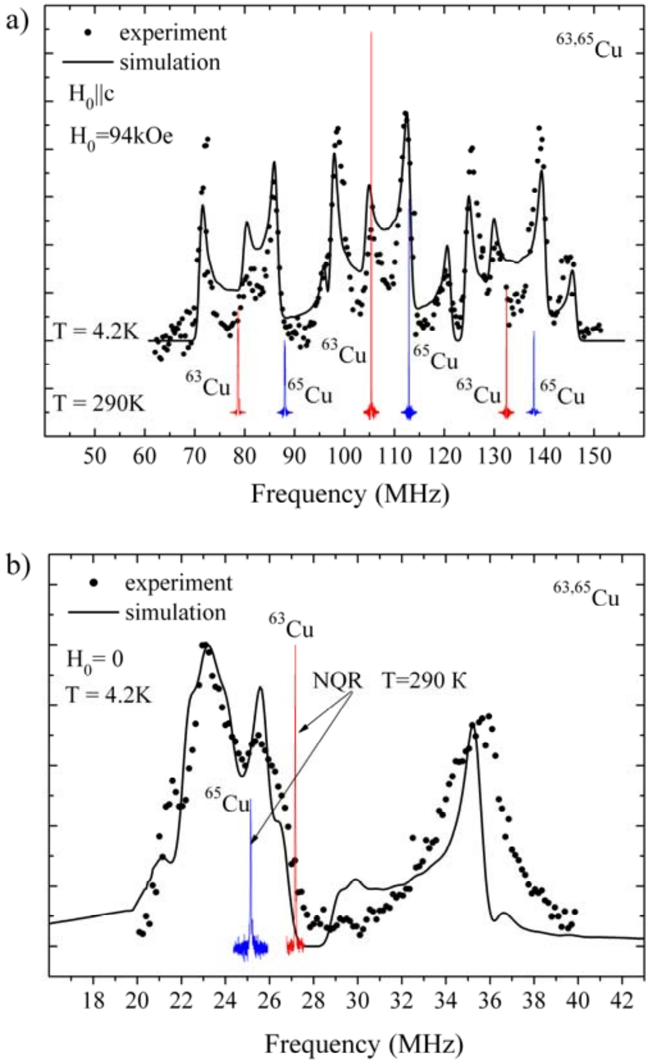

Fig.1. a) ^{63,65}Cu NMR spectra in the magnetically ordered phase of $LiCu_2O_2$ single crystal at T = 4.2 K for the external magnetic field directions $\boldsymbol{H}_0 \parallel \boldsymbol{c}$ (•). The narrow spectral peaks conform to ^{63,65}Cu NMR spectra at room temperature. Solid line represents the spectrum simulated in the model of planar helix.
b) ^{63,65}Cu NMR spectra in local magnetic field in the magnetically ordered phase of $LiCu_2O_2$ single crystal at T = 4.2 K (•).^{63,65}Cu spectra are also shown in a zero magnetic field at room temperature. Solid line represents the spectrum simulated in the model of planar helix.

The value of local magnetic field $\boldsymbol{h}_{\rm loc}(\boldsymbol{R})$ at site $\boldsymbol{R}$ ($\boldsymbol{R}$ – position of Cu^+) located on distance $\boldsymbol{R}+\boldsymbol{r}_{\rm i}$ from the nearest neighbor Cu^{2+} ion can be written as:

$$\boldsymbol{h}_{loc}(\boldsymbol{R}) = \sum_{i=1}^{4} A_{\alpha\alpha}(\boldsymbol{r}_i + \boldsymbol{R})\boldsymbol{S}(\boldsymbol{r}_i) \qquad (\alpha = x, y, z)\,, \tag{2}$$

where $\boldsymbol{S}(\boldsymbol{r}_{\rm i})$ is spin polarization on the ion Cu^{2+} site, and $A_{\alpha\alpha}(\boldsymbol{r}+\boldsymbol{R})$ is anisotropic tensor taking into account the both long range dipole field ($H_{\rm dip}$) and the "contact" hyperfine field ($H_{\rm hf}$) transferred from the nearest neighbor magnetic Cu^{2+} ions. The values of dipole fields on the Cu^+ (Li^+) sites have been estimated in the range of one coordination sphere by using an usual expression for $H_{\rm dip}$:

$$\boldsymbol{H}_{\rm dip} = \sum_{i=1} \left\{3\boldsymbol{r}(\boldsymbol{\mu} * \boldsymbol{r}) - \boldsymbol{\mu} * \boldsymbol{r}^2\right\} / \boldsymbol{r}^5\,, \tag{3}$$

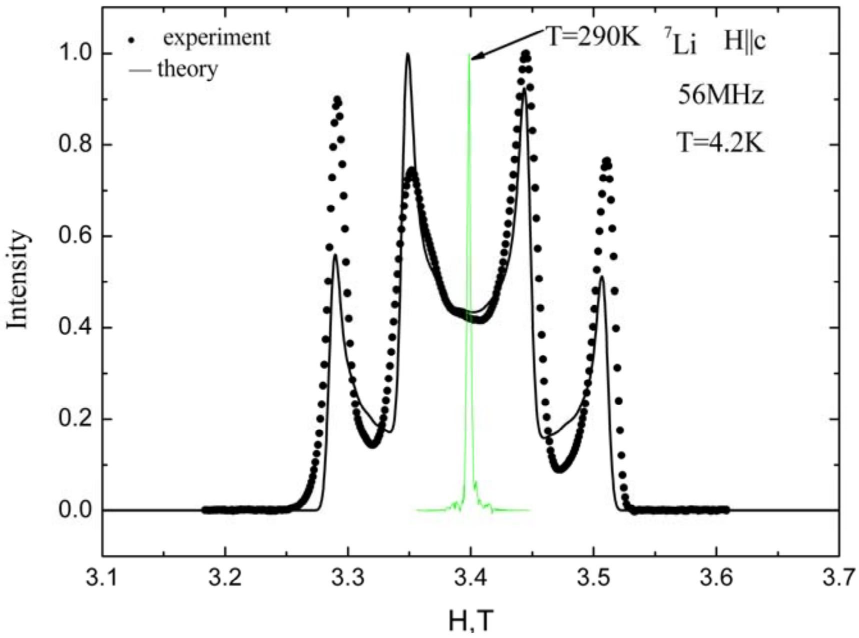

Fig.2. ^{7}Li field swept NMR spectra in the magnetically ordered phase of the $LiCu_2O_2$ single crystal (•). The narrow spectral peak conforms to ^{7}Li NMR spectrum at room temperature. Solid line represents the spectrum simulated in the model of planar helix at Cu^{2+} sites.

where $r^2=(x^2+y^2+z^2)$ is distance between Cu^{2+} and Cu^+ (Li^+), $\mu = \mu_{eff}(\mu_x, \mu_y, \mu_z)$ – the effective magnetic moment of the Cu^{2+} ion located on the crystal lattice sites with the coordinates (x, y, z). It was found out the ^{63,65}Cu spectra modification below T_c was caused mainly by the isotropic transferred hyperfine fields while the ^{7}Li spectra splitting was explained rather well by taking into account only dipole fields at the Li ion sites.

The spectra in fig.1 and fig.2 were simulated by using the special computer program, in which the spatial orientation of magnetic moments might be preset according to some model. The spatial orientation of magnetic moments was given by a set of Euler angles ψ (precession angle), γ (nutation angle),φ (rotation angle). As the parameters of the simulation, we varied the amplitude of the local field at the Cu^+ sites $|h_{loc}|$, the angles ψ and γ, the effective magnetic moment of the Cu^{2+} ion $\boldsymbol{\mu}$. Here, the angle ψ is the angle between the ***a*** axis and the projection of a helix plane normal ***n*** to the ***ab*** plane, and γ is the angle between the ***c*** axis and the helix plane normal ***n***. The theoretical spectrum in the fig.1a corresponds to the values $|h_{loc}|$ = 12.0(1) kOe, $\psi = 0$ and $\gamma = 35(2)^o$. The theoretical spectrum in the fig.1b corresponds to the same values of the simulation parameters $|h_{loc}|$ = 12.0(1) kOe, $\psi = 0$ and slightly bigger value of $\gamma = 40(2)^o$. This indicates the external magnetic field directed along the axis ***c***, turns the helix plane slightly. From the best simulation of spectrum in fig.2 the effective magnetic moment of the Cu^{2+} ion was determined: $\boldsymbol{\mu} \approx 1.0(1)\mu_B$.

References

[1] T. Masuda, A. Zheludev, A. Bush, et. al., Phys. Rev. Lett. **92**, 177201 (2004).

[2] A. A. Gippius, E. N. Morozova, A. S. Moskvin, et. al., Phys. Rev. B **70,** 020406 (2004).

[3] S. Park, Y. J. Choi, C. L. Zhang, and S-W. Cheong, Phys. Rev. Lett. **98**, 057601 (2007).

NMR microimaging for studying and monitoring the processes of inverse opal preparation via sol-gel technology

E.V. Morozov[1,2], O.V. Shabanova[2], V.F. Pavlov[2]

[1]Kirensky Institute of Physics SB RAS, 660036, Akademgorodok 50; Krasnoyarsk, Russia
[2]Special Designing and Technological Bureau «Nauka» KSC SB RAS, 660049, Mira 53; Krasnoyarsk, Russia

e-mail: morozov_sfu@mail.ru

Introduction

It is well known that the NMR microimaging is a unique and very effective tool to study the processes in different systems without their destruction [1]. Investigation of the functional material preparation processes in sol-gel technology is one of the perspective areas of MRI application. The sol-gel technology includes different processes such as sedimentation, gelation, drying, saturation etc [2]. By means of this method one can obtain binding materials, sorbate, gas sensors, optical waveguide and inverse opals which have special significance for photonic crystal preparing. In particular filling of three-dimensional spatial structure of the pores in inverse opal by some substances to result in photonic crystal possessed assigned properties [3].

In this work the results of NMR microimaging experiments for polymethylmethacrylate (PMMA) colloidal particles sedimentation and PMMA colloidal crystal saturation are presented.

Methods and materials

The water solutions of the polymethylmethacrylate colloidal particles (d=300 nm) prepared according to techniques [4] were used for investigation. The sedimentation process was observed for both free evaporation and without evaporation conditions. The PMMA colloidal crystal was saturated by organic substances (glycerine, isobutyl alcohol) and colloidal silica with different SiO_2 content. Imaging investigations were carried out using microimaging installation based on Bruker AVANCE DPX 200 at field 4.7T, with the probe PH MICRO 2.5 (coil diameter being 25mm).

Results and discussion

PMMA sedimentation

The PMMA sedimentation process was studied by means of acquisition time-dependent differently weighted NMR images and $T_{1,}T_2$-maps. The first experiments were carried out for free evaporation condition. The step-by-step sediment formation and formation of supernatant fractions with PMMA high content were observed during the experiment (fig.1). Indeed for long time before of sediment formation apparent on the pd-weighted images one can see a clear formation of wide layer with high content of colloidal particles. As the sediment thickness increase the width of supernatant fraction decrease. Also there is no any displacement of supernatant fraction. It is likely caused by decreasing of relaxation time all over the sample by means of evaporation of disperse medium (the water). In result the “sediment – supernatant fractions” and “supernatant fractions – sol” interfaces gradually join and the transition layers disappear.

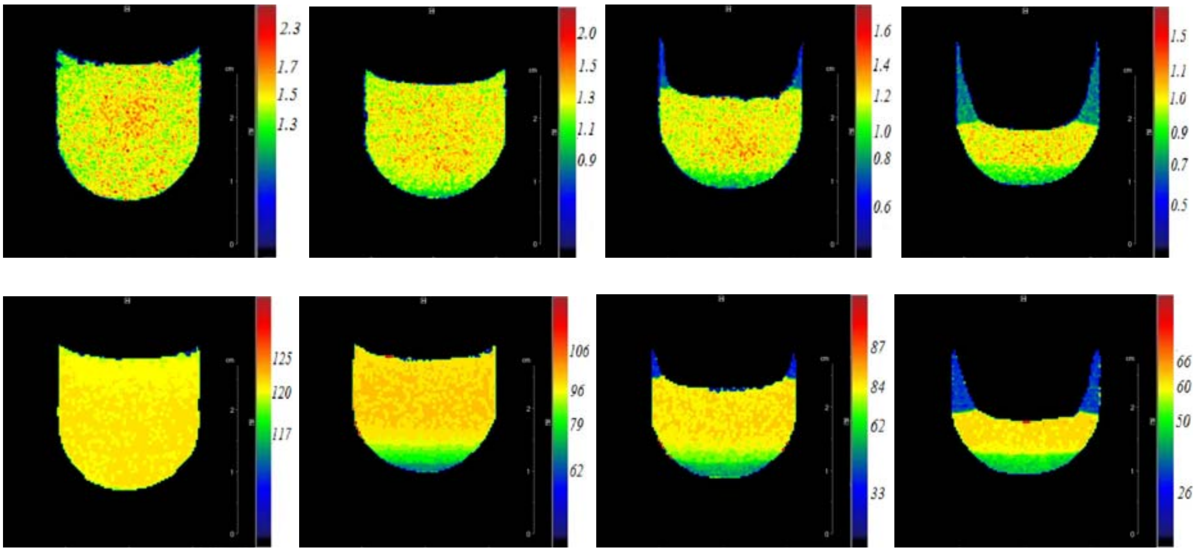

0 day 7 days 12 days 17 days

Fig.1. T_1 (s), T_2 (ms)-maps for sample with free evaporation condition; FOV 40 mm, 128x128 matrix, slice thickness 1 mm

T_1 and T_2 profiles of sample during the sedimentation are presented in fig.2. One can see there a stepped behavior of sedimentation very clear.

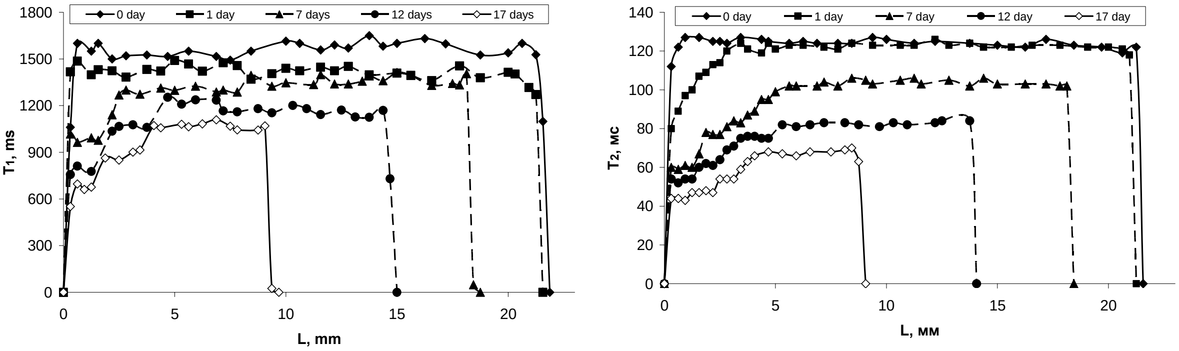

Fig.2. T_1 (at the left) and T_2 (at the right) time-dependent profiles for samples with free evaporation condition; all profiles are central longitudinal section of samples

When viewed the samples which has not evaporation of disperse medium one can see some differences. There is no overall decreasing of relaxation time which can be caused by the evaporation absence. Also such condition to give rise to transition layers observed more clear (fig.3,4). The sediment thickness increasing leads to extend of the supernatant fractions. Furthermore as the samples were allowed to settle longer, the stepped behavior of sedimentation was observed from the very “sol – pure water” interface.

The NMR images can provide us with available information about time-dependent displacement of interfaces. For instance it allows the dynamic of sediment formation be measured from series of images. The dynamic of “sol – pure water” interface descent also was measured. It turned out that the sediment formation rates are almost equal for both free evaporation and without evaporation conditions (~0.2 mm/d) and they are almost equal to solution layering rate for sample with second condition (fig.5).

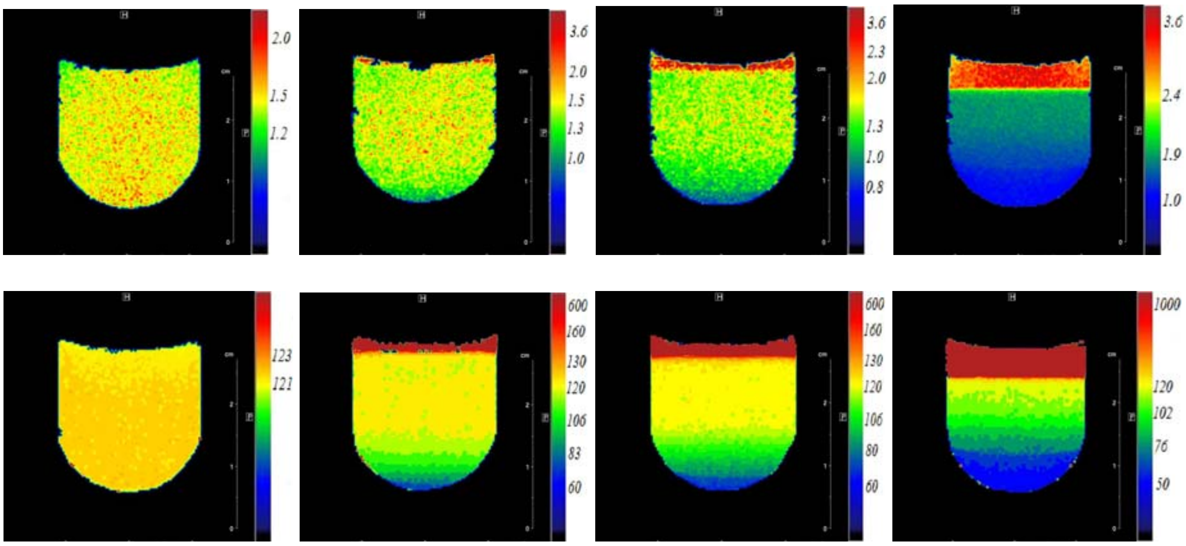

0 day 5 days 10 days 28 days

Fig.3. T_1 (s), T_2 (ms)-maps for sample without evaporation condition; FOV 40 mm, 128x128 matrix, slice thickness 1 mm

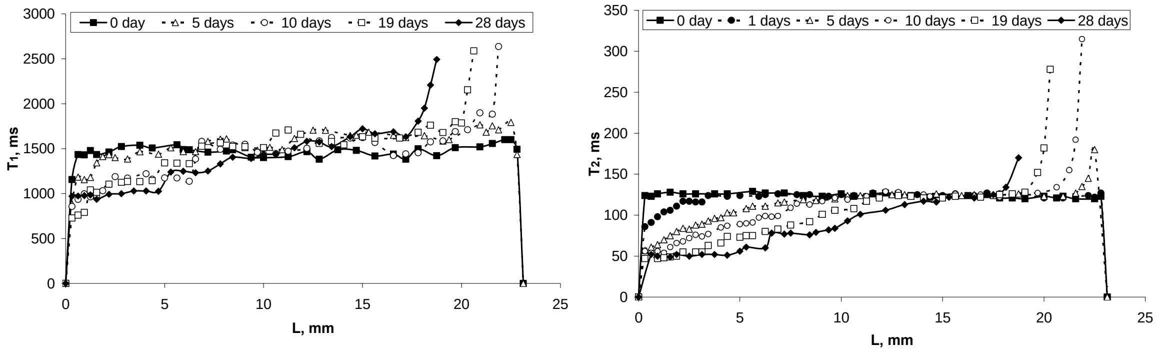

Fig.4. T_1 (at the left) and T_2 (at the right) time-dependent profiles for samples without evaporation condition; all profiles are central longitudinal section of samples

From the linearity of "sol – pure water" interface dynamic (fig.5) one can conclude that the colloidal PMMA particles are substantially monodisperse. However this fact is not agreed with very wide supernatant fractions. Furthermore these layers would begin from upper interface but they begin from sediment. The experimental results show that the thickness of "sol – pure water" interface does not extend during the sedimentation. Therefore if the dispersion of settling rates should be possible, it is too small to be cause for effect described above.

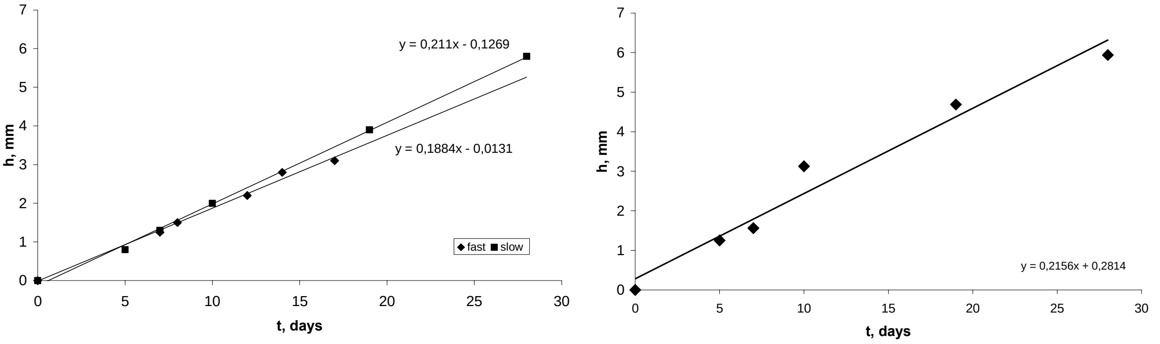

Fig.5. Time dependences of sediment thickness (at the left) and stratification (at the right); fast – free evaporation condition, slow – without evaporation condition

PMMA colloidal crystal saturation

To study a pattern of diffusant penetration, the different substances were used: organic liquids (glycerine, isobutyl alcohol) and colloidal silica (obtained from the sodium silicate by acid leaching). The results of imaging investigation show that the saturation process for bulk PMMA pellet is defined by uniform front of penetration except some cases of cracking and intrinsic inhomogeneities (fig.6).

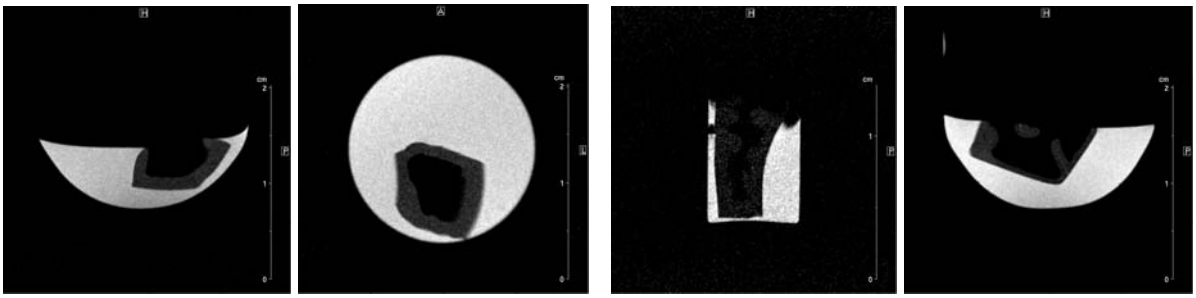

Fig.6. The saturation process of bulk PMMA (by the glycerine): uniform front of penetration (at the left), cracking and inhomogeneities (at the right); FOV 30 mm, 256x256 matrix, slice thickness 0.5 mm

Dynamic of glycerine and isobutyl alcohol penetration front to bulk PMMA pellet corresponds to $l \sim t^n$, where n=0.5-0.6 thereby one can conclude that dynamic corresponds to Fick diffusion laws. But the dynamic of the alkali silicate penetration front to bulk PMMA pellet corresponds to n=0.8-0.9 (fig.7). It may be caused by fact that the alkali silicate is a mixture.

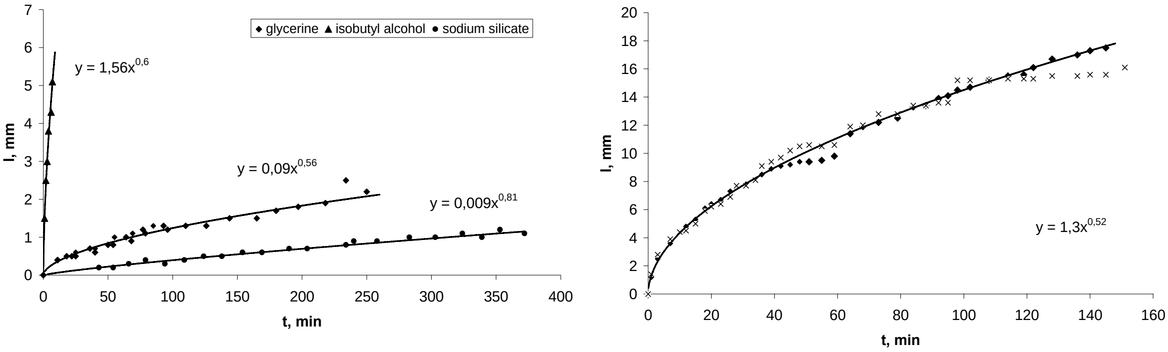

Fig.7. Dynamic of front penetration for bulk PMMA pellet (at the left) and for PMMA powder (at the right)

Dynamic of glycerine penetration front to PMMA unpressed powder corresponds to n=0.5 (fig.7,8). It allows us to conclude about prevalence of intragranular glycerine transport over the intergranular transport.

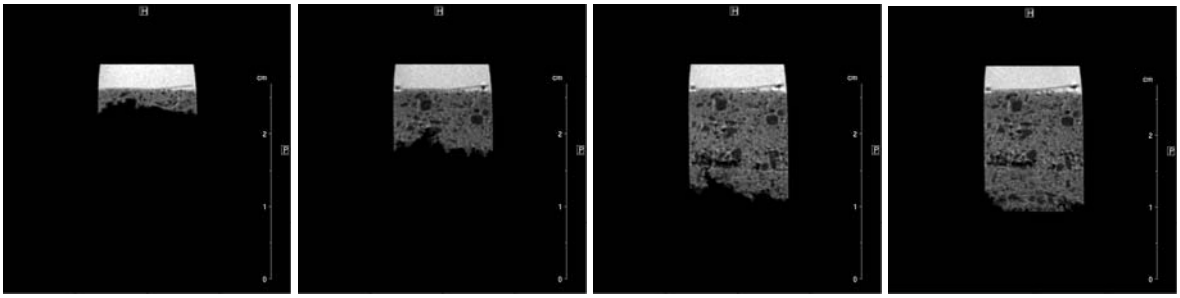

Fig.8. The saturation process of PMMA unpressed powder (by the glycerine); FOV 40 mm, 256x256 matrix, slice thickness 0.6 mm, images acquired after 5, 30, 100 and 150 min

Dynamic of colloidal silica penetration front to PMMA unpressed powder corresponds to n=0.5-0.6 but there are necessary to take into account the “age” of sol and the SiO_2 content. So the experimental results show that n is not affected by “age” of sol (n are almost equal for 20 min, 1,5h and 3h) but the diffusion rate drops dramatically as the time of gelling increases. Just the same, as the SiO_2 content increases the diffusion rate drops dramatically too but n is not changed. It allows us to match concentration of SiO_2 and sol “age” for sample to be penetrated without any cracking actually.

References

[1] Stapf S., Han Song-I. *NMR Imaging in Chemical Engineering*. John Wiley & Sons, p.560, 2006.

[2] Shabanova N.A., Sarkisov P.D. *The basis of nanodispersed silica sol-gel technology*. Akademkniga, 280 p, 2004. (*in Russian*)

[3] Gorelik V.S. Optical and dielectric properties of nanostructured photonic crystal doped by ferroelectrics and metals/ Fizika tverdogo tela, **51**, 2009. (*in Russian*)

[4] Schroden R., Balakrishan N. *«Inverse opal photonic crystals. A laboratory guide»*. University of Minnesota, p.32, 2001.

$2\Delta_0/k_BT_c$ ratio and temperature dependence of the superfluid density in overdoped $La_{2-x}Sr_xCuO_4$

M.V. Eremin, D.A. Sunyaev

Kazan (Volga region) Federal University, 420008, Russian Federation

e-mail: Mikhail.Eremin@ksu.ru, dasunr@rambler.ru

Introduction

Up to now there is no consensus about the nature of superconductivity in layered cuprates. In this context it is important to study the temperature dependencies of the superfluid density because this quantity is directly related to superconductivity. At the same time, its analysis requires preliminary information about the Fermi surface (band structure parameters), the symmetry and temperature dependence of the superconducting gap and a transparent description of the London penetration depth within tight binding approximation. At the moment all this information is available for $La_{2-x}Sr_xCuO_4$ superconductor and in what follows we analyze the temperature dependence of superfluid density and compare the results with available experimental data by Panagopoulos at al. [1]. Won and Maki [2] were first who pointed out that in case d-wave pairing the ratio $2\Delta_0/k_BT_c$ can be different from its standard BSC value 3.52. However their calculations were performed in week coupling approximation which in the strict sense is not appreciable for layered cuprates.

Our main result is that the temperature behavior of $1/\lambda_{ab}^2$ depends sensitively on the ratio $2\Delta_0/k_BT_c$ and we estimate this quantity for $La_{2-x}Sr_xCuO_4$ with for the doping concentration x= 0.20, x=0.22 and 0.24.

Calculations of superfluid density

The superconducting current density $\mathbf{j}_s$ is proportional to a vector potential $\mathbf{A}$ and written as (London's equation):

$$j_s = -\frac{c}{4\pi\lambda^2}A\,. \tag{1}$$

Here λ — is a so-called London's penetration depth of external magnetic field into a superconductor (magnetic penetration depth). This quantity is measured by various experimental techniques [1,3]. Obviously its temperature and doping dependencies contain important information about fundamental microscopic properties of a superconductor. The microscopic expression for superfluid density $n_s \propto 1/\lambda_{ab}^2$ for layered cuprates is discussed in detail in Ref. [4] (and Refs there in). It is written as follows:

$$\frac{1}{\lambda_x^2} = 4\pi\left(\frac{e}{c\hbar}\right)^2 \left\{ \sum_k \frac{\partial\varepsilon_k}{\partial k_x}\left[\frac{|\Delta_k|^2}{E_k^2}\frac{\partial\varepsilon_k}{\partial k_x} - \frac{(\varepsilon_k-\mu)}{2E_k^2}\frac{\partial|\Delta_k|^2}{\partial k_x}\right]\left[\frac{1}{E_k}-\frac{\partial}{\partial E_k}\right]\tanh\left(\frac{E_k}{2k_BT}\right)\right\}. \tag{2}$$

Here it is assumed that the magnetic field is applied along the x-axis in CuO_2-plane (ab). ε_k is the energy dispersion of quasiparticles in the normal state, μ is the chemical potential, $E_k = \sqrt{(\varepsilon_k-\mu)^2 + |\Delta_k|^2}$ — Bogolubov's quasiparticle energy in the superconducting state, Δ_k is the superconducting energy gap, which depends on the momentum and temperature. At the first glance, the expression (2) has to be averaged over all possible orientations of the sample with respect to the external field, because the Fermi surfaces of $La_{2-x}Sr_xCuO_4$ are not cylinders. However, it is easy to prove analytically, that in the case of a tetragonal symmetry the expression (2) yields the same result for *any* orientation of the external field in the *ab* plane. Therefore one can safely write $1/\lambda_x^2 = 1/\lambda_{ab}^2$.

Rich information is available about the energy dispersion of quasiparticles in the normal state of $La_{2-x}Sr_xCuO_4$ [5]. Angle-resolved photoemission spectra are well fitted by the tight binding energy dispersion of the following form:

$$\varepsilon_k = \mu - 2t_1\left(\cos k_x a + \cos k_y a\right) - 4t_2 \cos k_x a \cos k_y a - 2t_3\left(\cos 2k_x a + \cos 2k_y a\right). \qquad (3)$$

Parameters of the conduction band t_1, t_2 and t_3 correspond to the effective hopping integrals between first, second and third neighbors on a square sublattice of Cu sites in CuO_2 plane. For different doping index (*x*) they are different [5]. Because the nature of pseudogap phenomenon in uderdoped samples $La_{2-x}Sr_xCuO_4$ is not clear yet, we focus on the overdoped compounds only. Following the approximation adopted in Ref. [5] we also neglect the small orthorhombic distortions in $La_{2-x}Sr_xCuO_4$. In this case the superconducting gap function corresponds to the d-wave symmetry

$$\Delta_k = \frac{\Delta_0(T)}{2}(\cos k_x a - \cos k_y a)\,. \qquad (4)$$

The temperature dependence of $\Delta_0(T)$ was studied previously in the analyses of the NMR data (Knight shift and relaxation rate) in Ref. [6]. It was found that for the optimally doped $YBa_2Cu_3O_7$ and $Bi_2Sr_2CaCu_2O_8$ it can be approximated as:

$$\Delta_0(T) = \Delta_0 \tanh\left[1.75\left(\frac{T_c}{T} - 1\right)^{0.5}\right] \qquad (5)$$

The value of Δ_0 is considered as an independent fitting parameter for each doping index (*x*). The results of our calculations are summarized in fig.1 in comparison with the experimental data taken from Ref. [1]. The set of the hopping integrals and value of the chemical potential are given in Table 1.

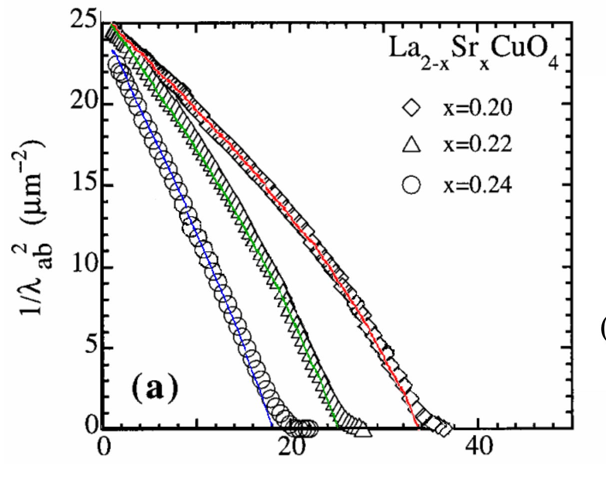

Fig.1. Temperature dependencies of superfluid densities in overdoped $La_{2-x}Sr_xCuO_4$. Symbols (rhomb, triangles and circles) – experimental data from Ref. [1], lines – our calculations using formula (2). The $2\Delta_0/k_BT_c$ ratios are: (6.1±0.1), (5.9±0.1) and (5.3±0.1), for x=0.20, x=0.22 and x=0.24, correspondently.

Table 1. Chemical potential and effective hopping integrals (in eV), based on ARPES data [5]

$La_{2-x}Sr_xCuO_4$	μ, eV	t_1, eV	t_2, eV	t_3, eV
x = 0.20	0.215	0.25	-0.034	0.017
x = 0.22	0.22	0.25	-0.325	0.0162
x = 0.24	0.227	0.25	-0.032	0.0159

It is important to stress that a curvature of the superfluid density versus temperature curve is quite sensitive to the ratio $2\Delta_0/k_BT_c$. This fact allows us to identify their values for each of the experimental curves.

Discussion.

The ratios for $2\Delta_0/k_BT_c$ obtained by us are in agreement with findings for this quantity from the experimental data. Indeed, according to angle-resolved photoemission [7] and scanning tunneling spectroscopy [8], the averaged value for optimally doped $La_{2-x}Sr_xCuO_4$ is about 5.5. However, the error bars are quite large which is perhaps related to quality of the surface. In particular, according to Ref. [9], the gap distribution in the overdoped $La_{2-x}Sr_xCuO_4$ with x = 0.22 studied by scanning tunneling spectroscopy is $2\Delta_0/k_BT_c = 5.5 \pm 2.5$. Uncertainly in our case is much smaller. Moreover our calculations have revealed an important trend in the evolution of this ratio. It gradually decreases with doping (in overdoped region). This trend can be interpreted as a weakening of the strong correlation effect in overdoped side of phase diagram for $La_{2-x}Sr_xCuO_4$. It is interesting to compare the ratio $2\Delta_0/k_BT_c$ extracted by us with those obtained from a solution of the BSC equation

$$\Delta_k = \frac{1}{N}\sum_k J(k-k')\frac{\Delta_{k'}}{2E_{k'}}\tanh\left(\frac{E_{k'}}{2k_BT}\right). \tag{6}$$

Here $J(q) = 2J(\cos q_x a + \cos q_y a)$ is a Fourier transform of the short-range pairing potential, which included all possible interactions between nearest neighbors in CuO_2 plane (For example superexchange, screened Coulomb repulsion and phonon mediated interaction). The solutions of equation (6) are presented in Table 2.

Table 2. Solutions of equation (6) for short range interaction

$La_{2-x}Sr_xCuO_4$	T_c, K	J, meV	$2\Delta_0/k_BT_c$
x = 0.20	Tc = 34	J = 85	4.02±0.01
x = 0.22	Tc = 25	J = 91	4.21±0.01
x = 0.24	Tc = 18	J = 93.7	4.36±0.01

Note that the momentum and temperature dependencies fairly well correspond to Eqs. (4)-(5).

The analysis of the temperature dependencies of the superfluid density $n_s \propto 1/\lambda_{ab}^2$ in $YBa_2Cu_3O_{6+x}$ and single layer tetragonal compound $Tl_2Ba_2CuO_{6+\delta}$ (T_c = 78 K), performed in ref. [4], showed that in the overdoped compound $Tl_2Ba_2CuO_{6+\delta}$ (T_c = 78 K) the ratio $2\Delta_0/k_BT_c$ decreases with respect to that of an optimally doped $YBa_2Cu_3O_{6+x}$ (T_c = 92 K). In present paper we have found the same trend for overdoped $La_{2-x}Sr_xCuO_4$. This fact seems to reflect a quite general property of layered cuprates

This conclusion is also supported by the fact that the temperature dependence of the superconducting energy gap (5) in overdoped $La_{2-x}Sr_xCuO_4$ is described fairly well by equation (6).

Conclusion

In summary, we have analyzed the temperature dependence of the superfluid density in overdoped $La_{2-x}Sr_xCuO_4$. Our calculations have revealed important trend of changes the ratio $2\Delta_0/k_BT_c$. It gradually decreases with doping in overdoped region. The temperature dependence of the energy gap is fairly well described by simple BCS equation with short range pairing potential yielding a d-wave symmetry of the superconducting gap.

We thank Josef Roos, and Ilya Eremin for discussions. This work was supported in part by the Russian Foundation for Basic Research, Grant # 09-02-00777-a and Swiss National Science Foundation, Grant IZ73Z0 128242.

References

[1] B.D. Rainford, J.R. Cooper, W.Lo, J.L. Tallon, J.W. Loram, J. Betouras, Y.S. Wang and C.W. Chu, "Effects of carrier concentration on the superfluid density of high-T_c cuprates", Phys. Rev. B, Vol. 60, No. 21, December 1999, pp. 14617-14620.

[2] H. Won and K. Maki, *d*-wave superconductor as a model of high-T_c superconductors, Phys. Rev. B., Vol. 49, No. 2, January 1994, pp. 1397-1402

[3] J. Hofer, K. Conder, T. Sasagawa, Guo-meng Zhao, M. Willemin, H. Keller, and K. Kishio, "Oxygen-Isotope Effect on the In-Plane Penetration Depth in Underdoped $La_{2-x}Sr_xCuO_4$ Single Crystals", Phys. Rev. Lett., Vol. 84, No. 18, May 2000, pp. 4192-4195.

[4] M.V. Eremin, I.A. Larionov, and I.E. Lyubin, "London penetration depth in the tight binding approximation: orthorhombic distortion and oxygen isotope effects in cuprates", J. Phys. Condens. Matter, Vol. 22, No. 18, April 2010, pp. 185704-185709.

[5] T. Yoshida, X.J. Zhou, K.Tanaka, W.L. Yang, Z. Hussain, Z.-X. Shen, A. Fujimori, S. Sahrakorpi, M. Lindroos, R.S. Markiewicz, A. Bansil, Seiki Komiya, Yoichi Ando, H. Eisaki, T. Kakeshita, and S. Uchida "Systematic doping evolution of the underlying Fermi surface of $La_{2-x}Sr_xCuO_4$", Phys. Rev. B, Vol. 74, No. 22, December 2006, pp. 224510-1–224510-5.

[6] T. Mayer, M. Eremin, I. Eremin and P.F. Meier, "Spin dynamics of itinerant holes in HTSC cuprates: the singlet-correlated band model and its applications", J. Phys.: Condens. Matter, Vol. 19, No.11, March 2007, 116209 (18pp)

[7] Andrea Damascelli, Zahid Hussain, Zhi-Xun Shen, "Angle-resolved photoemission studies of the cuprate superconductors". Rev. Mod. Phys., Vol. 75, No. 2, April 2003, pp. 473-541.

[8] Øystein Fischer, Martin Kugler, Ivan Maggio-Aprile, and Christophe Berthod, Christoph Renner "Scanning tunneling spectroscopy of high-temperature superconductors", Rev. Mod. Phys., Vol. 79, No. 1, March 2007, pp. 353-419.

[9] T. Kato, T. Noguchi, R. Saito, T. Machida, H. Sakata. "Gap distribution in overdoped $La_{2-x}Sr_xCuO_4$ observed by scanning tunneling spectroscopy". Physica C Vol. 460–462, March 2007, pp. 880-881.

Synthesis and EPR study of liquid crystalline iron(III) complexes on the bases of 4,4’-dodecyloxybenzoiloxybenzoil-4-salicyliden-n’-ethyl-n-ethylenediamine

M.S. Gruzdev[1], N.E. Domracheva[2], U.V. Chervonova[1], A.M. Kolker[1]

[1]Institute of Solution Chemistry of the Russian Academy of Sciences, 153045, Akademicheskay 1, Ivanovo, Russian Federation.

[2]Zavoisky Physical-Technical Institute of the Kazan Scientific Center of the Russian Academy of Sciences, 420029, Sibirsky Tract 10/7, Kazan, Russian Federation.

e-mail: *gms@isc-ras.ru*

Currently metallocomplexes surrounded by dendrimer ligands have attracted considerable interest of scientists [1]. Such compounds have found applications by catalytically active and useful as redox sensors [2]. These materials may find applications as components in molecular electronics and photochemical molecular devices for solar energy conversion and information storage [3]. Reports about preparation and investigation of complexes containing iron(III)-ions and azometine ligands have particular interest [4, 5]. One of the most important characteristics of these compounds is that even a small modifications of the structure can significantly change a key properties of complexes, namely, can lead to high-spin (S = 5/2) or low-spin (S = 1/2) states on Fe(III) and also spin-crossover behavior [6].

The liquid-crystalline iron(III) complexes based on asymmetric tridentate azometine ligand such as 4,4’-dodecyloxybenzoiloxybenzoil-4-salicyliden-N’-ethyl-N-ethylenediamine with four counter-ions NO_3^-, PF_6^-, Cl^-, BF_4^- named as **I**, **II**, **III**, **IV** according to their counterions, respectively, were synthesized and studied [7].

Characterization of the compounds

The analysis of near infrared spectra of complexes (**I-IV**) shows the presence of Schiff base formed by N-ethylethylenediamine. The bands at 5850-5839 and 5709-5703 cm^{-1} are corresponded to tertiary and secondary amine respectively [8]. In range 3800-2600 cm^{-1} the bands of stretching vibrations of $-CH_2-$ (2921-2851 см$^{-1}$) are predominated. The intensity of bands of protons of aromatic rings ($\nu_{H\text{-}Ph}$ 3071 cm^{-1}) is smaller then bands of stretching vibrations $-CH_2-$. The interaction with proton of cation are observed to complexes which contain strong electronegative anions PF_6^- and BF_4^- in external coordination sphere and it leads to formation hydrogen band expressed by relatively medium broad absorption band at 3179 cm^{-1}. Forming of ligand occurs in the course of reaction between aldehyde and amides in solution, and it confirmed by strong absorption band at 1639 cm^{-1} which is characteristic to bond of (HC=N) [9] situating near absorption band of (C=O), 1738-1734 cm^{-1} [10]. Also in FT-IR spectrum one can see absorption bands of counter-ions: nitrate (1383 cm^{-1} (**I**)), hexafluorophosphate (844, 556 cm^{-1} (**II**)), chloride (543, 215 cm^{-1} (**III**)) and tetrafluoroborate (1032, 534, 522 cm^{-1} (**IV**)) [10, 11]. The presence of coordinated iron(III)-ion is well registered by far FT-IR spectra. In all spectra the absorption bands of iron(III) at 511 (stretching vibrations of Fe-N), 471 (vibrations of iron-ion), 420 (stretching vibrations of Fe-O bond), 323 and 279 cm^{-1} (vibrations of M-anion bond) [12] are observed. The presence of vibrations of metal–counter-ion coordination bond was published in few papers [12, 13].

The stability of the complexes and the amount of iron were determined by mass-spectrometry (MALDI-ToF-MS). The azometine with molecular weight is ~618 is detected in all mass-spectra of complexes. As the presence of iron-ion in coordination sphere of complex was established, the calculation of molecular weight increasing at the expense of iron and counter-ions addition was carried out. The results of mass-spectrometry are agreed with data of elemental analysis. It was found that reaction of iron salts with asymmetric tridentate ligand leads to complexation with the ratio of iron-ion to ligand as 1:1 [14].

The molecular structure of complexes **I**, **III** and **IV** is built up by mono(tridentate) ligand (L), water molecule and two counter anions [Fe(L)X_2(H_2O)], where X = NO_3^-, Cl^-, BF_4^-. An exceptional case among the compounds investigated present Fe (III) complex with PF_6^- counter-ion. The compound **II** is a monocationic mono(ligand) complex, $[Fe(L)X(H_2O)_2]^+X^-$, where the iron(III) ion has an octahedral configuration formed by three ligator (ONN) atoms of tridentate ligand, by one counter-ion and two water molecules (see Scheme 1).

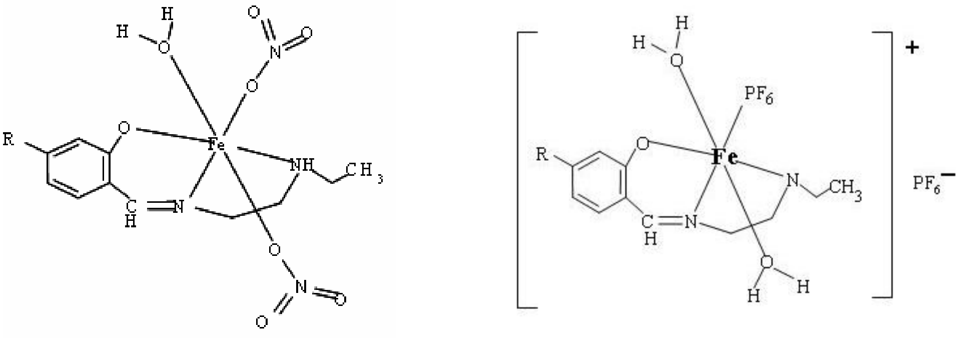

EPR results

EPR demonstrates that each of the complexes studied consists of two types of iron centers: low-spin (LS, S = 1/2) and high-spin (HS, S = 5/2). The alignment of LS complex **II** in the anisotropic solvent (the nematic liquid crystal N-8) allowed us to obtain information about correlation the magnetic (principal) g- axes with respect to the molecular symmetry axes. Analysis of the dependence of the EPR line intensity of LS centers on the angle ξ (between the director $\boldsymbol{n}$ and the external magnetic field) shows that the principal axes of the g-tensor and the molecular axes coincide in complex **II**; the long molecular y axis orients along the director $\boldsymbol{n}$ and the degree of orientation this axis is $S_y = 0.71$. The knowledge of the crystal structure for the analogous non liquid-crystalline complex allows us to establish that the long molecular y axis of LS complex **II** lies in (ONN) coordination plane and its direction is determined by the elongated alkyl tails; two water molecules of LS complex **II** occupy *trans* positions to the coordination (ONN) plane; one PF_6^- counter-ion is ionic bound to Fe(III) ion and occupies the fourth position in this plane, whereas the other PF_6^- counter-ion lies in the second coordination shell.

Using the existing g-tensor theory of low-spin d^5 configuration in the octahedral crystal field having axial (tetragonal, Δ/λ) and rhombic (V/λ) distortions, the ground-state wave function parameters (A, B, C), orbital reduction factors (k), and energy level splitting ($\Delta E_{12}/\lambda$, $\Delta E_{13}/\lambda$) were calculated from the experimental g-tensors (see Table I, where λ is the one-electron spin-orbit coupling constant). Table I shows that the value of parameter B for LS complexes **I**, **III** and **II** (in N-8 and of the first-type) is very large which indicates that the unpaired electron resides in the d_{xy} orbital, and $(d_{xz},d_{yz})^4(d_{xy})^1$ state is the ground.

The unusual behavior was observed for monocationic Fe(III) complex **II**. The EPR intensities of both LS and HS centers of that complex obtained by numerical double integration exhibit a significant temperature dependence with a maximum at about T_N = 7 K. Above T_N the EPR integrated intensities follow a Curie-Weiss law with a Curie-Weiss constant θ_1 = -14.1 K and θ_2 = -15.1 K for LS and HS centers, respectively. If we normalize the integrated intensity of each molecule fraction to the unit and superpose these curves together, we can see a completely identical magnetic behavior of LS and HS centers. This identity shows clearly that LS and HS iron(III) ions of complex **II** are coupled together and form a dimer structure, where PF_6^- counter-ion and water molecules play the role of bridging units.

Table I.

Complex	g_x	g_y	g_z	A	B	C	k	Δ/λ	V/λ	$\Delta E_{12}/\lambda$	$\Delta E_{13}/\lambda$
II (of the first-type)	-2.215	-2.215	1.935	0.1007	0.9939	0	0.848	2.677	0.007	7.662	8.597
II (of the second-type)	1.975	-1.98	-2.165	0.7436	0.0005	0.6657	0.793	-5.506	1.489	8.984	21.056
II (in N-8)	-2.209	-2.228	1.945	0.089	0.9951	0.003	0.954	2.866	0.107	8.123	9.259
I	-2.22	-2.23	1.948	0.0925	0.9954	0.0017	0.935	2.817	0.062	8.042	9.049
III	-2.225	-2.23	1.935	0.0936	0.9938	0.0008	0.9646	2.7989	0.0331	8.012	8.971

Another interesting feature of complex **II** is the appearance of the second-type LS centers which is characterized by the magnetic parameters: $g_X = 1.975$, $g_Y = 1.98$ and $g_Z = 2.165$. This new type of LS centers is best of all observed in the liquid crystalline phase at high (387 – 405 K) temperature. EPR spectra simulation allows us to separate both types of LS signals and to trace the dynamics of changing the number of the second-type LS centers (n_2) relative to the first one (n_1) with temperature increase. The temperature dependence of increasing the number of the second-type LS centers (n_2) relative to the first one (n_1) can be characterized by equilibrium constant K and is described by equation $\ln K = \ln\left(\frac{n_2}{n_1}\right) = -\frac{\Delta H}{RT} + \frac{\Delta S}{R}$. The enthalpy ($\Delta H$) and entropy ($\Delta S$) of such dynamic process $\Delta H = 27.9$ kJ/mol and $\Delta S = 0.086$ kJ/mol are calculated from the straight line given by plotting ln K from the reverse T. The obtained enthalpy value is close to the activation energy Ea = 28.8 kJ/mol found for reorientation motion of PF_6^- anion.

The found parameters A, B, C for the second-type LS complex **II** show clearly that the situation is cardinally changed and the unpaired electron is localized now in ($d_{xz} \pm d_{yz}$) orbitals, thus $(d_{xy})^2(d_{xz},d_{yz})^3$ ground state is stabilized. It is interesting to note that the observed effect (changing of the ground state for LS complex **II**) is reversible with temperature.

The results of the observed dynamic process allow us to suppose that the revealed conversion of electron $(d_{xz},d_{yz})^4(d_{xy})^1/(d_{xy})^2(d_{xz},d_{yz})^3$ configurations is caused by reorientation of one coordinated PF_6^- anion from equatorial (ONN) planar position to the axial one that was before occupied by water (see Scheme 2)

The Moessbauer data confirm also the existence of such an effect on the basis calculation of the values of quadrupole splitting for electron $(d_{xz},d_{yz})^4(d_{xy})^1$ and $(d_{xy})^2(d_{xz},d_{yz})^3$ configurations.

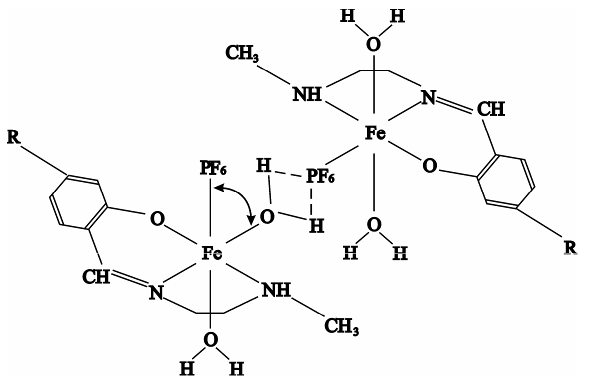

Acknowledgment

This research was supported by grant the President of the Russian Federation, № MK-1625.2009.3. The authors wish to thank Dr. Gorbunova Yu. G. (IGIC RAS) for MALDI-ToF-MS experiment.

References

[1] Wei-Shi Li and Takuzo Aida, *Chem. Rev.*, 2009, **109**, 6047-6076.

[2] C. Valerio, J. Fillaut, J.Ruiz, J.Guittard, J. C. Blais, and D. Astruc, *J. Am. Chem. Soc.*, 1997, **119**, 2588.

[3] J.-F. Létard, P. Guionneau and L. Goux-Capes *Towards Spin Crossover Applications // Top. Curr. Chem.*, 2004, Vol. 235, Springer-Verlag, Berlin, Heidelberg, New York, P. 221-249.

[4] V. M. Leovac, V. S. Jevtović, L. S. Jovanović and G. A. Bogdanović, *J. Serb. Chem. Soc.*, 2005, **70**, N. 3, 393-422.

[5] P. Sonar, C. M. Grunert, Y.-L. Wei, J. Kusz, P. Gütlich and A. D. Schlüter, *Eur. J. Inorg. Chem.*, 2008, 1613-1622.

[6] P. J. van Koningsbruggen, Y. Maeda, H. Oshio *Iron(III) Spin Crossover Compounds // Top. Curr. Chem.*, 2004, Vol. 233, Springer-Verlag, Berlin, Heidelberg, New York, P. 259-324.

[7] U. V. Chervonova, M. S. Gruzdev, A. M. Kolker, N. G. Manin, N. E. Domracheva, *Rus. J. Gen. Chem.*, 2010, in press.

[8] I. A. Vechkasov, N. A. Kruchinin, V. A. Polyakov, V. F. Rezinkin *Devices and methods of analysis in near-infrared range,* Ximia, Moscow, 1977, p. 280.

[9] E. Pretsch, P. Bühlmann, C. Affolter *Structure Determination of Organic Compounds. Tables of Spectral Data*, Springer-Verlag, Berlin, Heidelberg, New York. 2000. p. 406.

[10] L. A. Kazitsina, N. B. Kupletskaya *Application of UV, IR, and NMR spectroscopy in organic chemistry*, Vishaya schola, Moscow, 1971. p. 264.

[11] K. Nakanishi *Infrared spectra and structure of organic compounds*, Mir, Moscow, 1965, p. 216.

[12] K. Nakamoto *Infrared and Raman spectra of inorganic and coordination compounds*, Mir, Moscow, 1991, p. 509.

[13] A. Finch, P. N. Gates, K. Radcliffe, F. N. Dickson, F. F. Bentley *Chemical applications of far infrared spectroscopy,* Mir, Moscow, 1973, p. 285.

[14] M. S. Gruzdev, U. V. Chervonova, A. M. Kolker, N. E. Domracheva, *Rus. J. Str. Chem.*, 2011, in press.

The magnetic properties study of nanostructures with Fe_3O_4 by ferromagnetic resonance

A. Zyubin, A. Orlova, A.Goikhman, G.Kupriyanova and V. Nevolin

Immanuel Kant State University of Russia, 236041, A.Nevskogo 14, Kaliningrad, Russia

e-mail: azubin@mail.ru

Introduction

One of the important problems today is a development of new materials and combinations for applications in field of spintronics. The perspective material for such tasks is magnetite. It has a high Curie temperature (T_C) of 858 K [1], relatively high (~100-400 Oe) coercivity [2]. The band structure calculations predict the electron conductivity with a full (-100%) spin polarization arising from the negative electron spin polarization at Fermi level. These facts made magnetite a very interesting candidate for applications as ferromagnetic layer in spintronic devices such as magnetic tunnel junctions (MTJs) and magnetoresistive sensors. At the same time, the epitaxial thin films of Fe_3O_4 grown on different substrates, such as MgO(100), MgO(110), a-Al_2O_3(0001) , $MgAl_2O_4$ and $SrTiO_3$ have shown unexpected magnetic properties independently the substrate material [3]. In most structures for magnetite it's impossible to reach the saturation magnetization by fields up to 70 kOe, which negatively affect on the quality of magnetic tunnel junction, based on Fe_3O_4. Such behavior has been attributed to the antiphase boundaries arising in sample with inverse spinel structure. Furthermore, experimental investigation of magnetotransport properties of polycrystalline magnetite thin films at room temperature has show magnetoresistance values up to −2.4% at the maximum applied field of 1.1 T and, thus explanantion of magnetotransport properties of the Fe_3O_4 films could be given by inter-granular tunnelling of the spin-polarized electrons. The spin polarization was obtained only to be around −16% [4]. The most spin polarization (-80%) have been observed only in epitaxial magnetite film [5].

To improve its magnetic and transport properties it was suggested to use different magnetic buffer layers at the formation process of magnetite thin films, e.g. Fe and Cr. Results of investigation and characterization of *epitaxial* structures formed on single crystal substrate MgO were observed by Magen et al. [6]. In this work we report FMR study of the magnetic properties of the Fe_3O_4 and Fe/Fe_3O_4 systems realized in a *polycrystalline* bilayer and 3-layer structures to assess their applicability in a functional magnetic tunnel junction.

Experimental details

Thin film polycrystalline Fe_3O_4 and Fe-Fe_3O_4 samples were made by the pulsed laser deposition (PLD) technique at room temperature in ultrahigh vacuum ($P = 10^{-7}$ Pa) in one vacuum cycle with the following vacuum annealing up to temperatures T=500 ^oC [7]. Ferromagnetic resonance spectra of the films were taken using Radiopan electron spin resonance spectrometer operating at the X-band frequency 9.5 GHz and the modulation frequency 100 kHz. The first field derivative of the microwave power absorption was registered as a function of applied steady magnetic field at the room temperature. The samples were mounted on the side of a special holder passing through the center of the TE_{102} microwave cavity. The orientation of film was controlled by two axial goniometer with accuracy by 0.5^0. The in plane and out-of -plane dependences of FMR spectra and linewidths have been measured for all samples. The extracted magnetic parameters such as the effective magnetization, magnetic anisotropy and linewidths were studied.

Results

FMR signals were analyzed at different samples orientation relatively to the external static magnetic field. Angle θ between the normal to the sample surface and the magnetic field was varied from 0 to 360 degrees. The experimental results are presented at the table 1 and fig.1-3.

Table 1. Samples structure, with Hc, Ms and FMR line width ΔB, Bres values. In brackets the values thicknesses in (A) are given

#	Sample structure, synthesized on Si/SiO_2	$H_{c,}$ Oe	M_s emu/cm^3	ΔB, mT	B res
1	Fe (30)/Fe3Si(180)/SiO2(20) **(2640)**	20	775	6,7	112,1
2	Fe_3O_4(450)/Fe(120) (**2706**)	1000	70	18	336
3	Fe (60)/Fe_3O_4(150) **(2672)**	165	750	31,9	92,1
4	Fe(30)/Fe_3Si(150)/SiO_2(20)/Fe_30_4(120) /Fe (40)/ Pt(620) **(2669)**	15	1029	11,9	74
				6,7	126,7
5	Fe_3Si(190)/SiO2/Fe(60)/Fe_3O_4(160) **(2673)**	60	683	9,9	85,5
				16,2	125,1
6	Fe(40)Fe_3O_4(100)/MgO(30)/Fe_3Si(130 **(2642)**	850	1400	28	90
				12	132

The FMR research of Si/SiO_2/Fe_3O_4/Fe and Si/SiO2/Fe/Fe_3O_4 structures (sample #2 in Tab.1) showed that the spectrum parameters depends on sequence of layers. Two signals were observed for Si/SiO_2/Fe_3O_4/Fe: the narrow high intense signal in area B_{res} = 336mT with the line width ΔB=18мT, which doesn't depend on the sample orientation, and the wide weak signal with the intense lower by one order of magnitude, with resonance field and line width depends on the θ angle. Such signal behavior points at the presence of two magnetic phases in this sample: the dominating paramagnetic and the weak ferromagnetic ones. These ferromagnetic resonances data for Fe_3O_4/Fe sample is in an agreement with the VSM measurements. The high coercive force Hc~ 1000 Oe and weak unsaturated loop with unsatisfactory form with values of magnetization Ms~70 emu/cm^3 was registered.

For the sample (table 1, sample# 3) with reverse sequence of layers Si/SiO_2//Fe/Fe_3O_4 two close ferromagnetic signals are observed, the position and line widths of which depend on the sample orientation. Dramatically changes in the magnetic state of the sample with an iron bottom sublayer are confirmed by the significantly hysteresis loop (HL) changes. We obtained high values of magnetization Ms~750 emu/cm^3 at coercive force Hc~ 165 Oe (Table 1), and HL is saturated and its form is very close to rectangle.[7]. It was suggested to use Fe/Fe_3O_4 as a magnetic shifting layers for magnetic tunneling junctions.

Fig.1 shows FMR spectra (a) and linewidth (b) for $FeFe_3Si$/SiO_2 structure (sample #1 (Tab. 1). The $FeFe_3Si$ layer is interested as may be used as the second electrode in magnetic tunneling junctions. One intensive signal is observed at resonance field B_{res} = 112,1mT with the line narrow width ΔB=6,7mT . The resonance field and line width of signal depends on the θ angle.

FMR spectra for multilayer structures with the different arrangement of layers consist of two signals. The relationship between intensities of line, line widths and its resonance fields depend of arrangement of layers. Fig.2 shows FMR spectra (a) and linewidths (b) for different rotation angle to the external static magnetic field for Fe/Fe_3Si/SiO_2/Fe_3O_4/Fe/Pt. Two signals were observed: the high intense signal at B_{res} = 74mT with the line width ΔB=11,9mT, and medium intense signal at B_{res} = 126,1mT with ΔB=6,7mT.

Fig.3 shows FMR spectra (fig.3a) and hysteresis loop (fig.3b) for FeFe_3O_4/MgO/Fe_3Si. Two signals which depends on the θ angle too were observed. Sample #6 was made with using of MgO interface and have higher coercitivity than SiO_2 created samples. The resent experimental showed that the separate magnetization reversal is possible in this sample (fig.3b).

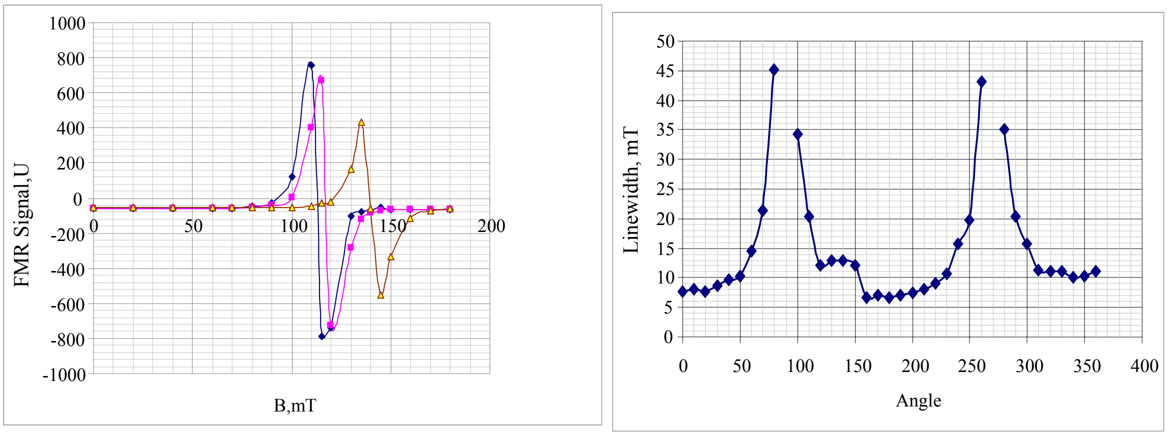

a b

Fig.1. FMR spectra (a): ◆ for 0 degrees, ■ for 20 degrees, ▲ for 40 degrees and linewidth (b) for sample #2 (Tab. 1) Fe/Fe3Si/SiO2 for different rotation angle to the external static magnetic field.

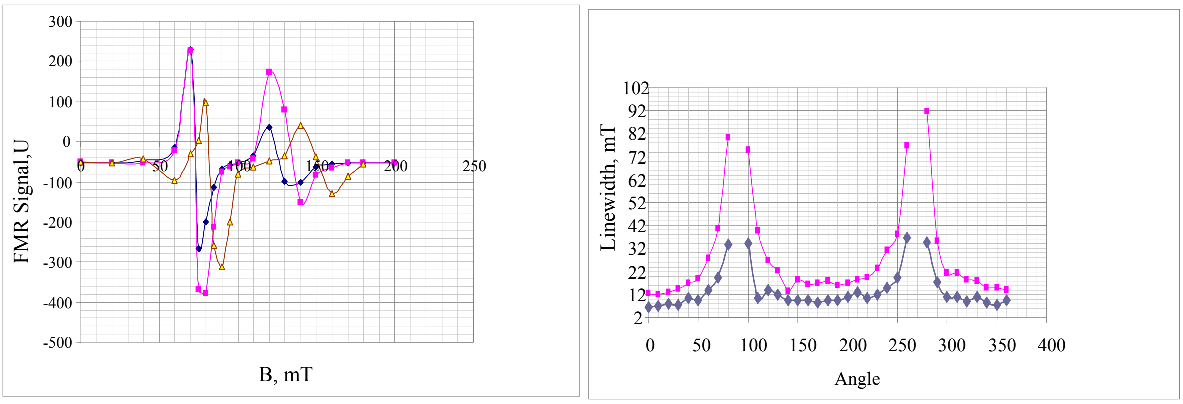

a b

Fig.2. FMR spectra (a): ◆ for 0 degrees, ■ for 20 degrees, ▲ for 40 degrees and linewidth (b) for sample #4 from Table 1 Fe/Fe3Si/SiO2/Fe_3O_4Fe/ Pt for different rotation angle to the external static magnetic field.

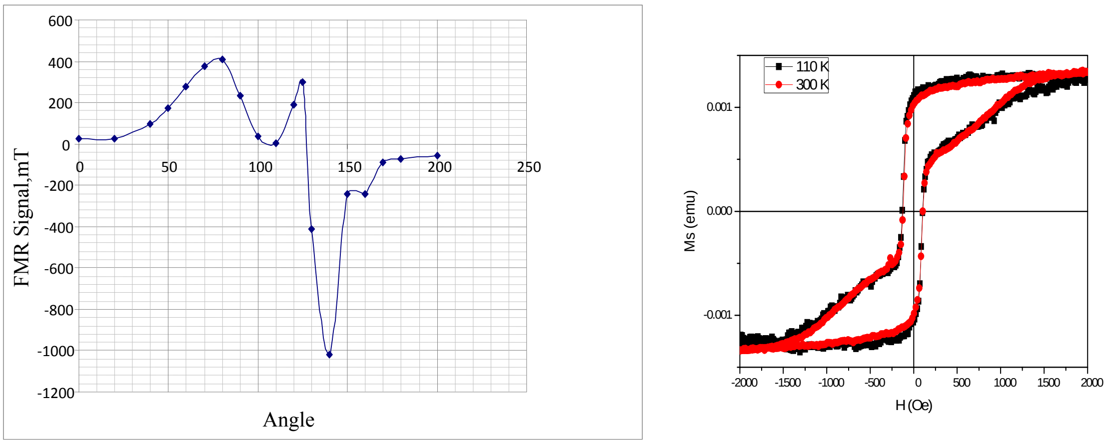

a b

Fig.3. FMR spectra (a) and hysteresis loop (b) for Fe/Fe_3O_4/MgO/Fe_3Si .

Summary

In this work the experimental study of magnetic properties of the Fe/Fe_3O_4 , Fe_3O_4 /Fe and Fe/Fe_3O_4/MgO/Fe_3Si systems realized in a polycrystalline structures was made by ferromagnetic resonance (FMR) technique. The investigations of magnetic properties of different bilayer structures, grown up on Si/SiO_2 substrate, and acquiring different sequence of layers: Fe/Fe_3O_4 and Fe_3O_4/Fe, by FMR, were done. The analysis showed that parameters of FMR spectra of multilayer structure are very sensitively to the arrangement of layers and nature of the interface. Such systems are interesting because recent investigations shows that form of the hysteresis loop become more rectangular and become saturated lower magnetic fields, but in three-layer structure Fe/Fe_3O_4/MgO/Fe_3Si (sample #5 in Table 1) we have independent switching between electrodes.

The present work was performed within the frames of the State contract No. 02.740.11.0550 and No. P148 dated from April 15th, 2010.

References

[1] M.L. Glasser and F.J. Milford, Phys. Rev. 130, 1783 (1963)

[2] M.L. Parames, J. Mariano, Z. Viskadourakis, N. Popovici, M.S. Rogalski, J. Giapintzakis, O. Conde, App. Surf. Sci 252 4610 (2006)

[3] D.T. Margulies, F.T. Parker, F.E. Spada, R.S. Goldmann, J. Li, R. Sinclair, A.E. Berkowitz, Phys. Rev. B 53 (1996)

[4] R Mantovan, A Lamperti, M Georgieva, G Tallarida and M Fanciulli. J. Phys. D: Appl. Phys. **43** (2010)

[5] Fonin M, Dedkov Yu S, Pentcheva R, R¨udiger U and G¨untherodt G (2007) *J. Phys.: Condens. Matter* **19**

[6] C. Magen, E. Snoeck, U.Luders, J. F. Bobo: Effect of metallic buffer layers on the antiphase boundary density of epitaxial Fe3O4 // J. of Appl. Phys. 104, 013913, (2008).

[7] A.Goikhman, G. Kupriyanova, E. Prokhorenko, A, Chernenkov, Vestnik I. Kant SU, vol 4 (2010).

Time-Resolved EPR Spectra of Photoexcited Copper Porphyrin

V.S. Iyudin[1], Yu.E. Kandrashkin[1], V.K. Voronkova[1], V.S. Tyurin[2], E.N. Kirichenko[2]

[1]Institution of the Russian Academy of Sciences Kazan E.K. Zavoisky Physical-Technical Institute, Kazan Scientific Center, Russian Academy of Sciences, 420029, Sibirsky tract, 10/7, Kazan, Russian Federation

[2]A.N. Frumkin Institute of Physical Chemistry and Electrochemistry, 119991, Leninskiy prosp. 31, Moscow, Russian Federation

e-mail: vasilius@yandex.ru

Time-resolved electron paramagnetic resonance (TREPR) is a powerful tool to study the spin involved processes initiated by the light irradiation. Most of the TREPR experiments carried out on the diamagnetic molecules which generate the excited singlet states after the laser flash. The following intersystem crossing populates the relatively long-lived triplet states of the molecules the EPR spectra of which are observed in the experiment. The light-induced processes are non-adiabatic and the spin states are strongly polarized. The spin polarization mechanisms of such systems are well-established [1].

Recently, the study of polarization states, arising from the interaction of such systems with other paramagnetic centers has become intense. These systems consist of one or more unpaired electrons in the ground state, which affect on the photophysical properties of the excited states of the chromophore [2-4]. The typical chromophores used for these experiments include porphyrins, anthracenes, fullerenes and some other organic molecules. In general, there are two types of paramagnetic centers, the stable radicals attached to the chromophore and the paramagnetic ions (Cu, V). An important class of the systems is porphyrin-based molecules, which are intensively utilized by living organisms due to unique redox potential. The photophysical properties of the porphyrins and the metallporphyrins were studied intensively during the decades, see for example [5]. The metallporphyrins attract increased interest during the last years because of the perspectives they open in constructing of nanoscale devices and nanostructured materials. The spin-involved interactions in metallporphyrins can be also important in the field of molecular-based magnetism and the study of the photoexcited states of such molecules can provide information about the intramolecular processes.

In spite of long-standing interest to photo-induced processes of paramagnetic metallporphyrins there are only few studies of the spin-involved properties by TREPR in these systems [6]. The enchanced spin polarization of the ground state of several copper porphyrins was demonstrated in the work [7]. The first spin-polarized TREPR spectra of the excited states of a paramagnetic metallporphyrin was reported for vanadyl octaethylpophyrin [8]. We report here the results of the TREPR study of copper 5,10,15,20-tetrakis(3-pyridyl)porphyrin (3PyNCu). Our results show spin-polarized signal from both, the ground doublet and the light excited quartet states.

The copper porphyrin can be considered as a complex consisting of ion Cu^{2+} ($3d^9$, S=1/2) which is ligated to four pyrrole nitrogens (fig.1). It has a doublet ground state due to unpaired electron located in the $d_{x^2-y^2}$ orbital. The photoexcitation at 542 nm affects on the prophyrin ring and forms the excited singlet state $^1(\pi,\pi^*)$ which can be transformed to the low-lying triplet state $^3(\pi,\pi^*)$. The interaction of the unpaired electron in the outer $d_{x^2-y^2}$ orbital of copper with π electrons of the conjugated porphyrin macrocycle determines the structure of the low-lying excited states. The ground and single excited $^1(\pi,\pi^*)$ states become sing-doublets $^2S_0$ and $^2S_1$, respectively, whereas the excited triplet state $^3(\pi,\pi^*)$ is split into trip-doublet $^2T_1(\pi,\pi^*)$ and trip-quartet $^4T_1(\pi,\pi^*)$. Here we follow the terminology of Gouterman [9] referring the doublet and quartet states to overall spin multiplicities and the terms "sing" and "trip" to the configuration of the π-electrons of the porphyrin macrocycle.

The experimental results presented in fig.1 propose the presence of two or more polarization contributions. The essential difference between rise and decay times of these two contributions indicates on the mutual independence of their nature. Therefore, we believe that these two patterns belong to different electronic states.

To analyze the net contribution we performed extra experiments. Fig.2 demonstrates the results obtained by several magnetic resonance methods. The fig.2a shows the ground-state spectrum measured using field modulation, which has been numerically integrated. Fig.2b shows echo-detected spectrum of the ground state of the system. And fig.2c represents spin-polarized TREPR spectrum of 3PyNCu. The comparison of the early TREPR spectrum with the data obtained by other resonance methods pointed that it should belong to the ground state of the copper porphyrin.

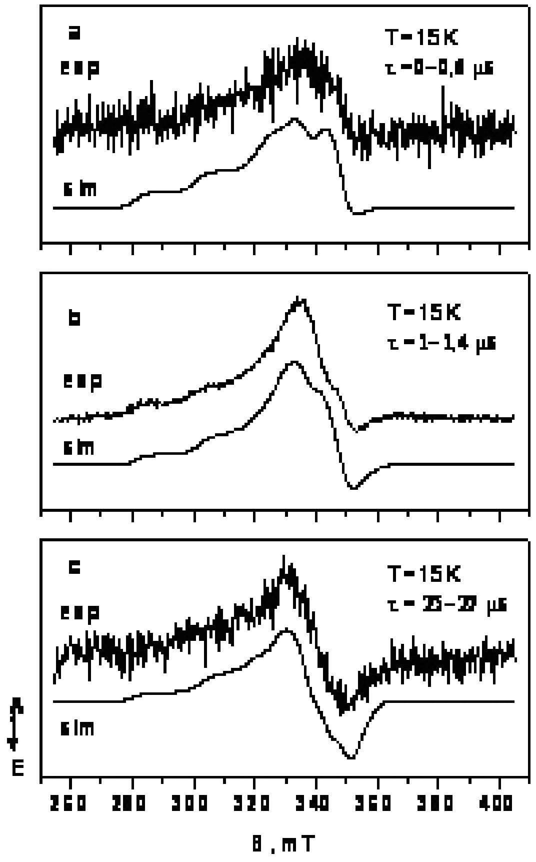

Fig.1 Time-resolved EPR spectra of 3PyNCu integrated in the intervals 0-0.6 μs (a), 1-1,4 μs (b) and 25-27 μs (c) with the simulations computed as described in the text.

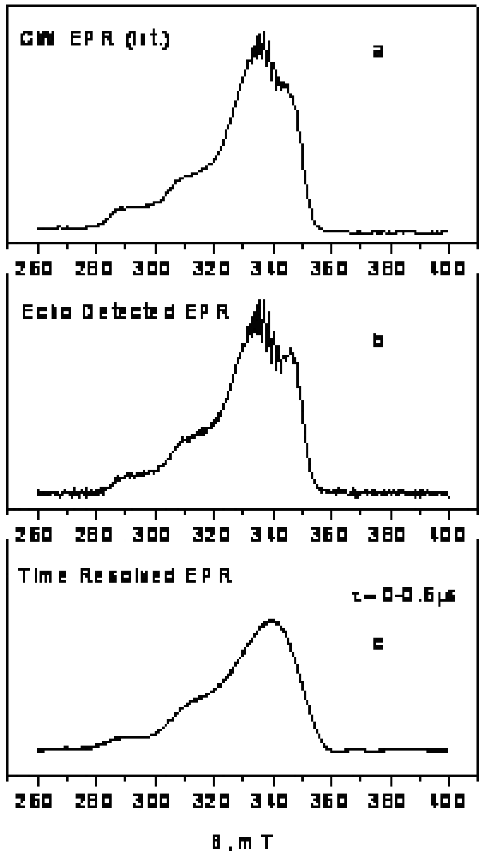

Fig.2 Combination of the numerically integrated steady-state spectra, echo detected and time resolved EPR spectra of 3PyNCu in frozen solution at 15K.

The ground state has the spin ½ and it cannot have the multiplet pattern unless the nuclear spins are involved in the generation of the electronic polarization, which is quite unfavorable for the metalporphyrins. We cannot exclude completely the presence of the charge-transfer states during the tens of microseconds but based on our experience we expect that the main contribution to the late TREPR signal is from the trip-quartet state $^4T_1$, the long-lived excited state with the spin S=3/2>1/2. To prove these statements we model the spectra numerically.

To simulate the spectrum of net contribution we assumed that two magnetic isotopes of copper (^{63}Cu, ^{65}Cu) have the same hyperfine structure and nitrogen isotopes are modeled by only most abounded isotope ^{14}N which has spin I_N=1. Thus spin-Hamiltonian of the system in the ground state of the system includes Zeeman interaction of the electron with the magnetic field and hyperfine interactions with copper and nitrogens:

$$H = \mu \mathbf{B}\cdot \mathbf{g}_{\mathrm{Cu}}\cdot \mathbf{S}_{\mathrm{Cu}} + \left(\mathbf{S}_{\mathrm{Cu}}\cdot \mathbf{A}^{\mathrm{Cu}}\cdot \mathbf{I}_{\mathrm{Cu}} + \sum_i \mathbf{S}_{\mathrm{Cu}}\cdot \mathbf{A}^{\mathrm{N}}\cdot \mathbf{I}_{\mathrm{N},i} \right) \quad (1)$$

where $\mathbf{g}_{\mathrm{Cu}}$ is g-tensor of the doublet ground state; $\mathbf{A}^{\mathrm{Cu}}$ and $\mathbf{A}^{\mathrm{N}}$ are the hyperfine coupling tensors for copper and nitrogen nuclei.

We also assume that spin-Hamiltonian (1) has axial symmetry and its g-tensors and hyperfine tensors are collinear. The comparison of the experimental and the simulated spectra (fig.3) shows that the presented model (1) reproduces the experimental spectrum in detail.

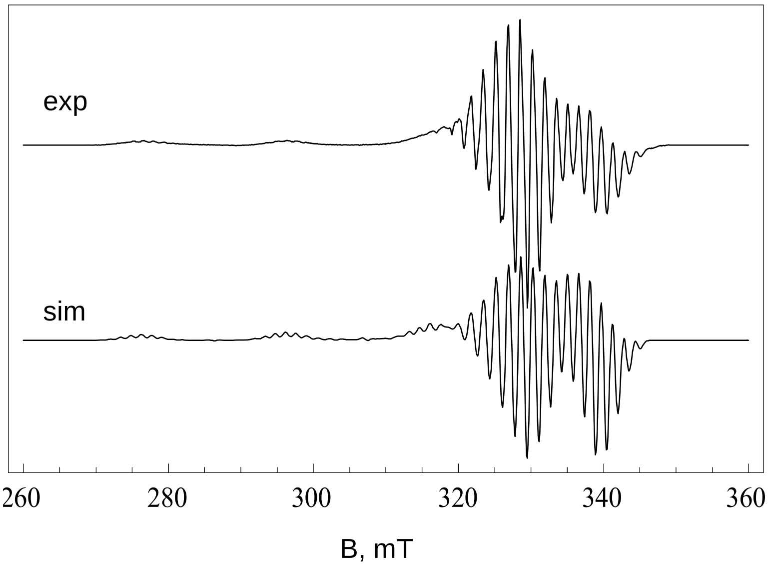

Fig.3 Steady-state EPR spectrum of 3PyNCu in frozen solution at T=80K using 100KHz field modulation (a) and its integral (b): experiment (upper trace) and simulation (lower trace).

The observable TREPR spectra are modeled as a combination of the signals from two states, the ground state with spin ½ and trip-quartet state with spin 3/2. The net contribution is simulated as a signal from the ground state with spin-Hamiltonian (1). All parameters, except the value of the g-tensor along the axis z, g_{zz} = 2.22, equal to parameters used to model CW spectrum (fig.3). The polarization of the ground state $\rho_{G,n}$ is assumed to be independent on the molecular orientation and aligned along the direction of the external magnetic field:

$$\rho_{G,n} = S_{Cu,z} \quad (2)$$

The multiplet contribution is simulated using spin-Hamiltonian:

$$H = \mu\, \mathbf{B}\cdot \mathbf{g}_{\mathrm{Q}}\cdot \mathbf{S}_{\mathrm{Q}} + (\mathbf{S}_{\mathrm{Q}}\cdot \mathbf{D}_{\mathrm{Q}}\cdot \mathbf{S}_{\mathrm{Q}} + \mathbf{S}_{\mathrm{Q}}\cdot \mathbf{A}_{\mathrm{Q}}\cdot \mathbf{I}_{\mathrm{Q}}) \quad (3)$$

where $\mathbf{S}_Q$ describes the operator of the quartet spin, $\mathbf{g}_Q$ is g-tensor of the quartet state, and $\mathbf{A}_Q$ is the tensor of the hyperfine interactions, and $\mathbf{D}_Q$ is a tensor of zero-field splitting.

Concluding remarks

In this work, we have demonstrated that copper porphyrins 3PyNCu manifest upon photoexcitation the spin-polarized signal from two states, from the ground doublet state and from the excited trip-quartet state. The signal from the doublet state shows enhanced spin polarization. The multiplet type of the polarization is predominantly detected from the excited quartet state.

References

[1] K.M. Salikhov, Yu.N. Molin, R.Z. Sagdeev, A.L. Buchachenko, Spin Polarization and Magnetic Effect in Radical Reactions, (Elsevier, Amsterdam, 1984)

[2] R. A. Binstead, M. J. Crossley, N. S. Hush, Inorg. Chem. 30, 1259-1264 (1991)

[3] F. Conti, C. Corvaja, A. Toffoletti, N. Mizuochi, Y. Ohba, S. Yamauchi, M. Maggini, J.Phys. Chem. A 104, 4962-4967 (2000)

[4] C. Corvaja, F. Conti, L. Franco, M. Maggini, C. R. Chim. 9, 909-915 (2006)

[5] Dolphin D., The Porphyrins, vol. III-IV (Academic Press, New York, 1978)

[6] M. Hugerat, A.van der Est, E. Ojadi, L.Biczok, H. Linschitz, H. Levanon, D.Stehlik, J. Phys. Chem., 100, (1996)

[7] V. Rozenshtein, A. Berg, H. Levanon, U. Krueger, D. Stehlik, Y. Kandrashkin, A. van der Est, Israel J Chem 43, 373-381 (2003)

[8] Y. E. Kandrashkin, M. S. Asano, A. van der Est, J. Phys. Chem. A 110, 9617-9626 (2006)

[9] E. Gouterman, In The Porphyrins, ed. By Dolphin D. vol.III. Chapter 1 (Academic Press, New York, 1978)

Magnetic properties and FMR study of nanocomposite multiferroic formed by Co ion implantation in $BaTiO_3$

N.I. Khalitov[1,2], R.I. Khaibullin[1,2], V.F. Valeev[2], E.N. Dulov[1], L.R. Tagirov[1,2], S. Kazan[3], A.G. Şale[3], F.A. Mikailzade[3]

[1]Kazan Federal University, Kremlevskaya 18, 420008 Kazan, Russia
[2]Kazan Physical-Technical Institute of RAS, Sibirsky Trakt 10/7, 420029 Kazan, Russia
[3]Department of Physics, Gebze Institute of Technology, 41400, Kocaeli, Turkey

e-mail: khalitovn@gmail.com

Introduction

Multiferroics attract considerable attention due to wide potential applications in fields of sensors, data storage, spintronics, etc. [1,2]. In these materials, the interaction between ferroelectric and ferromagnetic substances may produce magnetoelectric effect (MEE), in which change in magnetization can be induced by an electric field or vice versa. Magnetoelectric coupling in single-phase multiferroic materials, such as Cr_2O_3, $EuMnO_3$, $BiMnO_3$, $BiFeO_3$ et al, is weak or occurs at temperatures too low for practical applications [1]. In contrast, multiferroic composites based on the dispersion of magnetic nanoparticles in ferroelectric or piezoelectric matrices typically reveal giant MEE above room temperature that makes them suitable for technological applications [1,2]. Hence, the synthesis and characterization of new multiferroic nanocomposite materials are of great interest. In the given context, we implanted ferroelectric oxide, $BaTiO_3$, with high fluences of cobalt ions to form magnetic nanoparticles in the near-surface region of the irradiated substrate. The results of our structural, magnetic and FMR studies show that the ion implantation can be used to synthesize the desired magnetoelectric nanocomposite materials.

Experimental

The 10×10×0.5 mm^3 single-crystalline (001)-face oriented single-domain plates of $BaTiO_3$ (*CrysTec GmbH*, Germany) were implanted with 40 keV Co^+ ions at the ion current density of 8 $\mu A/cm^2$ to fluences in the range of $(0.5\text{-}1.5)\times10^{17}$ ion/cm^2. Implantation was carried out at room temperature by using the ion-beam accelerator *ILU-3* kept at residual vacuum of 10^{-5} Torr.

Depth profiles of cobalt concentration were calculated using the simulation-code *SRIM-2008* [3]. Element composition and surface morphology of the samples were investigated using commercial scanning electron microscope *«Zeiss» EVO-50XVP* with energy-dispersive X-ray (EDX) spectrometer *Oxford INCA Energy 330.*

The static magnetic measurements were carried out using home-made rotating sample magnetometer (coil magnetometry). Magnetic resonance measurements have been done using Bruker EMX model X-band (9.8 GHz) spectrometer. All the magnetic measurements were performed at room temperature for parallel (in-plane) or perpendicular (out-of-plane) orientations of the applied magnetic field with respect to the implanted surface of $BaTiO_3$ plates.

Result and Discussion

Both SRIM calculations and EDX element microanalysis show that cobalt concentration increases with increasing the fluence. For the highest fluence of 1.5×10^{17} ion/cm^2 it nominally reaches 35 at % in the implanted surface layer with the thickness of about 40 nm. Such high concentration of the dopant leads to its precipitation in the form of Co nanoparticles.

Magnetic properties of the implanted samples evolve from superparamagnetic to ferromagnetic with increase of the fluence (fig.1A). Saturation magnetization of the samples implanted by Co to the maximum fluence ($F=1.5\times10^{17}$ ion/cm^2) reaches 0.35×10^6 A/m. Taking into account that saturation magnetization of bulk cobalt equals to 1.4×10^6 A/m we can deduce that the granular film was formed in the near-surface region of irradiated $BaTiO_3$ with a metal filling factor of about 40%. The magnetic curves simulation, see details in Ref. [4], allowed defining the mean size of the formed nanoparticles – in-between of 5 and 7 nm.

The angular dependence of the magnetization curves is typical for thin magnetic granular films: for the in-plane orientation there is no magnetic anisotropy, while in the out-of-plane orientation the magnetic moment does not reach saturation even at the field of 500 mT (fig.1B). The easy-plane magnetic anisotropy is typical for thin ferromagnetic films.

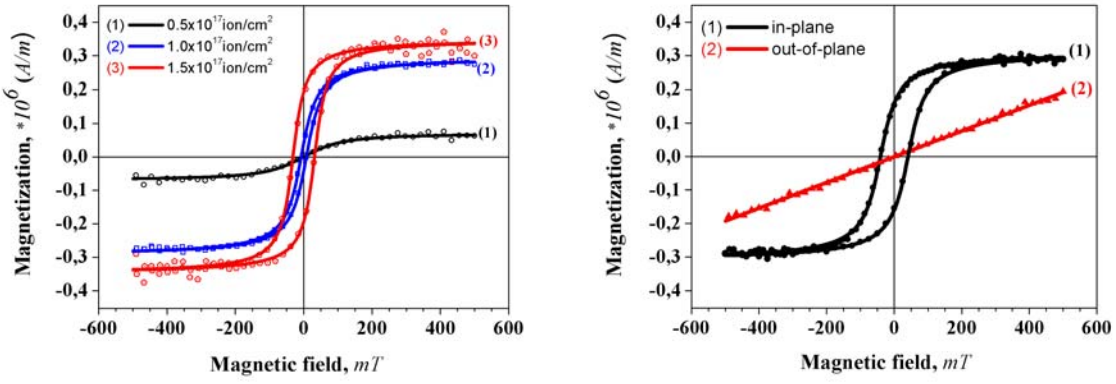

(A) (B)

Fig.1. Room-temperature magnetization curves of Co-implanted $BaTiO_3$ samples: A) in-plane measurements for the samples implanted with different fluences. B) in-plane and out-of-plane measurements for the sample implanted to highest fluence of 1.5×10^{17} Co ion/cm^2. Here symbols are experimental data, and solid line – the fitting.

In magnetic resonance measurements of Co-implanted $BaTiO_3$ sample (fig.2) we observed electron paramagnetic resonance (EPR) signals attributed to Fe^{3+} ions that are elemental impurities in the virgin plates of $BaTiO_3$, see details in Ref. [5]. In addition to the paramagnetic signal, we observed broad FMR signal at high-field region of spectrum as seen in fig.2(A). When the external magnetic field is parallel to the implanted surface of $BaTiO_3$ crystal (parallel geometry), the observed FMR signal intensity is very low compared to the EPR signals. During rotation of the sample as the magnetic field turns from the implanted surface toward to the normal to the implanted surface (perpendicular geometry), the broad FMR signal moves to the high-field region of spectrum, and intensity of this signal increased. The observed FMR in Co-implanted $BaTiO_3$ is attributed to magnetic cobalt nanoparticles formed as a result of high-influence implantation [5].

The main aim of this investigation is synthesis of a new type of magnetoelectric composite structures on the base of ferroelectric perovskite crystals implanted by ferromagnetic ions. In this context we studied influence of the electric field on magnetic properties of the samples. Fig.3 shows the results of FMR measurements of Co-implanted $BaTiO_3$ when electric field was applied to the sample. The measurements were performed in the out-of-plane geometry. From fig.3 one can see clear magnetoelectric effect, which becomes apparent as a change in effective magnetization in response on electric field applied in perpendicular direction. As it is seen in fig.3, increasing the magnitude of the electric field to 7.5 kV/cm shifts the ferromagnetic resonance field by amount of 45 Oe.

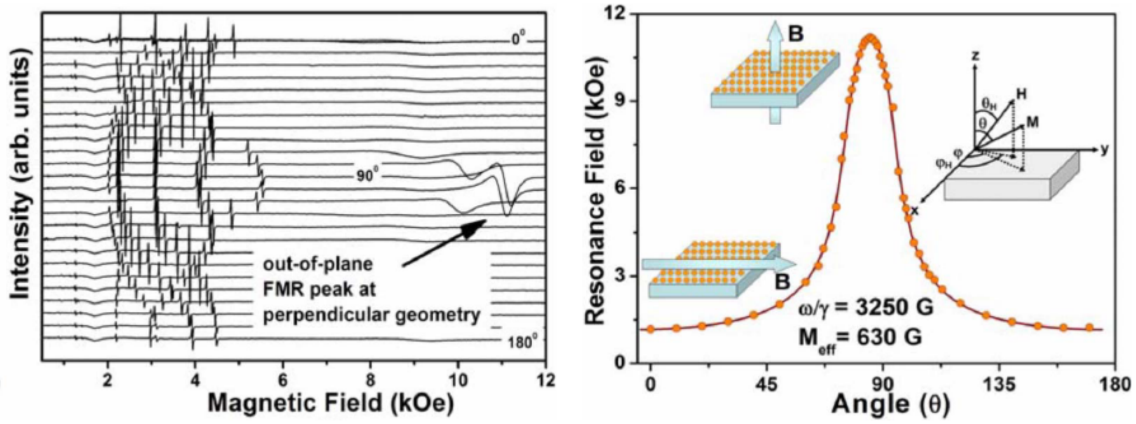

(A) (B)

Fig.2. (A) EPR and FMR signals, observed in $BaTiO_3$ implanted with Co ions to the fluence $F=1.0\times10^{17}$ion/cm^2, at different orientations of the applied magnetic field with respect to the sample surface. (B) Angular dependence of the FMR resonance field in Co-implanted $BaTiO_3$ in the out-of-plane geometry. The inset figure shows the coordinate system for the FMR measurements. (Redrawn from S.Kazan et al. [5] ©2010 The American Physical Society)

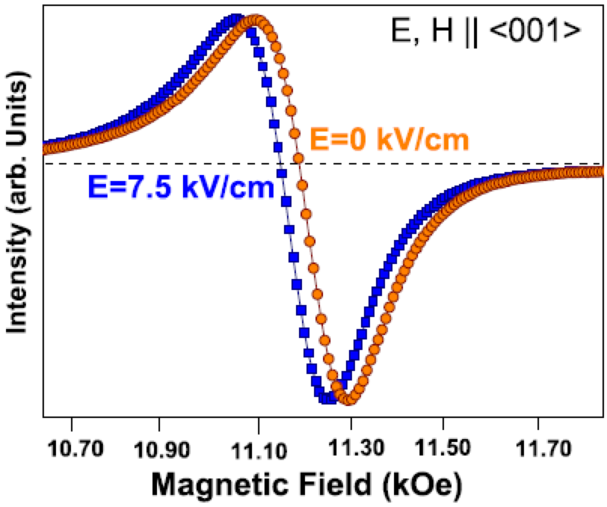

Fig.3. Electric field dependence of FMR spectra obtained in perpendicular orientation of the static magnetic field with respect to the implanted surface plane of the Co-implanted $BaTiO_3$ ($F=1.0\times10^{17}$ion/cm^2). The FMR spectrum shifts to lower fields when *E* increases from 0 to 7.5 kV/cm. (From S.Kazan et al. [5] ©2010 The American Physical Society)

Conclusion

In summary, we investigated the fluence dependence of magnetic properties of barium titanate implanted with cobalt ions. Magnetic measurements showed existence of Co nanoparticles in implanted $BaTiO_3$ with the mean size about 5-7 nm. These particles display superparamagnetic or ferromagnetic properties according to the fluence. FMR spectra also show existence of Co nanoparticles. Furthermore, the FMR spectrum shift was observed as a result of the external electric field influence on the sample magnetization. These results show availability of magnetic nanocomposites based on Co-implanted ferroelectric perovskite $BaTiO_3$ crystals for potential magnetoelectronic applications.

Acknowledgments

Our investigations were supported by the Ministry of Education and Science of the Russian Federation, contract No 02.740.11.0797, and by joint RFBR-TUBITAK Programme, grants No 10-02-91225_CT and No. 2009T061, respectively. The authors from GIT, Turkey, are indebted to Research Projects Commission of GIT for supporting this work by Grant No. 2009-A11.

Reference

[1] R. Grössinger, G.V. Duong, and R. Sato-Turtelli, *J. Magn. Magn. Mater.*, 320 (2008) 1972.

[2] C.-W. Nan, M.I. Bichurin, S. Dong, D. Viehland, and G. Srinivasan, *J. Appl. Phys.*, 103 (2008) 031101.

[3] J.F. Ziegler, J.P. Biersack, U. Littmark, The Stopping and Range of Ions in Solids, Pergamon Press, New York, 1985 (SRIM-2008 software at http://www.srim.org/).

[4] N.I. Khalitov, R.I. Khaibullin, V.F. Valeev, E.N. Dulov, L.R. Tagirov, S. Kazan, A.G. Şale, F.A. Mikailzade, *Nucl. Instr. and Meth. in Phys. Res. Sect.* ***B*** (2011) *(in press)*.

[5] S. Kazan, F.A. Mikailzade, A.G. Şale, M. Maksutoğlu, M. Acikgoz, R.I. Khaibullin, N.I. Khalitov, Ju.I. Gatiiatova, and V.F. Valeev, *Phys Rev. B*, 82 (2010) 054402.

Paramagnetic polymer materials containing nanosized silver particles

S.S. Khutsishvili, T.I. Vakul'skaya, N.P. Kuznetsova, T.G. Ermakova, A.S. Pozdnyakov, T.V. Kon'kova, S.A. Korzhova, G.F. Prozorova

RAS Institution the A.E. Favorsky Irkutsk Institute of Chemistry, Siberian Brunch, Russian Academy of Sciences, 1 Favorsky st. 664033 Irkutsk, Russia

e-mail: khutsishvili_sp@yahoo.com

In the recent years, the developments upon the nanocomposite materials containing metal particles and possessing complex properties relevant for of up-to-date catalysts, drugs, etc. have been widely spread. This trend is closely connected with the problem of nanoparticles' stabilization within the matrix.

This paper is devoted to a series of new nanocomposites on the basis of 1-vinyl-1,2,4-triazole (VT) polymer and its co-polymers with acrylonitrile (AN), 1-vinylpyrrolidone (VP), crotonic acid (CA), sodium salt of acrylic acid (Na-AA) and sodium salt of metacrylic acid (Na-MAA). The nanocomposites containing nanosized silver particles have been obtained and characterized. All the materials considered have proved to be paramagnetic and they have been studied by the EPR method. It is noteworthy that powder micro-crystalline samples, unlike monocrystals, show lower pronounced anisotropic properties, thus, as a rule, only averaged g-factor values can be measured for them. However, in the materials on the basis of transition metals, nanosized magnetic particles are often formed. These particles are able to unite into so called clusters where, due to a certain magnetic order, unpaired electrons are strongly correlated. The substances containing such ordered regions (domains) acquire ferromagnetic properties essentially affecting the EPR spectra.

The starting polymeric matrices, which are high-resistance organic semiconductors in the form of white powders, are diamagnetic. The combination of VT monomers with the other ones (AN, VP, CA, Na-AA and Na-MAA) in the co-polymers' macromolecules provides their high complexation ability towards the metal ions, due to the presence of heterocycle nitrogen atoms and, in particular, cyano-groups of acrylonitrile, and decreases the nanoparticles' agglomeration. The nanocomposites on the basis of co-polymer matrices, unlike those supported by VT solely, are insoluble in water. Nanocomposites on the basis of VT polymer have been obtained in aqueous solutions by $AgNO_3$ chemical reduction (by $NaBH_4$, glucose or formaldehyde) or by its thermal reduction in the presence of (co-)polymer matrix in solid phase. They represent monochrome fine-dispersed powders, usually dark brown or black ones. According to the transmission electron microscopy data for the VT-supported composite materials, its silver nanoclusters' have sizes of about 3-7 nm (silver content 2-22%). The X-ray phase analysis has shown that the nanoparticles' sizes for the composites on the basis of VT-AN copolymer matrix (typical diffraction peaks' broadening) are 17-20 nm (silver content 41-42%).

The poly-1-vinyl-1,2,4-triazole matrix shows especially high activity towards silver atoms by forming charge transfer complexes. Due to their crystallinity, their EPR spectra depend on the orientation of a sample in the magnetic field. As a result, we have ascertained the anisotropy and the presence of several individual signals referring to different types of paramagnetic centres (PC). The signals observed in the range of g=2.00 belong to the conduction electrons of reduced silver Ag(0) forming nanoclusters stabilized by polymeric matrix while the wide ones (от 500 до 900 G) in the range of g=2.2, to the polymeric complexes of diavalent metal. At the temperature of 125 K, a wide EPR signal of the silver containing nanocomposites separates into two more narrow components of g=2.29 (190 G) and g=2.14 (260 G), obviously, due to the Ag^{2+} ions located in the anionic layers of polymeric matrix.

Nanocomposite materials on the basis of VT-AN matrix possess electroconductivity (10^{-6}-10^{-9} Cm/cm) and paramagnetism (10^{19}-10^{20} spin/g). In their EPR spectra, narrow symmetric singlets of g-factor of 2.005 and of width of 5-8 G are observed. The studies upon the EPR signals' temperature dependencies and observations of their shapes and widths in conditions of microwave saturation have proved that these signals refer to zero-valence silver forming clusters stabilized by co-polymer matrix [1However, the complicated dependencies of the signals' intensities and widths on microwave power can be preconditioned by the size variations of the nanoclusters (from one to several nanoparticles) and by some other factors [2]. The relaxation characteristics of these nanocomposites have been estimated by the pulsed EPR method at 113 K ($T_1' = 6875$ ns and $T_1'' = 38574$ ns, $T_2' = 9$ ns and $T_2'' = 192$ ns have been determined by pulse patterns of π-T-π/2-τ-π for T_1, π/2-τ-π for T_2, где $\pi/2 = 20$ ns, $\tau = 200$ ns and T = 1000 ns (cw and pulse EPR spectra were recoded with an X-band Bruker ELEXSYS E-580 spectrometer)).

Since the EPR signals of zero-valence metals are registered in the range close to g-factor of free electron and they are similar to signals of polyconjugate polymers (triple CN-bond of acrylonitrile can polymerize under certain conditions forming double-chain conjugate polymers [3,4]), it has been necessary to exclude or single out the contributions of the latter into the nanocomposites' narrow signals. Control samples of the starting co-polymer, after heating at 210-250°C, have shown weak narrow singlets ($N = 1.6\times10^{16}$, g = 2.0052, $\Delta H = 5.3$ G, A/B = 1.0), thus, the spectra observed can be regarded as a superposition of two signals (one of polymer matrix and one of zero-valence metal). For this purpose, we have studied the dependency of EPR signals' characteristics on microwave power (so called saturation effect) (fig.1). The signals of the silver containing samples represent complicated curves (fig.2). There is an inflection point on the dependencies of line widths at microwave power of 0.2 mW implying that the signal is a superposition of two signals of similar g-factors and widths, but belonging to different PC. In accordance with this is the fact that, at higher power, this dependency for silver containing nanocomposite has two linear intervals with inflection point at 15 mW (fig.2). As for the dependency of the signals' intensities on microwave power, the saturation curve plateau starts already at 2.5 and continues till 65 mW. This means that the

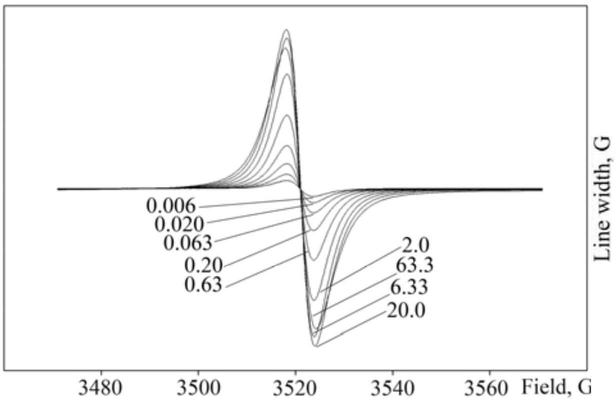

Fig.1. EPR spectra of the nanocomposites of silver and VT-AN co-polymer at various microwave powers (mW).

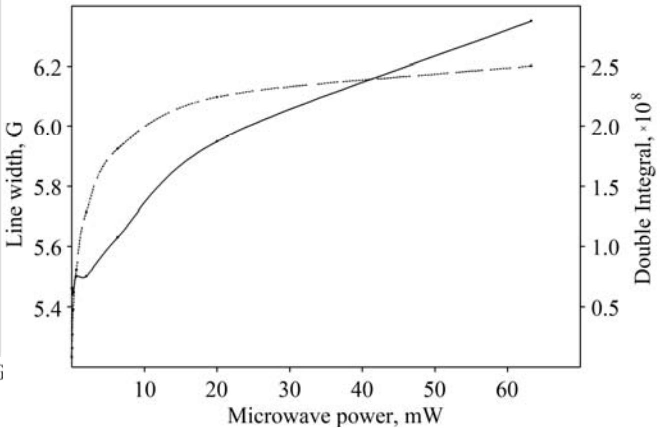

Fig.2. Dependency of signal width (solid line) and double integral (broken line) on microwave power for Ag(0)-containing VT-AN nanocomposites.

samples obtained contain both free electrons of zero-valence metals and organic radicals referring to polymeric matrix (the mentioned above polyconjugate polymer) due to the formation of double-chain structures by C≡N bond. During the saturation process, g-factor remains unchanged and the signal, symmetric. The lineshape is almost Lorentzian and at saturation it becomes absolutely Lorentzian, which points to the increase of metal nanoclusters' sizes [5]. As the temperature decreases, the EPR signal intensity, g-factor and signal width increase (table 1, fig.3).

T, K	Intens.	g-factor	ΔH, G
293	–	2.00450	5.47
223	3.817	2.00520	5.55
203	4.197	2.00525	5.57
183	4.907	2.00530	5.60
163	5.415	2.00540	5.64
143	5.898	2.00543	5.68
123	6.768	2.00553	5.70
113	7.893	2.00561	5.72

Table 1. Experimental EPR-characteristics for the nanocomposites of silver and VT-AN co-polymer.

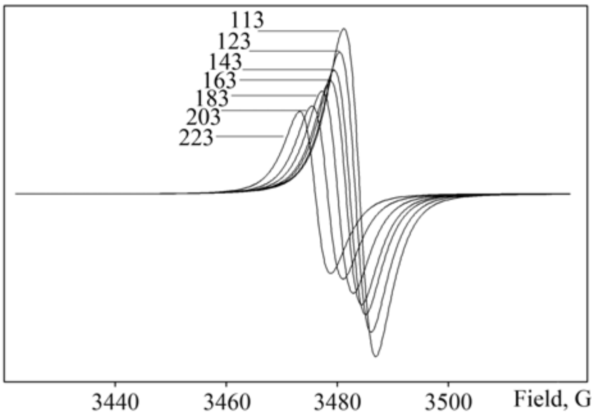

Fig.3. Temperature dependency (K) EPR spectra of the nanocomposites of silver and VT-AN co-polymer.

Note that, in Ag(0)-containing nanocomposite spectrum, weak doublet lines which are satellites of ^{107}Ag and ^{109}Ag isotopes with constants of 671 and 773 G, respectively [5], have been registered at 113 K at high and low fields. The ratio between the constants is 1.15 which coincides with one of magnetic moments of the silver isotopes and, thus, confirms the lines' references.

At the same time, nanocomposites on the basis of VT and $AgNO_3$ synthesized in the presence of $NaBH_4$ (fig.4), glucose or formaldehyde as reducers [6] contain, besides zero-valence silver, the complexes of diavalent silver giving wide signals in the EPR spectra depending on the nature of reducer. These wide signals (g=2.2, ΔH from 500 to 900 G) can be referred to polymeric complexes Ag^{2+} in tetragonal symmetry environment and their agglomerates of Ag^{2+}_n type (fig.5). Fine-crystalline character of the nanocomposites manifests

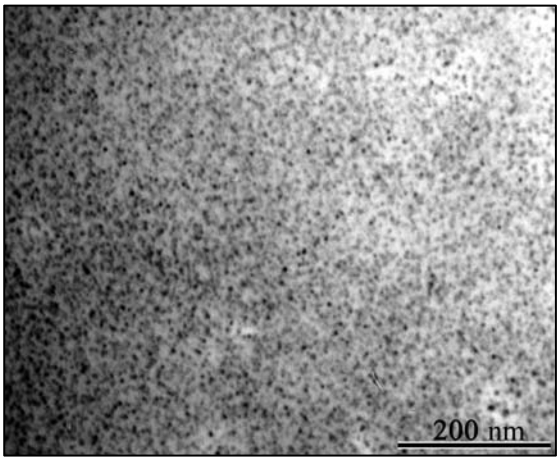

Fig.4. Electronic microphotography of nanoparticles in the composite.

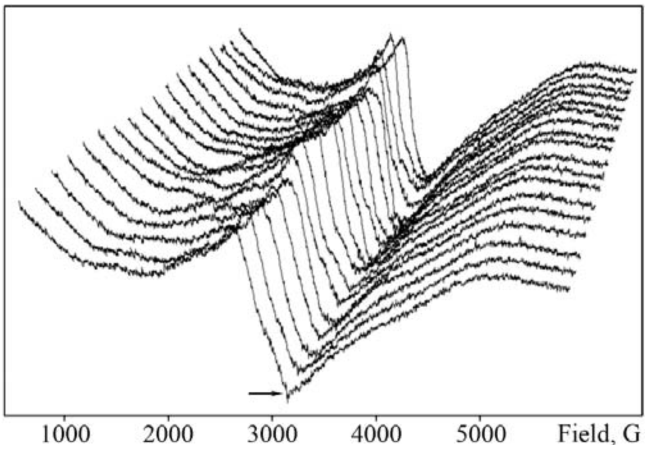

Fig.5. EPR spectrum of the nanocomposites of silver and VT polymer (the arrow shown the signal with g-factor in the range of 2.00).

itself in pronounced orientation dependence of the spectrum on magnetic field revealing anisotropy and individual signals of different PC, in particular, one in the range of g=1.92-2.00 belongs to reduced metal Ag(0) forming nanoclusters stabilized by polymeric matrix.

Nanocomposites, obtained from polymer matrix and silver nitrate in quantitative ratio of 20:1, produce very wide signals in the EPR spectra at room temperature. Those bands are superpositions of signals of at least tree PC types. If the ratio is 5:1, the spectrum is much more narrow, and it demonstrates two PC types in the sample. At fractionating the nanocomposites of high matrix content, the PC separation is also observed. The soluble fraction, unlike the insoluble one, produces more narrow EPR signals referring to two PC types.

The lines of g-factors in the range of 2.00 and widths of up to 8 G, like those of thermally obtained nanocomposites, refer to the $Ag(0)_m$ PC type. At low temperatures (125 K), a narrow isotropic signal becomes some more narrow and its intensity increases. Unfortunately, we have not managed to register ^{107}Ag and ^{109}Ag satellites separation even at this temperature. The fractionating of the nanocomposites at high $NaBH_4$ content leads to the spectrum with more narrow signals and vice versa which can be explained by more intense metal reduction to zero-valence state and by formation of diamagnetic complexes.

References

[1] Hoi Ri Moon, Ji Hyun Kim, Myunghyun Paik Suh. Redox-Active Porous Metal-Organic Framework Producing Silver Nanoparticles from AgI Ions at Room Temperature // Angewandte Chemie International Eddition. – 2005. – V. 44, N. 8. – P. 1261-1265

[2] Mandal A.R., Mandal S.K. Electron spin resonance in silver-doped PbS nanorods // Journal of Experimental Nanosciens. – 2010. – V. 5, N. 3. – P. 189-198.

[3] Yu.K. Tovbin, A.N. Ozerin. Kinematics of a Polyacrylonitrile Macromolecule Segment in the Uniaxially Oriented Materials // Vysokomolekulyarnye Soyedineniya. – 1995. – V. 37, N. 1. – P. 108-112.

[4] Topchiyev A.V., Geiderikh M.A., Davydov B.E., Kargin V.A., Krentsel B.A., Kustanovich I.M., Polak L.S. On the Possibility of Obtain Polymer Materials of semiconductor properties on the basis of polyacrylonitrile // Doklady of Russian Academy of Sciences – 1959. – V. 128, N. 2. – P. 312-315.

[5] Shabatina T.I. Reactions of Mesogenic Cyanophenyls at Low Temperatires and Cryoformation of Metal-Mesogenic Nanosystems // Vestnik Moskovskogo Universiteta. – 2002. – Seriia 2. Chemistry. – V. 43, N. 5. – P. 273-285.

[6] Myachina G.F., Korzhova S.A., Yermakova T.G., Sukhov B.G., Trofimov B.A. Silver Nanocomposites and Poly-1-vinyl-1,2,4-triazole // Doklady of Russian Academy of Sciences – 2008. – V. 420, N. 3. – P. 1-2.

Magnetic field effects on open chemical systems far from equilibrium

A.A. Kipriyanov Jr.[1], P.A. Purtov[1,2]

[1]Institute of Chemical Kinetics and Combustion SB RAS, 630090, Institutskaya 3, Novosibirsk, Russia.
[2]Novosibirsk State University, 630090, Pirogova 2, Novosibirsk, Russia.

e-mail: akipriyanov@yahoo.com

Introduction

The influence of magnetic fields on chemical processes has long been the subject of interest to the researchers. It has been established that under certain conditions relatively weak magnetic field of the order of several oersted could noticeably affect the rates of chemical. We mean such important and widespread processes as radical recombination, reaction of radicals with triplet molecules and paramagnetic complexes, etc.

However, numerous investigations show that commonly the influence of magnetic field on chemical reactions is insignificant, just a few percent, rarely, several tens percent. It has been shown that magnetic effect manifests itself in the competition of different channels of conversion in elementary reaction stages (the model of radical pairs). But there are a number of experiments shown magnetic field effects much larger than could be explained by standard theories.

It is well-known in nonequilibrium thermodynamics that sometimes even small perturbations can have serious consequences for nonlinear systems where feedbacks are of great importance. The reason is the disturbance of the state stability and the change in the regime of the process. One can assume that in some chemical or biological systems rather strong influence of weak magnetic fields is also brought about by the disturbance of stationary state stability and the change in the behavior of the system (or part of the system). The necessary condition for such an influence is the presence of magnetosensitive stage in the model under consideration, for example, radical recombination reaction.

Hence the search for rather simple but realistic systems where strong influence of relatively weak magnetic fields is possible is of great interest and the first attention should be given to open chemical systems that are far from equilibrium. For this purpose two chemical systems were treated theoretically.

Photochemical system

The first system under study describes dissociation reaction of cyclic ketones under the action of external radiation (laser) which results in biradicals and their subsequent recombination. This system is open, since it can exchange energy with reservoir. So the stationary state of the system will be determined both by stationary concentration of reactants, and by stationary temperature.

Thus, under the action of external radiation the molecule-precursor A produces biradical B that can subsequently recombine to give the initial molecule

$$A \xrightarrow{\hbar\nu} :B \rightarrow A. \tag{1}$$

The kinetic equation defining the concentration change of biradicals B is as follows

$$\frac{dn_B}{dt} = \frac{I_{abs}}{V N_A \hbar\nu} - K(T) n_B, \tag{2}$$

where n_B is biradicals concentration, $K(T)$ is monomolecular recombination rate constant of biradicals B depending on the temperature T of the reacting system, I_{abs} is the energy absorbed by the reacting system per unit time, ν is laser generation frequency, $\hbar$ is the Planck constant, V is the volume of solution excited by laser radiation, N_A is the Avogadro constant.

The first term in the right-hand side of equation (2) describes the production of biradicals due to photolysis. I_{abs} appearing in it is defined using the Buger-Lambert-Ber law on the assumption that at the given laser generation frequency only molecules A (biradicals) absorb

$$I_{abs} = I_0(1 - \exp(-n_A \varepsilon l)) \,. \tag{3}$$

where I_0 — incident radiation power, n_A — substance A concentration, ε — substance A extinction coefficient, l — dishes length with solution.

We accept the following temperature dependence of recombination rate constant

$$K(T) = K_0 \exp\left(-\frac{E_A}{R}\left(\frac{1}{T} - \frac{1}{T_0} \right) \right), \tag{4}$$

where T — the reacting system temperature, T_0 — the reservoir temperature that is kept constant, K_0 — the rate constant determined at the temperature T_0, E_A — recombination barrier, R — universal gas constant.

As already mentioned, the internal energy of the system changes due to radiation absorption and loss of heat to the reservoir kept at constant temperature T_0. The mean variation rate of external energy of the system may be written as

$$\frac{dE}{dt} = I_{abs} - \alpha(T - T_0), \tag{5}$$

where α — heat emission coefficient between the reacting system and reservoir, T — the mean temperature of the system.

Biradical life time τ is defined as the inverse value to biradical recombination rate

$$\tau = \frac{1}{K(T)} = \frac{1}{K_0}\exp\left(\frac{E_A}{R}\left(\frac{1}{T} - \frac{1}{T_0} \right) \right) = \tau_0 \exp\left(\frac{E_A}{R}\left(\frac{1}{T} - \frac{1}{T_0} \right) \right), \tag{6}$$

where τ_0 — biradical lifetime at the temperature T_0.

Leaving aside a specific example of biradical and calculation details, for definiteness we take that in experimental conditions biradical lifetime τ_0^m in the presence of magnetic field (of the order of several oersted) differs from biradical lifetime τ_0 in the absence of magnetic field approximately by 10 percent

$$\tau_0^m = 1.1\tau_0 \,. \tag{7}$$

Also leave aside a question of finding system parameters which allow the system has multiple stationary states, i.e. at certain laser intensity the reacting system could have three stationary temperatures and therefore, three different stationary concentrations of reactants.

For the realistic parameters (which are available in experiments) below we give stationary dependences of the reacting system temperature T and biradical concentration on external radiation value I_0, respectively. Solid line denotes the dependence in the absence of external magnetic field, dotted line – in the presence of magnetic field.

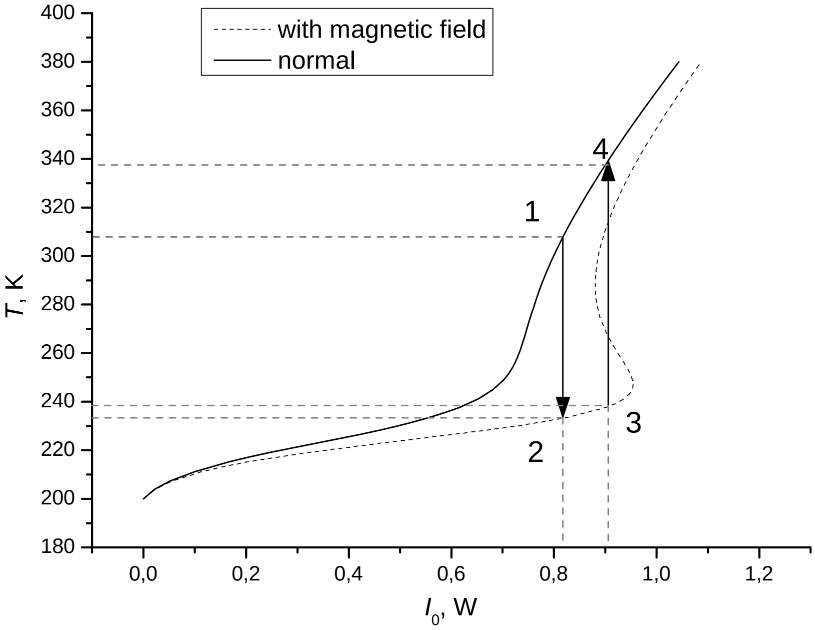

Fig.1. Stationary temperature dependence of the system on external radiation value in the presence and in the absence of magnetic field.

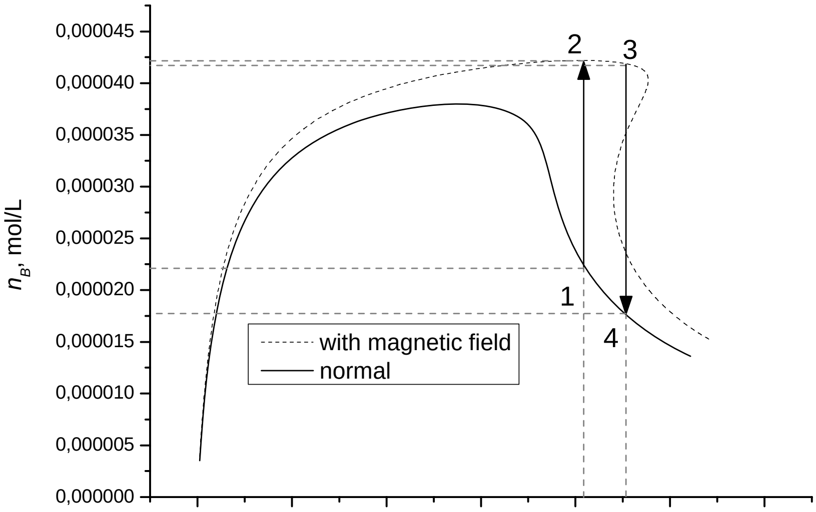

Fig.2. Stationary concentration dependence of biradicals on external radiation value in the presence and in the absence of magnetic field.

Hydrocarbon oxidation in liquid phase

The second system under study describes hydrocarbon oxidation in liquid phase in presence of inhibitor. The reaction system under discussion is a flow reactor of the volume V to the inlet of which hydrocarbon of concentration $[RH]_0$ is constantly delivered at the rate ω in the mixture with the inhibitor of concentration $[I]_0$ under oxygen saturation conditions; the reaction mixture constantly flows from the chamber at the same rate.

Elementary stages of the reaction are following

$$\begin{array}{ll} (8.1) & RH + O_2 \xrightarrow{k_1} R^\bullet \\ (8.2) & R^\bullet + O_2 \xrightarrow{k_2} RO_2^\bullet \\ (8.3) & RO_2^\bullet + RH \xrightarrow{k_3} ROOH + R^\bullet \quad , \\ (8.4) & ROOH \xrightarrow{k_4} 2R^\bullet\left(RO^\bullet + OH^\bullet\right) \\ (8.5) & RO_2^\bullet + RO_2^\bullet \xrightarrow{k_5} P_1 \\ (8.6) & RO_2^\bullet + I \xrightarrow{k_6} P_2 \end{array} \qquad (8)$$

where I — inhibitor; P_1, P_2 — stable reaction products. Here reaction (8.1) characterizes the process of the chain generation, reactions (8.2) and (8.3) define the chain evolution, reaction (8.4) — decay into radicals (degenerate chain branching), reactions (8.5) and (8.6) — chain termination.

Stationary states in the system are defined by following condition on reagents concentration

$$\frac{d[R^\bullet]}{dt} = \frac{d[RO_2^\bullet]}{dt} = \frac{d[ROOH]}{dt} = \frac{d[RH]}{dt} = \frac{d[I]}{dt} = 0. \qquad (9)$$

It is assumed that external magnetic field can affect recombination rate constants k_4, k_5, and violate the stability of a steady state (at certain parameters of the system) thus transferring the system to another steady state essentially differing from the initial one.

Fig.3 shows two stationary concentrations of peroxide radicals as a function of inhibitor concentration delivered into the reactor in the presence and in the absence of external magnetic field.

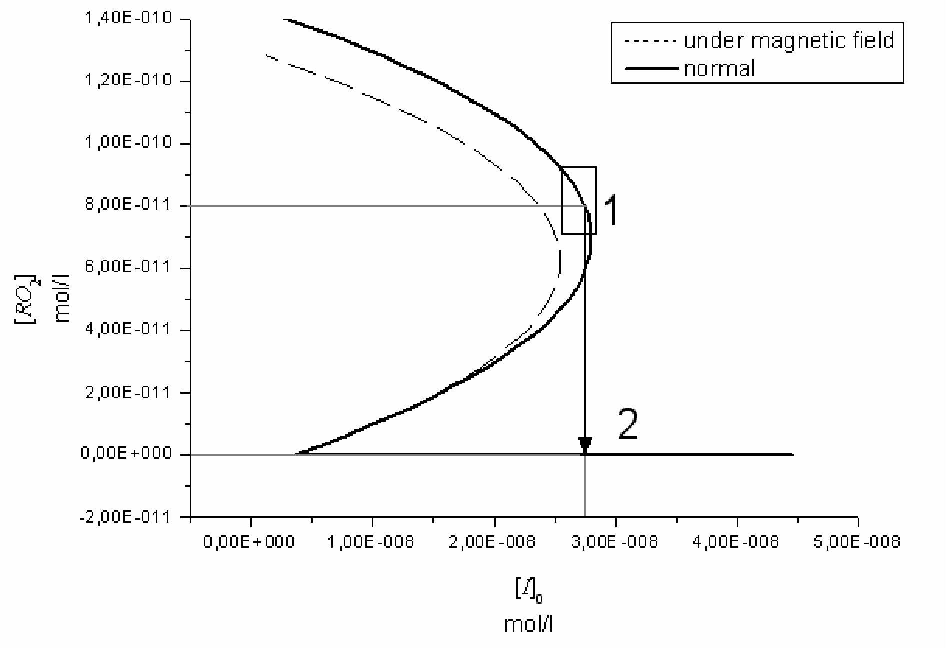

Fig.3. The dependence of stationary concentration of peroxide radicals on the concentration of inhibitor delivered into the reactor in the presence and in the absence of external magnetic field.

Results and discussion

External magnetic field affects on rate constants of reactions with paramagnetic particles. Though these effects are rather insignificant, they are responsible for the fact that in the system under study the set of stationary states in the absence of external magnetic field does not coincide with the set of stationary states in the presence of magnetic field. These distinctions are most noticeable in bistability region.

Consider photochemical system more carefully. The external radiation power I_0 is the control parameter. It is seen that at certain values of the control parameter there exist critical points: 0.88 W and 0.96 W. These are bifurcation points, since with increasing (or decreasing) laser power the number of stationary states changes abruptly – depending on laser radiation intensity I_0 stationary states with one or three different values of the reacting system temperature can be observed. At the parameter values slightly higher (or slightly lower) than the critical value the state is stable. In degeneration region of stationary states only stationary states lying between the curve maxima and minima (Fig.1) are asymptotically unstable.

Two characteristic regions can be distinguished where great effect of weak magnetic field on the system is noted: at the values of I_0 from 0.74 W to 0.88 W, and from 0.88 W to 0.96 W. Examine the behavior of the system at external radiation power 0.81 W. In the absence of magnetic field the reacting system is in the stationary state characterized by stationary temperature about 308 K. In the presence of magnetic field this stationary state becomes unstable, and at the given radiation power the system abruptly changes to high temperature branch, and to another stationary state with the temperature about 232 K. Now consider the second region, i.e., the external radiation power is 0.92 W. Let the magnetic field be present, then the reacting system will have the stationary temperature about 238 K. Switching off the magnetic field will make this stationary state unstable, and the system will abruptly go to another stationary state with the temperature about 344 K. This will lead to intensive heating of the system. As is seen from Fig.2, the change in stationary temperature will be accompanied by an abrupt change in stationary concentrations of reactants.

Analogous magnetic field effect could be observed in system described hydrocarbon oxidation in liquid phase. To reveal the essence of the effect, examine the behavior of the system at the inhibitor concentration $[I]_0 = 2{,}7 \cdot 10^{-8}$ mol/L. Let the system be in a steady state which corresponds to point 1 in the diagram. This steady state is stable, and concentration of peroxide radicals is $[RO_2^{\bullet}] = 8 \cdot 10^{-11}$ mol/L. Switching on the external magnetic field violates the stability condition of this state, and the system is to change to another branch of steady states. Thus with constant $[I]_0$ the system goes to another steady state under the action of external magnetic field. This state (point 2 in the diagram) will be characterized by another stationary concentration $[RO_2^{\bullet}] = 1 \cdot 10^{-17}$ mol/L of peroxide radicals.

So the possibility of strong effect of weak magnetic fields of the order of several oersted in the considered systems is theoretically predicted. External magnetic field may be responsible for the violation of the stationary state stability condition, and change radically the system properties. It is similar to the phase transition of the first kind, and will be accompanied by intensive heating (cooling) of the system, and abrupt change in concentrations of reacting substances.

Temperature dependence of molecular mobility of 1-butyl-2,3-dimethylimidazolium tetrafluoroborate ionic liquid according to NMR ^{19}F, ^{11}B and ^{1}H

A.A. Kuzovkov[1], Yu.S. Chernyshev[1]

[1]SPbSU, 198504, Ulyanovskaya st. b. 3, Petrodvorets, Saint-Petersburg, Russia

e-mail: undersan@gmail.com

Introduction

Ionic liquids represent organic salts, composed of organic cation and organic or inorganic anion having low fusion temperature and being in liquid state with temperatures from ~ 623 to 193 K. Ones have a lot of different unique properties, such as: low volatility, high electroconductivity, high termostability and electrooxidative process stability, low toxicity. Depending on combination of anion and cation these liquids can be both hydrophobic and water-soluble. It makes ionic liquids perspective objects for research in connection with broad spectrum of its eventual uses, particularly: solvents, catalysts, heat-transfer agents, supercapacitors, leaches, electrolytes, liquid crystals etc. Fundamental properties of these matters are understudied at this date.

Researching ionic liquid: 1-butyl-2,3-dimethylimidazolium tetrafluoroborate

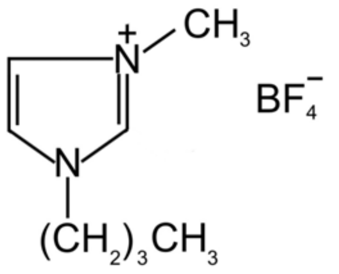

Linear formula: $C_9H_{17}BF_4N_2$

Measuring Technique

There were researched temperature dependences of diffusivity coefficient D of BF_4^- ion according to NMR ^{19}F, ^{11}B as well as diffusivity coefficient of cation comprising ^{1}H in this paper. We had studied two samples of 1-butyl-2,3-dimethylimidazolium tetrafluoroborate ionic liquid, one of which as it turned out of measurements, probably contains a portion of water.

Measurements were taken with spectrometer BRUKER SXP 2-100 on a frequency of 90 MHz (for ^{1}H) over the 253 K to 363 K.
For researching of diffusivity coefficient sequence 90^0 - τ - 180^0 was used, where τ was varied over the 45 to 160 msec. Cycle interval T measuring of NMR ^{19}F and ^{11}B was 4 seconds and measuring of NMR ^{1}H – 1 second. Spin-echo amplitude dependences on gradient square of magnetic field over a range of temperatures were analyzed. As an example on fig.1 spin-echo amplitude dependences on gradient square of magnetic field for ^{11}B nuclear at temperatures 303 and 363 K are shown. From these figures in line with equal

$$A(G) = A_0 \exp(-\frac{2}{3} D\gamma^2 G^2 \tau^3) \qquad (1)$$

the value of diffusivity coefficient D for our ionic liquid at conformable temperatures was determined. In equal (1) G — gradient of magnetic field [T/m], γ — magnetogyric ratio, A(G) — spin-echo amplitude. After that graph of dependence diffusivity coefficient on inverse temperature was plotted (fig.2)

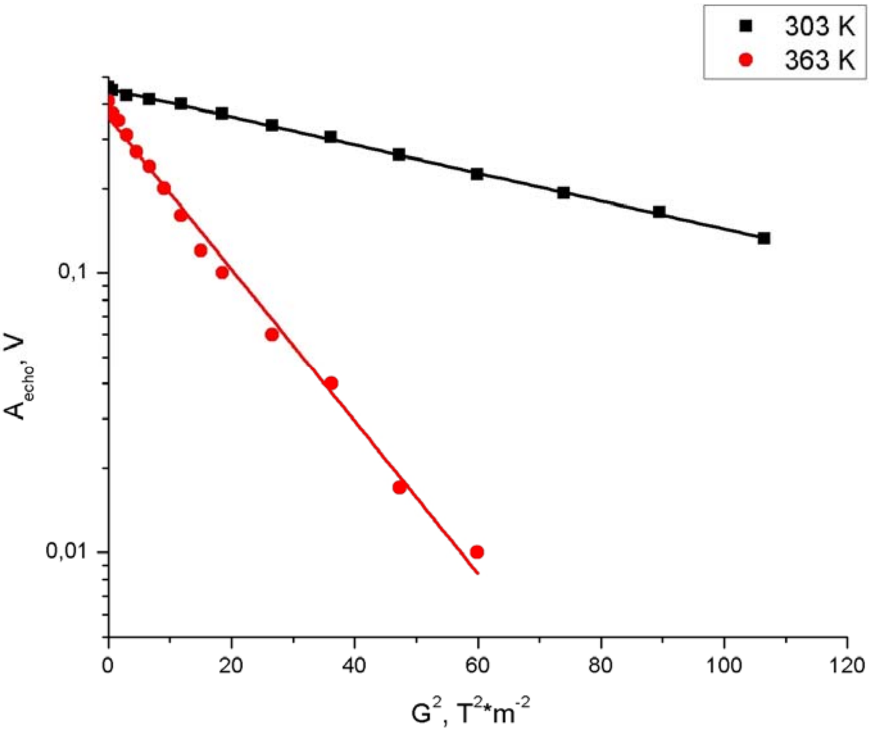

Fig. 1

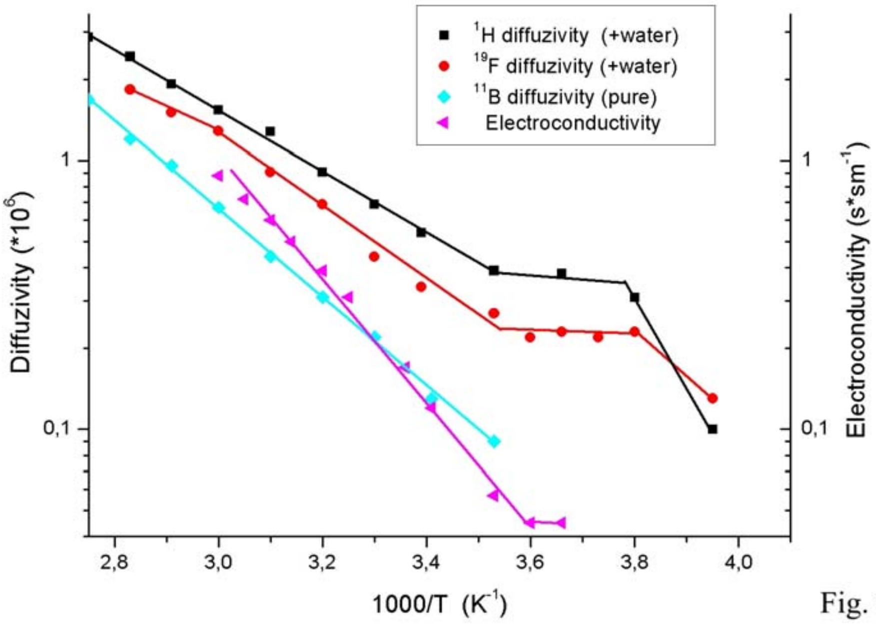

Fig. 2

Results

According to data of NMR ^{1}H and ^{19}F deviation from linearity of temperature dependence of diffusivity coefficient D at temperatures over 283-263 K for both nuclei as well as for ^{19}F in a range of temperatures 343-363 K was turned out that confirms supposition about restructuring of ionic liquid consisting in H-bond between ^{1}H and ^{19}F blackout and perfectly matches our results for diffusivity temperature dependence with electroconductivity data for the same ionic liquid derived in an article [2]. For a sample of pure ionic liquid on evidence derived from data NMR ^{11}B transconformation point in a range of 333 K supposing in an article relating to H-bond formation [4] wasn't revealed.

Radius of ion BF_4^- derived in terms of a formula $R=kT/6\pi\eta D$ (η=2.3 cP from an article [1]) at a temperature 303 K appeared equal R=1,9Å that appreciably surpasses a value 1,32Å, given in [3]. Probably, in our case, in the whole of temperature area still local ionic pair formation obtains and its radius can be of the order of 2,8Å [3].

This work is supported by the RFBR grant № 09-03-01105a.

References

[1] Jing-Fang Huang, Po-Yu Chen, I-Wen Sun, S. P. Wang, Department of Chemistry, National Cheng Kung University, Tainan 70101, Taiwan, ROC, Inorganica Chimica Acta 320 (2001) 7-11

[2] P.A.Z. Suarez, S. Einloft, J.E.L. Dullius, R.F. de Souza and J. Dupont, Instituto de Quimica, UFRGS, Av. Bento Goncalves, 9500, CEP 91501-970, Porto Alegre, RS, Brazil

[3] Akihiro Noda, Kikuko Hayamizu and Masayoshi Watanabe, Journal Phys. Chem. B 105 (2001) 4603 – 4610

[4] Roberto F. de Souza, Janine C. Padilha, Reinaldo S. Goncalves, Jairton Dupont, Electrochemistry Communications 5 (2003) 728 – 731

EPR-researches of biomaterials using the data of thermochemical ions-radicals

L.V. Khaidarshina

Institute of metal physics UB RAS, 620990, S. Kovalevskoy str., 18, Ekaterinburg, Russia.
e-mail: haidarshina@imp.uran.ru

Method of electronic paramagnetic resonance (EPR) apply to determination of physical properties of matter, molecules and mechanisms of chemical reactions [1]. Its peculiar feature is the opportunity to obtain the information about influence of an uncompensated electron microenvironment and also to estimate quantitatively the contents of paramagnetic impurities that allows determining the structure of one or another defect. However, application of the given method to, research of properties of the bioorganic substances containing mineral components is poorly developed. In particular, a comparative research of bone tissues under the degenerate changes. Objects with complex biological system have multicomponent EPR-spectra, which can be interpreted only using the models based on the quantum theory.

The purpose of this work is EPR-method capability check in the investigation of pathogenic changes in samples of a bone tissue in conditions of application the thermal processing.

According to the radiospectroscopic data, in many biomaterials free ions-radicals are observed; they generally can be formed during the thermochemical reaction taking place in substance at the annealing. [2].

At thermal processing of bone tissues, annealing causes the thermochemical transformations concerned with bonds break in organic molecules, which form a carcass of spongy bones, and the formation of uncompensated electrons on molecules fragments, that results in appearance of paramagnetic properties of this tissues. [3].

Investigations of samples of a spongy bone tissue were carried out using the radiospectrometer ESR70-03 DX/2 with working frequency 9,3 – 9,7 GHz (i.e. λ=3 cm). The standard sample $MgO:Mn^{2+}$ at 20°C has been applied for the spectrometer adjustment. As a material we have chosen the heads of the femoral joints with coxarthrosis (i.e. pathogenic) and healthy ones (i.e. normal). Then the samples with mass of 4-10 mg were cut out. They were placed in a furnace and annealed at temperatures from 20°C to 700°C with step of 20°C. After each cyclic annealing the EPR-spectra were obtained. The temperature dependences of the intensity, ions-radicals concentration, concerned with intensity, spectrum linewidth and g-factors are plotted, using the results of EPR-researches. (fig.1).

The analysis of the EPR-spectra concerned with defects in both inorganic and organic componets has shown, that there is no EPR-signals for normal and pathogenic bone tissues at the initial state (at room temperature 23°C). At the initial annealing stage the forms of EPR-spectra coincides for a normal bone tissue and a pathogenic one; the difference is shown for a normal bone tissue at 160°C, and for pathogenic one at 140°C.

EPR-spectra in an optimal temperature range of 420-460°C in which the stability of ions-radicals formation appear, are presented at fig.2. At fig.2 we can see, that intensity of signals for pathogenic samples is higher in this range , than for samples with a normal bone tissue; it is concerned with the formation of free ions-radicals with the maximal concentration in pathogenic samples.

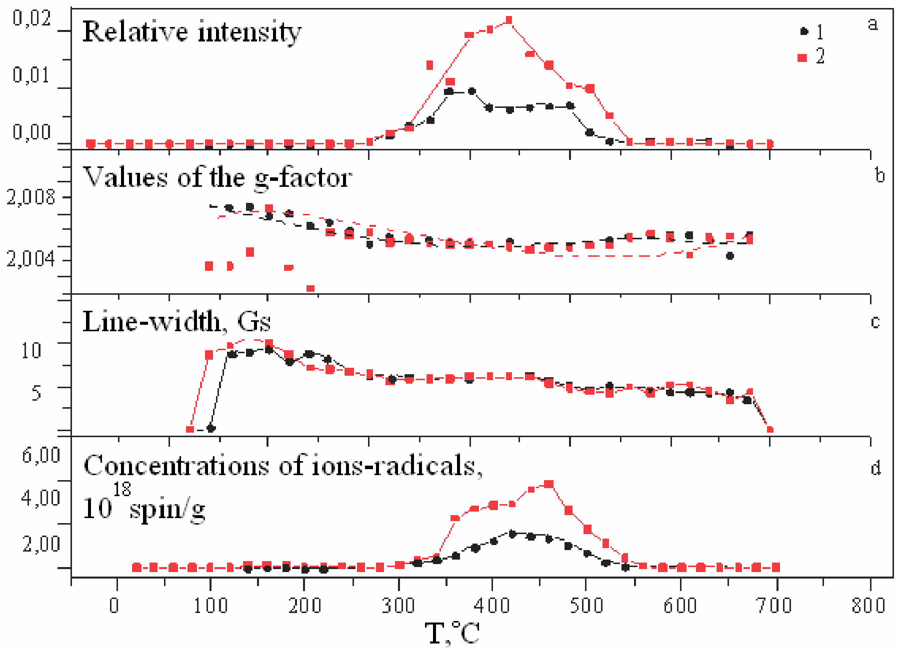

Fig.1. Temperature dependences of intensity (a), g-factor value (b), EPR line width (c) and thermochemical ions-radicals concentration R_{tc} (d) in the samples of normal (1) and pathogenic (2) bone tissues

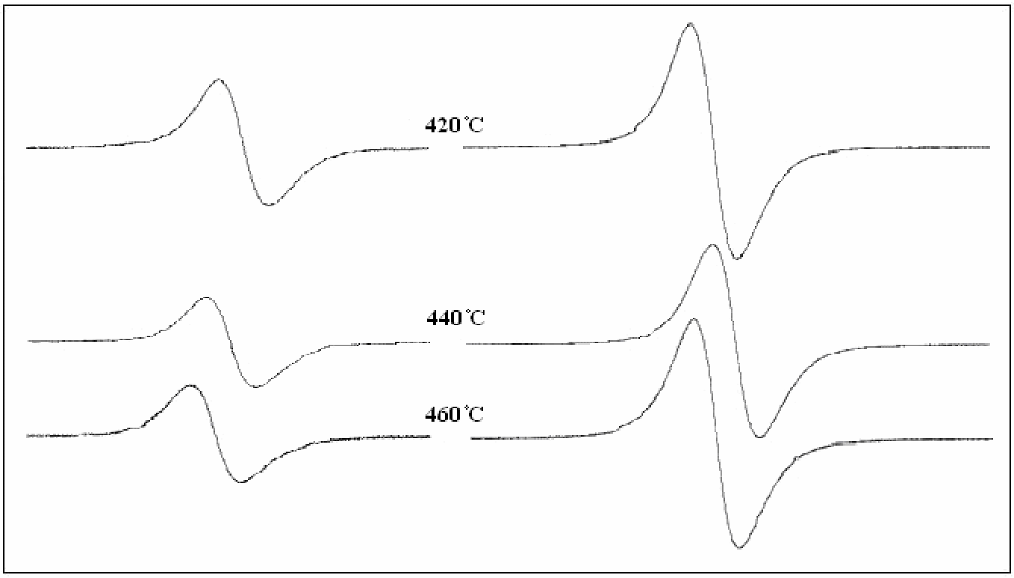

Fig.2. EPR-spectra of samples of normal (left) and pathogenic (right) bone tissues, annealed in the optimal range 420–460 ^{0}C, when the chemical ions-radicals concentration reaches its maximum

Thermochemical ions-radicals appear in bone samples at thermodestruction (thermodissociation) of low- and high-molecular organic substances, e.g. albumin, collagen, etc. Annealing does not cause formation of ions-radicals in inorganic component of a bone tissue, but transforms only an organic component [2].

Absence of EPR-signals from radicals R_{tc} for initial samples at room temperature is the evidence that degradation of an organic component is not accompanied by break of bonds in molecules with formation of the stable uncompensated electric charges on molecules fragments (ions-radicals) and changes of paramagnetic properties of a material. The signal intensity increases at the initial annealing stage, and then decreases; after the annealing at temperatures higher, than 700°C, the signal disappears for all samples (see fig.1). For a normal bone tissue the spectrum line width is 2,95-3,94 gauss, concentration of the ions-radicals is $3,5*10^{18}$ spin/g, g = 2,0024. For a pathogenic bone tissue this parameters changes, e.g. the range of linewidths decreases to 3,08-3,48 gauss, concentration of an ions-radicals increases to $5,7*10^{18}$ spin/g. G-factor values for both samples coincides in the margin of error, $g \approx 2,0027$.

It is possible to assume, that appearance and the subsequent disappearance of a signal in process of annealing are caused by thermoactivated transformations of an organic component of samples [2]. Moreover, the characteristic property of an ion-radical R_{tc} dynamics is the regular change of EPR-spectra parameters during the annealing process, in particular, the reduction of the g-factor value, narrowing of a linewidth and change of the signal maximum, which concerned with concentration of ions-radicals, at the temperatures of 140-160°C (fig.1).

In a range of 20 – 700°C this pictures are accompanied by the reduction of a bone tissue weight, that is concerned with the loss of adsorptive and structural water and burning-out of the organic substances presented by collagen and non-collagenic proteins with small molecular weight.

Using the EPR-method the difference in change of the spectrum form and concentration of ions-radicals in samples has been determined, as well as the linewidth narrowing with temperature increase for all samples that is the evidence of substance crystallinity reduction. There is a transformation of organic component of a bone tissue in pathogenic samples that results in crystallinity reduction of the inorganic component. Therefore intensity of signals of thermochemical ions-radicals in pathogenic samples is higher, than in normal ones. It is established, that the maximal concentration of ions-radicals is formed at sample processing in a range of optimal temperatures of 420-460°C, for a pathogenic bone tissue the concentration is higher.

In order to increase the EPR-researches efficiency we works on adaptation of more highly sensitive EPR-spectrometer, RE 1308, with working frequency 37 GHz (i.e. range is 8 mm).

This investigation has shown, that application of EPR-method for diagnostics of thermochemical radicals gives encouraging results, however its application is toilful and demands improvements of a research technique.

Thus, the application of EPR-method for research of dynamics of thermochemical radicals gives encouraging results, especially in temperature range (420-480 °C), which is optimal for the control. However, it is required a lot of additional complex researches to form the efficient diagnostic branch.

References

[1] Pul Ch. EPR-spectroscopy technique // «MIR», 1970, p. 553

[2] Votyakov S. L., Lemesheva S. L., Golovanova O. A. Thermochemical ions-radicals in organic component of a human bone tissue, influence of pathogenic changes // Materials of the III Russian conference with international participation. Syktyvkar 2009, p. 162–165

[3] Votyakov S. L., Borisov D. R., Ron' G. I., Mandra Yu. V. Radiation paramagnetic defects in biogenic apatites // Ekaterinburg, Publ. UB RAS, 1998. p.129-134

[4] Gilinskaya L. G., Zanin Yu. N. Stabilization factors of paramagnetic radicals CO_2^- CO_3^-, CO_3^{3-} in natural carbonateapatites // JSC, Vol. 39, № 5, 822-842 pp., 1998.

Spin probe techniques in supramolecular chemistry

A.I. Litvinov[1], F.G. Valeeva[1], N.N. Pashirova[1], R.A. Safiullin[2], L.Y. Zaharova[1],
M.K. Kadirov[1]

[1]A.E. Arbuzov Institute of Organic and Physical Chemistry, Kazan Scientific Center, Russian Academy of Sciences, 420088, Arbuzov str., 8, Kazan, Russia.

[2]Kazan State University, 420008, Kremlyovskaya str., 18, Kazan, Russia.

e-mail: zenituwka88@gmail.com

Electron spin resonance (ESR) has been widely applied to investigate the microenvironmental properties and dynamics of surfactant micelles using persistent nitroxide spin probes for several decades. The technique with a high time resolution of better than a few nanoseconds can give some information on the rapid fluctuation of aggregates with the nature of the surfactant and with the properties of its microenvironment. Also the advantage of the technique is that only the probe resonance is obtained and there is no interference from nuclear resonance signals.

If the nitroxide label tumbles rapidly in solution so that during one oscillation of the microwave field it can assume many orientations relative to the static magnetic field, then the anisotropic dipolar interacotion is averaged to zero and the observed coupling is due to the isotropic coupling only. Although the dipolar term has no effect on the line positions where there is rapid tumbling of the nitroxide, the mean square fluctuations in line positions contribute to the line widths. The rate of rotation is characterized by a rotation correlation time τ_c, defined as inverse rate or time it takes a molecule to rotate to an angle of one radian. Any shortening of the life time of the electron in its energy states will result in line broadening. The broadening depends on the orientation of the nitrogen nucleus in the magnetic field. The high field line $m_{N(-1)}$, will be broader than the low field line while the central line is least affected. According to the Kivelson`s theory of line widths in dilute solutions the rotation correlation time can be given by the expression:

$$\tau_c = 6.5 \cdot 10^{-10} \cdot W_0 \left(\sqrt{\frac{h_0}{h_{-1}}} + \sqrt{\frac{h_0}{h_{+1}}} - 2 \right) \text{(sec)}, \tag{1}$$

where, h_0 is the height of the central line, h_{-1} is the height of high field line, h_{+1} is the height of the low field line, and W_0 is the line width of central line [1,2].

TEMPO spin probe can also be used in cyclic voltamperometry due to it's reversible oxidation line. CV is the most versatile electroanalytical technique for the study of electroactive species. An electroactive probe helps in exploring the micellar environment in which it is solubilized [3,4].

Another class of spin probes used in this work are phenothiazine and it's derivatives. It is shown that during photoionization of phenothiazine it's paramagnetic radicals have significant lifetime only in presence of supramolecular structures (micelles, vesicles, liquid crystals, etc), the same is true for it's derivatives [5,6].

ESR spin probe TEMPO was used to study aggregation properties of cationic surfactants: CTAT, CTAB, TFFB-n (n=8, 10, 14, 16), DABCO; nonionic surfactants Triton X-100, 9COn (n=8,16), and amphiphilic copolymer Pluronic F127. Electrochemical oxidation technique was also used for further investigation of 9CO8 and 9CO16. Anionic surfactant SDS was studied using 10Me-phenothiazine spin probe.

The electron spin resonance spectra were recorded at 25 °C on a Brucker ELEXSYS E500 spectrometer operating at X-band with 100 kHz magnetic field modulation and 1.28 mW microwave power to avoid power saturation. The average relative error for the rotational correlation time was about 10%. 125W mercury-vapor lamp was used for photoionization of 10Me-phenothiazine probe. All spectra were run using 1 mm capillary tubes. The concentrations of spin probes in ESR measurements were 5×10^{-4} M. The probe concentration was small enough to be considered as a negligible perturbation. The ESR samples were equilibrated for 24 h before ESR measurements. Electrochemical voltamperometry was recorded using modified coaxial electrochemical cell [7,8]. The concentrations of TEMPO spin probe in electrochemical experiments were 1×10^{-3} M.

The surface tensions at the air/aqueous interface were determined by a du Nouy tensometer. The values were recorded after equilibrium had been attained, and they were the average value measured three times. The accuracy was about 0.1 m_N,m^{-1}. The measurements were conducted at 25 °C.

Spin probe rotation correlation times were calculated for all experiments with TEMPO probe. The results were then compared with surface tension of the same samples. In classic surfactant micelles spin probing reveals the same results for critical micellization concentration (cmc), as the tensiometry (fig.1).

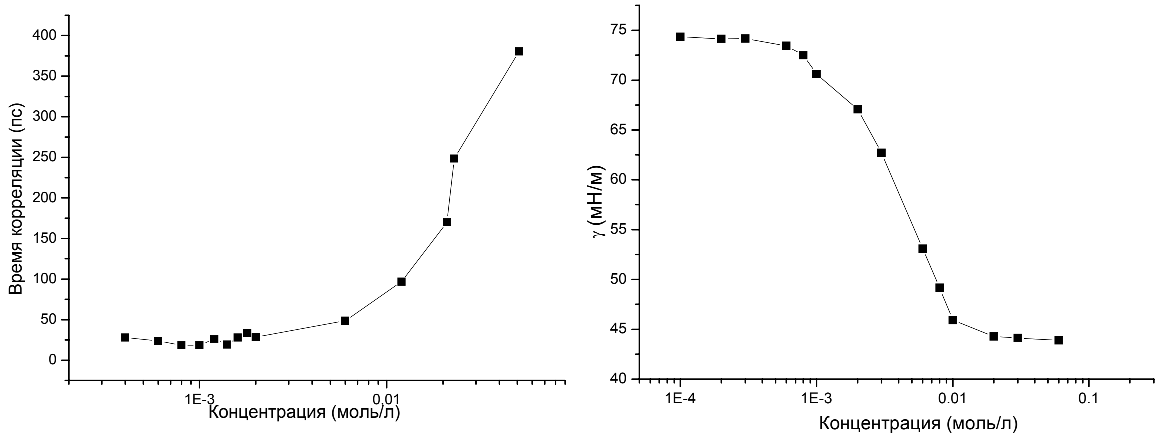

Fig.1. The rotational correlation time τ_c of the spine probe, TEMPO and surface tension as a function of the DABCO concentration; water, 25 °C.

Spin probing of more complex compounds reveal premicellar aggregation and structural reorganization (fig.2), though surface tension technique does not show that. CV was also performed for these amphiphiles (fig.3), which confirms the spin probe results.

10Me-phenothiazine was studied with ESR for possibility of it's use as spin probe. Solution of sodium dodecyl sulfate was used for this purpose at concentrations 0,005M and 0,1M to ensure absence and presence of micellar aggregates. The solution with lower concentration of surfactant, as expected, showed no spectrum, because 10Me-PTZ radicals have short lifetime. Micellar solution reveals ESR spectrum after 1min UV irradiation (fig.4). The result shows possibilities of it's application as spin probe in anionic supramolecular systems and in experiments with recharge of ionic micelles.

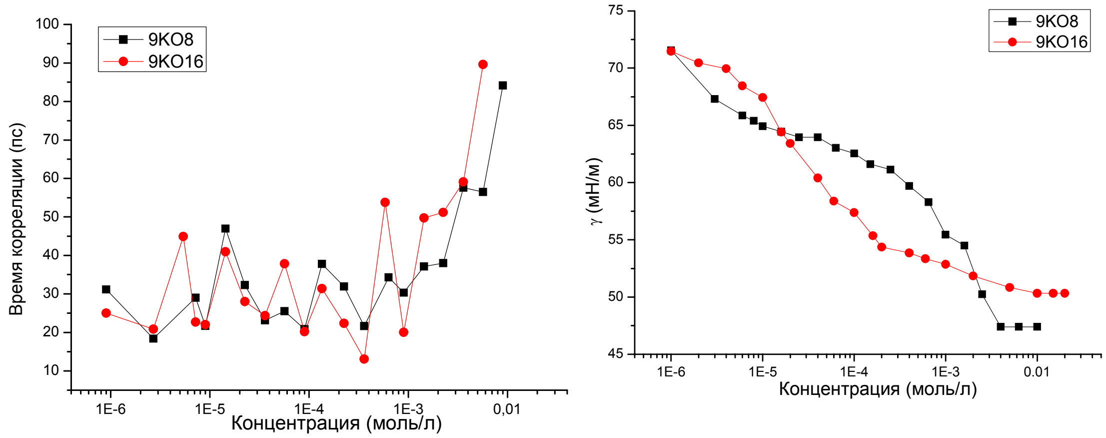

Fig.2. The rotation correlation time τ_c of the spine probe TEMPO and surface tension as a function of the 9CO8 and 9CO16 concentration; water, 25 ◦C.

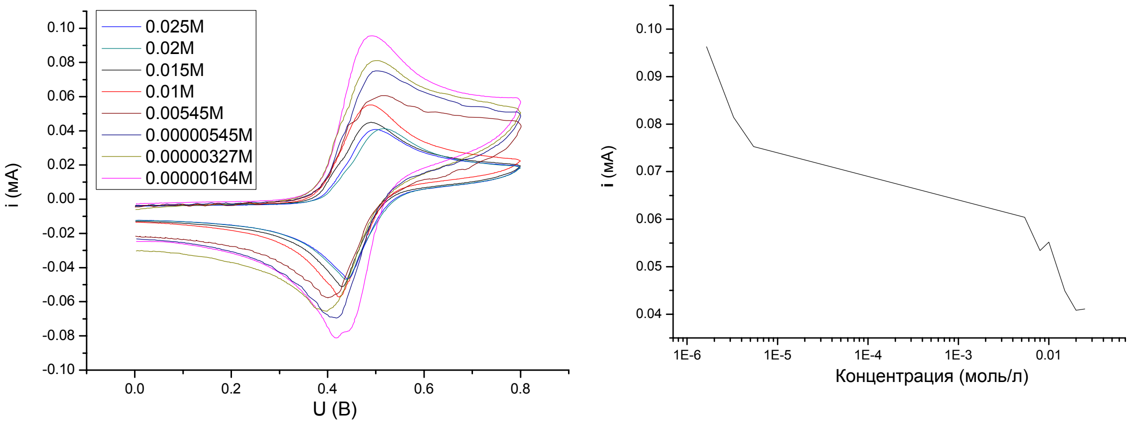

Fig 3. Reversible scan of TEMPO (1 mM) in micellar solution of 9CO8 and plot of peak current versus concentration of 9CO8 system.

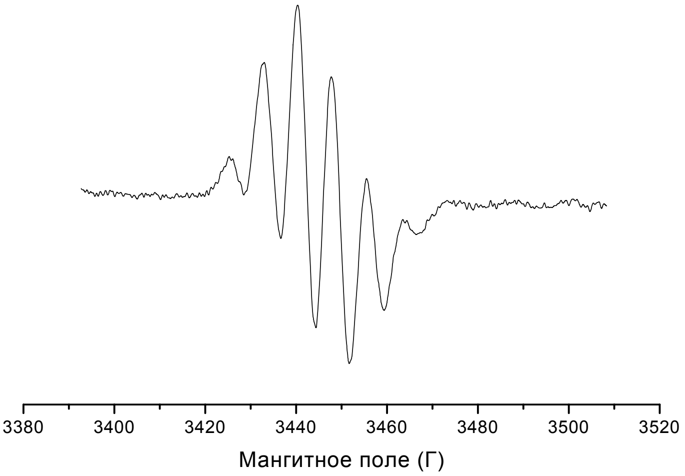

Fig.4. ESR spectrum of 10Me-phenothiazine in 0,1M water sotution of SDS

References

[1] Fendler. J. H. and Fendler, E. J., Catalysis in Micellar and Macromolecular Systems, Academic Press, New York, 1975, Ch. 2.

[2] Kivelson, D., .J. Chem. Phys. 33, 1094 (1960).

[3] A.B. Mandal, Langmuir 9 (1993) 1932.

[4] P.A. Hasan, J.V. Yakhmi, Langmuir 16 (2000) 7187.

[5] М.К. Кадиров Е.С. Нефедьев Известия АН. Сер. хим. – 2003. - №5. - С.1055-1059.

[6] Rakesh Kumar Mahajan, Navjot Kaur, Mandeep Singh Bakshi, Colloids and Surfaces A: Physicochem. Eng. Aspects 276 (2006) 221–227

[7] М.К.Кадиров, Е.С.Нефедьев, А.Г.Сафиуллин, М.И.Аюпов. Патент РФ 2120621, МКИ G01N24/10, G 01 R 33/10. (1998).

[8] М.К.Кадиров, Ю.Г.Будникова, О.Г.Синяшин. Патент РФ 67266, МПК G01N 27/26. (2007).

Electrochemistry-ESR of the sterically hindered imidazolidine zwitterions and its paramagnetic derivative

K. Kholin[1], M. Valitov[1], M. Kadirov[1], E. Tretyakov[2]

[1]A.E. Arbuzov Institute of Organic and Physical Chemistry, Kazan Scientific Center of the Russian Academy of Sciences, 8, akad. Arbuzova Street, 420088 Kazan, Russian Federation

[b]International Tomography Center, Siberian Branch, Russian Academy of Sciences, Institutskaya Street, 3a, 630090 Novosibirsk, Russian Federation

e-mail: kholin06@mail.ru

Nitroxide chemistry is an actively developing field of research [1–4], in which the electrochemical behavior of nitroxides remains one of the most interesting areas, because of the radical center is also an electrochemical active part of the molecules [5–8]. Their oxidation or reduction forms intermediates with high reactivity, as mentioned previously by Ullman et al. in their pioneering work [9].

We are interested in 4,4,5,5-tetramethyl-2-oxoimidazolidine-3-oxide-1-olate (anion **1**$^{\cdot-}$) which could, in principle, be used as a compact nitroxide paramagnetic anion for preparation of molecule based magnets. Deep blue solutions of the nitroxide paramagnetic anion **1**$^{\cdot-}$ are obtained by hydrolysis of 2-halo- [9] or 2-(azol-1-yl)-4,4,5,5-tetramethyl-4,5-dihydro-1H-imidazole-3-oxide-1-oxyls [10] under the action of an aqueous alkali. An alternative precursor of **1**$^{\cdot-}$ is 4,4,5,5-tetramethyl-1,2-dioxoimidazolidin-1-ium-3-olate (zwitterion) **2**; when bases, e.g. NaOH, K_2CO_3 in water or methanol, are added zwitterion **2** quickly transforms into **1**$^{\cdot-}$ (scheme 1). The paramagnetic anion **1**$^{\cdot-}$ is also formed from **2** after storing its solutions in ethanolic ammonia or amines for a week at 5°C. In MeOH (or EtOH) zwitterion **2** is gradually reduced to 1,3-dihydroxy-4,4,5,5-tetramethylimidazolidin-2-one (**H$_2$3**) [11]. We succeeded in crystallizing the $(Bu^tH_3N)^+1^{\cdot-}$ and $[(Bu^tH_2N)_2K]^+1^{\cdot-}$ paramagnetic salts directly from the reaction mixture under the conditions of cooling and in the presence of Bu^tH_2N, and we investigated the structure of these salts [11] Further development of the chemistry of **1**$^{\cdot-}$ demanded the investigation of the redox properties of both **1**$^{\cdot-}$ and **2**. In this work, we carried out an electrochemical study of **1**$^{\cdot-}$ and **2** using the combined cyclic voltammetry and ESR method (CV-ESR) [12].

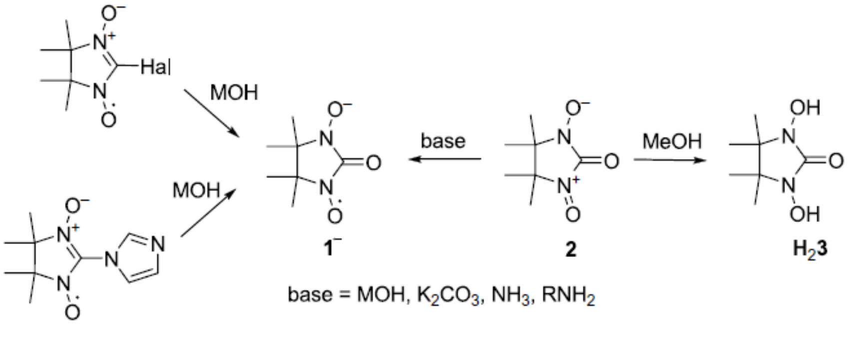

Scheme 1. Chemical transformations of zwitterion **2** and preparation of **1**$^{\cdot-}$

We used the combined cyclic voltammetry and ESR method to investigate the redox properties of the stable paramagnetic anion 4,4,5,5-tetramethyl-2-oxoimidazolidine-3-oxide-1-olate (**1**$^{\cdot-}$) and 4,4,5,5-tetramethyl-1,2-dioxoimidazolidin-1-ium-3-olate (**2**). The method allows simultaneous recording of usual voltammetric curves i(E) and dependences of the first derivative of overall ESR signal intensity s'(E) (in arbitrary units) during the scan of cell potential E. Direct comparison of CV curve and ESR signal intensity is not entirely valid, because the current is the first derivative of the charge that has passed through the cell, while the ESR signal level is proportional to the proper charge related to the depolarizer under study.

The CV (i(E)) and CV-ESR (s'(E)) curves obtained in the course of the electrochemical reduction of **2** in CH_3CN are shown in fig.1.

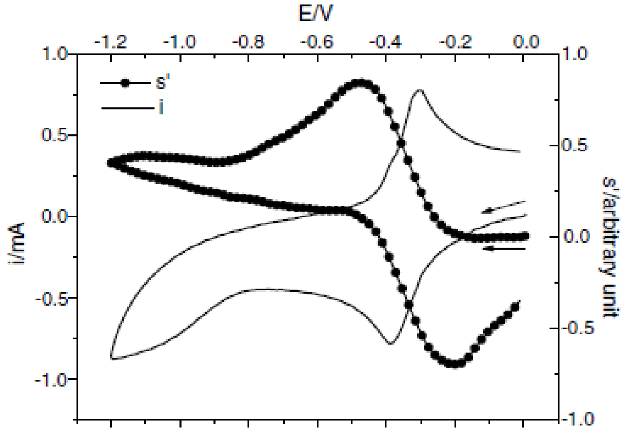

Fig.1. CV (i(E)) and CV-ESR (s'(E)) curves of the electrochemical reduction of zwitterion **2** ($5 * 10^{-3}$ mol* l^{-1}) in CH_3CN against the background of the $3 * 10^{-1}$ M solution of Et_4NBF_4 on a gold electrode. The potential scan rate was 0.1 V*s^{-1} (293 K).

The CV curve shows that a reversible electron transfer to **2** is observed at a potential E = -0.35 V, and at the first-peak potential ESR signal of single ESR-active species appears. The ESR spectrum of the resulting paramagnetic compound was a quintiplet, whose modeling gave a_N = 0.831 mT and g_{iso} = 2.0061. The magnetic resonance parameters were similar for the ESR spectrum of $\mathbf{1}^{\cdot-}$, which was obtained by adding a sevenfold excess of KOH (here and below, aqueous KOH) to the 5 *10^{-3} M solution of **2** in CH_3CN (fig.2).

Fig.2. Experimental ESR spectrum observed after the addition of a sevenfold excess of KOH to the 5 *10^{-3} M solution of **2** in CH_3CN.

Thus, at E = -0.35 V zwitterion **2** experienced a reversible one-electron reduction to paramagnetic anion $\mathbf{1}^{\cdot-}$ (scheme 2, reaction a).

$$\mathbf{2} \underset{+e}{\rightleftarrows} \mathbf{1}^{\cdot-} \qquad (a)$$

$$\mathbf{1}^{\cdot-} \underset{+e}{\rightleftarrows} \mathbf{3}^{2-} \qquad (b)$$

$$\mathbf{2} + \mathbf{3}^{2-} \longrightarrow 2\mathbf{1}^{\cdot-} \qquad (c)$$

Scheme 2. Electrochemical transformation of **2**.

As the negative potential grew further to E = -0.95 V, the CV (i(E)) curve acquired another wave (fig.1) as a result of the reduction of $\mathbf{1}^{\cdot-}$ to dianion $\mathbf{3}^{2-}$ (scheme 2b); the wave was irreversible under the given experimental conditions, but reversible at higher rates. The reason for the irreversible character of the second wave follows from the CV_ESR (s’(E)) curve; in the range of the potentials of the second wave, the intensity of the ESR signal grows at higher rates. Since in the range of applied potentials only ESR signal of **1**$^{\cdot-}$ was observed, one can draw a conclusion that a new process developed and led to the formation of **1**$^{\cdot-}$ after the formation potential of dianion **3**$^{2-}$ was reached; the formation rate of **1**$^{\cdot-}$ was higher than its consumption rate in reaction b (scheme 2). This process is probably comproportionation of **3**$^{2-}$ with **2** that is present in the electrochemical cell, leading to an increase in the concentration of **1**$^{\cdot-}$ (scheme 2c).

The addition of an equimolar amount of KOH to the 5 *10^{-3} M solution of **2** in CH_3CN led to a more complex ESR spectrum (fig.3).

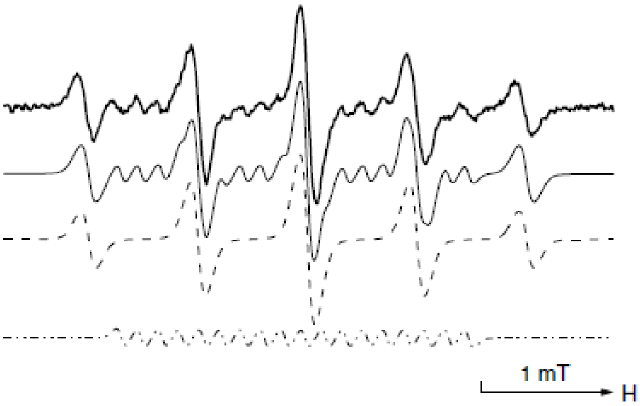

Fig.3. Experimental and simulated ESR spectra of the products formed by the addition of the equivalent amount of KOH to the 5 *10^{-3} M solution of **2** in CH_3CN and simulated spectra of the individual products.

As shown by the simulation, an experimental spectrum could be obtained by using a linear combination of the ESR spectrum of anion **1**$^{\cdot-}$ (a_N = 0.835 mT and g = 2.0061) with a contribution of 0.91 and the ESR spectrum of the protonated species **–H1**$^{\cdot}$ (a_{N1} = 0.994 mT, a_{N2} = 0.320 mT, a_H = 0.156 mT, g = 2.0069) with a contribution of 0.09. When the initial concentration of 2 was reduced tenfold, the ESR spectrum changed radically after the addition of the equimolar amount of KOH (fig.4).

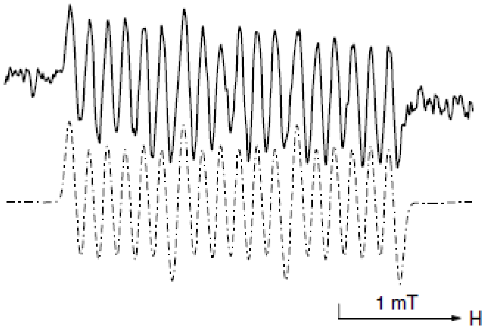

Fig.4. Experimental and simulated ESR spectra of 1-hydroxylamine-3-nitroxide **H1**$^{\cdot-}$ formed after the addition of the equivalent amount of KOH to the 5*10^{-4} M solution of **2** in CH_3CN. The number of accumulations was 31

The ESR spectrum showed that the dominant product in the reaction mixture was the nitroxide H1$^{\cdot}$ that was recorded as an admixture of **1**$^{\cdot-}$ in fig.2.

We carried out the electrochemical reduction of this reaction mixture. The first derivative of the ESR signal intensity (s’(E)) of **1**$^{\cdot-}$ increases at the potentials of this wave with a half-peak E = -0.15 V (fig.5). This suggests that due to the lack of added KOH the initial solution contained a certain amount of **2**, which was electrochemically reduced to **1**$^{\cdot-}$. Further growth of the anode potential gives rise to a second wave with a half-peak E = -0.55 V. This wave is accompanied by growth of the formation rate of **1**$^{\cdot-}$ after a certain decrease in it. It is reasonable to assume that this is the wave of the reduction of **1**$^{\cdot-}$ to **3**$^{2-}$, which, in turn, gives paramagnetic anions **1**$^{\cdot-}$ as a result of comproportionation with **2** (reaction c, scheme 2). The decrease in s'(E) is determined by reaction b, while the increase is the result of reaction c.

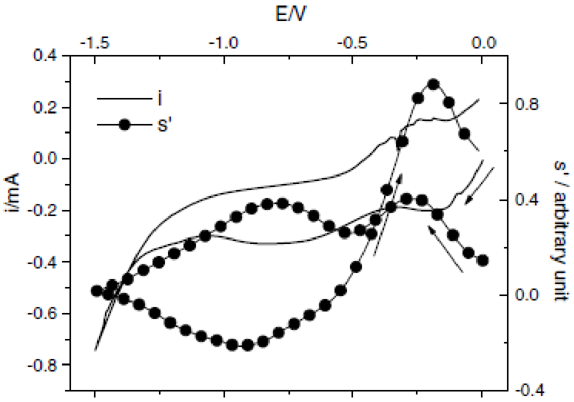

Fig.5. CV (i(E)) and CV–ESR (s'(E)) curves during the electrochemical reduction of the reaction mixture formed by the addition of the equivalent amount of KOH to the 5*10^{-3} M solution of **2** in CH$_3$CN against the background of 3*10^{-1}M Et$_4$NBF$_4$ on a gold electrode. The potential scan rate is 0.1 V s^{-1} (293 K).

Thus, our electrochemical-ESR study allowed us to understand the complex system of redox transformations in the **1**$^{\cdot-}$/**2** pair, which should be taken into account in selecting the conditions of reactions with **1**$^{\cdot-}$ and **2** and related compounds.

References

[1] L.B. Volodarsky, Pure & Appl. Chem. 62 (1990) 77–181.

[2] L.B. Volodarsky, V.A. Reznikov, V.I. Ovcharenko, Synthetic Chemistry of Stable Nitroxides, CRC Press, Boca Raton, Ann Arbor, London, Tokyo, 1994.

[3] R.G. Hicks, Org. Biomol. Chem. 5 (2007) 1321–1338.

[4] G.I. Likhtenshtein, J. Yamauchi, S. Nakatsuji, A.I. Smirnov, R. Tamura, Nitroxides: Applications in Chemistry, Biomedicine, and Materials Science, Wiley-VCH Verlag GmbH & Co. KGaA, Weinheim, 2008.

[5] R. Ziessel, G. Ulrich, R.C. Lawson, L. Echegoyen, J. Mater. Chem. 9 (1999) 1435 – 1448.

[6] E. Coronado, C. Gimenez-Saiz, M. Nicolas, F.M. Romero, E. Rusanov, H. Stoeckli-Evans, New J. Chem. 27 (2003) 490–497.

[7] H. Nishide, T. Suga, Electrochem. Soc. Interf. 14 (4) (2005) 32–33.

[8] T. Kurata, K. Koshika, F. Kato, J. Kido, H. Nishide, Polyhedron 26 (2007) 1776–1780.

[9] D.G.B. Boocock, E.F. Ullman, J. Am. Chem. Soc. 90 (1968) 6873–6874.

[10] E.V. Tretyakov, G.V. Romanenko, V.I. Ovcharenko, Tetrahedron 60 (2004) 99–103.

[11] E. Tretyakov, S. Fokin, G. Romanenko, V. Ikorskii, V. Ovcharenko, Polyhedron 26 (2007) 1917–1922.

[12] M.K. Kadirov, Yu.G. Budnikova, T.V. Gryaznova, O.G. Sinyashin, M.P. Bubnov, A.V. Krashilina, V.K. Cherkasov, Russ. Chem. Bull., Int. Ed. 56 (2007) 104–107.

Identification of shallow Al donors in ZnO monocrystals by means of High-Frequency EPR and ENDOR spectroscopy

Y.S. Kutin[1], G.V. Mamin[1], S.B. Orlinskii[1], N.I. Silkin[1], F. Herklotz[2], E.V. Lavrov[2], J. Weber[2]

[1]Kazan Federal University, Federal center of physical and chemical measurements, 420008, Kremlyovskaya St.18, Kazan, Russian Federation.

[2]Technische Universität Dresden, 01062, Dresden, Germany

e-mail: yuri_kutin@mail.com

ZnO is a wide direct band gap semiconductor with the energy gap of 3.4 eV at room temperature. It has been attracting a lot of attention due to its many applications in UV light-emitting diodes, solar cells and other optical and electronic components. The group III elements, such as Al, Ga and In are typical dopants in ZnO crystals. They act as shallow donors by substituting Zn atoms at their regular lattice sites.

The hyperfine interaction constants of Ga and In shallow donors in ZnO are large enough for the hyperfine splitting to be observed directly in EPR spectra [1]. In the case of Al, however, the constant is significantly smaller. The hyperfine splitting resulting from ^{27}Al nuclei is not resolved in EPR spectra and the chemical nature of the Al shallow donor cannot be established by means of conventional EPR. This makes the actual nature of shallow donors occurring as a result of Al-doping of ZnO somewhat ambiguous.

The enhanced spectral resolution of high-frequency EPR and electron nuclear double resonance (ENDOR) makes them a powerful tool for studying impurities and defects in a solid body. In this work we present the results of a high-frequency EPR and ENDOR study which reveal the shallow character of the substitutional Al impurity in ZnO.

All experiments were performed at 15 K with a Bruker Elexsys 680 EPR spectrometer with the microwave frequency around 94.9 GHz. ENDOR spectra were recorded using the standard Mims pulse sequence [2].

EPR spectra of the studied ZnO sample contain signals originating from the Mn^{2+} ion and an unknown shallow donor. The shallow donor EPR line is symmetric, its half-height width is about 0.5 mT. Fig. 1 shows its angular dependence, which can be fitted by

$$g = \sqrt{g_{\parallel}^{2}\cos^{2}\theta + g_{\perp}^{2}\sin^{2}\theta}, \tag{1}$$

where θ is the angle between the applied magnetic field and the crystallographic c axis direction. The g-tensor values $g_{\parallel} = 1.9578(5)$ and $g_{\perp} = 1.9564(5)$ are typical for shallow donors in ZnO [1]. The g-factor anisotropy is the same as obtained for the interstitial H donor, while the absolute values are somewhat larger, which indicates that this is a deeper donor as compared to the interstitial hydrogen [3].

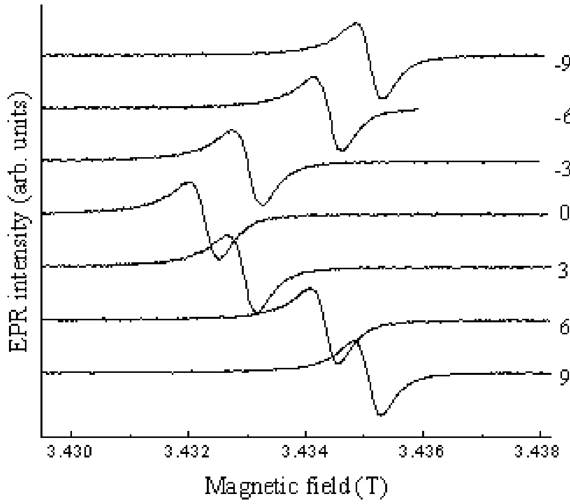

ig.1. Angular dependence of the shallow donor EPR line position. The microwave frequency is 94.1 MHz, $T = 15$ K.

In order to determine the chemical nature of the unknown shallow donor we performed high-frequency ENDOR experiments, which reveal interaction of the shallow donor electron with surrounding magnetic nuclei. The obtained ENDOR spectra show two groups of lines corresponding to ^{27}Al ($I = 5/2$, natural abundance 100%) and ^{67}Zn ($I = 5/2$, natural abundance 4.11%) nuclei.

Fig.2 shows the ENDOR lines of ^{67}Zn nuclei observed in the EPR signal of the shallow donor in two orientations (with the c axis parallel and perpendicular to the applied magnetic field). The broad, poorly resolved ENDOR line is placed symmetrically around the Zeeman frequency of ^{67}Zn. This structure implies that the shallow donor electron interacts with a large number of ^{67}Zn nuclei, which confirms that its wave function is significantly delocalized. The observed splitting of the ^{67}Zn line is caused by the quadrupole interaction.

Fig.3 shows the ENDOR spectrum of ^{27}Al nuclei as observed in the EPR signal of the shallow donor in two orientations (with the c axis parallel and perpendicular to the applied magnetic field). Two groups of ENDOR lines are placed symmetrically around the Zeeman frequency of ^{27}Al. The ENDOR transition frequencies with the quadrupole interaction taken into account in the case of axial symmetry and $S = 1/2$ [4] are given by

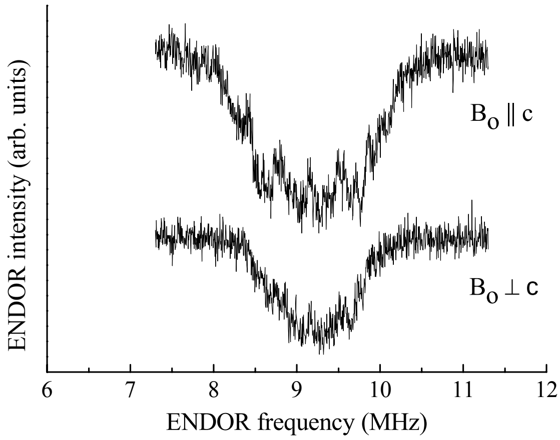

Fig.2. The ENDOR signals of the ^{67}Zn nuclei (I = 5/2) observed in the EPR signal of the shallow donor in two orientations. $T = 15$ K.

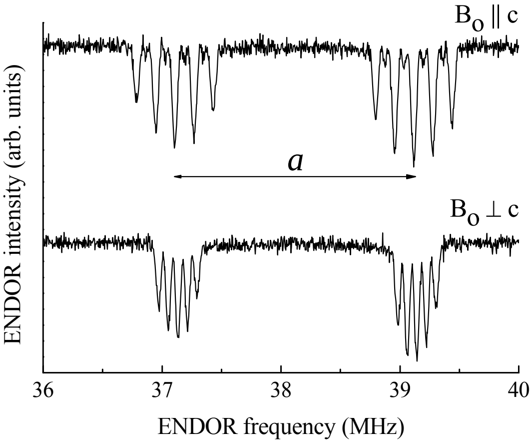

Fig.3. The ENDOR signals of the ^{27}Al nuclei (I = 5/2) observed in the EPR signal of the shallow donor in two orientations. $T = 15$ K.

$$\nu^{\pm}_{iENDOR}(m_I) = \left| \nu_n \pm \frac{a_i}{2} + \frac{3e^2qQ}{4I(2I-1)h} \cdot m_q \cdot (3\cos^2\theta - 1) \right|, \tag{2}$$

where a_i is the hyperfine interaction constant, Q is the constant of the quadrupole interaction and m_q is the average value of the nuclear quantum states $m_{I'}$ и m_I, between which the nuclear transition takes place. Nuclear spin of ^{27}Al is $5/2$, which implies that there are five values of $m_q = \pm 2, \pm 1, 0$, hence the splitting of the lines into two quintets as seen in fig.3.

The hyperfine interaction constant $a_{Al} = 2.010(2)$ MHz is shown in fig.3. It should be noted that while the hyperfine interaction is isotropic, it is somewhat stronger than in the case of the interstitial H donor ($a_H = 1.4$ MHz) [3].

The absolute value of $(3\cos^2\theta - 1)$ in Eq. (2) is twice as large for $\theta = 0°$ as it is for $\theta = 90°$. It is seen in Fig. 3 that when orientation of the sample changes from parallel to perpendicular the quadrupole splitting decreases by the factor of two ($161\,\mathrm{kHz}$ and $80.5\,\mathrm{kHz}$ respectively).

Let us rewrite the quadrupole term in (2) as follows [5]. For brevity we introduce $\nu_Q = \frac{3e^2qQ}{2I(2I-1)h}$. Since m_q can be rewritten as $(m_I - 1/2)$, the first-order shift in frequency caused by the quadrupole interaction is given by

$$\Delta\nu_m = -\frac{\nu_Q}{2}(m_I - 1/2)(3\cos^2\theta - 1)\,. \tag{3}$$

Frequency of the central transition $-1/2 \leftrightarrow 1/2$ is not shifted in the first order approximation.

When the c axis is parallel to the applied magnetic field ($\theta = 0°$) the adjacent lines are separated by $\Delta\nu = 161\,\mathrm{kHz}$. Since $(3\cos^2\theta - 1) = 2$, the shift in frequency for $m_I = 3/2$ becomes $\Delta\nu_m(m_I = 3/2) = -\frac{\nu_Q}{2}\cdot(3/2 - 1/2)\cdot 2 = -\nu_Q$, which implies that $\nu_Q = 161\,\mathrm{kHz}$. From here we calculate the quadrupole interaction constant for ^{27}Al as $\frac{e^2qQ}{h} = 1.073\,\mathrm{MHz}$.

In summary, we investigated a ZnO monocrystal sample doped with Al by means of high-frequency EPR and ENDOR spectroscopy at 95 GHz. The ENDOR spectra of ^{27}Al obtained in the study unambiguously show that Al in ZnO acts as shallow donor by substituting Zn at its regular lattice sites.

References

[1] B. K. Meyer, H. Alves, D. M. Hofmann, W. Kriegseis, D. Forster, F. Bertram, J. Christen, A. Hoffmann, M. Straßburg, M. Dworzak, U. Haboeck, and A. V. Rodina, Phys. Status Solidi B 241, 231 (2004).

[2] W.B. Mims, in Electron Paramagnetic Resonance, edited by S. Geschwind (Plenum, New York, 1972).

[3] D.M. Hofmann, A. Hofstaetter, F. Leiter, H. Zhou, F. Henecker, B. K. Meyer, S. B. Orlinskii, J. Schmidt, and P.G. Baranov, Phys. Rev. Lett. 88, 045504 (2002).

[4] S. B. Orlinskii, J. Schmidt, P. G. Baranov, M. Bickermann, B. M. Epelbaum, and A. Winnacker, Phys. Rev. Lett. 100, 256404 (2008).

[5] A. Abragam and B. Bleaney, Electron Paramagnetic Resonance of Transition Ions (Clarendon, Oxford, 1982).

EPR/ENDOR of hydroxyapatite nanocrystals doped by lead ions

A.T. Gubaidullin[3], E.S. Kovaleva[2], G.V. Mamin[1], S.B. Orlinskii[1], V.I. Putlaev[2],
A.A. Rodionov[1], N.I. Silkin[1], Yu.D. Tretyakov[2], B.V. Yavkin[1], M.Kh. Salakhov[1]

[1]Kazan Federal University, Federal Center of Shared Usage for Physicochemical Measurements

[2]Moscow State University

[3]Institute of Organic and Physical Chemistry KSC RAS, Kazan

e-mail: boris.yavkin@google.com

Introduction

Hydroxyapatite — $Ca_{10}(PO_4)_6(OH)_2$ — is one of the intensively studying materials in contemporary inorganic materials science. The interest in a hydroxyapatite researches is dictated not only by the number of its applications, e.g. bone tissue repairing[1], radionuclide sorption[2], but also by its complex structure that allows a lot of anionic and cationic substitutions. The important feature of the hydroxyapatite structure is the presence of the two nonequivalent calcium positions called Ca-1 and Ca-2. The distances between Ca-1 and the nearest phosphorous is 3.2Å and is 5.4Å for distance between Ca-1 and hydrogen; for Ca-2 these distances are 3.0Å and 2.8Å respectively. In this work authors studied hydroxyapatite doped by lead ions – $Ca_{10-x}Pb_x(PO_4)_6(OH)_2$ (PbHAP) and determined characteristics of Pb^{3+} paramagnetic centers and their localization within crystal.

Materials

Two powder samples with one hour and seven days synthesis time were studied. The average nanocrystal sizes were evaluated from X-ray diffraction spectra (fig.1a) at 20nm and 1µm, respectively.

The activation process is the isovalent substitution of Ca^{2+} ions for Pb^{2+}, but this valence state of lead ions isn't paramagnetic for the outer 6s electronic shell has two electrons with the opposite spins. To produce paramagnetic centers samples were treated by X-ray and

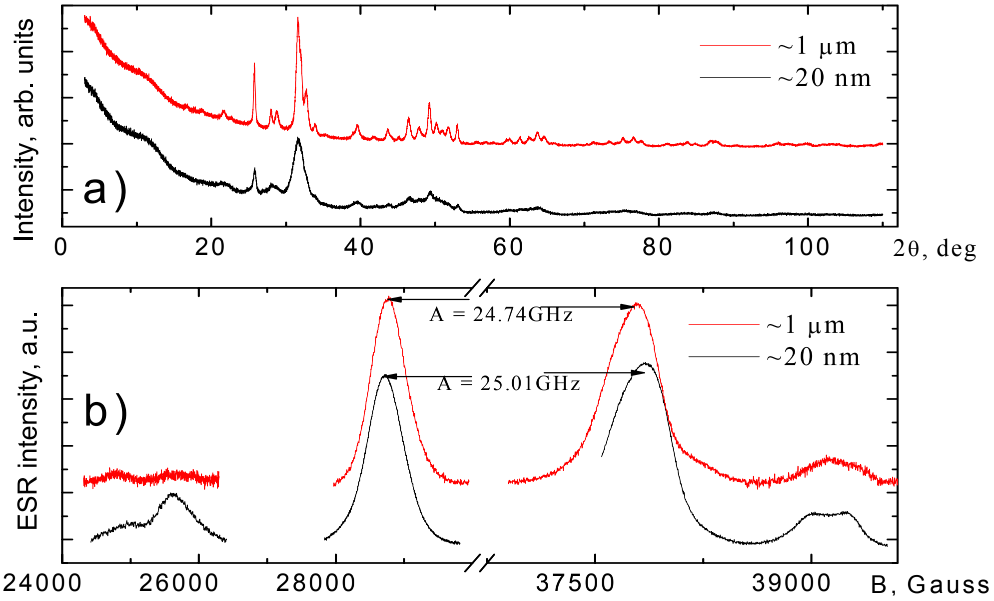

Fig.1. X-ray diffraction spectra (a) and EPR spectra (b) of nanocrystalline and microcrystalline lead doped hydroxyapatite.

eventually some amount of Pb^{2+} converted into Pb^{3+} with the electronic spin $S = ½$. It is important to note that the lead ions have the electronic spin as well as the nuclear spin. Only one of the natural isotopes, Pb-207, with natural abundance 21.6% has nuclear spin $I = ½$, whereas even isotopes with mass number 204,206 and 208 have no nuclear spin.

Methods

Samples were studied by high-frequency (94GHz) pulsed electron paramagnetic resonance (EPR) and electron-nuclear double resonance (ENDOR) with Bruker Elexsys 680 spectrometer. For low-temperature experiments helium-flow cryostat made by Oxford Instruments was used. EPR spectra were recorded by means of two-pulse echo sequence, ENDOR spectra were detected by Mims technique. X-ray irradiation of the samples were carried out in the URS-55 (U = 55kV, I = 16mA, W - anticathode) at room temperature, dose of radiation was assessed at 10kGy.

Results and summary

The EPR spectra of the non-irradiated hydroxyapatite samples activated by the lead ions did not show the presence of the paramagnetic centers within the nanocrystals.

The EPR spectrum of the PbHAP after X-ray exposure was composed of two lines, nonoverlapping with the g-factor~2 region, which is typical for the systems with $S = ½$, $I = ½$. The splitting between these two lines is proportional to the hyperfine structure parameter. Characteristics of the paramagnetic centers are evaluated from EPR spectra and are represented as follows: $A_{1\mu n}$ = 24.74(5)GHz, A_{20nm} = 25.01(5)GHz and g = 1.982(2) for both samples. One can see that the strength of the hyperfine interaction increases with decreasing of the nanocrystal sizes. Typical EPR spectrum is shown in fig.1b. The EPR lines with low intensity, which were recorded at low and high magnetic fields, arise from Pb ions in the growth solution, i.e. these ions are not embedded within hydroxyapatite crystal lattice. This assumption was proved because these lines disappeared from the EPR spectrum of PbHAP samples after annealing at 400°C.

In the theoretical work[3] authors claimed that Pb ions can substitute Ca only in the Ca-2 site. In the present paper the ENDOR method is used to determine the substitution position experimentally. The ENDOR spectra of phosphorous and hydrogen are shown in fig.2a and fig.2b, respectively. The more is the strength of the superhyperfine interaction, the less is the distance between paramagnetic electron and neighboring nuclei. The strength of the

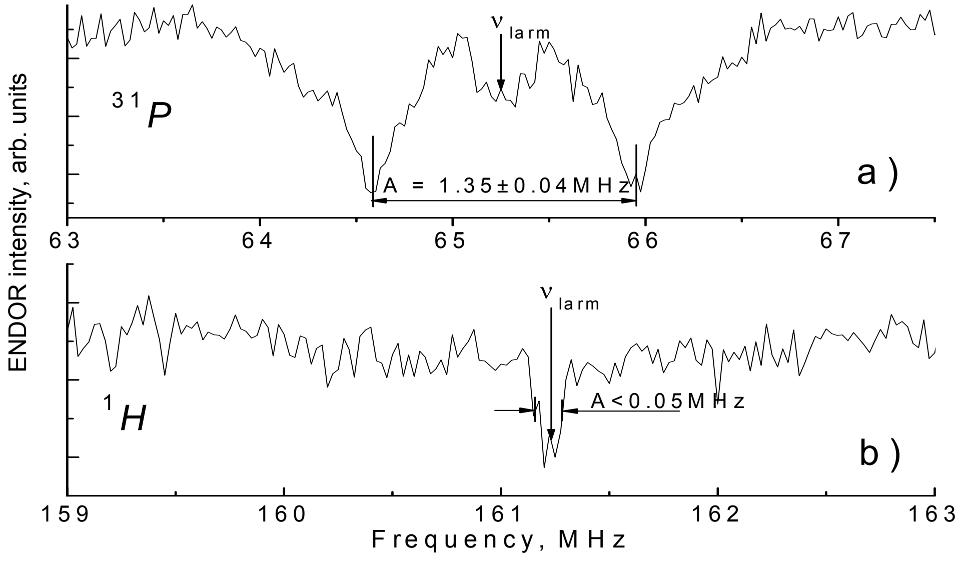

Fig.2. ENDOR spectra near to Larmor frequencies of phosphorous (a) and hydrogen (b) of nanocrystalline sample.

superhyperfine interaction is maximal for phosphorous nuclei, see fig.2a. From the hydroxyapatite structure analysis one can conclude that Pb substitutes Ca in Ca-1 position.

This work was supported by RNP № 6183 and DZN № 10-66.

References

[1] E. Kovaleva *et. al.*, Cent. Eur. J. Chem, 7, 168 (2009)

[2] Khrestenko R.V., Rudin V.N., Kalmikov S.N., Melikhov I.V., Vestnik Nizhegorodskogo Universiteta im. N. I. Lobachevskogo - 2008 - #5, pp 52-57

[3] K. Matsunaga, H. Inamori, and H. Murata, Phys.Rev. B **78**, 094101 (2008)

Electric field gradient in paramagnetic phase of compounds with structure of Kagome staircase $M_3V_2O_8$ (M = Co, Ni)

A.G. Smolnikov, V.V. Ogloblichev

Institute of Metal Physics, UB RAS, 620041, S. Kovalevskaya Str. 18, Ekaterinburg, Russia

e-mail: ogloblichev@imp.uran.ru

Geometrically frustrated magnet systems with common structural formula $M_3V_2O_8$ (M = Ni, Co), have been actively studied in physics of solid due to revealing a whole spectrum of phase changes in them. These systems with crystal structure of Kagome staircase are extremely perceptible to relatively unstable reactions and in such a way they can provide new and unusual examples of long and short-range magnet ordering.

$Ni_3V_2O_8$(NVO) and $Co_3V_2O_8$(CVO), studying in this work, have orthorhombic crystal structure *Cmca* (fig.1) [1-8]. Ions M^{2+} which are located in octahedron MO_6 form a great number of Kagome staircases which are divided between themselves by nonmagnetic layers of tetrahedrons VO_4. Kagome staircase contains two positions of atoms M^{2+}: M(S)-«spine» and M(C)-«cross tie». Vanadium is in non-magnetic state V^{5+} and doesn't have atoms M in the first coordinative sphere. The nearest neighbour of vanadium in this structure is an irregular tetrahedron from atoms of oxygen. Analyzing the parameters of electric-field gradient tensor $V_{\alpha\beta}$ one can receive the information about charge neighbours of the vanadium atom or about the tetrahedron deformation [9,10].

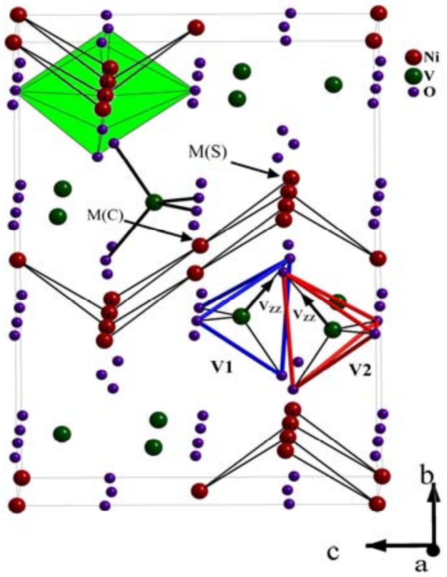

Fig.1. Crystal structure of compounds $M_3V_2O_8$

In paramagnetic area, T > 20K, in single crystals $Ni_3V_2O_8$ and $Co_3V_2O_8$ random distribution of hyperfine fields, and quadruple broadening of first-order determinates the form of line NMR of vanadium nuclear ^{51}V. For ^{51}V with spin $I = 7/2$ and electric quadruple moment $^{51}Q = 0.0515|e|\ 10^{-24}$ sm^2 2I lines should be observed: 2I-1 satellite transition between neighbouring levels plus central transition.

For getting an information about peculiarities of quadruple interaction parameters the detailed dependence of the form line NMR ^{51}V from the direction of the magnetic field ($H_0 \parallel bc$, $H_0 \parallel ac$, $H_0 \parallel ab$) for NVO and CVO was measured.At the direction of the field along *ac* and *ab* surfaces there are no evident splitting on 7 lines either in NVO or in CVO. However, at the direction of the magnetic fields along the surface *bc* and angle $\beta = 52(5)^o$ and $138(5)^o$=-$52(5)^o$ relatively of the axes *c* a maximum widening of the line is observed either for NVO or for CVO connected with appearing of satellites. Maximum widening testifies that the magnetic field is directed along principal value EFG, V_{ZZ}. As V_{ZZ} lies in plane *bc* under angle $52(5)^o$ to an axis *c*, to other planes it makes some varied angle: to plane $H_0||ab$ it varies from 38° to 90°, $H_0||ac$ - with 52° to 90°, - which does not lead to the considerable widening and thin structure of satellites of investigated compounds.

Dependence of resonance frequency of transition m →m-1 from angle θ and φ for nuclear with spin I and asymmetric tensor EFG $\eta = \left((V_{YY} - V_{XX}) / V_{ZZ}\right)$ in an external magnetic field looks like:

$$\Delta\nu(m \to m-1) = \nu_0 - \nu_Q \cdot (m - \frac{1}{2})(3\cos^2\theta - 1 + \eta \cdot \sin^2\theta \cdot \cos 2\varphi) \qquad (1)$$

where $\nu_Q = [3eV_{ZZ}Q]/[2I(2I-1)h]$ — quadruple frequency, θ — an angle between the direction of external magnetic field H_0 and the main axis of tensor EFG (V_{ZZ}), φ - an angle between the projection of a direction of a magnetic field to plane XY and an axis tensor EFG (V_{XX}) [9,10].

Each spectrum of vanadium was well described by three lines: two of them correspond to the quadruple split lines (*lines*1, *lines*2) of vanadium, and the third line (*line*3) with shift ^{51}K = 0 %, which position and form do not change with the temperature and orientation, we connect with the rests of oxide of vanadium V_2O_5 from which the sample has been prepared (fig.2).

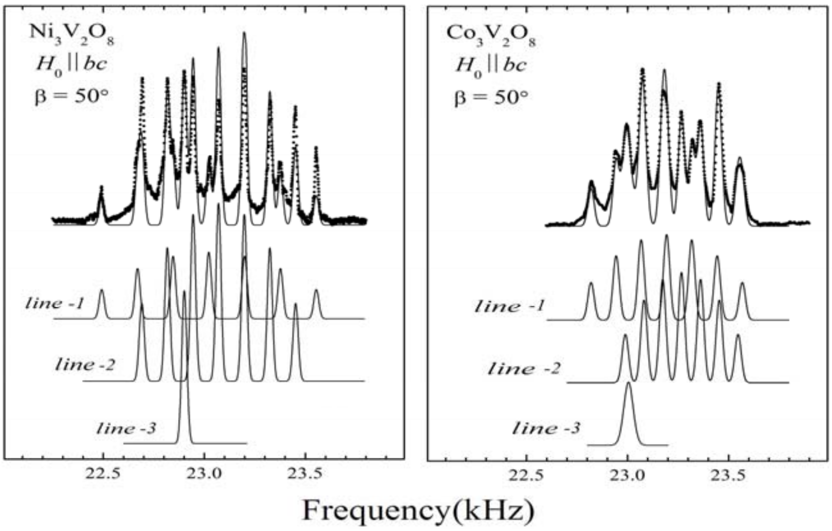

Fig.2. Nuclear magnetic resonance specters ^{51}V in compounds $Ni_3V_2O_8$ and $Co_3V_2O_8$ in magnetic field H_0 = 20kOe directed under an angle β = 50° to an axis *c* in a plane *bc* and temperature *T* = 300K. The spectrum is described by three lines: *line-1*, *line-2*; *line-3*

In a (fig.3) there is a dependence of distance between satellites $\Delta\nu$, from an angle $\beta = (52^o - \theta)$ between a direction of a magnetic field and crystallographic axis *c*, in compounds $Ni_3V_2O_8$ and $Co_3V_2O_8$ in orientation $H_0||bc$.

Data $\Delta\nu(\beta)$ are well describing by two functions (1), of identical values ν_Q = 180 (10) kHz η =0,5 (1) for NVO and ν_Q=120 (10) kHz η =0,6 (1) for CVO, but shifted rather each other on 85° from angle θ

The result analysis of calculation tensor EFG $V_{\alpha\beta}$ on vanadium atoms in model of dot charges showed, that there is two positions with different orientation of tensor axes EFG on vanadium atoms: principal value EFG V_{ZZ} lies in a plane *bc* and makes with an axis *c* an angle $\pm 52\ (5)^o$ for NVO and $\pm 52\ (5)^o$ for CVO, and asymmetrical parameters are respectively equal η =0,6 (1) and η =0,6 (1).

As to calculated values of quadruple frequencies they have values lower than observed in the experiment. Discrepancy of experimental and calculated figures of given quadruple frequencies lets us think that besides the screen contribution in EFG an essential role in

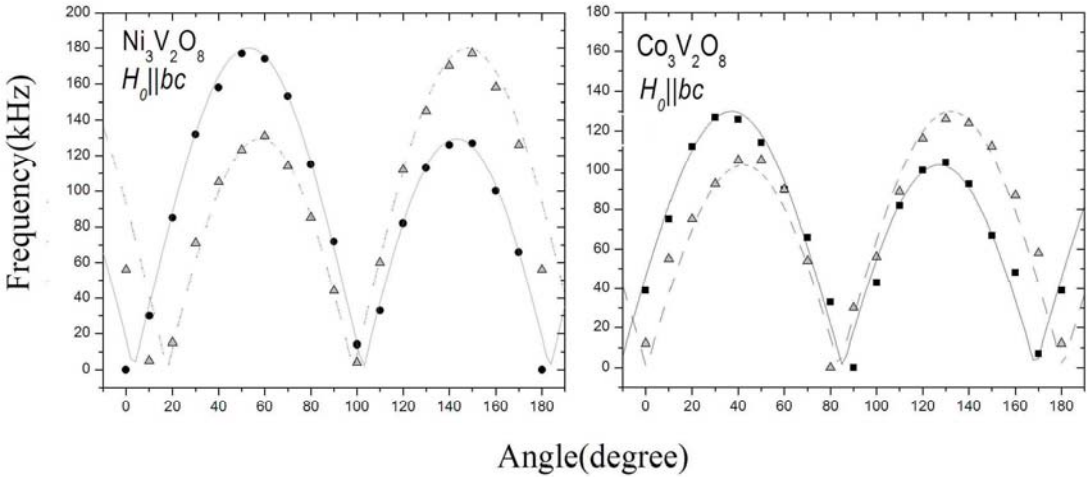

Fig.3. Dependence of distance between satellites $\Delta\nu$, from *line -1* и *line -2*, from an angle β in orientation $H_0 \parallel bc$. Continuous and a dashed line the result of processing is shown by function (1).

charging distribution round vanadium atom plays the valency contribution in these compounds.

Lower 150K there is impossible to track evolution of EFG parameters because of considerable magnetic line-broadening inhomogeneity and disappearance of thin spectra structure. However, as some works show [11,12] if heterogeneity of a magnetic field is less quadruple interaction then oscillations in attenuation of a spin echo arise, and the period of such oscillations is defined by quadrupole frequency.

On a (fig.4) the dependence a spin echo amplitude $E(2t)$ from the doubled delay between impulses 2t on a nuclear ^{51}V in single crystals $Ni_3V_2O_8$ and $Co_3V_2O_8$ is presented E(2t) represents an exponentially fading sinusoidal fluctuation. A continuous line is a result of approximation of data $E(2t)$ by the following expression:

$$E(2t) \propto \exp(-2t/T_2)[1 + A\cos(\pi\omega\tau)] \qquad (2)$$

at following values parameters: $A < 1$ – an amplitude of modulation, T_2 = 40(6) mks, $\omega(H_0||a)$ = 54(2) kHz, ω $(H_0||c)$ = 29(3) kHz for NVO and T_2 = 60(5) mks, $\omega(H_0 \parallel a)$ = 45(5)·kHz, $\omega(H_0 \parallel c)$ = 19(4) kHz for CVO.

Modulation frequencies of ω $(H_0||a)$ and ω $(H_0||c)$ coincide in limits errors with quadruple frequencies which were received from simulation of spectra in directions $H_0||a$ and $H_0||c$ at temperatures $T > 150$K.

These data indicate that changes of a charging environment round a vanadium kernel do not occur while the temperature lowering, hence, there is deformation of tetrahedron VO_4. Thus, it is possible to draw the following conclusions.

The result analysis of calculation tensor EFG in models of dot charges and a NMR of data on atoms of vanadium showed, that in compounds $Ni_3V_2O_8$ and $Co_3V_2O_8$ in which crystallographic nonequivalent vanadium atoms are not presented, there are two various orientations of axes EFG: V_{ZZ} lays in a plane *bc* and makes with an axis *c* angle ±52 (5)° for NVO and ±52 (5)° for CVO. Discrepancy of experimental and calculated figures of quadruple frequencies and asymmetrical parameters allows to assert that besides the contribution in EFG an essential role in these connections plays the valency contribution. The local symmetry and

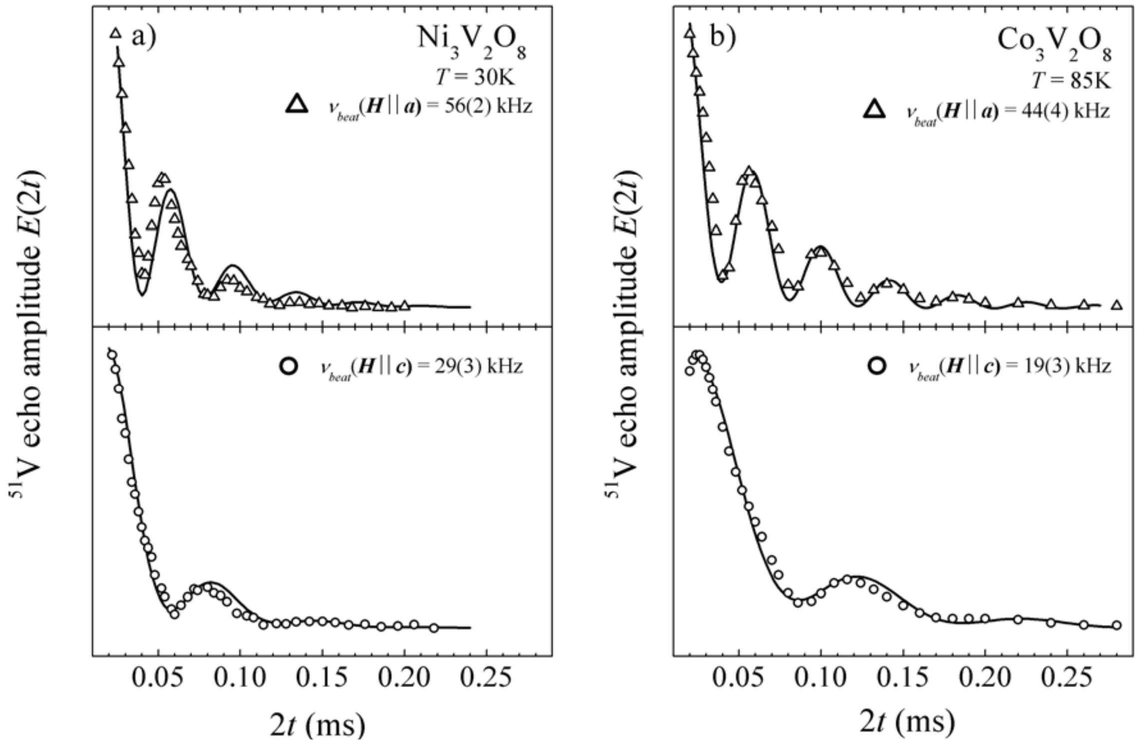

Fig.4. Dependence of amplitude of spin echo E (2t) from the doubled delay between impulses 2t on a nuclear ^{51}V in monocrystals $Ni_3V_2O_8$ at temperature T = 30K and $Co_3V_2O_8$ at T = 85K in two orientations of crystals $H_0 \| a$, $H_0 \| c$.

a charging environment on vanadium positions does not essentially change in the range of temperatures (30-300) K in structure NVO and CVO.

This work was supported in part by Russian Academy of Sciences Ural Branch (grant for young scientists (V.V.O.), by the Russian Foundation for Basic Research (Grants No 08-02-00029a, 0902-00310a).

References

[1] Y. Chen, J.W. Lynn, Q. Huang et al., Phys. Rev. B **74**, 014430 (2006).

[2] M. Kenzelmann, A.B. Harris, A. Aharony et al., Phys. Rev. B **74**, 014429 (2006).

[3] N. Rogado, M. Haas, G. Lawes et al., J. Phys.: Condens. Matter **15**, 907 (2003).

[4] A.B. Harris, Phys. Rev. B **76**, 054447 (2007).

[5] А.А. Мухин, В.Ю. Иванов, А.М. Кузьменко и др., Письма в ЖЭТФ **91**, 158 (2010).

[6] L.I. Vergara, J. Cao, L.C. Tung et.al., Phys. Rev. B **81**, 012403 (2010).

[7] Y. Yasui, Y. Kobayashi, M. Soda et.al., J. Phys. Soc. Jpn. **76**, 034706 (2007).

[8] E.E. Sauerbrei, R. Faggiani, and C. Calvo, Acta Cryst. B **29**, 2304 (1973).

[9] A. Abragam, The Principles of Nuclear Magnetism (Clarendon, Oxford, 1961).

[10] C.P. Slichter, *Principles of Magnetic Resonance* (Harper and Row, New York, 1963).

[11] H. Alloul and C. Froidevaux, Phys. Rev. **163**, 324 (1967).

[12] H. Abe, H. Yasuoka, and A. Hirai, J. Phys. Soc. Jpn. **21**, 77 (1966).

Mobility of tert-butyl alcohol in solid state studied by deuterium NMR Spectroscopy

A.M. Nischenko[1], D.I. Kolokolov[2], A.G. Stepanov[2]

[1]Novosibirsk State University, Pirogova 2, Novosibirsk 630090, Russia

[2]Boreskov Institute of Catalysis, Prosp. Akademika Lavrentieva, 5, Novosibirsk 630090, Russia

e-mail: arlenushka@gmail.com

Introduction

Our work was initially stimulated by the interest to the reaction of catalytic conversion of tert-butyl alcohol (TBA) to methyl tert-butyl ether (MTBE) in zeolite ZSM-5. MTBE has a great importance for fuel industry as an additive to the petrol raising of octane number. Due to the fact that dimensions of the TBA molecules are commensurate with the size of the zeolite pores their dynamics are strongly affected by zeolitic walls. Identification of the degree of influence of the zeolite on molecular dynamics has a great importance for understanding its unusual properties. Therefore, we should compare molecular dynamics of TBA in solid state with molecular dynamics of TBA inside zeolite ZSM-5.

There are a lot of works devoted to the problem of molecular dynamics of TBA in solid state [1–3], but, unfortunately, the mechanism of the motion and its parameters are still questionable.

In this paper we present the results of ^{2}H NMR studies on the dynamic behavior of TBA in solid state in a temperature range of 103–273 K. We have described ^{2}H NMR lineshapes for selectively deuterated TBA both in the methyl groups (TBA-d_9) and in the hydroxyl group (TBA-d_1) Also, for TBA-d_9 interpretation of the line shape of the ^{2}H NMR spectra and the temperature dependence of the spin-lattice relation times T_1 are made in terms of mobility, exhibited by the CD_3 and *tert*-butyl group.

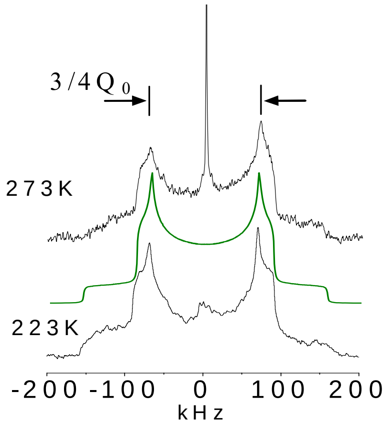

Fig.1. ^{2}H NMR spectra and their line shape simulations for hydroxyl group of TBA-d_1 at 223 and 273 K. Simulated ^{2}H NMR spectrum for TBA-d_1 is Pake-powder doublet with Q_0=208 kHz and η=0.12

^{2}H NMR lineshape analysis

^{2}H NMR spectroscopy is a powerful tool to probe molecular dynamics [4–5]. ^{2}H NMR line shape is sensitive to the motion in slow and intermediate (compare to the quadrupole coupling constant Q_0) regime [4]. Our line shape study is based on investigation of ^{2}H NMR spectra of deuterons located in methyl and hydroxyl group of TBA. The line shape simulations taking into account the molecular motion were made according to the formalism described in refs. [6-7].

We examined TBA-d_1 ^{2}H NMR spectra in the temperature range of 223-273 K, they are presented on the fig.1 The spectra of TBA-d_1 are static Pake-powder doublets, characterized by a quadrupolar constant Q_0=208 kHz and asymmetry parameter $\eta \approx 0.12$. Both the observed lineshape and the quadrupole splitting correspond to the rigid immobile molecules [8]. Thus the molecule as a whole is immobile on the ^{2}H NMR time scale.

The only motion that occurs in the TBA in solid state is represented by internal rotations of the methyl and *t*-bulyl groups. To elucidate this question ^{2}H NMR spectra of TBA-d_9 were recorded in a temperature range of 103-273 K, they are presented on the fig.2(A). It is seen that at 103 K spectrum is a Pake-powder doublet characterized by a quadrupolar constant $(3/4)Q_0$=178 kHz and asymmetry parameter $\eta \approx 0$. There is no any internal motion on ^{2}H NMR time scale at this temperature [8]. The motion is in the fast limit regime at 173-273 K, the spectra represent Pake-powder patterns characterized by quadrupole splitting, averaged by the motion, $(3/4)Q_2$=12 kHz ($Q_2=1/9Q_0$). The motionally averaged quadrupole splitting of 12 kHz indicates the presence of reorientations about two axes of symmetry C_3 and C'_3 (about C-C and C-O bound respectively) (see fig.3) [9]. single jump over the C-O bond the rate constant is taken to be k_2(C'_3 motion). We have assumed that the rate constants are defined by the Arrhenius law.

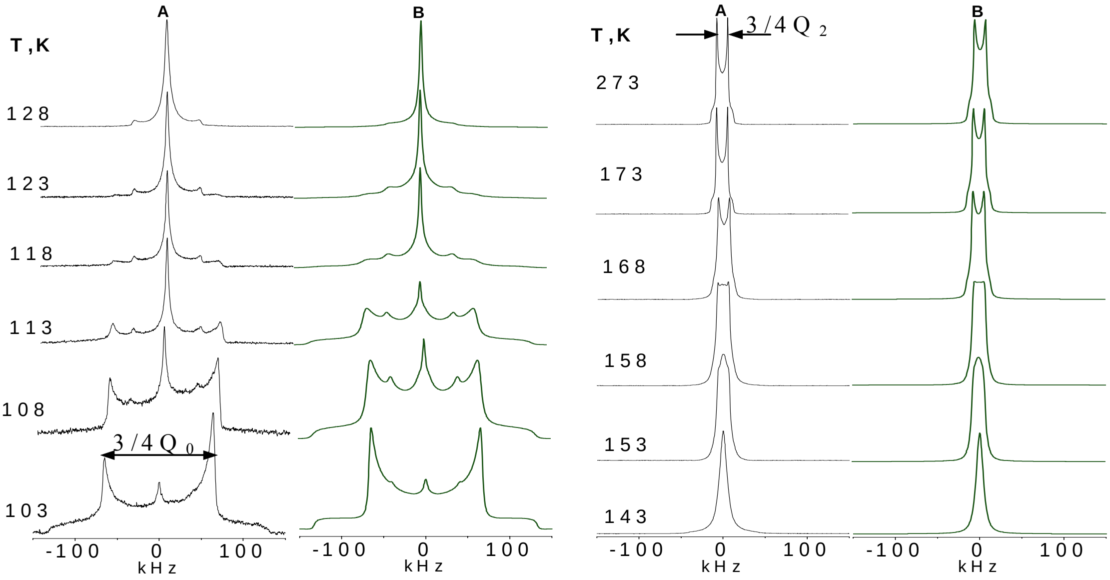

Fig.2. Temperature dependence of ^{2}H NMR lineshape for CD_3 group of TBA-d_9: experimental (A) and simulated (B) spectra.

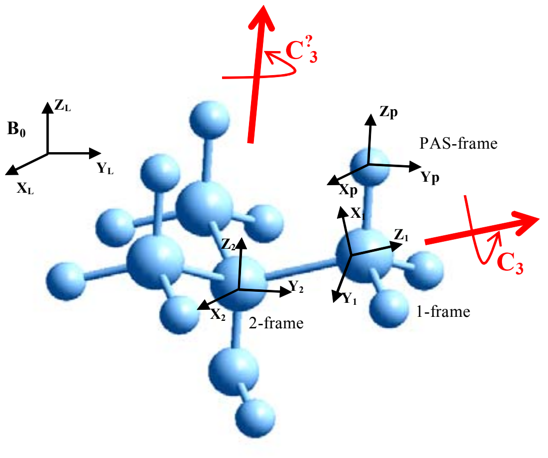

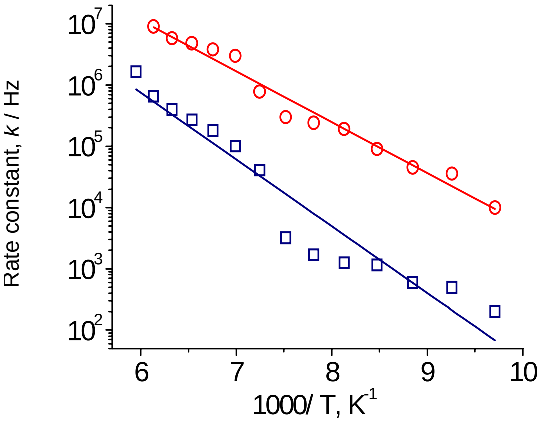

Fig.3. Schematic representation of the frame work construction, used in the jump

Fig.4. Arrhenius plots for rate constants at 103 -168 K, (□) for k_1, (○) for k_2

$$k_{1,2} = k_{0/1,2} Exp(-E_{1,2} / RT), \qquad (1)$$

where $E_{1,2}$ is the activation energy of motion.

Within the temperature range of 103-168 K the ^{2}H NMR lineshape for TBA-d_9 depends on temperature. Fig.3(B) shows the simulated ^{2}H NMR spectra for this temperature region. The values of k_1 and k_2 rate constants were used as the fitting parameters for certain temperature, the results are presented in the fig.4. The values for preexponential factors and the activation energies for rotational motions together with simulated parameters are given in Table1.

Table 1. Prameters for the motion of TBA obtained by lineshape analysis at 103-128 K. Q_0=178 kHz, η=0.01, θ_1=71°, θ_2=71

	E (kJmol^{-1})	k_0 (Hz)
C_3 rotation	21±2	16.4×10^{12}
C'_3 rotation	16±1	6.8×10^{12}

^{2}H NMR relaxation data.

In the fast motional regime (173-273 K) the deuterium spectra lineshape provides no information on parameters of molecular motion, so that measurements of the temperature dependence of spin-lattice relaxation time were used to estimate them [6].

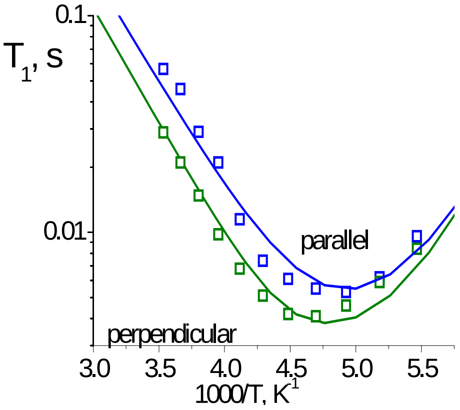

Fig.5. ^{2}H NMR spin-lattice relaxation times measured at perpendicular and parallel edges of powder patterns of TBA-d_9, together with simulation curves (solid lines).

Torchia and Szabo [10] have demonstrated that the value of T_1 is anisotropic in the presence of anisotropic motion. The presence of anisotropy of the T_1 values reveals some certain model of the motion. To clarify the model of the motion we have measured the spin-lattice relaxation at the parallel and perpendicular edges of the powder pattern [10]. The results together with simulations are shown in fig.5.

The result of fitting procedures demonstrates that the motion is still described with three fold jump model in this temperature range. The derived values of energy barries and pre-exponentional factors for C_3 and C'_3 motion are in good agreement with results obtained from lineshape analysis.

Summary

^{2}H NMR line shape and the spin-lattice relaxation time analysis allowed us to determinate the model and parameters of molecular dynamics of TBA molecules in the temperature range from 103 to 273 K.

In the experimental temperature range the molecule as a whole is immobile on the ^{2}H NMR time scale.

The lineshape and the spin-lattice relaxation time for TBA-d_9 are affected by intermolecular motion of both methyl and *t*-butyl groups.

Both these motions have been described by a three site jump model about C_3 and C'_3 axes of molecular symmetry.

The activation energies and pre-exponential factors for C_3 motion are 21 ±2 kJ/mol and 16×10^{12}Hz. For C'_3, they are 16 ±2 kJ/mol and 7×10^{12}Hz, respectively.

References

[1] J. R. During, S. M. Craven, J. H. Mulligan, et al., J. Chem. Phys. **58** (1973).

[2] E. Szczesniak, Mol. Phys. **59**, 679 (1986).

[3] D. W. Aksens and L. L. Kimtys, Magn. Res. Chem. **29**, 698 (1991).

[4] H. W. Spiess, in *Dynamic NMR Spectroscopy* (Springer-Verlag, Berlin, 1978), Vol. 15, p. 55.

[5] A. Abragam, *The Principles of Nuclear Magnetism* (Oxford University Press, Oxford, 1961).

[6] R. J. Wittebort, E. T. Olejniczak, and R. G. Griffin, J. Chem. Phys. **86**, 5411 (1987).

[7] V. Macho, L. Brombacher, and H. W. Spiess, Appl. Magn. Reson. **20**, 405 (2001).

[8] I. C. P. Smith, in *NMR of Newly Accessible Nuclei*, edited by P. Laszlo (Academic Press, London, 1983), Vol. 2, p. 1.

[9] A. G. Stepanov, M. M. Alkaev, A. A. Shubin, et al., J. Phys. Chem. B **106**, 10114 (2002).

[10] D. A. Torchia and A. Szabo, J. Magn. Reson. **49**, 107 (1982)

^{77}Se NMR and Theoretical Studies of $[Mo_3(\mu_3\text{-}Se)(\mu_2\text{-}Q)_3]^{4+}$ Clusters Q = O, S, Se

I.V. Mirzaeva, N.K. Moroz, S.G. Kozlova, P.A. Abramov

Nikolaev Institute of Inorganic Chemistry SB RAS, 630090, Acad. Lavrentiev Ave., 3, Novosibirsk, Russia

e-mail: dairdre@gmail.com

^{77}Se NMR spectroscopy has become a widely used tool for studies of organoselenium compounds and biological systems. However, there are much less works on its applications to inorganic compounds and, especially, very few works on chalcogenide transition metal clusters. Here we present ^{77}Se NMR and theoretical studies of $[Mo_3(\mu_3\text{-}Se)(\mu_2\text{-}Q)_3]^{4+}$ clusters Q = O, S, Se. These systems are used as catalysts and as building blocks for new functional materials.

^{77}Se NMR studies of $[Mo_3Se_4(acac)_3(py)_3]^+$, $[Mo_3SeO_3(acac)_3(py)_3]^+$, and $[Mo_3Se_4Cp^*{}_3]^+$ in $CDCl_3$ solution were carried out on Bruker Avance 500 spectrometer operating at 95.38 MHz. ^{77}Se chemical shifts were referenced to external H_2SeO_3 (δ = 1282 ppm) and then recalculated vs $SeMe_2$ (δ = 0 ppm).

Geometries of the clusters and of reference compounds $SeMe_2$ and H_2SeO_3 were optimized within the gas phase approach using ADF2008 [1] code. We used zero order regular approximation (ZORA) [2] to account for scalar relativistic effects together with BP density functionals [3-5]. Basis set consisted of relativistic Slater type orbitals of triple-ζ quality augmented with a set of polarized orbitals (TZP/ADF). Inner atomic shells were treated with frozen core approximation (Mo – 3d; Se – 3p; C, N, and O – 1s). NMR shieldings were calculated with DFT-GIAO method [6].

Table 1. Calculated and experimental ^{77}Se NMR shifts.

	Calc. δ^{77Se}, ppm	Exp. δ^{77Se}, ppm
$[Mo_3Se_4(acac)_3(py)_3]^+$	μ_3 1652 μ_2 2535	μ_3 1510 μ_2 2477
$[Mo_3SeS_3(acac)_3(py)_3]^+$	1642	-
$[Mo_3SeO_3(acac)_3(py)_3]^+$	1390	1356
$[Mo_3Se_4Cp^*{}_3]^+$	μ_3 1414 μ_2 2078	μ_3 1391 μ_2 2143
$[Mo_3Se_4Br_6]^{2-}$	μ_3 1767 μ_2 1950	-
$[Mo_3Se_4CN_6]^{2-}$	μ_3 1951 μ_2 2045	-
$[Mo_3SeS_3CN_6]^{2-}$	1853	-
$[Mo_3SeO_3CN_6]^{2-}$	1484	-

Calculated ^{77}Se NMR shifts for $[Mo_3Se_4(acac)_3(py)_3]^+$, $[Mo_3SeO_3(acac)_3(py)_3]^+$, and $[Mo_3Se_4Cp^*{}_3]^+$ are very close to experimental results (Table 1). Gas phase approach works well because selenium atoms are shielded from the media with terminal ligands. We also calculated ^{77}Se shifts for a number of similar systems to see if these values are characteristic for all $[Mo_3SeQ_3]^{4+}$ clusters. Although μ_3-Se atoms in all the clusters have nearly the same Bader charges (–0.49 *e* – –0.51 *e*) and Mo-Se distances (2.51 – 2.56 Å), which indicates similar Mo-Se bonding and, therefore, similar electronic structure around the Se nucleus, resulting NMR shifts for μ_3-Se fall in a fairly wide range 1356 – 1951 ppm. There is no straight correlation between Mo-Mo distances and μ_3-Se shifts either (fig.1). NMR shifts for μ_2-Se (Bader charges –0.40 *e* – –0.47 *e*; Mo-Se distances 2.43 – 2.45 Å) fall in the range 1950 – 2535 ppm.

Magnetic shielding of nucleus is a sum of diamagnetic (inner shells contribution) and paramagnetic parts. Chemical shifts are determined by the paramagnetic part. Each molecular orbital has the following contribution to the paramagnetic shielding:

$$u_{ai} \propto -\frac{1}{2(\varepsilon_i^0 - \varepsilon_a^0)} \langle \Psi_a | \hat{\mathbf{M}}_\mu | \Psi_i \rangle, \tag{1}$$

where $\varepsilon_i{}^0$ and $\varepsilon_a{}^0$ are the orbital energies of the occupied and unoccupied MOs and the integral represents the first-order magnetic coupling between the occupied and unoccupied orbitals. Therefore. NMR shifts in similar systems usually correlate with HOMO-LUMO energy gap. In our case, there is no such correlation (fig.2). This may be explained with the complicacy of the MOs that are highly delocalized and have only 1 – 10 % contribution of μ_3-Se atomic orbitals.

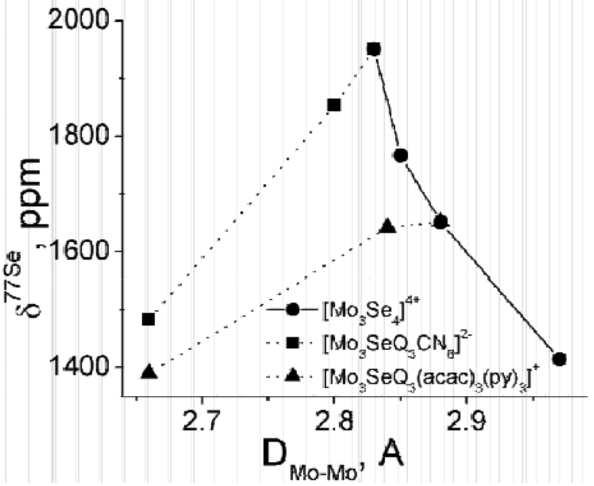

Fig.1. NMR shifts of μ_3-Se (δ^{77Se}) versus Mo-Mo distances

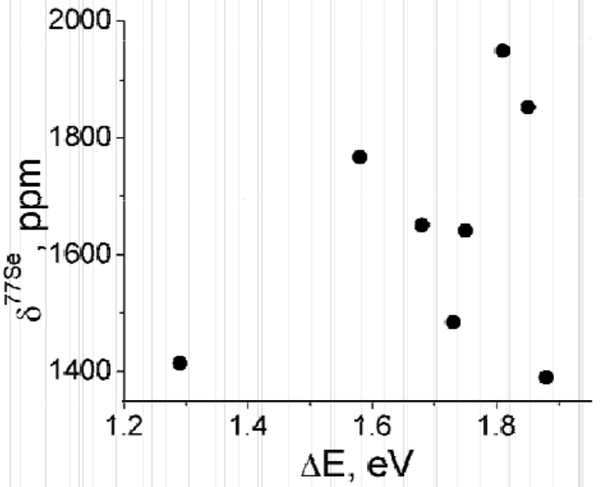

Fig.2. NMR shifts of μ_3-Se (δ^{77Se}) versus energy gap (ΔE) between highest occupied and lowest unoccupied MOs that contain μ_3-Se atomic orbitals..

References

[1] ADF2008, SCM, Theoretical Chemistry, Vrije Universiteit, Amsterdam, The Netherlands, http://www.scm.com

[2] G. Schreckenbach and T. Ziegler, Journal of Physical Chemistry 99, 606 (1995)

[3] D. Becke, Phys. Rev. A 38 (1988) 3098.

[4] J.P. Perdew, Phys. Rev. B 33 (12) (1986) 8822.

[5] H. Vosko, L. Wilk, M. Nusair, Can. J. Phys. 58 (1980) 1200.

[6] E. Van Lenthe, A.E. Ehlers, E.J. Baerends, J. Chem. Phys. 110 (1999) 8943.

Pulse EPR Investigation of the Triplet Fullerene C_{70} under continuous light illumination: Features of Three-Level System

T.I. Pichugina, M.N. Uvarov, L.V. Kulik

Institute of Chemical Kinetics and Combustion, 630090, Institutskaya, 3, Novosibirsk, Russia

e-mail: golavskay@gmail.com

Introduction

Most of the previous EPR investigations of $^3C_{70}$ have been performed by time-resolved techniques using photoexcitation by laser pulse. In the present work we demonstrated that $^3C_{70}$ can be observed by ED EPR under continuous light illumination. It is possible due to long $^3C_{70}$ lifetime. This approach allows observing echo signals of $^3C_{70}$ even in stationary state, i.e. with Boltzmann distribution of population within triplet spin sublevels. The observation of the $^3C_{70}$ in a stationary state allows one to reliably determine zero field splitting parameters. Note that in experiments in which $^3C_{70}$ was excited by laser pulse, the stationary state was not achieved, because of the unfavorable relation of the $^3C_{70}$ lifetime and the laser repetition rate.

We found that under continuous light illumination new features at the central region of the ED EPR spectra of $^3C_{70}$ appear. The features are unobservable at time-resolved EPR spectra detected after laser flash, and cannot be simulated within the usual approach, when two microwave (mw) transitions are treated independently (two-level system approximation).

Theory

Light irradiation excites C_{70} to its singlet state S_1 (lifetime is about 0.7 ns [1,2]) The triplet state spin sublevels T_+, T_0, and T_- are populated due to intersystem crossing with rate constants k_+, k_0, and k_- (fig.1.) respectively, which depend on orientation of the $^3C_{70}$ molecule relatively to the magnetic field vector $\boldsymbol{B_0}$ [3].

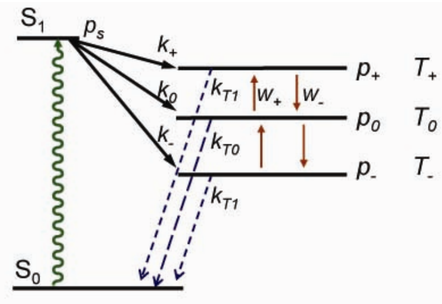

Fig.1. Triplet sublevels relaxation diagram

The ratio between spin-lattice relaxation rates w_+ and w_- is determined by Boltzmann factor $w_+ / w_- = \exp(\Delta E / kT) \approx 1 + \Delta E / kT$

The combined kinetic equations for populations p_+, p_0, and p_- of the triplet spin sublevels T_+, T_0, and T_- are following:

$$\begin{aligned}
\frac{dp_+}{dt} &= -p_+ w\cdot(1+\tfrac{\Delta E}{kT}) + p_0 w + k_+ p_s - k_{T1} p_+ \\
\frac{dp_0}{dt} &= -p_0 w - p_0 w\cdot(1+\tfrac{\Delta E}{kT}) + p_+ w\cdot(1+\tfrac{\Delta E}{kT}) + p_- w + k_0 p_s - k_{T0} p_0 \\
\frac{dp_-}{dt} &= -p_- w + p_0 w\cdot(1+\tfrac{\Delta E}{kT}) + k_- p_s - k_{T1} p_-
\end{aligned} \tag{1}$$

where p_s is population of the singlet excited state by light illumination, and $w \equiv w_-$

At continuous light illumination the steady state is achieved. In this case in the limit of high temperature $\Delta E/kT << 1$, and when spin-lattice relaxation rate w is much lower then the rates of triplet decays k_{T0}, k_{T1}, we can derive the equations for polarizations of the triplet levels:

$$\Delta P_1 = -\Delta P_2 = p_S \cdot \left(\frac{k_0}{k_{T0}} - \frac{k_+}{k_{T1}} \right), \qquad (2)$$

where $\Delta P_1 = p_0 - p_+$ and $\Delta P_2 = p_- - p_0$. The polarizations (2) depend on molecule orientation due to of anisotropy of rates k_{T0}, k_{T1}, k_+ and k_0.

In the case when spin-lattice relaxation rate w is much faster than the rates of triplet decay the equilibrium polarizations distribution is established:

$$dP_1 = dP_2 = S \cdot \frac{\Delta E}{kT} \cdot \frac{k_0 + 2k_+}{k_{T0} + 2k_{T1}} \qquad (3)$$

In this situation the triplet level polarizations do not depend on molecule orientation since the constructions $k_0 + 2k_+ = k_{Tx} + k_{Ty} + k_{Tz}$ have no orientation dependence [3].

Experiment

Fullerene C_{70} (Aldrich, 99 % purity) was dissolved in decaline (1:1 mixture of *cis*- and *trans*-decalin, Sigma-Aldrich), at a concentration of about 3×10^{-4} M. The solution was put in quartz tubes of a 4.6 mm diameter. Three freeze-pump-thaw cycles were executed to remove air, and then tubes were sealed under vacuum. For sample photoexcitation we used continuous irradiation of the visible light of Xe lamp,filtered in the range between 350 nm and 700 nm.

ED experiments were carried out on an X-band ELEXSYS ESP-580E EPR spectrometer equipped with a dielectric cavity (Bruker ER 4118 X-MD-5) inside an Oxford Instruments CF 935 cryostat. The mw frequency was 9.651 GHz. To obtain the echo signal, a two-pulse mw pulse sequence $t_p - \tau - 2t_p - echo$ was used, with various pulse lengths. The echo signal in the time domain was integrated on a built-in spectrometer integrator.

Temperature was controlled by a cold nitrogen flow and measured with a copper-constantan thermocouple attached to the sample. The numerical simulation of the ED EPR spectra was performed using a MATLAB 7.0 program package.

Results and Discussion

The echo signal of $^3C_{70}$ in decaline glass taken at scanning magnetic field (ED EPR spectrum) is shown at fig.2. for temperatures in the range of 5-50K. Here, the pulse sequence $\pi/2 - \tau - \pi - \tau - echo,$ with delay $\tau = 120$ ns, and pulselength $t_p = 16$ ns for $\pi/2$ pulse was applied. The spectra are normalized to the same low-field maximum intensity. One can see from fig.2 that ED EPR spectrum at 30 K is spin-polarized, and this effect increases with temperature decreases. The polarization of ED EPR spectrum of $^3C_{70}$ is anisotropic which is in agreement with expression (2) for polarizations of triplet sublevels in the case of low spin-lattice relaxation rate. The spectrum for 5K at fig.2. is very similar to ED spectra of laser pulse generated $^3C_{70}$ obtained earlier [3]. The spectra are normalized to the same low-field maximum intensity. Already at 50 K (fig.2.) ED EPR spectra look like the classical Pake doublet with equilibrium Boltzmann population distribution of the triplet sublevels [4].

For detailed investigation the echo signal of $^3C_{70}$ for temperature 50K we used the pulse sequence $\pi/2 - \tau - \pi - \tau - echo,$ with delay τ = 300 ns, and pulse length t_p = 100 ns for $\pi/2$ pulse. This pulse sequence allowed to increase pulse selectivity. The spectrum is shown at fig.3.

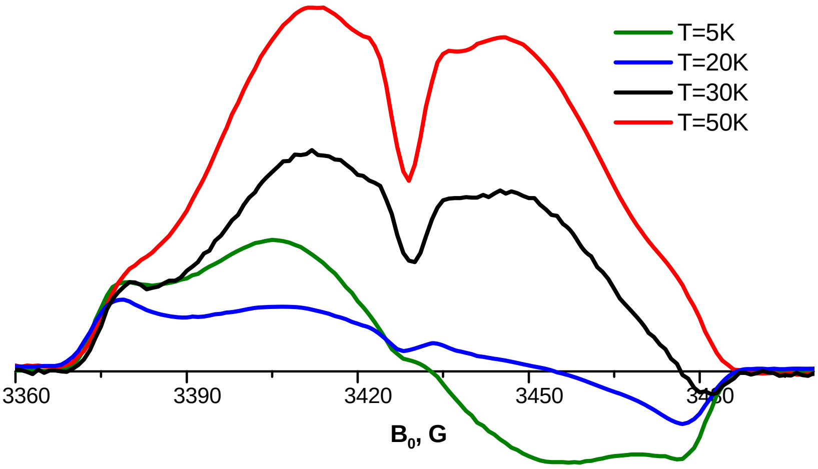

Fig.2. ED EPR spectrums $^3C_{70}$ in decaline

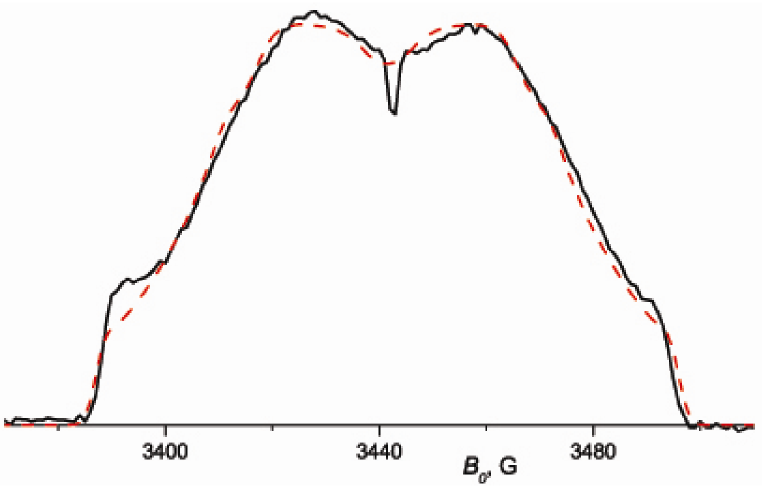

Fig.3. ED EPR spectrum $^3C_{70}$ in decaline at 50K

Initially we suppose that the electron spin echo signal intensity is proportional to polarization of two allowed transitions $T_0 \leftrightarrow T_+$, and $T_0 \leftrightarrow T_+$ (two-level system approach), the population distribution of the triplet sublevels is Boltzmann. The simulated ED EPR spectrum with ZFS parameters $D = 54.5$ G and E regularly distributed at the range of 2÷15 G is also presented at fig.3, (dash line). In general, the simulation is in agreement with the experimental ED EPR spectrum. Only the feature at the central part of the ED EPR spectrum appearing as a local dip is not reproduced by the described model. So we conclude that this two-level approach is not applicable for the central region, however it works well for the part of the spectrum far from the center.

We supposed that this feature arises because at the centre of the ED EPR spectrum the resonance energies for two allowed $T_0 \leftrightarrow T_+$ and $T_0 \leftrightarrow T_-$ transitions are equal $\left(\hbar\omega_{0+} = \hbar\omega_{0-}\right)$, so mw pulses simultaneously excite both transitions.

Numerical simulation of the ED EPR spectrum of $^3C_{70}$ was also performed by calculating the evolution of the triplet density matrix under pulse sequence action $t_p - \tau - 2t_p - \tau - echo$, where t_p, τ were fixed $t_p = 16\text{ns}$, $\tau = 200\,\text{ns}$ and the variable parameters were microwave power and magnetic field. We assumed the Boltzmann distribution at the initial conditions of the T_+, T_0, and T_- populations, the zero-field splitting parameters were D = 54.5 G and E regularly distributed at the range of 2÷15. This model did not include relaxation phenomena.

The averaging was performed over the time domain, over molecules orientation in the decaline matrix and taking into account the Gaussian broadening of the individual line width.

On fig.4(a – c) the ED EPR spectra of $^3C_{70}$ in decaline at 70K was obtained with mw pulse pattern 16ns – 200ns – 32ns – echo is shown. The amplitude of the first microwave pulse $\pi/2$, $2\pi/3$, and π corresponded magnetization rotation for energy transition $T_0 \leftrightarrow T_+$ and $T_0 \leftrightarrow T_-$. With the angle increasing the broad part of the ED EPR spectrum is reducing. However, the local dip turns into peak at the center of the spectrum.

The simulated spectra are also shown on fig.4(d – f). One can see that under the used approach the center feature of ED EPR spectra was reproduced well.

At fig.5. the simulation of the $^3C_{70}$ ED signal intensity dependence on microwave power corresponded to magnetization rotation angle is presented for different positions of the spectrum as labeled at fig.4. The simulation for positions 2, and 3 shows the typical behavior for two-level system approach: ESE signal maxima for $\pi/2-\tau-\pi-$mw pulse pattern, the absence of the ESE signal after $\pi-\tau-2\pi-$pulses, and inverted ESE signal with further increasing mw pulse power. However, simulation the ESE signal intensity dependence at 1 position of the spectrum shows unusual behavior for two-level system: the π-pulse does not invert the ED signal in the centre of the spectrum but recovers the central dip (fig.4d) into the single central spike (fig.4f)

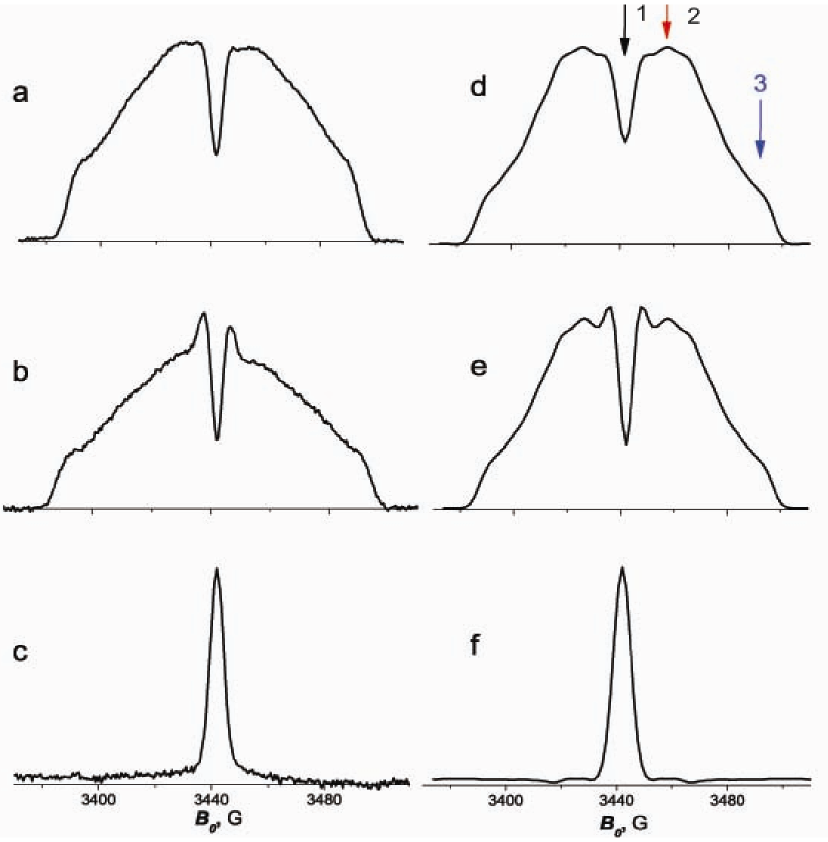

Fig.4. ED EPR spectrums $^3C_{70}$ in decaline at 70K (a, b, c) and numericall simulation (d, e, f) at different amplitude of the first microwave pulse

Conclusion

We found that the EPR spectra of $^3C_{70}$ in glassy matrices at liquid nitrogen temperatures and higher can not be simulated successfully with fixed E value due to complicated dynamic

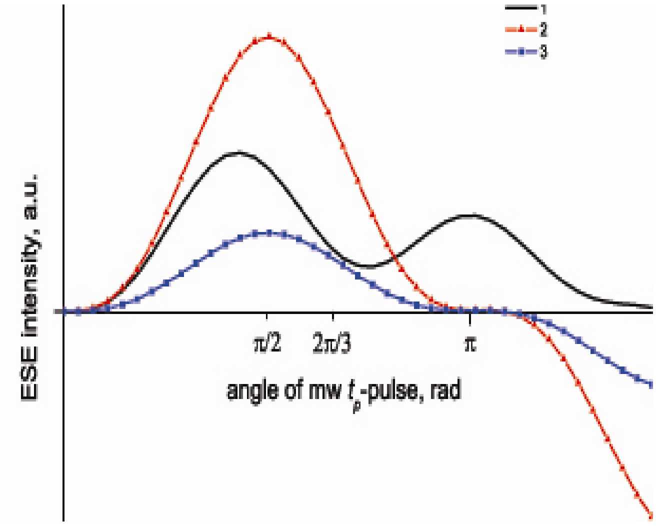

Fig.5. Intensity of electron spin echo signal at different mw pulses power for points 1,2,3 (show fig.4)

processes of the $^3C_{70}$ molecule. To simulate the EPR spectra it is needed to assume the following conditions: D = 54.5 G, E is regularly distributed at the range of 2 ÷ 5 G.

The feature in the center of ED EPR spectra of $^3C_{70}$ originates from simultaneous excitation of the two allowed spin transitions of the triplet by mw pulses. It is characterized by anomalous pulse angle dependence of ED intensity. The widely used two-level system approximation does not describe this spectral feature, while strict simulations based on the density matrix evolution of the S = 1 three-level system reproduces this feature well.

Acknowlegements

This work was supported by program of Presidium of Russian Academy of Sciences, project №55.

References

[1] M.N. Uvarov, L.V. Kulik, M.A. Bizin, V.N. Ivanova, R.B. Zaripov, S.A. Dzuba, J. Phys. Chem. A 112, 2519 (2008).

[2] M.R. Wasilewski, M.P. O'Neil, K.R. Lykke, M.J. Pellin, D.M. Gruen, J. Am. Chem. Soc. 113, 2774 (1991)

[3] M.N. Uvarov, L.V Kulik., S.A. Dzuba J. Chem. Phys. 131, 144501 (2009).

[4] E. Wasserman, L.C. Snyder, W.A. Yager, J. Chem. Phys. 41, 1763 (1964).

Thermalization of the system “^{3}He-aerogel” at low temperatures

A.V. Klochkov[1], V.V. Kuzmin[1], R.R. Gazizulin[1], E.M. Alakshin[1], M.S. Tagirov[1],
D.A. Tayurskii[1], N. Malders[2]

[1]Faculty of Physics, Kazan (Volga region) Federal University, Kazan, Russia
[2]Physics and Astronomy Department, University of Delaware, Newark, USA

e-mail: slava625@yandex.ru

At present time the influence of aerogel on properties of superfluid ^{3}He is the matter of interest [1,2]. Unique structure of an aerogel leads to anomaly small thermal conductance and the question about real temperature of aerogel still has not been solved. In this paper we report experimental data on this subject.

The aerogel sample (95%) was cut out in the shape of cylinder (d=5mm, h=12mm) and was sealed leak tight in the glass tube (pyrex) to the gas handling system. The temperature of NMR cell have been controlled by ^{4}He vapor pumping and in all presented experiments was 1.5 K.

The longitudinal magnetization relaxation time T_1 of ^{3}He was measured by the saturation recovery method using FID signal. The spin-spin relaxation time T_2 was measured by Hahn method. The hand made pulse NMR spectrometer has been used (frequency range 3 – 50 MHz). The pulse NMR spectrometer is equipped by resistive electrical magnet with a magnetic field strength up to 1T. The necessary amount of ^{3}He for full coverage of an aerogel surface was adjusted like in [3,4]. On all experimental data (fig.1-4) the time scale is the time after beginning of ^{3}He condensation procedure.

The process of ^{3}He condensation (adsorption) consists of two exponential processes (fig.1). Probably, the first one is the redistribution of ^{3}He molecules inside of the NMR cell (characteristic time τ=2min) and the second one is the adsorption itself and further thermalization of the system “^{3}He-aerogel”(τ=15min).

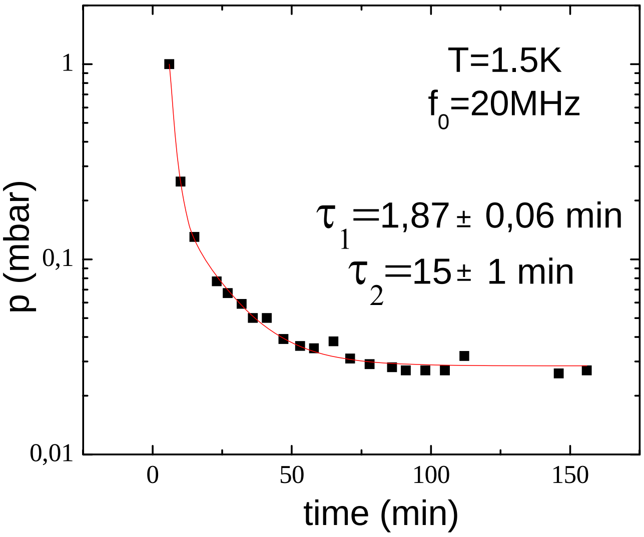

Fig.1. The process of ^{3}He condensation in aerogel

On the fig.2 the evolution of ^{3}He spin echo amplitude in the same time frame as on fig.1 is presented. The characteristic time of this process is about 26 min.

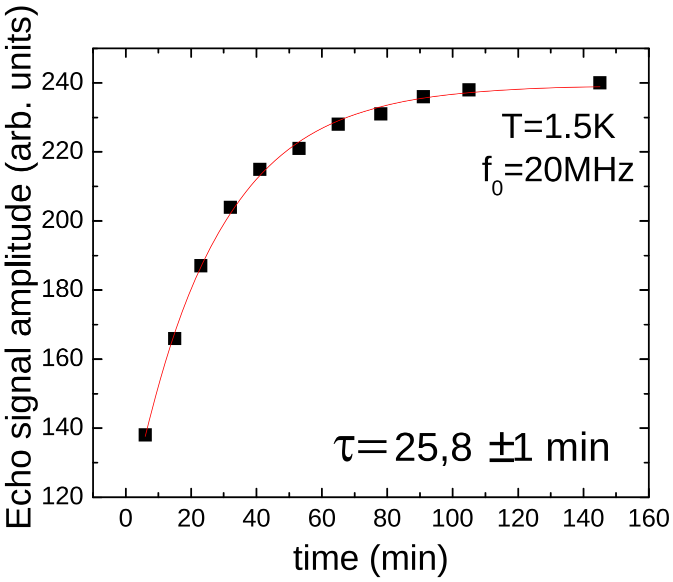

Fig.2. The evolution of ^{3}He spin echo amplitude during thermalization process

On the fig.3 and fig.4 the evolution of transverse relaxation time T_2 and longitudinal relaxation time T_1 are presented. About the same characteristic times are observed.

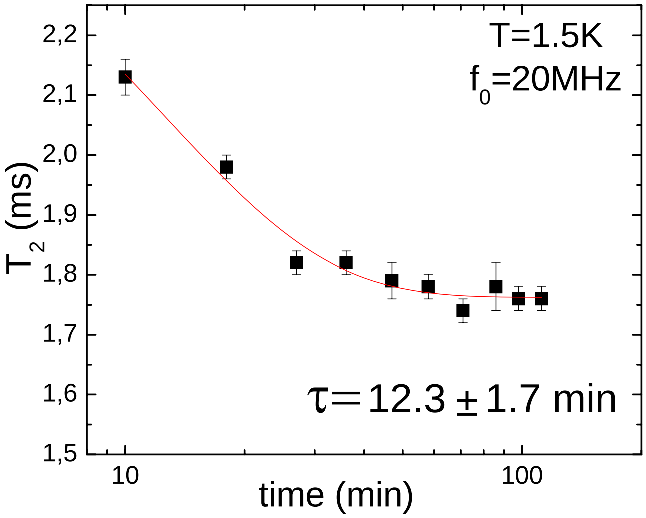

Fig.3. The evolution of transverse relaxation time T_2 of ^{3}He during thermalization process

All presented experimental data show that thermalization processes in the system “^{3}He-aerogel” takes time less than 25 min. We didn’t observe any longer processes in thermalization. Taking into account the fact, that NMR cell with an aerogel was cooled down to 1.5K within 2 hours prior of ^{3}He condensation we can conclude, that the temperature of “^{3}He-aerogel” system became 1.5K. Cooling of aerogel takes place by the diffusion of ^{3}He molecules between an aerogel surface and the glass tube wall.

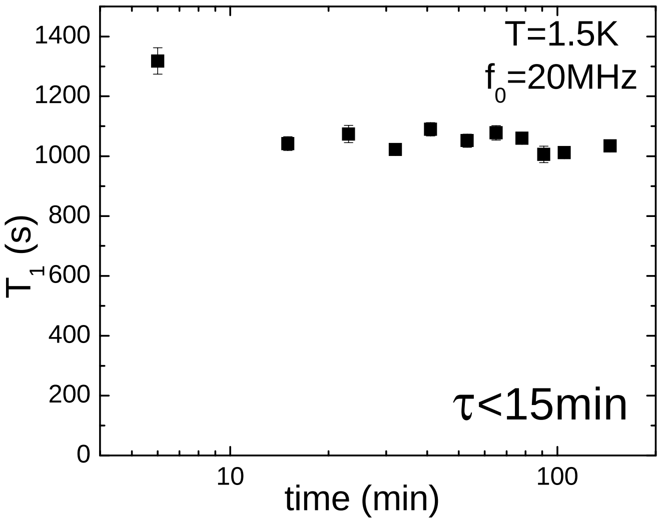

Fig.4. The evolution of longitudinal relaxation time T_1 of ^{3}He during thermalization process

This work is supported by Russian Fund for Basic Research (grant N 09-02-01253).

References

[1] Porto J and Parpia, *J Phys. Rev. Lett.* **74**, 4667 (1995)

[2] Sprague D, Haard T, Kycia J et al., *Phys. Rev. Lett*. **75**, 661 (1995)

[3] A. V. Klochkov, V. V. Kuzmin , K. R. Safiullin et al., *JETP Letters*, **88**, 823 (2008)

[4] A. Klochkov, V. Kuzmin, K. Safiullin et al., *Journal of Physics: CS*, **150**, 032043 (2009)

Multifrequency EPR of Asphaltenes

D.T. Sitdikov[1], G.V. Mamin[1], S.B. Orlinskii[1], N.I. Silkin[1], R.V. Yusupov[1], T.N. Yusupova[2]

[1]Kazan Federal University, 420008, Kazan, Russia.

[2]A.E. Arbuzov Institute of Organic and Physical Chemistry, 420088, Kazan, Russia.

e-mail: sitdikov-ksu@rambler.ru

Introduction

Heavy oils rich in asphaltene are increasingly being exploited to sate the increasing thirst for petroleum around the world. Asphaltenes are a well known problem for the oil industry. Their tendency to form deposits on wells, tubing, piping, and also during refining processes causes heavy losses to the oil industry every year

Asphaltenes have been extensively studied in the literature and are defined by a solubility class of molecules, insoluble in n-paraffins/soluble in toluene, with a very high molecular weight. They are made of polar aromatic compounds with mainly carbon (80-86 %), hydrogen (6-8 %), oxygen (0.5-2 %), nitrogen (0.5-2 %), sulfur (2-9 %), and metals (Ni and V associated with porphyrin structures). Asphaltenes are characterized by broad size and molecular pattern distributions [1].

From all studies, asphaltenes seem to be described through two average models:

- the “continental” type [2], in which asphaltenes are represented as large central aromatic region (fig.1),
- the “archipelago” type [3], where asphaltenes are made of smaller aromatic regions linked by bridging alkanes (fig.2).

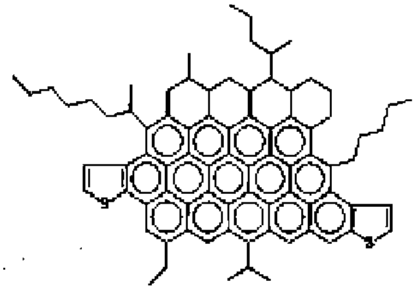

Fig.1. Representation of asphaltene models “continental” type [2].

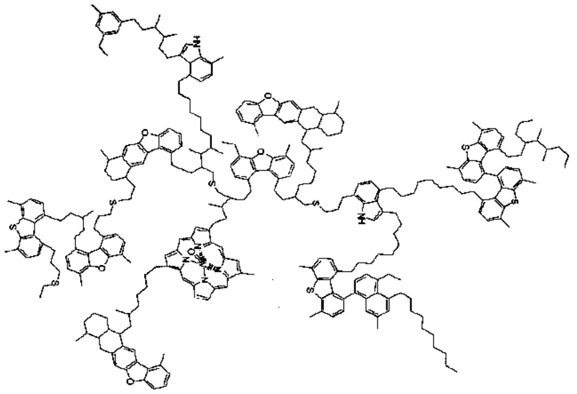

Fig.2. Representation of asphaltene models “archipelago” type [3].

The size of these structures ranges in a wide window from 10 to several hundreds of angstroms.

Existence of two types of asphaltene molecules with different chemical structure complicates heavy oils processing. It becomes necessary to evolve fraction with one type asphaltene molecules – “continental” or “archipelago”.

Results and discussion

Samples of asphaltenes (I-0) were obtained from Zuzeevsk bitumen and separated to three fractions:

- I-2 fraction predominantly consists of “continental” asphaltene molecules
- I-1 fraction predominantly consists of “archipelago” asphaltene molecules
- I-3 fraction consists of identical quantity “continental” and “archipelago”.

Powder spectra of asphaltenes consist of 16 superfine lines of vanadyl ($V^{4+}+O^{2-}\rightarrow VO^{2+}$, $3d^1$, S=1/2) and single intensive line corresponded to unpaired electrons of free radicals.

Every samples single line is believed to consist of two types of free radicals (IA и IB), that corresponded to asphaltene molecules with “continental” and “archipelago” type accordingly.

Amplitude decrease of electronic spin echo (I_{echo}) with delay between impulses (τ) can be described by function [4]:

$$I_{echo} = A_{IA}\cdot e^{-\frac{\tau}{T_{2IA}} - m_{IA}\cdot\tau^2} + A_{IB}\cdot e^{-\frac{\tau}{T_{2IB}} - m_{IB}\cdot\tau^2},$$

where T_{2IA}, T_{2IB} — times of transverse relaxations of free radicals IA and IB; A_{IA}, A_{IB} — factors proportional to concentration of free radicals IA and IB; m_{IA}, m_{IB} — factors considering spin diffusion in free radicals IA and IB.

Approximation is presented on fig.3.

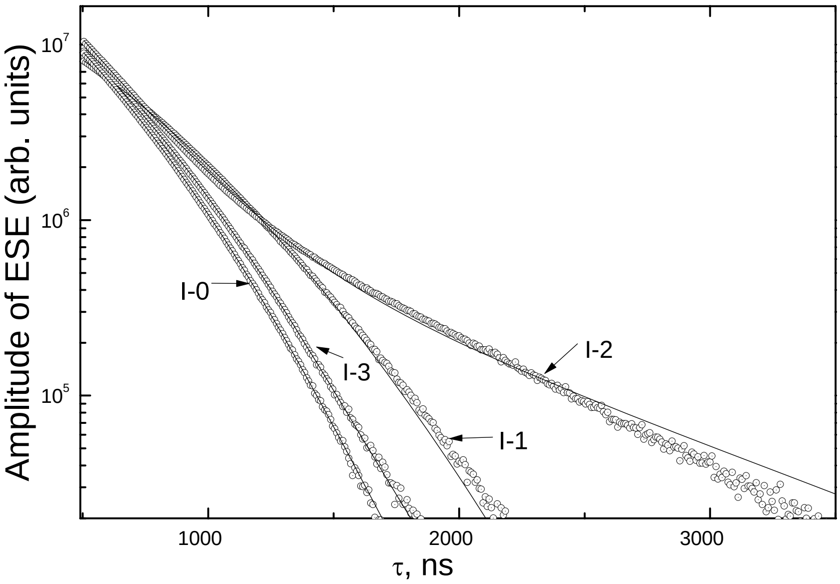

Fig.3. Amplitude decrease of electronic spin echo (I_{echo}) with delay between impulses (τ) for all samples (I-0, I-1, I-2, and I-3).

The factors A_{IA} и A_{IB} ratio gives us the ration between concentrations of free radicals IA and IB. Sample I-1 predominantly consists of free radicals IB (76%); I-2 fraction consists of free radicals IA (97%); I-3 fraction consists of roughly equal amount of free radicals IA and IB. The concentration ration of free radicals in sample I-0 agrees is almost equal to I-3 fraction.

From EPR spectra of I-1, I-2, I-3 fractions, which were detected by amplitude of electronic spin echo, relative concentrations of free radicals IA и IB and vanadyl were calculated (fig.4). Correlation curve can be fit by a straight line, therefore vanadyl should be detected with free radicals IB and have chemical bounds with "archipelago" asphaltene molecules.

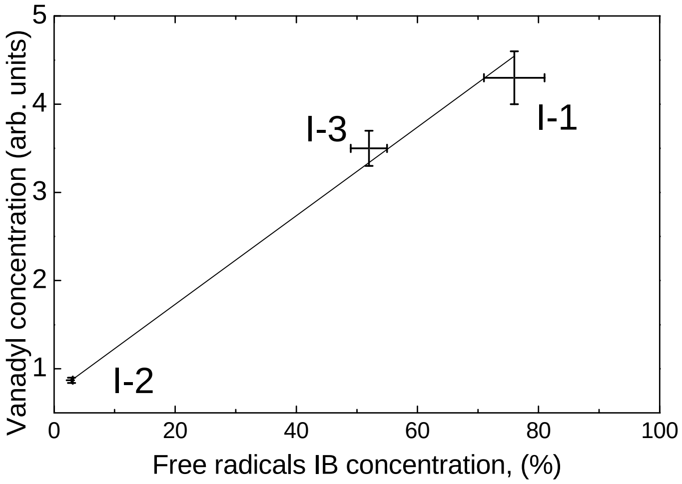

Fig.4. Free radicals IB concentration dependence with the content of vanadyl in fractions I-1, I-2, I-3.

Splitting to two pairs of lines has been detected in ENDOR spectrum of free radicals with I-1 fractions made with high accumulation near Larmor frequency fit to hydrogen (protons) cores.

Lateral lines of ENDOR spectrum (rectangle in fig.5) can be contributed by the aromatic ring [5]. Number of rings and their relative positioning determine form and distance between lateral lines. The central ENDOR peak (oval in fig.5) mainly stems from the dipolar hyperfine coupling of the remote H nuclei on the side chains [5]. Splitting of central ENDOR peak determine average size of asphaltene molecules. Hyperfine interaction at about 80 KHz is

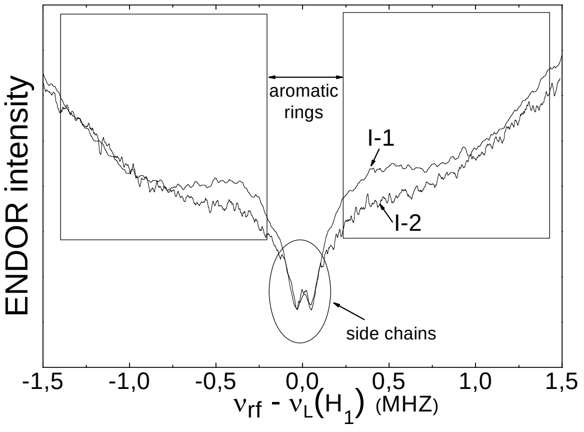

Fig.5. ENDOR spectra of I-1 and I-2 fractions detected by the Mims method of application.

observed when the distance between electron and hydrogen is about 1 nm. Thus, average size of asphaltene molecules in I-1 fractions is 1-2 nm.

In ENDOR spectra of two extremes fractions I-1 and I-2 (fig.5) the splitting of central ENDOR peak coincide, therefore asphaltene molecules in fractions I-1 and I-2 have similar sizes ≈ 1 nm. Form of lateral line is different and can be connected with different number and (or) relative position of aromatic rings in asphaltene molecules – “continental” and “archipelago”.

Conclusions

The CW and pulse W-band EPR spectra of asphaltenes were measured and interpreted, their spectroscopic and relaxational characteristics were obtained. It was established, that vanadyl consist in “archipelago” type asphaltene molecules.

It was shown, that EPR spectroscopy allows us to define two types of molecular structure in asphaltenes – “continental” and “archipelago”, as well as measuring their relative concentrations and studying their structure and local environment.

References

[1] Marchal, C. Asphaltene diffusion and adsorption in modified NiMo alumina catalysts followed by ultraviolet (UV) spectroscopy / Charles Marchal, Eswar Abdessalem, Melaz Tayakout-Fayolle, and Denis Uzio // Energy Fuels – 2010 – 24 – P. 4290–4300.

[2] Murgich, J. Molecular recognition and molecular mechanics of micelles of some model asphaltenes and resins / Juan Murgich, Jesus Rodriguez M., and Yosslen Aray // Energy & Fuels – 1996 – 10 – P. 68-76.

[3] Sheremata, J. M. Quantitative molecular representation and sequential optimization of athabasca asphaltenes / Jeff M. Sheremata, Murray R. Gray, Heather D. Dettman, and William C. McCaffrey // Energy & Fuels – 2004 – 18 – P. 1377-1384.

[4] Salihov, K.M. Electronic spin echo and its application / K.M. Salihov, A.G. Semenov, Yu.D. Cvetkov – N.: Nayka, 1976. - 342 p.

[5] Aguirre, A. Multifrequency EPR analysis of the positive polaron in I_2-doped poly(3-hexylthiophene) and in poly[2-methoxy-5-(3,7-dimethyloctyloxy)]-1,4-phenylenevinylene / A. Aguirre, P. Gast, S. Orlinskii // PCCP. – 2008. – V.10. – P. 7129–7138.

A new nuclear magnetic resonance approach for ontological diseases diagnostic on serum albumin properties

T.N. Nikolaeva, V.D. Skirda, Yu.A. Fatrahmanova, A.Sh. Gissatullina

Kazan federal university, 420008, Kremlevskaya str. 18, Kazan, Russia

e-mail: tattina@list.ru

One of the most effective ways of dealing with cancer is to develop reliable methods for early detection and prevention of malignant neoplasms. The most convenient object for the search methods of early diagnosis of cancer is blood. Washing all the organs and tissues of the body, blood is guaranteed to carry information on significant changes at the cellular level, which are characteristic for the earliest stages of cancer. The vast majority of blood-borne substances (such as fatty acids, proteins, hormones, etc.) is directly dissolved in the blood plasma or related to its components (lipoproteins, albumin).Therefore blood plasma with high probability is a source of information of cancer disease. Which is more blood plasma quite easily distinguished by the standard procedure and compared with whole blood it is more stable.

Experimentally shown that the magnetic resonance characteristics of the blood plasma of patients with cancers differ from the corresponding characteristics of healthy donors. In particular, presence of any malignancy leads to increase of blood plasma spin-lattice relaxation time values [1]. This phenomenon was termed as "systemic effect".

However, the "systemic effect" is characterized by rather small relative difference in the times of the proton spin-lattice relaxation of plasma or serum for the sick and healthy patients. Obviously, for practical application of this effect in the early diagnosis of cancer the difference should be increased. There are two ways of solving this problem. The first one is to reduce the variability of the T_1 and the second one is to selective influence on onkospecific components of blood plasma.

Following the second way it worth saying that according to the literature data one of the onkospecific components of blood is albumin. It is known [2-5] that albumin changes its conformation set in case of oncology disease. Which is tested by a special paramagnetic label called 16-doxyl stearic acid. Its state is detected by electron spin resonance.

The molecule of 16-doxyl stearic acid is paramagnetic, so it can be assumed that an analysis of the EPR spectrum is not the only way to testing its condition. For this purpose simpler test - influence on the spin-lattice relaxation of blood plasma protons can be used.

Based on the foregoing, the objective of this work is to study by nuclear magnetic resonance properties of albumin molecules and conditions of their interaction with molecules of 16-doxyl stearic acid, including the case when plasma onkospecific metabolites or their analogues presence in blood.

Methods

In this research the double and triple system composed of components such as chemically pure water, ethyl alcohol, 16-DSC and plasma were investigated. Plasma was obtained from donors by taking blood from the ulnar vein into the vacuum tube with anticoagulant (ethylenediaminetetraacetic acid - EDTA) and its centrifugation for 15 minutes with the acceleration of 1,500 g. 16-doxil stearic acid was purchased from the Sigma Chemicals firm. The structural formula is shown in fig.1.

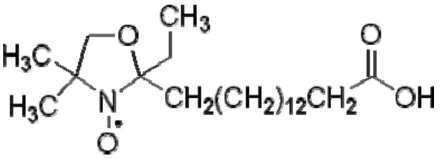

Fig.1. The structural formula of 16-doxil stearic acid

Experiments of measuring proton relaxation times were performed on an NMR analyzer "Chromatec Proton-20M", produced by CJSC SCB "Chromatec" (Joshkar-Ola, Russia). The spin-lattice relaxation time, T_1, of protons in the sample was determined by 90 °-τ1-90 ° x-read-90 °-x-τ2-90 ° x-read-90 °-x-τ3-... The mean T_1 was determined from data fit between τ_i values of 2 to 350 ms. The obtained recovery curves of longitudinal magnetization were satisfactorily described by a simple monoexponential function. Thus this fact allowed to determine the spin-lattice relaxation time with high accuracy (error less than 5%). The temperature of all measurements was +37 ± 0,1 ° C

Results and discussion

The concentration of serum albumin and the value of spin-lattice relaxation times of blood plasma protons are shown fig.2. It is obvious that there is no correlation between these characteristics.

The biological system is multicomponent, what leads to a number of complexities in working with this system. Also important is the fact that, as a rule, the studied biological objects, including blood plasma, contain large amounts of water. In fact, by virtue of amphiphilic nature the 16-doxyl stearic acid does not dissolve in water. In this connection it may be a problem of interaction of paramagnetic labels with water components of the investigated biological object. The majority of published works, avoiding the problem of undissolved 16- doxyl stearic acid in aqueous solutions, pre-dissolve it in ethanol or dimethyl

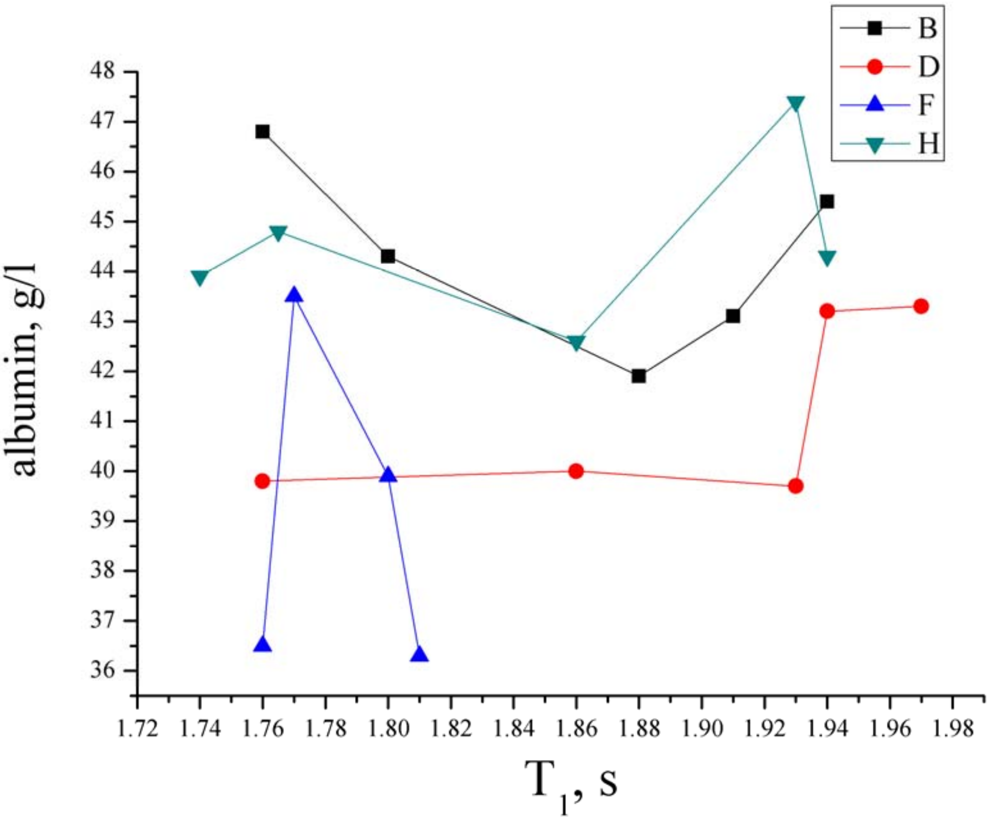

Fig.2. Distribution of concentration of serum albumin(g/l) and the value of spin-lattice relaxation times T1 (s)of blood plasma protons. The symbols B, D, F, and H are related with different donors.

sulfoxide (DMSO). That is why, the study of interaction of 16-doxyl stearic acid with components of blood plasma arises the problem of investigating the influence of the alcohol on system performance. It is also unclear which of the system components (16-doxyl stearic acid or alcohol?) has the dominant influence on the proton T_1 values of plasma/16-doxyl stearic acid/alcohol system? In this context, the appropriate research was conducted and it was shown that the dominant influence on the spin-lattice relaxation of the ternary system plasma/16-doxyl stearic acid/alcohol has paramagnetic label - 16-doxyl stearic acid.

In addition, during the study of the model molecular systems such as bufer/albumin/16-doxyl stearic acid/alcohol and plasma/16-doxyl stearic acid/alcohol preliminary experimental data was obtained (fig.3). This news does not contradict the basic hypothesis that a molecule in the blood plasma 16-doxyl stearic acid interacts primarily to serum proteins - albumin.

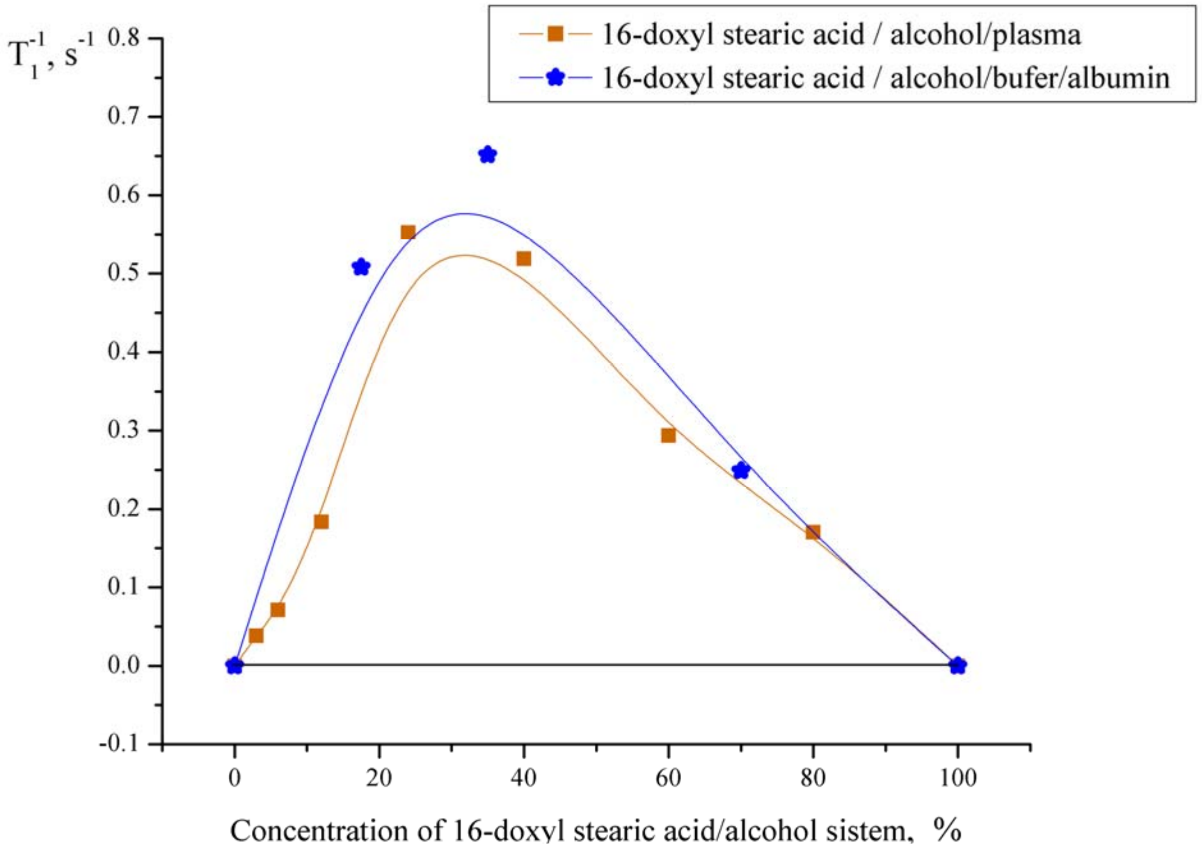

Fig.3. Dependence of the nonadditive contribution to the average velocity of the spin-lattice relaxation of protons of molecules in mixtures of plasma / solution of 16-doxyl stearic acid in alcohol and a buffer / albumin solution of 16-doxyl stearic acid in alcohol from the mixture. Concentration of 16-doxyl stearic acid in alcohol was 2 g / l. The concentration of albumin in the buffer was 40 grams per liter. Temperature of measurement 37°C.

In our opinion, the obtained results are optimistic in terms of further studies of nuclear spin-lattice relaxation in systems such as plasma/16-doxyl stearic acid/alcohol in case of solving the problem of early diagnosis of cancer.

References

[1] Floyd, R. A. Time course of tissue water proton spin-lattice relaxation in mice developing ascites tumor [text] / R. A. Floyd, J. S. Leigh, B.Chance, M. Miko // Cancer Research. – 1974. – Vol.34(1) – P. 89-94.

[2] Muravsky V. Method for the detection of changes in the transport properties of albumin in an albumin-containing samples, ESR-spectrometer for carrying out said method, and for diagnostic purposes and for controlling albumin-containing preparations. [Text] /V. Muravsky // U.S. Patent No. 7166474 B2Issued on Jan. 23, 2007.

[3] Kazmierczak, C. Electron Spin Resonance Spectroscopy Albumin: A Novel New Test for Cancer and Monitoring Steven [Text] /C. Kazmierczak, A. Gurachevsky, G. Matthes, V. Muravsky // Clinical Chemistry – 2006 – V.52 P.1-6 – ISSN 0009-9147

[4] Matthes, G. Albumin transport analysis of different collectedand processed plasma products by electron spin resonance spectroscopy [Text] / G. Matthes , G. Seibt, V. Muravsky, G. Hersmann , G. Dornheim // Transfusion and Apheresis Science - 2002 –V. 27 - P. 129–135 – ISSN 1473-0502

[5] Gurachevsky, A. Intra-albumin migration of bound fatty acid probed by spin label ESR [Text] / A. Gurachevsky, E. Shimanovitch, T. Gurachevskaya, V. Muravsky // Biochemical and Biophysical Research Communications - 2007 -V. 360 - P. 852–856 – ISSN 0006-291X

Solution BCS equation in case of spin fluctuation pairing

M.V. Eremin, M.A. Malakhov

Kazan Federal University, Kremlevskaya, 18, Kazan 420008, Russian Federation
e-mail:MMalakhov89@yandex.ru

The BCS the equation is written as

$$\Delta_{\mathbf{k}} = \frac{1}{N}\sum_{k'} V(\mathbf{k}-\mathbf{k'})\frac{\Delta_{\mathbf{k'}}}{2E_{\mathbf{k'}}}\tanh\left(\frac{E_{\mathbf{k'}}}{2k_B T}\right), \tag{1}$$

were Δ_k — energy gap, E_k — Bogolyubov's quasiparticle energy, $V(\mathbf{k}-\mathbf{k'})$ — Fourier transform of pairing potential. In case of phonon mediated pairing the potential is constant and gap parameter independent from wave vector. In layered cuprates the superconducting gap parameter dependent on wave vector as $\Delta_k = \Delta_d(T)(\cos k_x - \cos k_y)/2 + ...$ Next important feature of HTSC is that the ratio $2\Delta_d(T=0)/k_b T$ is about 5, what is hard to explain by just short range pairing potential, when $V(q) = 2J_{eff}(\cos q_x a + \cos q_y a)$. J_{eff} is the effective superexchange coupling parameter. The goal of present work is to solve equation (1), when pairing potential in Eq. (1) is proportional to spin- susceptibility.

In our calculation we start from, so called spin fluctuation model [1]:

$$V_{eff}(\mathbf{k}-\mathbf{k}') = \frac{C}{1+[\mathbf{Q}-(\mathbf{k}-\mathbf{k}')]^2\xi^2}, \tag{2}$$

were $\mathbf{Q} = (\pi,\pi)$. ξ — correlation length. C — constant of interaction.

Equation (1) was solved numerically using matrix method. Part of our calculations is displayed in fig.1. Solid line – approximation by function:

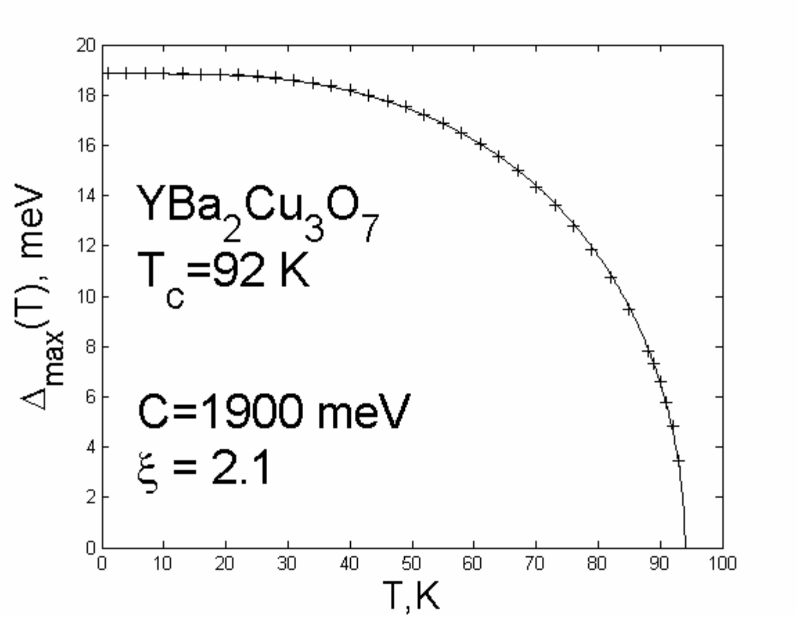

Fig.1. Calculated temperature dependence of gap parameter $2\Delta_{\max}(T)$. Symbols correspond to results of numerical solutions, line – approximation by function (3).

$$\Delta_{\max}(T) = \Delta_{\max} \tanh\left(1.72\sqrt{[T_c/T]-1}\right), \tag{3}$$

were $\Delta_{\max}$ - maximum value of $\Delta_{\mathbf{k}}$.

It is interesting to note that this temperature dependence is the same to those case when we had taken the paring potential just in short range form. i. e. $V(q) = 2J_{eff}(\cos q_x a + \cos q_y a)$. But the ratio $2\Delta_d(T=0)/k_b T$ now increases. Instead value 4.4 we have got $2\Delta_{\max}/k_B T_c = 4.65$, which is more close to experimental estimation (about 5) via temperature dependence of spin lattice relaxation rate at Cu(2) site, tunneling spectroscopy and photoemission data [2].

Second peculiarity of our solutions — existence of high order components of the gap like $\Delta'_k = \Delta'_d(\cos 2q_x a - \cos 2q_y a)$ and so on. Presence of high order harmonic in superconducting gap function of layered cuprates was pointed out in number of experimental papers [3-6].

This work was partially supported by the Russian Foundation for Basic Research, Grant # 09-02-00777-a and Swiss National Science Foundation, Grant IZ73Z0 128242.

References

[1] A.Millis, H.Monien and D.Pines, Phys. Rev. B 42:167 (1990)

[2] S. Hufner, M.A. Hossain, A. Damascelli, and G.A. Sawatzky, Rep. Prog. Phys. 71, 062501 (2008).

[3] J. Mesot *et al.*, Phys.Rev. Lett. 83, 840 (1999).

[4] S. V. Borisenko *et al.*, Phys.Rev. B 66, 140509 (2002).

[5] G. Blumberg *et al.*, Phys.Rev.Lett. 88, 107002 (2002).

[6] H. Matsui *et al*. Phys.Rev.Lett. 95, 017032 (2005).

EPR, structural characteristics and intramolecular movements of some phenoxyl radicals in toluene

I.R. Nizameev[1], M.S. Pudovkin[2], M.K. Kadirov[1]

[1]A.E. Arbuzov Institute of Organic and Physical Chemistry, Kazan Scientific Center, Russian Academy of Sciences, 420088, Arbuzov Str., 8, Kazan, Russia.

[2]Kazan State University, 420008, Kremlyovskaya Str., 18, Kazan, Russia.

e-mail: irek_rash@mail.ru

Phenols are a class of chemical compounds that have long been the subject of high interest of chemists and industrialists. The most common application of substituted phenols in the industry is their using as antioxidants [1-3]. The antioxidant properties of these phenols are caused by easy separation of the phenolic hydrogen and efficient purification of peroxy and alkoxy radicals which are key reagents in the autooxidation [4]. It is well known [5-6] that the efficiency of the antioxidant action of some phenolic stabilizers is determined by their spatial structure. At the same time the information about the spatial structure of these compounds in solutions and the conformations of their oxidation products is not enough.

Chemical changes in a phenolic moiety do almost not affect the reactivity and other properties of the unreacted phenolic fragments if the last separated by an aliphatic chain containing three atoms at least [7-8].

In this paper we considered some mono- and polynuclear phenols (fig.1).

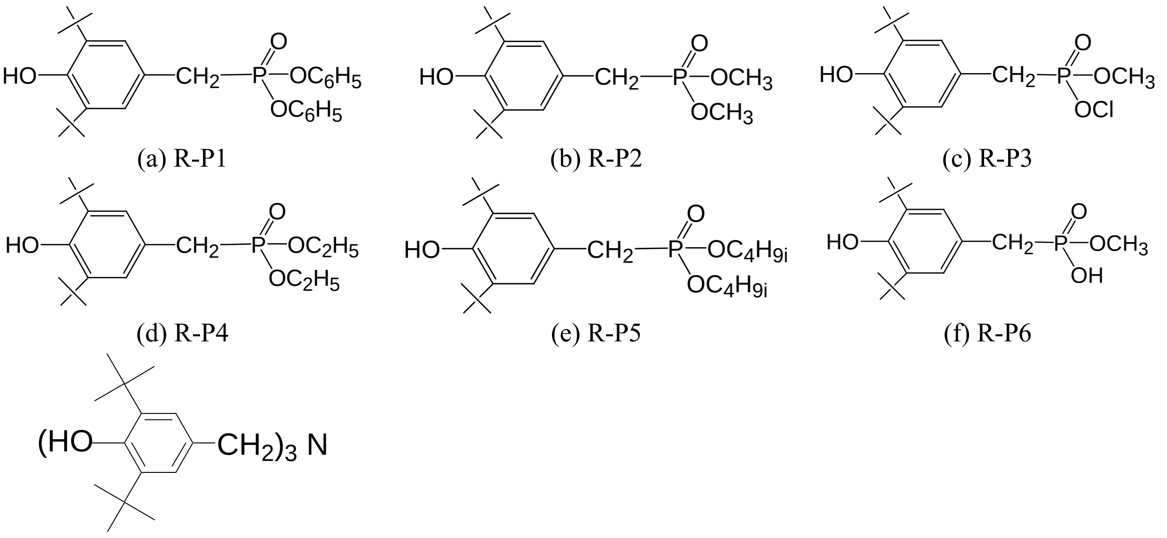

(a) R-P1 (b) R-P2 (c) R-P3

(d) R-P4 (e) R-P5 (f) R-P6

(g) 3R-N

Fig.1. (a-g). Considered phenols with a short notations

Free radicals were obtained by oxidation of source compounds dissolved in toluene ($1 \cdot 10^{-3}$M) using PbO_2. Freezing-pumping-defrosting technique was used to remove oxygen from the samples.

EPR spectra were recorded on Elexsys E500 (Bruker, Germany). Rectangular TE102 cavity was used in all measurements. Temperature dependences of the spectra were investigated using special temperature variator (Bruker, Germany).

Magnetic resonance parameters and relative intensities of the spectral components were determined by computer simulations of experimental EPR spectra using the simulation program WinSim.

The oxidation of phenol represents a detaching hydroxyl hydrogen and forming the phenoxyl radical.

Fig.2 shows EPR spectra of the free radical **R$^\cdot$-P1** obtained from phenol **R-P1** in the temperature range 170-309 K in toluene.

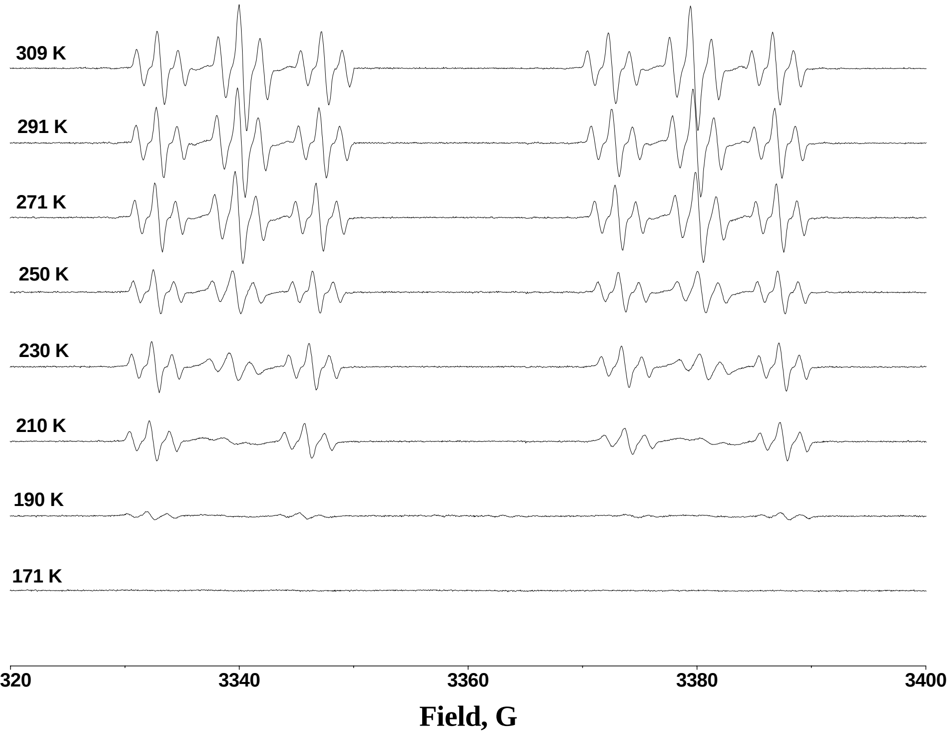

Fig.2. Temperature dependence of EPR spectra for **R$^\cdot$-P1**

One may notice that the rise in temperature leads to increasing an intensity of the triplets central lines. The ratio of the lines intensities is 1:2:1 at a temperature 309K.

This phenomenon is explained by the existence of energetically equivalent conformers 1 and 2 (fig.3). There are conformational transitions between these conformers. If we consider only β-protons the EPR spectrum should have four lines. If the β-protons are in nonequivalent positions, then $A_1 \neq A_2$, hyperfine structure (HFS) constants are not equal. So we can see 4 lines of equal intensity. If $A_1 = A_2$, i.e. both β-protons are equivalent, we observe 3 lines with intensity ratio 1:2:1.

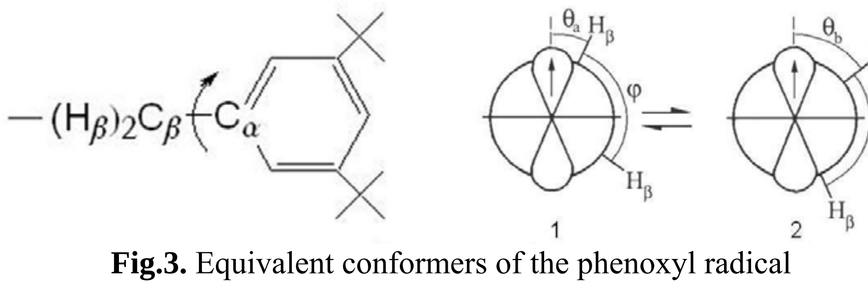

Fig.3. Equivalent conformers of the phenoxyl radical

Transitions between two conformers lead to transfer of β-protons from one position to another. It causes a modulation of hyperfine splitting in opposite phase. As a result an alternation of the EPR line widths is observed. When temperature is increasing these transitions become intensive, their frequency become comparable with a difference between the HFS constants of β-protons.

These preferred conformers can be estimated from the EPR spectra using the relation

$$a_{H(\beta)} = b \cos^2\theta, \qquad (1)$$

where parameter b is equal to 23.3 G for β-protons at the para-position to phenoxyl group [7].

For the EPR lines which in the initial spectrum are not overlapped the displacement is associated with a lifetime τ (correlation time) of conformational transitions by an equation [9]

$$\sqrt{\Delta H_0^2 - \Delta H_e^2} = \frac{\sqrt{2}}{\gamma_e}\tau\,, \tag{2}$$

where ΔH_0 is a distance between the lines in the absence of mutual transformations of 1 and 2, ΔH_e is that in the presence of mutual transformation. The temperature dependence of τ can be represented as

$$\tau = \tau_0 \exp\left(\frac{E_a}{RT}\right). \tag{3}$$

The graph of dependence of ln(τ) on the 1/T is a straight line (straight line of Arrhenius). Tilt of this line is equal to E_a/R. It is easy to verify that E_a = 4.5 kcal/mol.

A similar temperature dependence of the EPR spectra were observed for the other phosphorus phenols: **R-P2**, **R-P3**, **R-P4**, **R-P5**, **R-P6** (difference is only in the constants of the HFS). The activation energies for these compounds are equal to 4.7, 3.1, 3.5, 5.4, 4.8 kcal/mol respectively.

So, for this group of phenoxyl radicals freezing of conformers does not occur. The explanation of this effect is less hindered rotation due to the smaller steric influence of substituents.

Fig.4 shows the EPR spectra of free radical **3R·-N** in the temperature range 170-350 K in toluene. In a rigid matrix below the freezing point of pure toluene (178 K) one can see four broad lines; the middle two of them are becoming gradually broader when temperature increases (170-250 K). Consequently, these lines are reduced in intensity and come closer to each other.

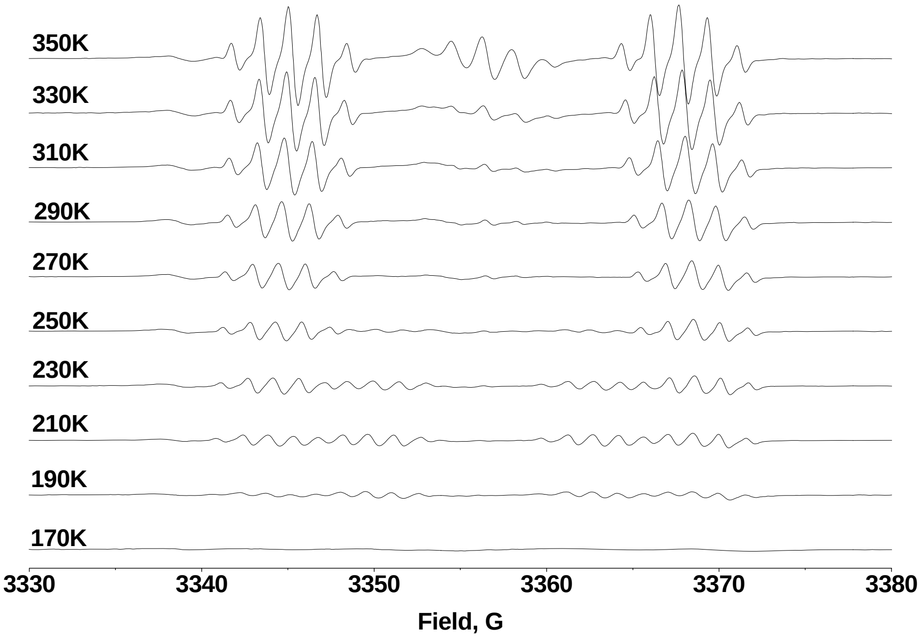

Fig.4. Temperature dependence of EPR spectra for **3R-N**

Correlation time of rotation for the case when β-atoms of hydrogen transit from one position to another and thereby cause the effect of EPR linewidth alternation can be written as [11]

$$\tau = \left(\sqrt{\frac{2I_{\pm 1}}{I_0}} - 1 \right) \frac{8T_{2,0}^{-1}}{\gamma_e^2 (a_1 - a_2)^2}, \qquad (4)$$

$I_{\pm 1}, I_0$ are intensities of flank non-overlapping lines of multiplets corresponding to the projections of the nuclear magnetic moment $m_I(CH_2) = \pm 1,0$; $T_{2,0}^{-1}$ is contribution to the line width of the other relaxation mechanisms, γ_e is gyromagnetic ratio of electron.

Since for **3R˙-N** radical $a_1(H_\beta)$ and $a_2(H_\beta)$ are different at low temperature from each other we can calculate the correlation time. In our case $\tau \approx 8.2 \cdot 10^{-10}$ s. Using (1) one can verify that $\theta_1 = 26°$ and $\theta_2 = 60°$.

So for the tris (2,6-di-tert-butyl-4-methyl-phenol) amine (**3R-N**) individual conformers can be detected at low temperature. Therefore the correlation time of transition between these conformers can be calculated.

Thus the linewidths alternation of the EPR spectra of considered phenoxyl radicals is due to the intramolecular motions.

References

[1] Талзи Е.П. Соросовский образовательный журнал. 2000. Т.6. №7. С.35-41.

[2] Ковтун Г.А., Пустарнакова Г.Ф. Катализ и нефтехимия. 2001. №7. С. 24-26.

[3] Тарбанько В.Е., Варганов С.А., Петухов Д.В. Химия растительного сырья. 1998. №3. С.99–106.

[4] Походенко. В.Д., Хижный В.А., Бидзиля В.А. Успехи химии. 1968. Т.37. №6. С.998-1024.

[5] Гурвич Я.А., Арзаманова И.Г., Заиков Г.Е. Хим. физика. 1996. Т.15. №1. с.23.

[6] Антонова Е.А., Парамонов Д.В. Вестник Московского университета. Сер.2. Химия. 1999. Т.40. №4. С.283-286.

[7] Рогинский В.А. М.: Наука. 1988. с.247.

[8] Бучаченко А.Л. Известия АН СССР. 1963. №6. С.1120-1123.

[9] Gutowsky H.S., Holm C.H. J. Chem. Phys. 1956. №25. C.1228.

EPR study of the vanadium-doped forsterite crystal

I.N. Gracheva[1], A.A. Rodionov[1], V.B. Dudnikova[2], M.Kh. Salakhov[1], N.I. Silkin[1],
V.F. Tarasov[3], R.V. Yusupov[1], E.V. Zharikov[4,5]

[1]Kazan Federal University, 420008, Kremlevskaya 18, Kazan, Russia
[2]M.V. Lomonosov Moscow State University, 119991, Leninskie Gory, Moscow, Russia
[3]Zavoisky Physical-Technical Institute KSC RAS, 420029, Sibirskii trakt 10/7, Kazan, Russia
[4]Mendeleev University of Chemical Technology of Russia, 125047, Miusskaya pl. 9, Moscow, Russia
[5]Prokhorov General Physics Institute RAS, 119991, Vavilova ul. 38, Moscow, Russia

e-mail: subirina@gmail.com

Oxide single crystals doped with the *3d*-ions in different valence states including the unusual ones often serve as the materials for quantum electronics. Forsterite Mg_2SiO_4 is one of such oxides. This material has gained much interest in the late 80s when tunable laser action in the near IR range was obtained on this crystal doped with the tetravalent chromium. Impurity Cr^{4+} ions substitute for the silicon which has a tetrahedral oxygen surrounding [1].

Vanadium is also a promising dopant of the forsterite crystals. First, vanadium-doped forsterite can be used as saturable absorber in the near IR range [2]. Second, a wideband fluorescence of the Mg_2SiO_4:V in the region of 1.6 – 2.0 μm makes these crystals promising as the laser active medium [3].

Pure natural forsterite is rare but the high quality crystals can be grown, for example, by the Czochralski technique. Forsterite has an orthorhombic symmetry (space group *Pbnm*) with the lattice constants a = 4.75 Å, b = 10.20 Å and c = 5.98 Å [4]. There are two types of the octahedrally-coordinated magnesium sites in the forsterite structure. Oxygen octahedral surrounding of the first type sites M1 are distorted to the symmetry C_i. Symmetry of the octahedral complexes of the second type is C_s, this magnesium site is M2. Tetrahedra containing silicon are distorted to the symmetry C_s. In principal, impurity vanadium ions can substitute for either magnesium in one of the octahedrally-coordinated sites M1 or M2 or for silicon in tetrahedrally-coordinated site. Besides, vanadium ions in forsterite can be in different oxidation states. In [5] results of the optical studies of the vanadium-doped forsterite crystals grown by the Czochralski technique were reported. The data indicated that the samples contained mainly the tetrahedrally-coordinated V^{4+} ions; presence of the trivalent V^{3+} centers in the samples was not excluded. Annealing in the oxidizing atmosphere resulted in partial transformation of the dopant to the V^{5+} state.

Optical studies do not allow the precise determination of the active center structure. Meanwhile, it is important to define accurately the properties of the impurity centers that are formed in the vanadium-doped forsterite. Especially it is crucial to know the oxidation state of vanadium and the lattice site it substitutes. For such studies the electron paramagnetic resonance (EPR) spectroscopy suites well. In this paper the first detailed EPR study results are reported for the forsterite crystal doped with vanadium.

Single crystals of Mg_2SiO_4 doped with 0.02 mol.% of vanadium were grown by the Czochralski technique. Studied sample was synthesized in an argon atmosphere with the admixture of 2 vol. % of hydrogen. Samples were oriented with X-ray diffraction and cut in the shape of the rectangular parallelepipeds. Crystallographic a, b, and c axes were perpendicular to the sample faces. Orientation accuracy was ±2°. Measurements were performed with Bruker ESP300 continuous wave (*cw*) X-band EPR spectrometer in the temperature range of 4 – 60 K. Rectangular TEM_{012} mode cavity was used with $\mathbf{H}_1 \perp \mathbf{H}_0$, where $\mathbf{H}_0$ is a permanent magnetic field and $\mathbf{H}_1$ – magnetic component of the microwave. Angular dependencies of the EPR spectra in the *ab*, *bc* and *ac* crystal planes were measured with the sample rotation about the *c*, *a* and *b* axes, respectively. Studies were performed mainly at $T = 10$ K as a significant broadening of the spectra due to relaxation processes developed with the temperature increase. With an arbitrary sample orientation the intense EPR spectra of the two magnetically-inequivalent centers in the magnetic field range corresponding to $g \sim 2$ were observed. Spectra had the typical hyperfine structure of ^{51}V consisting of eight components (natural abundance 99.8%, nuclear spin $I = 7/2$). No any additional EPR signals with the intensity comparable with that of the described spectra in the magnetic field range of 100 – 16000 Oe were observed. Observation of the signals at $g < 2$ would indicate the presence of paramagnetic centers with $S > ½$ in the crystal. This fact shows unambiguously that in the X-band the investigated sample spectra are dominated by the tetravalent vanadium V^{4+} which has an electronic configuration $3d^1$ and $S = 1/2$.

Angular dependencies of the spectra with H_0 oriented in the crystallographic planes *ab* and *ac* are shown in fig.1. It is obvious that the magnetic properties of the V^{4+} ion are significantly anisotropic: angular dependencies of the spectrum center and the distance between the hyperfine components are observed.

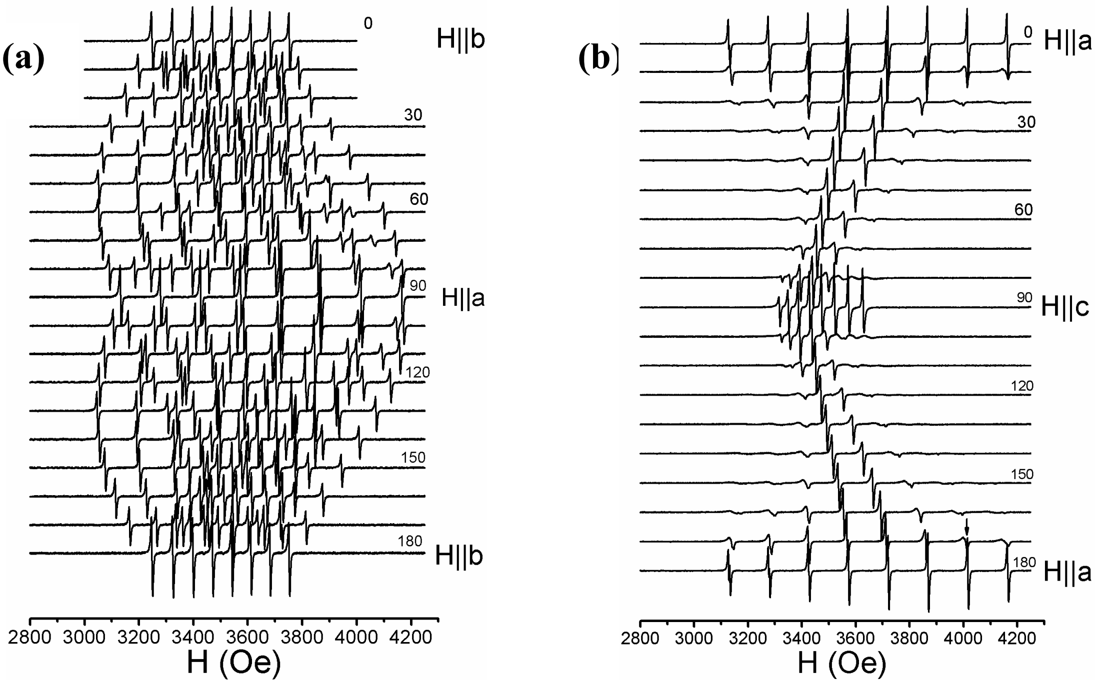

Fig.1. Angular dependencies of the EPR spectrum of V^{4+} impurity centers in forsterite at $T = 10$ K: a) in the *ab* plane of the crystal; b) in the *ac* plane.

Angular dependencies of the resonance field values of the EPR spectral lines in the *ab* and *ac* planes are shown in fig.2. Spectra dependencies on the angle were analyzed using spin Hamiltonian:

$$H = \beta \mathbf{H}\tilde{\mathbf{g}}\mathbf{S} + \mathbf{I}\tilde{\mathbf{A}}\mathbf{S}, \qquad (1)$$

where $\tilde{\mathbf{g}}$ and $\tilde{\mathbf{A}}$ were assumed to be tensors which principal axes were arbitrarily oriented and three principal values differed from each other. Axes of the *g*- and *A*-tensors didn't correlate. Calculations of the resonance fields were performed using *EasySpin* module subroutines [6]. Orientations of the tensor principal axes were specified by Euler angles. Fit of the angular

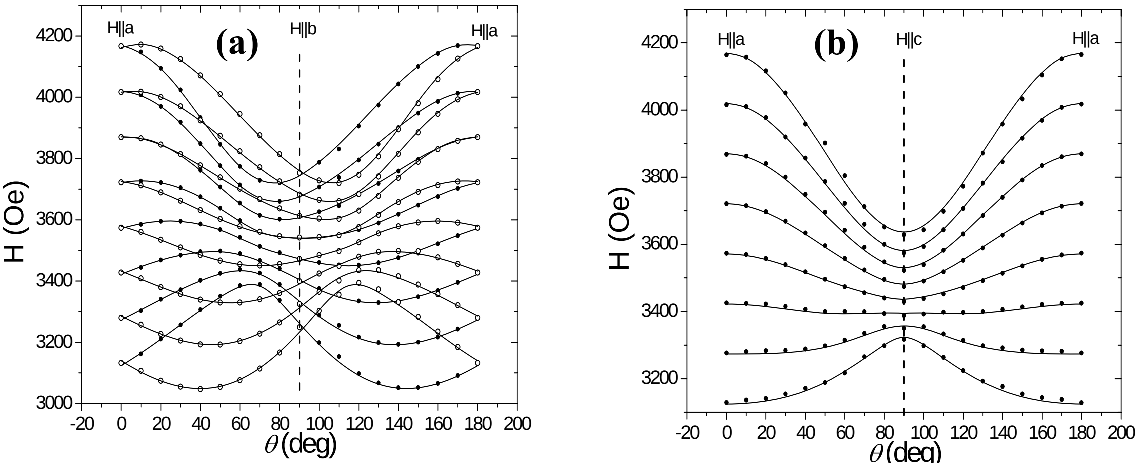

Fig.2. Angular dependencies of the resonance field values for the EPR spectrum components with the magnetic field oriented in the *ab* (a) and the *ac* crystal planes (b). Solid curves are the results of the fit using Hamiltonian (1).

dependencies of the resonance fields was performed by least-square technique in *Matlab*. Results of the fit are shown in fig.2 by solid lines. Clearly, the observed angular dependencies are described well within the frames of the paramagnetic center model characterized by spin ½ and anisotropic *g*- and *A*-tensors. Fit procedure has given the following values of the tensor principal values:

$$g_{xx} = 1.9078 \pm 0.0012;\ g_{yy} = 1.9203 \pm 0.0012;\ g_{zz} = 1.8264 \pm 0.0011;$$

$$A_{xx} = (127.7 \pm 0.5)\ \text{MHz} = (42.5 \pm 0.2)\times10^{-4}\ \text{cm}^{-1};$$

$$A_{yy} = (120.0 \pm 0.5)\ \text{MHz} = (40.0 \pm 0.2)\times10^{-4}\ \text{cm}^{-1};$$

$$A_{zz} = (401.0 \pm 1.4)\ \text{MHz} = (136.7 \pm 0.5)\times10^{-4}\ \text{cm}^{-1}.$$

Orientations of the *g*- and *A*-tensor principal axes with respect to crystallographic axes are described by the matrices presented in Table 1 (signs '±' in front of the direction cosine values correspond to the magnetically-inequivalent centers). *Y*-axes of the *g*- and *A*-tensors of the centers coincide with the *c* axis of the crystal, the angles between the *g*-tensor *z*-axes of the centers and *a* axis of the crystal are (15±2)° and (165±2)°; angles between the respective *A*-tensor *z* axes and crystallographic axis *a* are (-21±2)° and (-159±2)°.

Table 1. Orientations of the principal axes *x*, *y* and *z* of the *g*- and *A*-tensors with respect to crystallographic axes *a*, *b*, *c* (accuracy of the values is ±0.009).

Tensor axes	Crystallographic axes		
	a	*b*	*c*
g_x	0.259	±0.966	0
g_y	0	0	1
g_z	±0.966	-0.259	0
A_x	-0.358	±0.934	0
A_y	0	0	1
A_z	±0.934	0.358	0

It is interesting that when magnetic field is rotated in the *bc* and *ac* planes a significant angular dependence of the EPR linewidths is observed whereas when magnetic field is rotated about *c* axis in the *ab* plane linewidths are essentially unchanged. In our opinion, this observation is a clear indication of the magnetic center orientation disorder with respect to the *c* crystal axis. Such a disorder would lead to the EPR line broadening if there is a strong angular dependence of its resonance field. Indeed, the stronger the anisotropy of the resonance field value of the hyperfine pattern component in fig.2b, the stronger its width angular dependence. Quantitatively, in such situation the angular dependence of the linewidth should be proportional to the absolute value of the first derivative of the resonance field value $|dH_{res}/d\theta|$. Comparison of the observed linewidth dependence of one of the eight hyperfine components with a properly scaled $|dH_{res}/d\theta|$ for the component is shown in fig.3. Scaling coefficient was determined by the least-square technique and is equal to 6.0±0.2°. This value characterizes an orientation disorder of the centers. Thus, the linewidth characterized by the field difference between the maximum and the minimum of the absorption derivative is described by the angle distribution of ±(3±0.2)° with respect to the crystalline *c* axis.

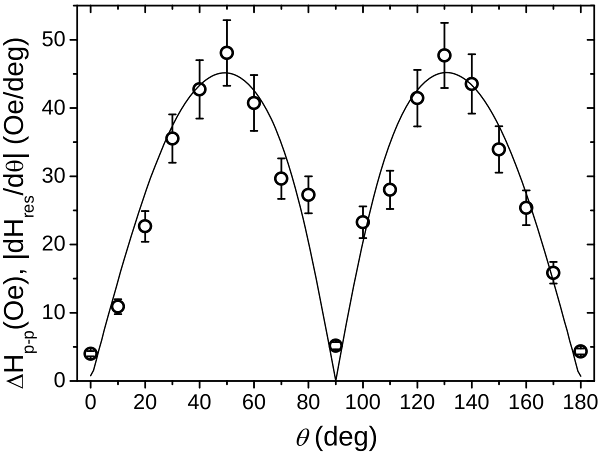

Fig.3. Angular dependence of the EPR linewidth for the hyperfine component of the V^{4+} center spectrum indicated in fig.1, b by the arrow (circles). Solid line is a properly scaled absolute value of the first derivative of the angular dependence for the same component (see text).

As far as the exact position of the V^{4+} ion in the crystal is concerned, an arbitrary orientation of the field $\mathbf{H_0}$ will produce four magnetically-inequivalent centers in the spectrum if the ions substitute for the magnesium site M1 and two magnetically-inequivalent centers if vanadium ions are in the M2 site [7]. In the case of the vanadium occupying the silicon site is equivalent from the symmetry considerations to its localization in the M2 site, so, two magnetically-inequivalent centers would be found.

Properties of the observed angular dependencies indicate that the V^{4+} ions in forsterite are located either in the M2 position substituting for Mg^{2+} in octahedral environment or in the silicon site. However, the optical data reported in [5] allows to resolve the dichotomy. Indeed, triplet structure of the excited state observed in the optical absorption spectra [5] characterizes the V^{4+} ions only in the tetrahedrally-coordinated silicon site.

We would like to notice also that the observation of an intense EPR signal of the tetravalent vanadium does not exclude presence of the vanadium in the crystal in a different oxidation state. Indeed, the EPR signals with the intensity two orders of magnitude weaker than the described one were found in the field range corresponding to $g > 2$. Some of the weak signals possessed the characteristic 8-component vanadium hyperfine structure, some had the large width. In our opinion, these signals most probably originate from V^{2+} and V^{3+} ions, respectively. Nevertheless, the detailed study of these centers is beyond the limits of the current report.

Thus, the X-band *cw*-EPR study of the Mg_2SiO_4:V crystal grown by the Czochralski technique in a reducing atmosphere has shown that in these growth conditions one type of the V^{4+} centers ($S = ½$) is formed predominantly in the crystal. These centers correspond to the V^{4+} ions localized in the silicon site with tetrahedral oxygen surrounding. Principal values of the *g*- and *A*-tensors of the studied centers as well as their orientations in crystal were defined. Presence of the V^{4+}-center orientation disorder with respect to the c-axis was shown and characterized.

Authors are grateful for a financial support from RFBR, project No. 09-07-97006 and the grant of the President of the Russian Federation NSh-267.2010.2.

References

[1] V. Petricevic, S.K. Gayen, R.R. Alfano, K. Yamagishi, H. Anzai and Y. Yamaguchi. *Appl. Phys. Lett.* **53**, 2590 (1988).

[2] E.V. Zharikov and V.A. Smirnov. Wide Gap Luminescent Materials: Theory and Applications (Kluwer Academic, Nowell, MA, 1997), pp. 13-337.

[3] A.G. Avanesov, V.G. Dvornikova, V.V. Zhorin, et al. *J. Appl. Spectrosc.* **59** (1–2), 582 (1993).

[4] C. Klein and C. Hurlbut, Jr. Manual of Mineralogy, 20th ed., Wiley, pp. 373-375 (1985).

[5] T.F. Veremeichik, E.V. Zharikov, V.B. Dudnikova, A.V. Gaister, N.N. Eremin, V.A. Smirnov, K.A. Soubbotin, V.S. Urusov, and I.A. Shcherbakov. *Optical Materials* **19**, 319 (2002).

[6] S. Stoll and A. Schweiger. *J. Magn. Reson.* **178**, 42 (2006).

[7] H. Rager. *Phys. Chem. Minerals* **1**, 371 (1977).

Table of Contents

TABLE OF CONTENTS

ACTUAL PROBLEMS OF MAGNETIC RESONANCE AND ITS APPLICATION

XII International Youth Scientific School

Program Lecture Notes Proceedings

Kazan
4 – 8 October 2009

Подписано в печать 29.09.10.
Бумага офсетная. Печать ризографическая.
Формат 60x84 1/8. Гарнитура «Times New Roman». Усл.печ.л. 24,75
Уч.-изд.л. 23,01. Тираж 90 экз. Заказ 171/9

Отпечатано с готового оригинал-макета в типографии
Издательства Казанского университета

420008, г. Казань, ул. Профессора Нужина, 1/37
тел. (843) 233-73-59, 292-65-60

ISBN 978-5-98180-835-7

9 785981 808357 >